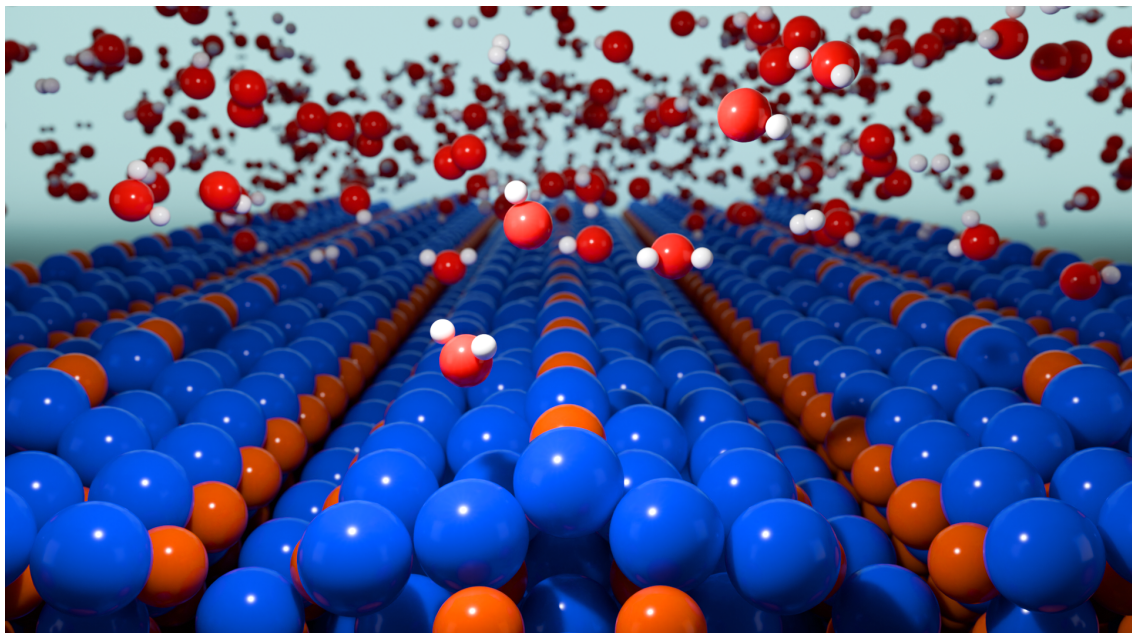


III-V surface physics for photoelectrochemical water splitting



Dissertation submitted for the degree of
Doctor rerum naturalium (Dr. rer. nat.)

Isaac Azahel Ruiz Alvarado

Department of Physics, Faculty of Science
Paderborn University

Paderborn, April, 2025

Promotionskommission

| | |
|---------------------------|---|
| Vorsitzender: | Prof. Dr. Donat As Optoelectronic semiconductors – Group III-nitrides Department Physik – Universität Paderborn |
| Gutachter: | Prof. Dr. Wolf Gero Schmidt Theoretical Materials Physics Department Physik – Universität Paderborn |
| Gutachter: | Prof. Dr. Friedhelm Bechstedt Institut für Festkörpertheorie und Optik – Friedrich-Schiller-Universität Jena |
| Vertreter des Mittelbaus: | Dr. Tobias Henksmeier Optoelectronic materials and devices Department Physik – Universität Paderborn |

Erklärung

Hiermit erkläre ich, Isaac Azahel Ruiz Alvarado geboren am 12.01.1995 in Salinas de Hidalgo, S.L.P., México, dass ich die vorliegende Dissertation ohne fremde Hilfe und ohne Benutzung anderer als der angegebenen Quellen angefertigt habe und, dass diese in gleicher oder ähnlicher Form noch keiner anderen Prüfungsbehörde vorgelegt habe. Alle Ausführungen, die wörtlich oder sinngemäß übernommen worden sind, sind als solche gekennzeichnet.

Ort, Datum

Unterschrift

Abstract

InP and AlInP are used extensively in numerous technological applications, in grand part due to their astounding electronic and optical properties. In particular both materials are used show promise in solar-powered photoelectrochemical water splitting devices. These devices are often limited by factors like corrosion that hinder the water-splitting reaction. In order to increase the efficiencies of these devices it is necessary to understand not only how the surfaces of the semiconductors oxidize but also how the water-splitting mechanism takes place in the water/surface interface.

In this work the electronic properties of oxidized Al/In-rich AlInP and InP surfaces are investigated from density functional theory (DFT) calculations. Oxygen evolution and hydrogen reduction reactions are investigated for the water splitting mechanism on top of the In-rich InP surface. The absolute position of the conduction and valence bands are calculated in respect to the water evolution and reduction potentials utilizing hybrid functionals. For the P-rich InP surface H defects are looked into as the origin behind experimentally observed strong band bending. How the H vacancy interacts with water molecules is also computed. Finally the reflectance anisotropy spectroscopy (RAS) is calculated for different AlInP(001) surfaces by solving the Bethe-Salpeter equation. The origin behind the spectra fingerprints is explored and assigned to specific surface motifs.

Zusammenfassung

InP und AlInP werden aufgrund ihrer herausragenden elektronischen und optischen Eigenschaften in zahlreichen Anwendungen genutzt. Insbesondere zeigen beide Materialien großes Potenzial für die photoelektrochemische Wasserspaltung. Die Effizienz sowie die Haltbarkeit der Elektroden werden jedoch durch Korrosion stark beeinträchtigt. Um die Leistungsfähigkeit der Systeme zu verbessern, ist es notwendig, nicht nur den Oxidationsprozess der Oberflächen, sondern auch den Mechanismus der Wasserspaltung an der Grenzfläche zwischen Wasser und Halbleiter zu verstehen.

In dieser Arbeit werden die elektronischen Eigenschaften oxiderter Al/In-reicher AlInP- und InP-Oberflächen mithilfe von Dichtefunktionaltheorie (DFT)-Berechnungen untersucht. Die Sauerstoff- und Wasserstoffentwicklungsreaktionen für die Wasserspaltung auf der In-reichen InP-Oberfläche werden analysiert. Die absoluten Positionen der Leitungs- und Valenzbänder werden in Bezug auf die Redoxpotentiale der Wasserspaltung unter Verwendung hybrider Funktionale berechnet. Für die P-reiche InP-Oberfläche werden H-Defekte als mögliche Ursache der experimentell beobachteten starken Bandverbiegung untersucht. Zudem wird berechnet, wie H-Vakanzien mit Wassermolekülen wechselwirken. Schließlich werden Reflexionsanisotropiespektren (RAS) für verschiedene AlInP(001)-Oberflächen durch Lösung der Bethe-Salpeter-Gleichung berechnet. Die Ursprünge der spektralen Signaturen werden analysiert und spezifischen Oberflächenmotiven zugeordnet.

Contents

Abstract**Zusammenfassung**

| | | |
|----------|---------------------|----------|
| 1 | Introduction | 1 |
|----------|---------------------|----------|

| | | |
|----------|----------------|----------|
| I | Methods | 5 |
|----------|----------------|----------|

| | | |
|----------|-----------------------------|----------|
| 2 | Electronic structure | 7 |
|----------|-----------------------------|----------|

| | | |
|-------|---|----|
| 2.1 | Density Functional Theory | 8 |
| 2.1.1 | Hohenberg-Kohn Theorems | 8 |
| 2.1.2 | Kohn-Sham method | 10 |
| 2.1.3 | Exchange-correlation energy | 12 |
| 2.1.4 | Ionic forces | 15 |
| 2.1.5 | Electronic structure and the band gap problem | 16 |
| 2.2 | Hybrid functionals | 18 |
| 2.2.1 | Range-separated hybrid functionals | 19 |
| 2.3 | GW approximation | 19 |
| 2.3.1 | Green's function | 20 |
| 2.3.2 | Hedin's equations | 20 |
| 2.3.3 | Numerical implementation | 23 |

| | | |
|----------|--|-----------|
| 3 | First-principles atomistic thermodynamics | 25 |
|----------|--|-----------|

| | | |
|-------|--|----|
| 3.1 | Surface formation energy | 25 |
| 3.1.1 | Chemical potential for molecules | 26 |
| 3.1.2 | Surface-free energy | 27 |
| 3.2 | Lattice vibrations | 28 |
| 3.3 | Defects in crystals | 29 |
| 3.4 | Nudged elastic band method | 30 |
| 3.4.1 | Climbing image NEB | 31 |

| | |
|---|-----------|
| 4 Optical spectroscopy | 33 |
| 4.1 Dielectric response function | 33 |
| 4.2 Local-field effects | 36 |
| 4.3 Bethe-Salpeter equation | 37 |
| 4.3.1 The electron-hole interaction | 39 |
| 4.3.2 Absorption Spectrum | 41 |
| 4.3.3 Model-BSE | 42 |
| 4.4 Reflectance anisotropy spectroscopy | 42 |
| II Results | 45 |
| 5 O₂ and H₂O on In-rich InP surfaces | 47 |
| 5.1 Methodology | 48 |
| 5.2 InP(001) In-rich surface oxidation | 48 |
| 5.2.1 Adsorption geometries | 49 |
| 5.2.2 Electronic properties | 51 |
| 5.3 Water adsorption on InP mixed-dimer surface | 52 |
| 5.3.1 Molecular water adsorption | 54 |
| 5.3.2 Increased water coverage | 56 |
| 5.3.3 Water splitting reaction mechanism | 59 |
| 5.3.4 Band alignment for In-rich InP surface | 65 |
| 5.4 Conclusions | 67 |
| 6 P-rich InP surface: Defects and water | 69 |
| 6.1 Hydrogen defects | 70 |
| 6.1.1 Substrate doping and charged defects | 72 |
| 6.2 Water adsorption | 73 |
| 6.3 Conclusions | 76 |
| 7 Al/In-rich AlInP surface oxidation | 79 |
| 7.1 Surface geometry | 80 |
| 7.2 Surface oxidation | 82 |
| 7.2.1 Electronic properties | 85 |
| 7.3 Conclusions | 86 |
| 8 Optical spectra for AlInP surfaces | 89 |
| 8.1 Methodology | 90 |
| 8.2 P-rich surfaces | 91 |
| 8.2.1 2D-2H surface | 91 |
| 8.2.2 Other P-rich surfaces | 93 |
| 8.2.3 Effect of bulk ordering | 94 |
| 8.3 In-rich AlInP(001) | 96 |
| 8.3.1 The rInMD surface model | 96 |
| 8.3.2 Other cation-rich surfaces | 98 |
| 8.4 Conclusions | 99 |

| | |
|---|------------|
| 9 Summary & Conclusion | 101 |
| Bibliography | 105 |
| List of Publications | 123 |
| Additional scientific publications | 124 |
| Conference proceedings | 124 |
| A Relaxed geometries of relevant surfaces | 125 |
| B Electronic structures of relevant surfaces | 129 |



* Mayan numerals have been used instead of roman numerals for the front matter.



Chapter 1

Introduction

Energy demand is ever-growing, and meeting it is becoming more and more challenging. The demand is currently primarily satisfied by fossil fuels, accounting for more than 80% of global consumption[1]. However, fossil fuels present many disadvantages, among many, being non-renewable and a pollutant to our environment. This has resulted in an increased effort in finding alternative energy resources. In the search for renewable resources, among others, hydrogen has received a lot of attention as an alternative fuel due to, e. g., being a clean fuel, light weight, and high energy density[2–4]. Currently, one of the main reasons why we have not transitioned to a hydrogen-fuel society are the difficulties in its production. While molecular hydrogen can be produced from steam methane reforming, it is not a completely carbon-free method as part of the reaction, as carbon dioxide is produced as a residue[5]. An alternative is solar-powered photoelectrochemical water splitting, where solar energy is stored in chemical bonds by splitting water molecules into molecular hydrogen and oxygen[6]. This process is sustainable as it uses solar energy and water to produce hydrogen, and water is regenerated when consuming the hydrogen to release the stored energy.

The water-splitting reaction requires a potential of 1.23 V equivalent to the difference between the water oxidation and water reduction. An efficient photovoltaic material is required to overcome this overpotential and drive the water oxidation and reduction reactions at desirable rates. For a semiconductor to drive the reaction without additional bias potential would require that the water oxidation and reduction potentials lie within the material's band gap. This restricts the search for candidates with a large enough band gap, but not too large to ensure that the majority of the solar spectrum can be taken advantage of. These problems are avoided by tandem structures, consisting of two or more photovoltaic absorber layers with different energy band gaps stacked together. Indeed, silicon-based tandem solar cells have been shown to surpass the efficiency limits of single photoabsorbers[7].

Deterioration of the semiconductors in working conditions is also an important issue that has to be considered when exploring materials. The photoinduced deterioration, i. e., photocorrosion of the semiconductors due to chemical and photochemical reactions in aqueous electrolytes is a significant drawback that decreases the operation lifetime. Therefore, a thorough understanding of the mechanism is crucial for guaranteeing the photostability of devices[6, 8].

Semiconductor alloys comprising group III (B, Al, In, Ga) and group V (N, P, As, Sb) elements, commonly referred to as III-V semiconductors, are used extensively in microelectronic and optoelectronic devices because of their excellent combination of properties. III-V semiconductors have found significant use in diverse fields, i. e., in quantum dots[9], quantum wells[10] and nanowires[11] devices. In particular, these alloys have also been implemented in solar cells with

exceptional efficiencies [12–14]. The current solar cell record for highest solar-to-energy efficiency is held by a quadruple junction III-V photovoltaic with a solar energy conversion efficiency of 47.6% [15]. Indium phosphide and its ternary and quaternary alloys have found extensive application in a wide range of fields, being, for example, the basis for high-speed integrated circuits [16, 17], photonic devices[18] and in nanotechnology devices [19, 20]. InP has also a long history of being used in combination with other materials for solar-powered water splitting devices, [21–25].

The great success of binary V-III in water splitting applications is however restricted to a couple of alloys with fixed band gaps and lattice constants. This last point is important for tandem structures where defects caused by mismatched lattice constants in the interface between semiconductors. These problems are tackled by ternary III-V alloys, allowing for fabricating semiconductors with desired band gaps and lattice constants[26]. An excellent ternary semiconductor is aluminum indium phosphide which has been extensively used in optoelectronic devices[27–31]. Adjusting the absolute position of the band edges with regard to the water splitting energies is also possible using ternary materials. The search for optimal ternary III-Vs for use in tandem systems has led to the creation of a cell with solar-to-hydrogen efficiency of 14% and potentiostatically assisted efficiency of 17% [32]. This tandem structure consists of a GaInP based top absorber, a GaInAs bottom absorber, and an AlInP window layer for electron collection. Furthermore, the AlInP window layer surface was oxidized, resulting in a mixed In/Al oxide layer which was subsequently functionalized. Such oxide layers can be detrimental for carrier recombination by forming barriers for holes[33].

Although AlInP has been successfully used in several different applications, a lot of its aspects and properties still remain unclear. Only recently, and in the context of this work, the AlInP surface reconstructions have been proposed and investigated both experimentally and theoretically [34]. Several experimental techniques were used in order to probe surface reconstructions chemically and electronically. Besides the ones reported in Ref. [34], there are optical techniques for surface probing, e. g., reflectance anisotropy spectroscopy (RAS), that allow measurement *in situ* while growing the samples. Understanding the origin of optical spectra characteristic of individual surfaces would not only allow for probing the surface while growing, but ultimately control the growth of specific geometries. The connection between the optical spectra from RAS and the surface can be understood from theoretical calculations by investigating the macroscopic dielectric function[35]. This has been successfully implemented for other semiconductors in the past[36–38]. Although experimental RAS measurements have been produced before for AlInP, no theoretical studies had been performed before[39, 40]. Fully investigating both the electronic and the optical properties of AlInP would lead to fabrication of devices with tailored properties and increased efficiencies.

The devices for photoelectrochemical water splitting discussed so far are prone to corrosion when operating in contact with water, resulting in oxide layers[6, 41]. Sometimes, an oxide layer is beneficial and desired on some devices as a passivating layer[32, 42]; other times oxidation can be detrimental for the electron mobility[33, 43]. Understanding the effects of the interface between oxide layer and the semiconductor is therefore necessary for further development of devices. This is especially true for semiconductors like AlInP that are highly reactive towards oxygen. There are many studies, both experimental and theoretical in nature, that characterize the interface between InP and oxide layer [44–46]. Although the surface determines the exact oxide species formed, In–O–In and In–O–P bonds are expected to form[47]. Nevertheless, there are still many unknowns when it comes to exploring the full oxide interface for InP, e. g., how the ox-

idation progresses and affects on the electronic structure. Comparatively, even less information is available when discussing AlInP surfaces. On the experimental end, progress has been made, e. g., on the insulator and electronic properties of native oxide layers[48]; However, the exact composition and nature of the interface remained unclear, in large part due to the unknown surface geometries. A good starting point for exploring the interface is to make comparisons between other III-V semiconductors, in particular those containing phosphorus. This is another reason why a more complete understanding of InP oxides is of great interest.

There is a clear drive for the understanding of the water splitting mechanism on InP surface due to the promising results. Yet, there is still much to understand regarding the interaction between water and the surface: Initial experimental[49] and theoretical[50] studies suggested that dissociative water adsorption results in In–O–P bonds. The water splitting reaction is split into the oxygen evolution reaction (OER) and hydrogen evolution reaction (HER). Water dissociating would be the first step for the OER associative mechanism; however, the full reaction has not been explored on an InP surface. It is known which bulk materials present band edges compatible with the water oxidation and reduction potentials[42]. Having said that, additional surface states are sure to modify the electronic structure and possibly change whether the water-splitting reaction is possible without a bias potential on the surfaces. In addition to corrosion, surface defects also play an important role in the efficiency of devices; still, this is not fully understood, especially in contact with a liquid electrolyte. These defects could provide an opportunity for water to adsorb at the surface or impede the water-splitting process altogether.

This motivates the present study, which will focus on understanding the electronic and optical properties of AlInP and InP. In Part I, the fundamental theoretical concepts handled throughout this work are introduced. Starting in Chapter 2 the density functional theory (DFT) in the Kohn-Sham formalism is described. Here, the limitations of this theory and the different approximations needed to circumvent these are discussed. Beyond DFT, Hybrid functionals and GW approximation (GWA) are also introduced for more accurate calculations when dealing with the electronic structure. Furthermore in Chapter 3 is dedicated to using DFT calculations for a better comparison with experiments by including thermodynamic quantities. More precisely, the Gibbs free energy is explained for the calculation of the surface formation energy, also necessary when dealing with surface defects. Afterwards, the nudged elastic band (NEB) method is also described, which serves to study the pathways that adsorption or desorption processes take for the water-splitting chemical reactions. Finally, in Chapter 4 the macroscopic dielectric function is derived, needed for the optical spectroscopy calculations. In the beginning the equations are introduced in the independent particle approximation (IPA). Beyond IPA exchange and excitonic effects are included in the solution of the Bethe-Salpeter equation (BSE). The connection from the macroscopic dielectric function to the RAS calculations is also explained in this chapter.

Part II of this work is dedicated to the discussion of the results obtained for InP and AlInP from the application of the concepts introduced in the first part. Two main phases are known for the InP surface: The In-rich and the P-rich surfaces. The former is discussed in Chapter 5. More precisely the surface geometry and electronic structure are calculated and discussed for oxidized In-rich InP surfaces. The full water-splitting mechanism as well as the band-alignment of the water/surface interface are also explored in this chapter. Chapter 6 focuses on the P-rich InP surface defects and how they interact with water. The AlInP surfaces and oxide layers are considered in Chapter 7. Within Chapter 8, the fingerprints of the optical spectra for different AlInP surfaces are identified and compared directly to RAS measurements. The final Chapter 9 serves as the conclusion to this thesis with a summary and outlook of the topics addressed in this work.

Part I

Methods

Chapter 2

Electronic structure

All fundamental properties of a solid can be derived by describing the system in a quantum mechanics picture. The wavefunction Ψ is the mathematical description of the system, containing the information of its quantum state. The Schrödinger equation, then, describes how the system and its wavefunction evolves over time. In an atomic scale, a solid can be interpreted as a collection of interacting particles, nuclei surrounded by a cloud of electrons. Therefore, the state of a system is described by all the M nuclei and N electrons. The description of the wavefunction $\Psi(\mathbf{R}_1, \mathbf{R}_2, \mathbf{R}_3, \dots, \mathbf{R}_M, \mathbf{r}_1, \mathbf{r}_2, \mathbf{r}_3, \dots, \mathbf{r}_N, t)$ in real-space depends on the positions of each particle, where \mathbf{R}_I is the position of the nuclei I , \mathbf{r}_i the position of electron i and t the time. The time-independent Schrödinger equation of this system is given by

$$\hat{H}\Psi_n = E_n \Psi_n, \quad (2.1)$$

where \hat{H} is the many-body Hamiltonian and E_n the eigenvalues of the eigenstates Ψ_n . The Hamiltonian represents the total-energy contribution from the interacting particles and is commonly expressed as the sum of all the energy operators: the kinetic energy of the moving particles \hat{T} and the electronic potential energy caused by the electrostatic interaction of particles \hat{V} .

$$\hat{H} = \hat{T} + \hat{V}. \quad (2.2)$$

The kinetic energy is given by the momentum operator \hat{p} ; this operator can be separated in the contributions of the electrons of mass m_e and the nuclei of mass M_I . Throughout this chapter, atomic units will be used to simplify notation. The corresponding kinetic energy contributions are then

$$\hat{T}_e = - \sum_{i=1}^N \frac{1}{2} \nabla_i^2 \quad (2.3a)$$

$$\hat{T}_n = - \sum_{I=1}^M \frac{1}{2M_I} \nabla_I^2. \quad (2.3b)$$

The electrostatic interaction, also known as Coulomb interaction, between the different particles is given by three operators, defined by the type of particles interacting: electron-electron repulsion, electron-nucleus attraction and nucleus-nucleus repulsion. Respectively, the operators are:

$$\hat{V}_{ee} = \sum_{i=1}^N \sum_{j=1}^{i-1} \frac{1}{|\mathbf{r}_i - \mathbf{r}_j|} \quad (2.4a)$$

$$\hat{V}_{\text{en}} = - \sum_{i=1}^N \sum_{I=1}^M \frac{Z_I}{|\mathbf{r}_i - \mathbf{R}_I|} \quad (2.4b)$$

$$\hat{V}_{\text{nn}} = \sum_{I=1}^M \sum_{J=1}^{I-1} \frac{Z_I Z_J}{|\mathbf{R}_I - \mathbf{R}_J|}, \quad (2.4c)$$

where Z_k is the atomic number.

Unfortunately, it is impossible to find the exact solution for the many-body system. Furthermore, the many-body equation is not separable in much simpler single particle equations due to the interaction terms, equations 2.4. Numerical solutions to the problem do exist, however, but even these require vast amounts of computational effort to solve. Thus, approximations are in order, the first of which is the Born-Oppenheimer or adiabatic approximation[51]. The nuclei are much more massive than the electrons; the kinetic energies thus differ by a factor of the order of magnitude of $m_e/M_I \sim 10^{-3}$. In other words, the electrons are moving much faster than the nuclei, and therefore the nuclei can be considered static compared to the relative speeds of the electrons. Under this approximation, the electrons are considered as quantum particles moving in an electric field generated by the nuclei. The potential acting on the electrons due to the nuclei field is now renamed as the external potential \hat{V}_{ext} . This term can also include other “external” potentials, like the Zeeman effect[52]. The nuclei kinetic energy term \hat{T}_{nn} is not needed to describe the interacting electrons and can be omitted for the calculations and only added in the last step.

2.1 Density Functional Theory

Density functional theory (DFT) is a theory of correlated many-body systems. There exist different methods to treat the many-body problem; among them, DFT stands out as a relatively low computational cost method. The principle tenet of DFT is that any property of a system of interacting particles can be expressed as a functional of the ground-state electron density. The electronic density becomes the principle quantity behind the DFT. For a system of N particles interacting with an external potential, \hat{V}_{ext} , the expectation value of the electronic density is

$$n(\mathbf{r}) = \left\langle \sum_i \delta(\mathbf{r} - \mathbf{r}_i) \right\rangle = N \int d^3 r_2 \int d^3 r_3 \dots \int d^3 r_N \Psi^*(\mathbf{r}_1, \mathbf{r}_2, \dots, \mathbf{r}_N) \Psi(\mathbf{r}_1, \mathbf{r}_2, \dots, \mathbf{r}_N). \quad (2.5)$$

The theoretical framework of the DFT is given by the Hohenberg-Kohn Theorems. The utility of the DFT is given with the Kohn-Sham method, where the many-body interacting problem is replaced with an independent particle problem. This section serves as a general introduction to the DFT following the references [53, 54].

2.1.1 Hohenberg-Kohn Theorems

Solving the Schrödinger equation gives the external potential that determines all states of the system, including the ground-state $\Psi_0(\mathbf{r}_1, \mathbf{r}_2, \dots, \mathbf{r}_N)$, which in turn allows for determining the ground-state electronic density, i. e., one can obtain a map from the external potential \hat{V}_{ext} to the electronic density $n_0(\mathbf{r})$. Hohenberg and Kohn, in their famous 1964 paper[55] showed that this

mapping can be inverted and that all properties of the system can be considered functionals of this electronic density. Schematically, this mapping is shown in the following relation

$$V_{\text{ext}}(\mathbf{r}) \Leftrightarrow \Psi_0(\mathbf{r}_1, \mathbf{r}_2, \dots, \mathbf{r}_N) \Leftrightarrow n_0(\mathbf{r}). \quad (2.6)$$

Indeed, the heart of density functional theory is based on the two theorems first proven by Hohenberg and Kohn.

Theorem 2.1. *For any system of interacting particles in an external potential $V_{\text{ext}}(\mathbf{r})$, the ground-state density $n_0(\mathbf{r})$, determines the external potential, $V_{\text{ext}}(\mathbf{r})$, up to a trivial additive constant.*

Since the density uniquely determines the $V_{\text{ext}}(\mathbf{r})$ and the Hamiltonian up to an additive constant, then in turn all the wavefunctions can be determined. As a consequence, the ground-state expectation value of all observables are functionals of the ground-state density $n_0(\mathbf{r})$. Therefore, every observable can be determined from the density. Among these, the ground-state energy, perhaps the most important observable.

Theorem 2.2. *The ground-state of the energy of the system is the global minimum of the energy functional $E[n]$. The density that minimizes this functional is the ground-state density $n_0(\mathbf{r})$.*

This means that the ground-state energy of a system can be obtained from the energy functional $E[n]$. The energy functional can be split into the internal and external contributions and from the variational principle the following relation is obtained

$$E[n] = F[n] + \int d^3r V_{\text{ext}}(\mathbf{r}) n(\mathbf{r}) \geq E[n_0] = E_0, \quad (2.7)$$

where the E_0 is the ground-state energy of the system with an external potential $V_{\text{ext}}(\mathbf{r})$. The density defined here is associated with the ground-state wavefunction of some external potential. This is called “V-representability”[53, 54]. The functional $F[n]$ includes all internal energy contributions, the kinetic and potential, from the interacting electrons. Levi[56–58] and Lieb[59] gave an alternative definition to the functional, which is more generalized and permits degenerate states, otherwise not available in the Hohenberg-Kohn Theorems. Under the proposed constrained search formalism, the functional is written as

$$F[n] = \min_{\Psi \rightarrow n} \{ \langle \Psi | \hat{T}_e + \hat{V}_{ee} | \Psi \rangle \}, \quad (2.8)$$

the minimization is constrained to all wavefunctions that yield the density $n(\mathbf{r})$. Thus, the ground-state energy E_0 is found with the following procedure

$$E_0 = \min_n \left\{ F[n] + \min_{\Psi \rightarrow n} \int d^3r V_{\text{ext}}(\mathbf{r}) n(\mathbf{r}) \right\} = \min_n E[n], \quad (2.9)$$

the outer minimization is carried through all $n(\mathbf{r})$, releasing the constraint imposed by equation 2.8. Thus, the universal functional $F[n]$ independent of the external potential has been established, and by the optimization of this functional, the exact ground-state energy of the interacting many-body system can be found. The functional is defined for any density n derivable from some wavefunction of the N -electron system. This is called “ N -representability”, in contrast to the “V-representability” density of the Hohenberg-Kohn Theorems [53].

2.1.2 Kohn-Sham method

The appeal of DFT is clear, as the equations involved are much simpler than the many-body problem with $3N$ degrees of freedom for N electrons. However, until this point, no method has been proposed to find the functionals other than the original formulations in terms of the wavefunction of the many-body problem. A year after his original paper, in 1965, Kohn together with Sham proposed a set of equations to simplify the problem[60]. The basic principle behind the Kohn-Sham (KS) approach is to assume that the ground-state density of the interacting system is exactly equal to that of an auxiliary system of non-interacting particles, also called independent particles. The auxiliary Hamiltonian is constructed to have the usual kinetic operator, and all the electron-electron interactions are represented in an effective potential operator \hat{V}_{eff} . In other words, the auxiliary system of N non-interacting particles in an effective potential gives a ground-state density such that it is identical to the interacting system.

The electron density expressed in terms of N one-particle orthonormal orbitals φ_i of the non-interacting system is

$$n(\mathbf{r}) = \sum_i^N |\varphi_i(\mathbf{r})|^2. \quad (2.10)$$

The kinetic energy of the N non-interacting particles system is

$$T_s[n] = \sum_i^N \left\langle \varphi_i \left| -\frac{1}{2} \nabla^2 \right| \varphi_i \right\rangle = -\frac{1}{2} \sum_i^N \int d^3r \varphi_i^*(\mathbf{r}) \nabla^2 \varphi_i(\mathbf{r}). \quad (2.11)$$

The total-energy functional in terms of the non-interacting kinetic energy $T_s[n]$ is expressed as:

$$E[n] = T_s[n] + E_H[n] + E_{\text{xc}}[n] + \int d^3r V_{\text{ext}}(\mathbf{r}) n(\mathbf{r}), \quad (2.12)$$

here it is convenient to separate the interaction energy functionals, $E_H[n]$ the Hartree energy and $E_{\text{xc}}[n]$ the exchange-correlation energy. The Hartree energy is the classical Coulomb interaction of the electron density $n(\mathbf{r})$ interacting with itself

$$E_H[n] = \frac{1}{2} \int d^3r d^3r' \frac{n(\mathbf{r})n(\mathbf{r}')}{|\mathbf{r} - \mathbf{r}'|}. \quad (2.13)$$

All remaining interaction terms, the exchange and correlation effects from the interacting particles of the many-body system, are contained within the exchange-correlation energy E_{xc} , this term will be explored further in section 2.1.3. From equation 2.8 the exchange-correlation energy can be written as:

$$E_{\text{xc}}[n] = F[n] - T_s[n] - E_H[n] = \langle \hat{T}_e \rangle - T_s[n] + \langle \hat{V}_{\text{ee}} \rangle - E_H[n]. \quad (2.14)$$

It can be seen that this energy term contains the difference between the interacting many-body system from the auxiliary system of the independent particles for the kinetic energy and the internal interactions.

The ground-state energy is obtained from the minimization of the energy functional with respect to the electron density, from equation 2.9. The solution to the optimization problem is given

2.1 Density Functional Theory

by the stationary points of the Lagrangian of the energy functional subject to the constraints of the orthonormal orbitals, $\int d^3r \varphi_i^*(\mathbf{r}) \varphi_i(\mathbf{r}) = 1$, i. e., the solutions to the Euler-Lagrange equation

$$\frac{\delta}{\delta \varphi_i^*(\mathbf{r})} \left\{ E[n] - \sum_j^N \epsilon_j \left[\int d^3r |\varphi_j(\mathbf{r})|^2 - 1 \right] \right\} = 0, \quad (2.15)$$

where ϵ_j are the Lagrangian multipliers, which guarantee conservation of particles. Performing the functional derivatives together with the expression $\frac{\delta n(\mathbf{r})}{\delta \varphi_i^*(\mathbf{r})} = \varphi_i(\mathbf{r})$ leads to the KS Schrödinger-like equations:

$$\left\{ -\frac{1}{2} \nabla^2 + V_{\text{eff}}[n(\mathbf{r})] \right\} \varphi_i(\mathbf{r}) = \epsilon_i \varphi_i(\mathbf{r}), \quad (2.16)$$

where now the ϵ_i are the eigenvalues of the KS orbitals $\varphi_i(\mathbf{r})$ and the V_{eff} is the effective potential in which the non-interacting electrons exist. All the terms forming the interacting system, together with the external potential, are grouped in this effective potential, which is also called the KS potential, as

$$V_{\text{eff}}[n] = V_{\text{H}}[n] + V_{\text{xc}}[n] + V_{\text{ext}}(\mathbf{r}), \quad (2.17)$$

with

$$V_{\text{H}}[n] = \frac{\delta E_{\text{H}}[n]}{\delta n(\mathbf{r})} = \int d^3r' \frac{n(\mathbf{r}')}{|\mathbf{r} - \mathbf{r}'|} \quad \text{and} \quad V_{\text{xc}}[n] = \frac{\delta E_{\text{xc}}[n]}{\delta n(\mathbf{r})}. \quad (2.18)$$

The set of equations 2.16, 2.17 and 2.10 are known as the Kohn-Sham equations. Here, the effective potential is determined from the electron density in equation 2.17, the density in turn is calculated from equation 2.16 and equation 2.10. The equations thus need to be solved self-consistently in an iterative manner, starting from an initial guess of the electronic density. In this fashion, the exact ground-state electronic density can be found, with the ground-state energy determined via equation 2.12 as

$$E_0 = \sum_i^N \epsilon_i - E_{\text{H}}[n_0] + E_{\text{xc}}[n_0] - \int d^3r V_{\text{xc}}[n] n_0(\mathbf{r}), \quad (2.19)$$

where the eigenvalues fulfill the following relation

$$\sum_i^N \epsilon_i = \sum_i^N \left\langle \varphi_i \left| -\frac{1}{2} \nabla^2 + V_{\text{eff}}[n] \right| \varphi_i \right\rangle. \quad (2.20)$$

It is clear that the KS eigenvalues and eigenstates determine a fictitious non-interacting system called the KS non-interacting system. The KS orbitals and energies thus have no physical meaning and are a mathematical tool used to construct meaningful physical quantities.

The KS equations present an exact method that allows the calculation of the true ground-state density of the many-body problem from a fictitious independent particle system. From the Hohenberg-Kohn Theorems, the potential can be uniquely determined. Finally, the ground-state wavefunctions can be retrieved from the potential, and the full information of the many-body interacting system would be known. The only quantity yet to be determined is the exchange-correlation functional E_{xc} needed to exactly solve the problem.

2.1.3 Exchange-correlation energy

As described in the previous section, in principle the KS equations are an exact method for calculating the ground-state electronic density and energy. However, the main problem with DFT is that a universal exchange-correlation functional $E_{\text{xc}}[n]$ is unknown. The non-classical interactions and the quantum-mechanical effects of the electrons are described by the exchange-correlation energy term. Despite not having an expression for the exact exchange-correlation energy, simple approximations for this energy functional still provide remarkably accurate ground-state properties for most systems. Two of the most common and used approximations are discussed in this section, the local density approximation (LDA) and the generalized gradient approximation (GGA). But first the exchange-correlation hole will be explored.

Exchange-correlation hole

The success of these approximations depends on satisfying a number of properties of the so-called exchange-correlation “hole”. Since the effect of the exchange-correlation is to lower the energy, it can be interpreted as the electron interacting with a positive exchange-correlation “hole”. Physically, this hole originates from the Pauli exclusion principle and the Coulomb repulsion for the exchange and correlation holes, respectively. The physical interpretation is that if an electron is at point \mathbf{r} there exists a region around it where the probability of finding a second electron is zero.

The relation between the exchange-correlation energy and the hole is derived from the adiabatic connection by Harris [61]. The adiabatic connection gives a link between the interactive and non-interacting systems. This is expanded from the constrained search of equation 2.8 to include a parameter λ

$$F_{\lambda}[n] = \min_{\Psi \rightarrow n} \langle \Psi | \hat{T}_e + \lambda \hat{V}_{ee} | \Psi \rangle = \left\langle \Psi_n^{\lambda} | \hat{T}_e + \lambda \hat{V}_{ee} | \Psi_n^{\lambda} \right\rangle. \quad (2.21)$$

The parameter λ characterizes the strength of the electron-electron interaction and varies from 0 (the non-interacting case) to 1. With the added constraint that the density must be maintained constant through the variation, equation 2.14 now reads

$$E_{\text{xc}} = \int_0^1 d\lambda \frac{\partial F_{\lambda}[n]}{\partial \lambda} - E_H[n] = \int_0^1 d\lambda \left\langle \Psi_n^{\lambda} | \hat{V}_{ee} | \Psi_n^{\lambda} \right\rangle - E_H[n]. \quad (2.22)$$

The right side of the equality is a result of the Hellmann-Feynmann theorem [62, 63], discussed more extensively in section 2.1.4. The joint probability of finding an electron at \mathbf{r} and a second electron at \mathbf{r}' is given by the correlation function

$$n(\mathbf{r}, \mathbf{r}') = \frac{1}{2} \left\langle \sum_{i \neq j} \delta(\mathbf{r} - \mathbf{r}_i) \delta(\mathbf{r}' - \mathbf{r}_j) \right\rangle. \quad (2.23)$$

Putting together equations 2.22, 2.23 and 2.13 finally yields

$$E_{\text{xc}} = \frac{1}{2} \int \int d^3 r d^3 r' \frac{n(\mathbf{r}) \bar{n}_{\text{xc}}(\mathbf{r}, \mathbf{r}')}{|\mathbf{r} - \mathbf{r}'|}, \quad (2.24)$$

where the average exchange-correlation hole \bar{n}_{xc} is given by

$$\bar{n}_{\text{xc}}(\mathbf{r}, \mathbf{r}') = \int d\lambda n_{\text{xc}}^{\lambda}(\mathbf{r}, \mathbf{r}') = \frac{2}{n(\mathbf{r})} \int_0^1 d\lambda n^{\lambda}(\mathbf{r}, \mathbf{r}') - n(\mathbf{r}'). \quad (2.25)$$

From equation 2.24 the exchange-correlation energy can be interpreted as the classic Coulomb interaction between the density $n(\mathbf{r})$ and the average exchange-correlation hole \bar{n}_{xc} . An important relation for the exchange-correlation hole is the so-called sum rule, which extends from equations 2.23 and 2.25

$$\int d^3r' \bar{n}_{xc}(\mathbf{r}, \mathbf{r}') = -1. \quad (2.26)$$

This mathematical formulation of $\bar{n}_{xc}(\mathbf{r}, \mathbf{r}')$ physically represents a hole around point \mathbf{r}' with a positive unit charge. The sum rule, equation 2.26, is used as a test for approximations of the exchange-correlation energy.

In the non-interacting limit $\lambda = 0$ there is no coulomb correlation and the hole is purely an exchange hole, which originates from Pauli's exclusion principle. This can be seen better from equations 2.22 and 2.25 setting $\lambda = 0$: The wavefunctions are just the independent particle KS wavefunctions, given by a Slater determinant of the non-interacting single particle KS orbitals φ_i . Thus, the exchange hole defined as

$$n_x(\mathbf{r}, \mathbf{r}') = n_{xc}^0(\mathbf{r}, \mathbf{r}'), \quad (2.27)$$

is given by the KS orbitals as

$$n_x(\mathbf{r}, \mathbf{r}') = -\frac{1}{n(\mathbf{r})} \left| \sum_i \varphi_i^*(\mathbf{r}) \varphi_i(\mathbf{r}') \right|^2. \quad (2.28)$$

The above equation is the exact formulation of the exchange hole. From equation 2.26 the sum rule for the exchange hole is

$$\int d^3r' n_x(\mathbf{r}, \mathbf{r}') = -1. \quad (2.29)$$

The correlation hole is defined as the difference between the exchange-correlation hole and the exchange hole

$$n_c(\mathbf{r}, \mathbf{r}') = \bar{n}_{xc}(\mathbf{r}, \mathbf{r}') - n_x(\mathbf{r}, \mathbf{r}'), \quad (2.30)$$

and its sum rule

$$\int d^3r' n_c(\mathbf{r}, \mathbf{r}') = 0 \quad (2.31)$$

It is clear that the above equations are an exact formulation of the exchange-correlation energy; however, it is still to be exactly defined as a functional of the density. Different approximations exist that describe the exchange-correlation energy as a function of the electronic density.

Local density approximation

The simplest of the approximations for describing the exchange-correlation functional E_{xc} is the local density approximation by Kohn and Sham [60]. The KS approach described in the previous section separates the independent-particle kinetic energy and the long-range Hartree terms. The remaining unknown part of the energy functional is approximated as a local functional of the density; this is known as the local density approximation (LDA),

$$E_{xc}^{\text{LDA}}[n] = \int d^3r n(\mathbf{r}) \epsilon_{xc}^{\text{LDA}}[n(\mathbf{r})], \quad (2.32)$$

where $\epsilon_{xc}[n(\mathbf{r})]$ is the exchange-correlation energy per particle of a homogeneous electron gas (HEG) that depends only on the density $n(\mathbf{r})$ at position \mathbf{r} . The functional $\epsilon_{xc}[n(\mathbf{r})]$ is expressed as the sum of the exchange $\epsilon_x[n(\mathbf{r})]$ and correlation $\epsilon_c[n(\mathbf{r})]$ contributions. The exchange functional $\epsilon_x[n]$ described by Dirac in 1930[64] in the Hartree-Fock approximation is given by,

$$\epsilon_x^{\text{LDA}}[n] = -\frac{3}{4\pi} \left(3\pi^2 n(\mathbf{r}) \right)^{1/3}. \quad (2.33)$$

Accurate values for the correlation functional $\epsilon_c[n]$ of the HEG were originally obtained numerically from Monte-Carlo calculations by Ceperley and Alder [65]. Analytical forms of the correlation function can be obtained from the interpolation of these values. Perdew and Zunger [66] parametrized the original values and obtained the following form

$$\epsilon_c^{\text{LDA}}[n] = \frac{\gamma}{1 + \beta_1 \sqrt{r_s} + \beta_2 r_s}, \quad (2.34)$$

where $r_s = (\frac{3}{4\pi n})^{1/3}$ is the Wigner-Seitz radius and the parameters are $\gamma = -0.1423$, $\beta_1 = 1.0529$ and $\beta_2 = 0.3334$ for a spin-unpolarized system. Perdew and Zunger also included parameters for spin-polarized systems in their original work.

The success of the LDA, despite being an approximation born from the HEG, is that it can also be reliably applied for non-homogeneous systems like atoms, molecules and solids. This is achieved by the good description of the exchange-correlation hole and the fulfillment of the sum rule. Despite this, the LDA tends to underestimate the exchange energy and overestimate the correlation energy. Fortunately, the errors in the exchange and correlation parts tend to cancel each other to a certain degree. The LDA is not without its limitations; it favors more homogeneous systems and tends to overestimate binding energies in molecules and solids [67]. The LDA also suffers from the “band-gap problem” and self-interaction errors [68, 69], which require corrections specially for localized electrons. This leads to an underestimation of the fundamental band gap width for semiconductors and insulators. The problem is present for all (semi-) local functional approximations and will be explained in sec. 2.1.5.

Generalized gradient approximation

A logical extension to the LDA is to include derivatives of the electronic density, in order to account for the non-homogeneous nature of the density. The exchange-correlation energy E_{xc} is treated as a functional of the electronic density, and its derivative is what is known as the generalized gradient approximation (GGA).

$$E_{xc}^{\text{GGA}}[n] = \int d^3r f(n(\mathbf{r}), \nabla n(\mathbf{r})). \quad (2.35)$$

The difficulty lies in finding an analytical function f that satisfies equation 2.26 and the constraints imposed by other calculations or experiments. Several different functions f have been proposed over the years, each with their own advantages and disadvantages. Perdew and Wang [70] proposed a parametrization of the GGA (PW91) constructed by looking at the second-order expansion of the density gradient for the exchange-correlation hole and cutting off the spurious long-range parts to satisfy the hole sum rules. The PW91 incorporates a rather overcomplicated and overparametrized function f , in 1996 Perdew, Burke and Ernzerhof introduced a successful simplification and extension [71, 72] by the name of PBE.

2.1 Density Functional Theory

The GGA exchange-correlation functional is also split into both the exchange and correlation parts, similar to LDA. The functional preserves the properties of the LDA, while all additional parameters are fundamental constants. The exchange functional is

$$E_x^{\text{GGA}}[n] = \int d^3r n(\mathbf{r}) \epsilon_x^{\text{LDA}}[n] F_x(s), \quad (2.36)$$

where the gradient contribution to the exchange functional is

$$F_x(s) = 1 + k - \frac{k}{1 + \mu s^2/k}. \quad (2.37)$$

The correlation-energy contribution is defined as

$$E_c^{\text{GGA}}[n] = \int d^3r n(\mathbf{r}) [\epsilon_c^{\text{LDA}}[n] + H^{\text{PBE}}(r_s, \zeta, t)], \quad (2.38)$$

where

$$H^{\text{PBE}} = \gamma \phi^3 \ln \left\{ 1 + \frac{\beta}{\gamma} t^2 \left[\frac{1 + At^2}{1 + At^2 + A^2 t^4} \right] \right\}, \quad (2.39a)$$

$$A = \frac{\beta}{\gamma} \left\{ \exp \left[-\frac{\epsilon_c^{\text{LDA}}}{\gamma \phi^3} \right] - 1 \right\}^{-1}, \quad (2.39b)$$

$$\phi = \frac{1}{2} \left[(1 + \zeta)^{\frac{2}{3}} + (1 - \zeta)^{\frac{2}{3}} \right], \quad (2.39c)$$

and, finally, the generalized, dimensionless density gradients as

$$s = \frac{|\nabla n|}{2k_F \phi n} \quad \text{and} \quad t = \frac{|\nabla n|}{2k_s \phi n}, \quad (2.40)$$

with $k_F = (3\pi^2 n)^{\frac{1}{3}}$ and $k_s = \sqrt{\frac{4k_F}{\pi}}$. The relative spin polarization is $\zeta = \frac{n_{\uparrow} - n_{\downarrow}}{n}$. The remaining factors are the constants $\mu = 0.21951$, $k = 0.804$, $\gamma = 0.031091$ and $\beta = 0.066725$. The generalized gradients s and t measure the rate of change of the density n on the scales of the local Fermi length $1/k_F$ and the local Thomas-Fermi screening length $1/k_s$, respectively.

One of the most important results of the GGA is the reduction of the binding energy, correcting the over-binding of the LDA in molecules and solids and improving the agreement with the experiment. Despite the many improvements GGA has over the LDA the softening of the bonds increases the lattice constants and the decrease of the bulk moduli[73]. Similar to LDA, the GGA also suffers from self-interaction error[69].

2.1.4 Ionic forces

Of particular interest concerning molecules and solids is the prediction of the geometric structure of the systems. This can be accomplished through the study of inter-atomic forces, which allow the calculation of the ground-state positions of the ions. Additionally, the calculation of the forces grants the description of thermodynamic processes from molecular dynamics to transitions states.

The force acting upon an ion I can be described as the rate of change of the total energy as a function of the ion position R_I . The Hellmann-Feynman theorem relates the derivative of the

energy with respect to any parameter λ of the Hamiltonian to the expectation value of the derivative of the Hamiltonian with respect to that parameter. The theorem was proven independently by many authors: The original formulae used today were provided in the works by Güttinger in 1932 [74] and Pauli in 1933 [75], reformulations were later made by Hellmann in 1937 [62] and Feynman in 1939 [63]. The general expression can be written as

$$\frac{\partial E_{\text{tot}}}{\partial \lambda} = \left\langle \Psi_{\lambda} \left| \frac{\partial \hat{H}}{\partial \lambda} \right| \Psi_{\lambda} \right\rangle. \quad (2.41)$$

The Hamiltonian of total energy E_{tot} as given by equation 2.2 includes the previously neglected term V_{nn} , equation 2.4c. The kinetic and potential energies of the electron-electron interactions do not depend on the position of the nuclei; thus, their derivatives with respect to this position do not contribute to the force. The force acting on an ion (or nucleus) I with position \mathbf{R}_I is then given by the expression

$$F_{\mathbf{R}_I} = -\frac{\partial E_{\text{tot}}}{\partial \mathbf{R}_I} = - \int d^3r n(\mathbf{r}) \frac{\partial V_{\text{ext}}(\mathbf{r})}{\partial \mathbf{R}_I} - \frac{\partial V_{\text{nn}}}{\partial \mathbf{R}_I}. \quad (2.42)$$

The forces here depend only on the ground-state charge density $n(\mathbf{r})$ and the other ions. Obtaining accurate forces depends on the choice of the approximation that describes the exchange-correlation functional. The ground-state position of the ions is derived by minimizing the forces acting over the ions; different algorithms exist for this task, including the quasi-Newton algorithm (RMM-DIIS) [76] or the conjugate gradient algorithm [77].

2.1.5 Electronic structure and the band gap problem

As discussed briefly in section 2.1.2, the KS eigenvalues have no physical interpretation, the sole exception being the highest occupied eigenvalue ϵ_N . The physical meaning can be derived from the Slater-Janak theorem [78], which gives a mathematical interpretation to all the KS eigenvalues. With the concept of partial occupation numbers f_i , a connection to the total energy is given for the eigenvalues as

$$\frac{\partial E}{\partial f_i} = \epsilon_i. \quad (2.43)$$

The physical meaning of the highest occupied eigenvalue ϵ_N can be found by looking at the energy difference between a system with N and $N - 1$ particles

$$E(N) - E(N - 1) = \int_0^1 df_N \frac{\partial E}{\partial f_N} = \int_0^1 df_N \epsilon_N(N - 1 + f_N) = \epsilon_N(N - \delta), \quad (2.44)$$

here, the particle number of the system is indicated in the parenthesis; the last part is obtained from the mean value theorem. Since the exact functional $E(N)$ is a series of straight lines with discontinuities at integers N , [79] the above equation is equal to $\epsilon_N(N)$. That is, the ionization energy $I = E_{N-1} - E_N$ is equal to minus the highest occupied KS eigenvalue of the N particle system $\epsilon_N(N)$. Similarly, the electron affinity $A = E_N - E_{N+1}$ can be found with the same reasoning from

$$E(N + 1) - E(N) = \int_0^1 df_{N+1} \frac{\partial E}{\partial f_{N+1}} = \int_0^1 df_{N+1} \epsilon_{N+1}(N + f_{N+1}) = \epsilon_{N+1}(N + \delta). \quad (2.45)$$

From these results, it is tempting to define $A = \epsilon_{N+1}(N)$ and extend the same analysis for all eigenvalues ϵ_i . The KS eigenvalues of the N -particle system could then be used as addition and removal

energies to calculate meaningful observables such the band structure and band gap. However, the electron affinity is actually defined as the eigenvalue $\epsilon_{N+1}(N+1)$ which belongs to the different $(N+1)$ -particle system. Nevertheless, the KS eigenvalues of the N -particle system are used to calculate the band structure, often describing it qualitatively exceptionally close to the actual band structure. There is, however, a discrepancy between the calculated band gap ϵ_g^{KS} and the true band gap E_g . Because of this, it is often referred to as the “band gap problem”. It should be noted that the discrepancy stems from the mistreatment of the KS eigenvalues as electron addition and removal energies and not an inherit problem of the KS equations. The band gap is defined as the difference in ionization energy and electron affinity

$$E_g = \epsilon_{N+1}(N+1) - \epsilon_N(N) = \epsilon_g^{\text{KS}} + \Delta_N^{\text{KS}}, \quad (2.46)$$

where the KS band gap is $\epsilon_g^{\text{KS}} = \epsilon_{N+1}(N) - \epsilon_N(N)$ and the correction between the true band gap is $\Delta_{\text{xc}} = \epsilon_{N+1}(N+1) - \epsilon_{N+1}(N)$ often called the derivative discontinuity. As discussed above, $E(N)$, although linear between integer values of N , presents discontinuities at N , as such the derivatives are discontinuous and as a consequence Δ_{xc} is not equal to zero. The derivative discontinuity is better expressed with an alternative form of equation 2.46, [79–81] by looking at the functional derivative of the energy for a variation of the density

$$E_g = I - A = \lim_{\delta \rightarrow 0^+} \left[\frac{\delta E}{\delta n(\mathbf{r})} \Big|_{N+\delta} - \frac{\delta E}{\delta n(\mathbf{r})} \Big|_{N-\delta} \right]. \quad (2.47)$$

From equation 2.12 the discontinuity can only arise from the kinetic energy and the exact exchange-correlation contributions; the rest are continuous in the density. The discontinuity in the kinetic energy is the only contribution of the KS band gap [81, 82]

$$\epsilon_{N+1}(N) - \epsilon_N(N) = \lim_{\delta \rightarrow 0^+} \left[\frac{\delta T_s}{\delta n(\mathbf{r})} \Big|_{N+\delta} - \frac{\delta T_s}{\delta n(\mathbf{r})} \Big|_{N-\delta} \right]. \quad (2.48)$$

Therefore, the discrepancy between the real band gap and the KS band gap is given only by the derivative discontinuity of the exchange-correlation functional[79–81] as

$$\Delta_{\text{xc}} = \lim_{\delta \rightarrow 0^+} \left[\frac{\delta E_{\text{xc}}}{\delta n(\mathbf{r})} \Big|_{N+\delta} - \frac{\delta E_{\text{xc}}}{\delta n(\mathbf{r})} \Big|_{N-\delta} \right]. \quad (2.49)$$

It is clear that in order to describe the correct band gap, the KS eigenvalues are not enough. Both LDA and GGA have continues exchange-correlation functions, and thus Δ_{xc} is equal to 0. Additional improvements would yield a better ϵ_g , but unless the discontinuity is described, the KS eigenvalues alone will not give the true band gap. This is the reason standard DFT calculations underestimate the true band gap.

There are several techniques used to better describe the electronic structure. The correct description of the self-interaction of the electron in the exchange-correlation functional through Green’s functions provides an improvement over the LDA/GGA and includes the derivative discontinuity, thus describing the electronic structure more accurately. Another approach is to divide the exchange functional into contributions from DFT and from the Hartee-Fock (HF) method. The HF correctly includes the derivative discontinuity in the exchange functional but is missing the correlation term. In the following sections, the approximations used in this work will be described.

2.2 Hybrid functionals

The main idea behind the hybrid functional approach is to construct a so-called hybrid functional from orbital dependent HF with an explicit dependent density functional. Since the exchange is by far the most dominant term in the exchange-correlation energy, it is an incentive to treat the term exactly and approximate the rest. Hybrid functionals are the most accurate functionals available as far as energetics are concerned and widely used to describe the electronic structure accurately. The hybrid formalism arises from the adiabatic connection between the non-interacting KS system and the fully interacting real system by a coupling constant λ , as discussed in further detail in sec. 2.1.3. The integral of equation 2.24 can be rewritten in the simple form

$$E_{xc} = \int_0^1 d\lambda E_{xc,\lambda}, \quad (2.50)$$

where E_{xc}, λ is approximated in terms of the end points. In particular, for $\lambda = 0$, the so-calculated energy is the Hartee-Fock exchange energy, given exactly by the exchange hole in equation 2.28 from the KS orbitals. A theoretical rationale was introduced by Perdew, Ernzerhof and Burke [83] for the approximation of the functional $E_{xc,\lambda}$. For any density functional approximation, $E_{xc,\lambda}^{\text{DFA}}$, a coupling constant similar to equation 2.50 can be defined such that exchange and correlation energies fulfill the relations $E_x^{\text{DFA}} = E_{xc,\lambda=0}^{\text{DFA}} = E_x$ and $E_c^{\text{DFA}} = E_{xc}^{\text{DFA}} - E_x^{\text{DFA}}$ imposed by equations 2.27 and 2.30, respectively. The hybrid model for $E_{xc,\lambda}$ was proposed as

$$E_{xc,\lambda}^{\text{hyb}} = E_{xc,\lambda}^{\text{DFA}} + (E_x - E_x^{\text{DFA}})(1 - \lambda)^{n-1}, \quad (2.51)$$

where $n \geq 1$ is a constant that controls how rapid the correction to the density functional approximation vanishes as $\lambda \rightarrow 1$. Equation 2.51 reduces to the exact exchange energy E_x at the limit $\lambda = 0$ and to $E_{xc,\lambda}^{\text{DFA}}$ at or near $\lambda = 1$ where the approximation $E_{xc,\lambda}^{\text{DFA}}$ is more accurate. The hybrid functional is then

$$E_{xc}^{\text{hyb}} = \int_0^1 d\lambda E_{xc,\lambda}^{\text{hyb}} = E_{xc}^{\text{DFA}} + \frac{1}{n}(E_x - E_x^{\text{DFA}}). \quad (2.52)$$

The parameter n is chosen from perturbation theory by expanding $E_{xc,\lambda}$ in powers of λ and stopping at the lowest order that gives the best description of the exact E_{xc}, λ . For $n = 2$ the second-order perturbation theory is enough and equation 2.52 reduces to the half-and-half hybrid, originally proposed by Becke [84]. The approximation for the value of $n = 4$, has been tested to be the best fit for a large set of molecules and comparable to several models with fitted parameters [85]. It is commonly referred to as PBE0 when the PBE is used for the density functional approximation, equation 2.52 is then

$$E_{xc}^{\text{PBE0}} = \frac{1}{4}E_x^{\text{HF}} + \frac{3}{4}E_x^{\text{PBE}} + E_c^{\text{PBE}}. \quad (2.53)$$

The exact exchange functional is calculated from equation 2.24 with the exact exchange hole equation 2.28 as

$$E_x^{\text{HF}} = -\frac{1}{2} \sum_{ij} \iint d^3r d^3r' \frac{\varphi_i^*(\mathbf{r}) \varphi_j^*(\mathbf{r}') \varphi_i(\mathbf{r}') \varphi_j(\mathbf{r})}{|\mathbf{r} - \mathbf{r}'|}, \quad (2.54)$$

here the superscript HF refers to the fact that the exact exchange-correlation is calculated from the Slater determinant KS orbitals, as it is the case in the non-interacting Hartee-Fock approximation.

Although strictly speaking, E_x is not the HF exchange energy since the KS and HF independent particle orbitals are not equivalent, however, there is very little numerical difference. Throughout the literature, the HF superscript is utilized.

2.2.1 Range-separated hybrid functionals

Calculating the exact exchange energy via equation 2.54 for large molecules and solids is rather computationally expensive. Therefore, Heyd, Scuseria and Ernzerhof developed a new method based on a screened Coulomb potential [86–88]. The exchange interactions in the Hybrid method decay over the distance; the decay is accelerated by substituting the full Coulomb potential with a screened potential. The screened potential is applied only to the exchange interaction in order to screen the long-range part of the exchange energy. The Coulomb operator is split into the short-range (SR) and long-range (LR) components by following partition

$$\frac{1}{|\mathbf{r} - \mathbf{r}'|} = \underbrace{\frac{\operatorname{erfc}(\mu |\mathbf{r} - \mathbf{r}'|)}{|\mathbf{r} - \mathbf{r}'|}}_{\text{SR}} + \underbrace{\frac{\operatorname{erf}(\mu |\mathbf{r} - \mathbf{r}'|)}{|\mathbf{r} - \mathbf{r}'|}}_{\text{LR}}, \quad (2.55)$$

where erf is the error function, erfc the complementary error function, and μ is an adjustable parameter that defines the range separation. At the limit $\mu = 0$, the LR term becomes zero, and the SR term is equivalent to the full Coulomb operator and hence is equivalent to the PBE0 formalism. At the other extreme, when $\mu \rightarrow \infty$, the opposite is the case and the exchange energy is treated fully in the PBE approximation.

The exchange terms from equation 2.53 are split in the LR and SR components. For realistic values of μ the contributions by the HF and PBE exchange to the LR tend to be rather small and tend to cancel each other, i. e., $E_x^{\text{HF},\text{LR}} \sim E_x^{\text{PBE},\text{LR}}$ [86]. In this approximation, the equation for the screened Coulomb potential hybrid density functional HSE is

$$E_{\text{xc}}^{\text{HSE}} = \frac{1}{4} E_x^{\text{HF},\text{SR}}(\mu) + \frac{3}{4} E_x^{\text{PBE},\text{SR}}(\mu) + E_x^{\text{PBE},\text{LR}}(\mu) + E_{\text{c}}^{\text{PBE}}. \quad (2.56)$$

With the HSE hybrid method, only the SR exchange is treated in the hybrid PBE0 formalism, while the LR exchange is calculated fully in the PBE approximation. The SR component of the HF exchange is given by substituting the full Coulomb potential in equation 2.54 by the SR Coulomb potential. The SR of the PBE exchange energy is obtained by incorporating the corresponding error function into the enhancement factor, and the LR follows. The full expressions and their derivations can be found in Ref. [86].

The optimum value for μ has been found to be approximately 0.2 \AA^{-1} , it is the best fit for predicting enthalpies of formation, ionization potentials and electron affinities while preserving a good accuracy for the band gap, for a wide range of materials [89]. Setting $\mu = 0.2 \text{ \AA}^{-1}$ for this screened hybrid functional model is referred to as HSE06 [89] and is the value of choice throughout this work whenever hybrid functionals are used.

2.3 GW approximation

The main idea behind this section is to treat the many-body problem as an independent particle system plus the Coulomb interaction as a perturbation; this is referred to as the many-body

perturbation theory. Such a problem can be formulated using Green's functions, which allow the correct description of addition and removal of particles. It is sufficient to look at the one-particle and the two-particle Green's functions, since many of the observables of interest of the many-body are derived directly from them. This section presents a general introduction to the GW approximation and its implementation; further information can be found in references [90, 91].

2.3.1 Green's function

The one-particle Green's function of an N -particle system in the ground state is described by the correlation function and formulated in the second quantization of quantum mechanics read

$$G(\mathbf{r}, t; \mathbf{r}', t') = -i \left\langle N \left| \hat{T} \left[\hat{\psi}(\mathbf{r}, t) \hat{\psi}^\dagger(\mathbf{r}', t') \right] \right| N \right\rangle, \quad (2.57)$$

where $\hat{\psi}^\dagger(\mathbf{r}, t)$ and $\hat{\psi}(\mathbf{r}, t)$ are the time-evolution field operators in the Heisenberg picture for electron creation and annihilation, respectively. \hat{T} is the time-ordering operator for fermions, which rearranges the field operators according to their time variable. Two situations are described by the time-ordering operator: (i) the propagation of an electron ($t > t'$) from (\mathbf{r}', t') to (\mathbf{r}, t) , or (ii) the propagation of a hole ($t < t'$) from (\mathbf{r}, t) to (\mathbf{r}', t') . The connection between the electron addition and removal spectra and the Green's function is observed in the frequency space Green's function in the Lehmann representation. This is obtained by inserting the closure relation $\sum_i |N \pm 1, i\rangle \langle N \pm 1, i|$ of the complete set of the $(N \pm 1)$ -system and performing the Fourier transform with respect to time,

$$G(\mathbf{r}, \mathbf{r}'; \omega) = \lim_{\eta \rightarrow 0^+} \sum_i \frac{\psi_i^{N+1}(\mathbf{r}), \psi_i^{N+1*}(\mathbf{r}')}{\omega - \epsilon_i^{N+1} + i\eta} + \sum_i \frac{\psi_i^{N-1}(\mathbf{r}), \psi_i^{N-1*}(\mathbf{r}')}{\omega - \epsilon_i^{N-1} - i\eta}. \quad (2.58)$$

Here, the Dyson amplitudes $\psi_i^{N\pm 1}(\mathbf{r})$ defined as

$$\psi_i^{N+1}(\mathbf{r}) = \langle N | \hat{\psi}(\mathbf{r}) | N+1, i \rangle \quad \text{and} \quad \psi_i^{N-1}(\mathbf{r}) = \langle N-1, i | \hat{\psi}(\mathbf{r}) | N \rangle, \quad (2.59)$$

and the excitation energies

$$\epsilon_i^{N+1} = E_i(N+1) - E_0(N) \quad \text{and} \quad \epsilon_i^{N-1} = E_0(N) - E_i(N-1). \quad (2.60)$$

These energies correspond to the excitation energies of the $(N \pm 1)$ particle systems. Therefore, the one-particle Green's function contains information regarding the direct and inverse photo-electron spectroscopy.

To simplify the notation, the superscripts $(N \pm 1)$ will be dropped and the compact notation of natural numbers to represent space-time coordinates will be adopted, e.g. denoting $(1) \equiv (\mathbf{r}_1, t_1)$, etc.

2.3.2 Hedin's equations

The aim is to find a closed set of equations with different terms that are either known or can be reasonably well approximated, similarly to the KS equations. A good starting point is from the equation of motion of the Green's function in the Heisenberg picture

$$i \frac{\partial}{\partial t_1} G(1, 2) = \delta(1, 2) + h(r) G(1, 2) - i \int V_{ee}(1^+ 3) G(1, 3, 2, 3^+), \quad (2.61)$$

here $\delta(1, 2) = \delta(\mathbf{r}_1 - \mathbf{r}_2)\delta(t_1 - t_2)$, the one-particle operator $h(r) = -(1/2)\nabla^2 + V_{\text{ext}}(\mathbf{r})$ and $V_{\text{ee}}(1, 2) = V_{\text{ee}}(\mathbf{r}_1, \mathbf{r}_2)\delta(t_1 - t_2)$. A positive infinitesimal time η ensures the correct time ordering with $(1^+) = (\mathbf{r}_1, t_1 + \eta)$. This, however, is not a closed equation because it includes the two-particle Green's function, defined by a four field operators as

$$G(1, 2, 3, 4) = -\left\langle N \left| \hat{T} \left[\hat{\psi}(1)\hat{\psi}(2)\hat{\psi}^\dagger(4)\hat{\psi}^\dagger(3) \right] \right| N \right\rangle. \quad (2.62)$$

The two-particle Green's function contains the reaction of an electron to the propagation of another electron. The two-particle function can be expressed through the functional derivative approach with respect to a fictitious local potential U that is set to zero at the end of the calculations. The functional derivative of the one-particle Green's function calculated in the interacting picture is

$$\left. \frac{\delta G(1, 2)}{\delta U(3)} \right|_{U=0} = G(1, 2)G(3, 3^+) - G(1, 3, 2, 3^+). \quad (2.63)$$

Inserting this into the last term of equation 2.61, the equation of motion is then

$$\left[i \frac{\partial}{\partial t_1} - h(r) - V_H \right] G(1, 2) - \int \Sigma(1, 3)G(3, 2)d3 = \delta(1, 2). \quad (2.64)$$

Using the definition of the inverse Green's function, $\int G(1, 2)G^{-1}(2, 3)d2 = \delta(1, 3)$, the self-energy has been defined as

$$\Sigma(1, 2) = i \iint V_{\text{ee}}(1^+, 3) \frac{\delta G(1, 4)}{\delta U(3)} G^{-1}(4, 2)d3d4 = -i \iint V_{\text{ee}}(1^+, 3) G(1, 4) \frac{\delta G^{-1}(4, 2)}{\delta U(3)} d3d4. \quad (2.65)$$

The delta function on the right side of equation 2.64 shows that $G(1, 2)$ is indeed a Green's function. By definition, all the many body exchange and correlation effects are taken into account in the self-energy. In a system where the interaction between particles is defined only by the Hartree potential, i. e., the self-energy is set to zero, the equation of motion is reduced to

$$\left[i \frac{\partial}{\partial t_1} - h(r) - V_H(1) \right] G_0(1, 2) = \delta(1, 2). \quad (2.66)$$

Using equations 2.64 and 2.66, together with the inverse definition for G_0 yield the Dyson equation

$$G(1, 2) = G_0(1, 2) + \iint G_0(1, 3)\Sigma(3, 4)G(4, 2)d3d4. \quad (2.67)$$

One can insert the Lehmann representation equation 2.58 into the frequency representation of equation 2.64 in order to obtain a description of the collective behavior of the group of particles, the so-called quasiparticle equation

$$[h(\mathbf{r}) + V_H(\mathbf{r})] \psi_i + \int \Sigma(\mathbf{r}, \mathbf{r}'; \epsilon_i) \psi_i(\mathbf{r}') d^3 r' = \epsilon_i \psi_i(\mathbf{r}). \quad (2.68)$$

It must be understood, although the quasiparticle equation 2.68 resembles the KS equation 2.16, the functions $\psi_i(\mathbf{r})$ and energies ϵ_i , however, do not represent independent particle quantities and are defined as properties of the many-body system.

An electron or hole propagating in an interacting system perturbs the particles in its vicinity. As discussed in sec. 2.1.3 the Coulomb interaction creates a correlation hole around the particle

and moves together with it. This ensemble behaves in many ways as a single-particle and is referred to as a “quasiparticle”. In a way, the quasiparticle describes the interaction of the particle with itself via the many-particle system and changes its own energy. Thus, the difference in energy of the quasiparticle and particle is described by the self-energy Σ . The one-particle Green’s function then describes the propagation of the quasiparticle through the system with wavefunctions $\psi_i(\mathbf{r})$ and excitation energies ϵ_i .

The quasiparticle interacts via a weak screened potential W , instead of the strong Coulomb potential. The screened potential is related to the Coulomb potential through the inverse of the dielectric function, as follows

$$W(1, 2) = \int \epsilon^{-1}(1, 3) V_{ee}(3, 2) d3. \quad (2.69)$$

The dielectric function is linked to the polarization function P as

$$\epsilon(1, 2) = \delta(1, 2) - \int V_{ee}(1, 3) P(3, 2) d3. \quad (2.70)$$

Both the dielectric and polarization functions are defined by an effective potential U_{eff} created by the induced charge of the Coulomb potential. The variation of the effective potential and its relation to the other quantities is

$$\delta U_{\text{eff}} = \delta U(1) + \iint V_{ee}(1, 3) \chi(1, 2) U(2) d2 d3 \quad (2.71a)$$

$$\chi(1, 2) = \left. \frac{\delta n(1)}{\delta U(2)} \right|_{U=0} \quad (2.71b)$$

$$\epsilon^{-1}(1, 2) = \left. \frac{\delta U_{\text{eff}}(1)}{\delta U(2)} \right|_{U=0} \quad (2.71c)$$

$$P(1, 2) = \left. \frac{\delta n(1)}{\delta U_{\text{eff}}(2)} \right|_{U=0} \quad (2.71d)$$

$$\Gamma(1, 2; 3) = - \left. \frac{\delta G^{-1}(1, 2)}{\delta U_{\text{eff}}(3)} \right|_{U=0}. \quad (2.71e)$$

Here, $\chi(1, 2)$ is the reducible polarizability and $\Gamma(1, 2; 3)$ the vertex function. Finally, the full set of complete integro-differential equations can be derived. The following set of equations together with the Dyson equation 2.67 are referred to as Hedin’s equations[92]

$$W(1, 2) = V_{ee}(1, 2) + \iint V_{ee}(1, 3) P(3, 4) W(4, 2) d3 d4 \quad (2.72a)$$

$$\Sigma(1, 2) = i \iint W(1^+, 3) G(14) \Gamma(4, 2; 3) d3 d4 \quad (2.72b)$$

$$\Gamma(1, 2; 3) = \delta(1, 2) \delta(1, 3) - \iiint \frac{\delta \Sigma(1, 2)}{\delta G(4, 5)} G(5, 6) \Gamma(6, 7; 3) G(7, 4) d4 d5 d6 d7 \quad (2.72c)$$

$$P(1, 2) = -i \iint G(1, 3) \Gamma(3, 4; 2) G(4, 1) d3 d4. \quad (2.72d)$$

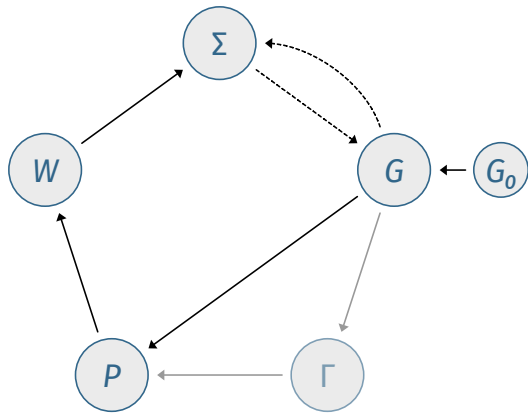


Figure 2.1: Schematic representation of the self-consistent cycle of Hedin's equations following the arrows around the pentagon. The G_0W_0 approximation follows the black solid arrows. Finally, the self-consistent GW_0 cycle follows the black solid and dashed arrows.

Hedin's equations are exact, and the self-consistent solution would, in principle, solve the many-body problem exactly. The self-consistent cycle is schematically shown in Fig. 2.1, following the arrows around the pentagon. Unfortunately equation 2.72c contains a functional derivative, and therefore Hedin's equations cannot be solved self-consistently by computer code but may be iterated analytically to obtain useful approximations. In the most common of these approximations, the vertex function is assumed to be diagonal and unitary, neglecting the integral in the right-hand side of equation 2.72c. The vertex function is reduced to the simple form

$$\Gamma(1, 2; 3) = \delta(1, 2)\delta(1, 3). \quad (2.73)$$

With this vertex function approximation, the polarization and self-energy functions form equations 2.72 are reduced to

$$P(1, 2) = -iG(1, 2)G(2, 1), \quad (2.74a)$$

$$\Sigma(1, 2) = iG(1, 2)W(1^+, 2). \quad (2.74b)$$

This is known as the GW approximation (GWA)[92], where the vertex corrections have been neglected. The key component of the GWA is the screened potential W , which is used to derive the self-energy in equation 2.74b.

2.3.3 Numerical implementation

The KS wave functions have been shown to match very closely the quasiparticle wavefunctions, $\phi_i^{\text{KS}} \approx \psi_i^{\text{QP}}$, for many materials [93]. Comparing equation 2.16 and 2.68, the quasiparticle energies can be approximated from first-order perturbation theory with a correction from the self energy

$$\epsilon_i^{\text{QP}} \approx \epsilon_i^{\text{KS}} + \left\langle \varphi_i^{\text{KS}} \left| \sum \left(\epsilon_i^{\text{QP}} \right) - V_{\text{xc}}(\mathbf{r}) \right| \varphi_i^{\text{KS}} \right\rangle. \quad (2.75)$$

The self-energy Σ must be computed self-consistently at energy ϵ_i^{QP} , this is achieved by the first order Taylor expansion around the KS eigenvalues ϵ_i^{KS} ,

$$\Sigma(\mathbf{r}, \mathbf{r}', \epsilon_i^{\text{QP}}) \approx \Sigma(\mathbf{r}, \mathbf{r}', \epsilon_i^{\text{KS}}) + \left(\epsilon_i^{\text{QP}} - \epsilon_i^{\text{KS}} \right) \frac{\partial \Sigma(\mathbf{r}, \mathbf{r}', \omega)}{\partial \omega} \bigg|_{\omega=\epsilon_i^{\text{KS}}}, \quad (2.76)$$

which leads to the correction to the KS energies as

$$\epsilon_i^{\text{QP}} \approx \epsilon_i^{\text{KS}} + Z_i \left\langle \varphi_i^{\text{KS}} \left| \Sigma \left(\epsilon_i^{\text{KS}} \right) - V_{\text{xc}}(\mathbf{r}) \right| \varphi_i^{\text{KS}} \right\rangle, \quad (2.77)$$

with the renormalization factor Z_i given by

$$Z_i = \left(1 - \left\langle \varphi_i^{\text{KS}} \left| \frac{\partial \Sigma(\mathbf{r}, \mathbf{r}', \omega)}{\partial \omega} \right|_{\omega=\epsilon_i^{\text{KS}}} \right| \varphi_i^{\text{KS}} \right)^{-1}. \quad (2.78)$$

The self-consistent GWA is in principle a five-step procedure; a good starting point is the non-interacting Green's function G_0 . The Green's function is defined by equation 2.66 is obtained from equation 2.58 for a KS wavefunctions $\varphi_i^{\text{KS}}(\mathbf{r})$

$$G_0(\mathbf{r}, \mathbf{r}', \omega) = \sum_i \frac{\varphi_i^{\text{KS}}(\mathbf{r}) \varphi_i^{*\text{KS}}(\mathbf{r}')}{\omega - \epsilon_i^{\text{QP}}}, \quad (2.79)$$

starting with the first approximation, $\epsilon_i^{\text{QP}} \approx \epsilon_i^{\text{KS}}$. The self-consistent cycle continues with the calculation of the polarization function P in the independent-particle approximation by inserting G_0 in equations 2.74a. Next, the screened Coulomb potential is determined from equations 2.69 and 2.70. It is followed by the determination of the self-energy from equation 2.74b, again using G_0 . Finally, in the last step of the cycle, the quasiparticle energies are obtained from equation 2.77. Performing only one iteration of the GW approximation self-consistent cycle is enough to correct the KS energies and obtain satisfactory results. This is referred to as single shot GW or G_0W_0 . This procedure is shown schematically in Fig. 2.1 following the solid black arrows. A partial self-consistent approximation is performed by updating the Green's function quasiparticle energies without updating the wavefunctions. This is followed by updating the self-energy and leaving the screened potential in the DFT level. The partial self-consistent GW approximation is referred to as GW_0 ; it is shown in Fig. 2.1 by following the dashed arrows. The GW_0 method is more computationally expensive than the G_0W_0 but offers improved results with excellent agreement to experiments [94, 95].

It should be noted that during the GW_0 , although the eigenvalues are updated, the KS orbitals are not allowed to be updated. Furthermore, the Green's function used is, strictly speaking, only a solution to the Dyson equation for the single-shot approach. There are other implementations of the GW approximation, including a full self-consistent, one where the screened Coulomb potential W is also updated. However, this approximation shows the consequences of neglecting the vertex function corrections and giving unsatisfactory results: In particular, there is an overestimation of the band gap compared to experiment [96]. Because of fortuitous error canceling, the GW_0 approach reproduces best the experimental band gaps rather than a full self-consistent method.

Chapter 3

First-principles atomistic thermodynamics

The effects from temperature and pressure are not included in the electronic structure calculations: strictly speaking, the results from DFT calculations are only valid for $T = 0K$ and $p = 0$ atm. However, the results from DFT can be used as inputs for thermodynamic considerations for a system at finite temperature and pressure. The pressure and temperature are included in the Helmholtz free energy

$$F = U - TS, \quad (3.1)$$

and the Gibbs free energy, which expresses the thermodynamic potential for a system in constant pressure and temperature

$$G(p, T) = F + pV = U - TS + pV. \quad (3.2)$$

Here V is the volume of the system and U is the internal energy and S the entropy.

Thermodynamic considerations allow a direct link between DFT results and experimental findings, from the thermodynamically stable geometries of surfaces, the stability of defects and their concentrations, to the phase transitions of chemical reactions on the surfaces. In this chapter, different methods are presented that combine DFT results with thermodynamic properties of solids.

3.1 Surface formation energy

The composition and geometries of solid surfaces are studied from a thermodynamic point of view by considering a system in the grand canonical ensemble. In this ensemble, the surface is considered to be in thermal equilibrium with a reservoir and can freely exchange particles and energy. Considering a reservoir large enough to set the chemical potential for the system, the minimum Helmholtz free energy is given by the grand potential

$$\Omega = U - TS - \sum_i N_{A_i} \mu_{A_i}(T, p), \quad (3.3)$$

where the Helmholtz free energy, the internal energy and entropy, are defined for the surface, N_{A_i} is the number of particles of type A_i in the surface and μ_{A_i} their chemical potential. The range of the chemical potential is restricted by their bulk values

$$\mu_{A_i} \leq \mu_{A_i, \text{bulk}}, \quad (3.4)$$

otherwise, the individual bulk materials would form instead of the surface. It is often more convenient to work with differences in the chemical potential defined as follows

$$\Delta\mu_{A_i} = \mu_{A_i} - \mu_{A_i, \text{bulk}}. \quad (3.5)$$

In this case, the chemical potential $\Delta\mu_{A_i}$ is constrained to be less or equal to zero.

3.1.1 Chemical potential for molecules

The chemical potential for molecules can be calculated as a function of pressure p and temperature T using a polyatomic ideal-gas model. The partition function of an ideal gas can be approximated by subdividing the contributions from the molecule's degree of freedom: the translational, electronic, rotational, vibrational and nuclear partition functions. The nuclear contribution can be omitted since it is rarely altered by chemical processes. The chemical potential $\Delta\mu_X$ for a molecule X is approximated as

$$\Delta\mu_{A_i}(p, T) = k_B T \left[\ln \left(\frac{p\lambda^3}{k_B T} \right) - \ln (Z_{\text{rot}}) - \ln (Z_{\text{vib}}) \right], \quad (3.6)$$

where the first, second and third terms are given by the translational, rotational and vibrational contributions to the free energy, respectively. Here, k_B is the Boltzmann constant, λ the de Broglie thermal wavelength

$$\lambda = \sqrt{\frac{2\pi\hbar^2}{m_X k_B T}}, \quad (3.7)$$

where m_X is the mass of the molecule.

The rotational and vibrational partition functions for polyatomic gas are given by [97]

$$Z_{\text{rot}} = \frac{(2k_B T)^{3/2} (\pi I_1 I_2 I_3)^{1/2}}{\sigma^{\text{sym}} \hbar^3} \quad (3.8a)$$

$$Z_{\text{vib}} = \prod_{\alpha} \left[1 - \exp \left(-\frac{\hbar\omega_{\alpha}}{k_B T} \right) \right]^{-1}, \quad (3.8b)$$

where I_i is the moment of inertia, ω_{α} the vibrational frequency, and σ^{sym} accounts for the symmetry of the molecule. On the other hand, for diatomic molecules, like H_2 or O_2 , the partition functions can be described as [97]

$$Z_{\text{rot}} = \frac{2k_B T I}{\sigma^{\text{sym}} \hbar^2} \quad (3.9a)$$

$$Z_{\text{vib}} = \left[1 - \exp \left(-\frac{\hbar\omega}{k_B T} \right) \right]^{-1}, \quad (3.9b)$$

It should be noted that the zero-point energy (ZPE) is not included in equations 3.8b and 3.9b, as such it is also absent from the right side of equation 3.6. The ZPE is the lowest possible energy

3.1 Surface formation energy

a quantum-mechanical system can have. At absolute zero temperature, the systems retain some vibrational motion, the so-called zero-point vibrations. The ZPE energy is given by the expression

$$E_X^{\text{ZPE}} = \sum_{\alpha} \frac{\hbar\omega_{\alpha}}{2}, \quad (3.10)$$

and is included in the calculation of μ_X . The chemical potential in equation 3.5 is approximated as

$$\mu_X(T, p) = E_X^{\text{ZPE}} + E_X^{\text{tot}} + \Delta\mu_X(T, p), \quad (3.11)$$

where the contribution from the electronic partition function is the ground-state energy E_X^{tot} , which is approximated from zero temperature DFT calculations.

3.1.2 Surface-free energy

The surface-free energy can be broken into its electronic, vibrational and configurational free energy contributions. The dominant term in free energy is the total energy included in the electronic free energy. It is crucial to point out that the quantities of interest only compare differences in the Helmholtz free energy or in the Gibbs free energy; as such, most of the contributions, aside from the dominant term, can be omitted due to error canceling. Nevertheless, taking into account the additional entropic terms can elucidate subtle effects not possible with only DFT calculations. Such is the case when exploring phase transitions of Si(111)-In nanowires [98] or calculating accurate transitions in metals at high temperatures [99], to name a few. The configurational entropy is explored further on in section 3.3. The electronic free energy is

$$F_{\text{el}} = E_{\text{tot}} - TS_{\text{el}}, \quad (3.12)$$

where the total energy can be approximated to the zero-temperature ground-state energy from DFT calculations. The electronic entropy S_{el} is calculated from

$$S_{\text{el}} = k_B \int dE \bar{n}(E) [f \ln f + (1-f) \ln(1-f)], \quad (3.13)$$

here \bar{n} is the electronic density of states and f is the Fermi distribution. The density of states is approximated to the density of states at zero temperature obtained from DFT calculations. The electronic entropy is most important in materials with no band gap, i. e., metals. For solids with mid-gap states, the contribution also becomes relevant.

The surface vibrational entropy can be calculated with relatively little effort by use of the simple harmonic approximation. The approximation for the vibrational free energy [100] takes the form of

$$F_{\text{vib}} = \frac{\Omega}{8\pi^3} \int d^3\mathbf{k} \sum_{\nu} \left(\frac{1}{2} \hbar\omega_{\nu}(\mathbf{k}) + k_B T \ln \left[1 - \exp \left(-\frac{\hbar\omega_{\nu}(\mathbf{k})}{k_B T} \right) \right] \right), \quad (3.14)$$

where $\omega_{\nu}(\mathbf{k})$ are the wave-vector dependent phonon frequencies. Similar to the electronic free energy, the phonon frequencies are approximated by neglecting thermal effects in their calculations, i. e., taking the phonon frequencies from standard DFT calculations.

3.2 Lattice vibrations

A phonon is a quasi-particle that represents the collection of lattice excitations. In the Oppenheimer approximation[51], the nuclei velocities are considered independent of the electronic energies. If the nuclei are treated classically, the equation of motion for a nucleus I in position \mathbf{R}_I and mass M_I is described by

$$M_I \frac{\partial^2 \mathbf{R}_I}{\partial t^2} = F_I(\mathbf{R}) = -\frac{\partial E(\mathbf{R})}{\partial \mathbf{R}_I}, \quad (3.15)$$

where $\mathbf{R} \equiv \{\mathbf{R}_I\}$ is the set of all nuclear coordinates. The total energy is expanded in Taylor series around the set of equilibrium positions of the nuclei $\mathbf{R}^0 = \{\mathbf{R}_I^0\}$

$$E(\mathbf{R}) = E(\mathbf{R}^0) + \sum_{I\alpha} -F_{I\alpha}(\mathbf{R}^0)u_{I\alpha} + \sum_{I\alpha J\beta} \Phi_{I\alpha J\beta}(\mathbf{R}^0)u_{I\alpha}u_{J\beta} + \mathcal{O}(\mathbf{R}^3), \quad (3.16)$$

the indices α and β are used for the Cartesian components. Here, $u_{I\alpha} = \mathbf{R}_{I\alpha} - \mathbf{R}_{I\alpha}^0$ is the displacement of the atoms with respect to the equilibrium position and the second derivative of the energy, the second-order force-constant is

$$\Phi_{I\alpha J\beta}(\mathbf{R}^0) = \left. \frac{\partial^2 E(\mathbf{R})}{\partial \mathbf{R}_{I\alpha} \partial \mathbf{R}_{J\beta}} \right|_{\mathbf{R}=\mathbf{R}^0} = -\left. \frac{\partial F_{I\alpha}(\mathbf{R})}{\partial \mathbf{R}_{J\beta}} \right|_{\mathbf{R}=\mathbf{R}^0}. \quad (3.17)$$

In the equilibrium conditions, the force acting on atom I is zero, $F_{I\alpha}(\mathbf{R}^0) = 0$ [100]; this is called the zero-force condition[54]. Inserting equation 3.16 in equation 3.15 and omitting higher-order contributions, the equation of motion becomes

$$M_I \ddot{u}_{I\alpha} = - \sum_{J\beta} \Phi_{I\alpha J\beta}(\mathbf{R}^0)u_{J\beta}. \quad (3.18)$$

The solutions to the coupled system of equations take the form of plane waves traveling parallel to \mathbf{q}

$$u_{I\alpha,\nu}(t, \mathbf{q}) = \frac{1}{\sqrt{M_I}} A^\nu(\mathbf{q}) e_{I\alpha,\nu}(\mathbf{q}) e^{i\mathbf{q} \cdot \mathbf{R}_I} e^{-i\omega_\nu t}, \quad (3.19)$$

with amplitudes $A^\nu(\mathbf{q})$ and the phonon mode eigenvectors $e_{I\alpha,\nu}(\mathbf{q})$. Replacing in equation 3.18, it is rewritten as

$$\omega_\nu^2 e_{I\alpha,\nu}(\mathbf{q}) = \sum_{J\beta} D_{I\alpha J\beta}(\mathbf{q}) e_{J\beta,\nu}(\mathbf{q}), \quad (3.20)$$

where

$$D_{I\alpha J\beta}(\mathbf{q}) = \frac{1}{\sqrt{M_I M_J}} \Phi_{I\alpha J\beta}(\mathbf{R}^0) e^{i\mathbf{q} \cdot (\mathbf{R}_J - \mathbf{R}_I)}, \quad (3.21)$$

is the dynamical matrix[100] for a given wave vector \mathbf{q} . By solving the eigenvalue problem, equation 3.20, the phonon frequencies $\omega_\nu(\mathbf{q})$ and eigenvectors $e_{I\alpha,\nu}(\mathbf{q})$ at any arbitrary point \mathbf{q} can be obtained. The second-order force constants $\Phi_{I\alpha J\beta}$ can be computed using different methods; the most direct approach is to express the total energies, or the forces, as a function of the position of the nuclei. This approach is referred to as “frozen phonons”[54] and the partial derivatives

are solved numerically using the finite difference method. The second-order force constants are computed from finite differences as

$$\Phi_{I\alpha J\beta}(\mathbf{R}^0) = -\frac{\partial F_{I\alpha}(\mathbf{R})}{\partial \mathbf{R}_{J\beta}} \bigg|_{\mathbf{R}=\mathbf{R}^0} \approx -\frac{1}{2} \frac{[F(\mathbf{R}^0 + \Delta \mathbf{R}_{J\beta}) - F(\mathbf{R}^0 - \Delta \mathbf{R}_{J\beta})]}{\Delta \mathbf{R}_{J\beta}}, \quad (3.22)$$

for small displacements $\Delta \mathbf{R}_{J\beta}$.

3.3 Defects in crystals

The first law of thermodynamics indicates that when defects are introduced to a system, there will be an energy difference. In order to estimate the concentration of defects present in a crystal, first it is necessary to determine the energy needed to form the defects in a perfect system. The change in Gibbs free energy ΔG upon the introduction of N defects distributed over M possible sites is given by:

$$\Delta G = G - G_{\text{perf}} = N\Delta G_f - T\Delta S_{\text{conf}}, \quad (3.23)$$

where G_{perf} is the Gibbs free energy of the system without defects, ΔS_{conf} the configuration entropy change, and ΔG_f the Gibbs free energy change due to the defect formation, described as:

$$\Delta G_f = G_{\text{def}} - G_{\text{perf}} - \sum_i \Delta n_i \mu_i. \quad (3.24)$$

Here, G_{def} is the Gibbs free energy of the system with one defect, μ_i the chemical potential of atoms type i , and Δn_i the difference in the number of atoms between the system with and without defects. For $\Delta n_i > 0$ corresponds to the addition of atoms, i. e., interstitial and substitutional defects; and $\Delta n_i < 0$ corresponds to a reduction number of atoms, i. e., vacancy defects. All other entropic contributions, except the configuration entropy, are included in the ΔG_f term. The configuration entropy can be determined with the Boltzmann equation of entropy for a disordered system

$$S = k_B \ln W, \quad (3.25)$$

where S is the entropy of a system, for which W is the number of all possible configurations. The distribution of N defects in M possible sites is given by the binomial coefficient. The configuration entropy is then

$$\Delta S_{\text{conf}} = k_B \ln \frac{M!}{N!(M-N)!}. \quad (3.26)$$

There will always be a number of defects at temperatures above 0 K, that cannot be removed by thermal treatment. Such type of defects are intrinsic defects. At thermal equilibrium the minimum in the free energy change, ΔG , for a certain number of defects is found when $\left(\frac{\partial \Delta G}{\partial N}\right)_T = 0$ [101], that is:

$$\left(\frac{\partial \Delta G}{\partial N}\right)_T = \Delta G_f - k_B T \frac{\partial}{\partial N} \ln \frac{M!}{N!(M-N)!} = 0. \quad (3.27)$$

For numerous defects and defect sites, Stirling's approximation (i. e., $\ln x! \approx x \ln x - x$) can be used to eliminate the factorials and reduce the last term to

$$\left(\frac{\partial \Delta G}{\partial N}\right)_T \approx \Delta G_f - k_B T \ln \frac{M-N}{N} = 0. \quad (3.28)$$

The number or concentration of defects in thermal equilibrium is then

$$N = \frac{M}{1 + e^{\Delta G_f/k_B T}} \quad (3.29)$$

For a small concentration of defects $N \ll M$, equation 3.29 can be approximated to:

$$N \approx M e^{-\Delta G_f/k_B T}. \quad (3.30)$$

The application of the above equation to determine the concentration of each defect type individually will give a non-physical result. This is because it fails to take into account the fact that the number of possible sites is reduced by all other defect types. To address this issue, the following coupled system of equations[102], for the number of defects type k , is introduced as

$$N_k = \left(M - \sum_{l \neq k} N_l \right) \left/ \left(1 + e^{\Delta G_f^{(k)}/k_B T} \right) \right. \quad (3.31)$$

It can be shown that

$$N_k = M \frac{e^{\Delta G_f^{(k)}/k_B T}}{1 + \sum_l e^{\Delta G_f^{(l)}/k_B T}}. \quad (3.32)$$

With equation 3.33 $\sum_l N_l < M$ will always be fulfilled, thus avoiding the problems of overcounting present in equations 3.29 and 3.30.

3.4 Nudged elastic band method

The rate constants for chemical reactions and phase transitions are described within the transition state theory (TST) [103–105]. The TST method relies on two central assumptions: (a) The transition reaction is slow enough that a Boltzmann distribution is established and maintained for the reactants in every degree of freedom. (b) There is a dividing surface that a reaction trajectory between initial and final states crosses only once. This dividing surface is referred to as the transition state. The task is now finding the minimal energy reaction path. The maxima of such a path correspond to saddle points in the potential energy surface. Although originally the TST method was employed for finding transition rates, the minimum energy path and the saddle points are of great interest since they describe the reaction itself.

Several techniques exist for finding the minimum reaction energy path and the saddle points; a particular efficient method is the nudged elastic band (NEB) method[106, 107]. The method can be combined with electronic structure calculation, such as DFT. The path consists of the initial and final states of the system and is connected through a series of "images" that represent the intermediate configurations. A spring interaction links adjacent images in order to ensure continuity of the path, mimicking an elastic band. The method then iteratively optimizes the path by adjusting the position of each image along the band, minimizing the forces until the minimum energy path is achieved. This path is known as the "nudged" path.

An elastic band composed of $n + 1$ images can be defined by $[\mathbf{R}_0, \mathbf{R}_1, \dots, \mathbf{R}_N]$, where \mathbf{R}_i are the set of Cartesian positions of the atoms of image i . \mathbf{R}_0 and \mathbf{R}_N correspond to the starting and final states and are left fixed throughout the calculation. The NEB method distinguishes itself from other methods by defining the force acting on each image as the sum of the spring force parallel

3.4 Nudged elastic band method

to the path and the true force perpendicular to the path. The NEB force for image i is then defined as

$$F_i^{\text{NEB}} = F_i^{\text{s}\parallel} - F_i^{\nabla\perp}, \quad (3.33)$$

where the true force $F_i^{\nabla\perp}$ is the force due to the gradient of the potential (equation 2.42) perpendicular to the path

$$F_i^{\nabla\perp} = \nabla E(\mathbf{R}_i) - (\nabla E(\mathbf{R}_i) \cdot \hat{\tau}_i) \hat{\tau}_i, \quad (3.34)$$

here $\hat{\tau}_i$ is the normalized local tangent of image i . The local tangent is determined according to Ref. [108]. The parallel spring force is

$$F_i^{\text{s}\parallel} = k(|\mathbf{R}_{i+1} - \mathbf{R}_i| - |\mathbf{R}_i - \mathbf{R}_{i-1}|) \cdot \hat{\tau}_i, \quad (3.35)$$

where k is the spring constant. The unique construction of equation 3.33 allows the spacing of each image along the band to be controlled only by the spring force; this force is referred to as “nudging”. Equivalently, only the true force contributes to the path convergence.

3.4.1 Climbing image NEB

Since the spring constant is the same for all images, the images will be distributed equidistantly along the path. However, this means that an image at the saddle point is not guaranteed. The saddle points along the path are obtained with the climbing image NEB (CI-NEB) method[109]. In the CI-NEB method, the image with the highest energy is driven up to the saddle point. This is accomplished by not including the spring force and inverting the true force. First, regular NEB calculations are performed; after a couple iterations, the image i_{max} with the highest energy is determined, and the NEB force is given by

$$F_{i_{\text{max}}} = -\nabla E(\mathbf{R}_{i_{\text{max}}}) + 2(\nabla E(\mathbf{R}_{i_{\text{max}}}) \cdot \hat{\tau}_{i_{\text{max}}}) \hat{\tau}_{i_{\text{max}}}. \quad (3.36)$$

Convergence will then maximize this image along the band and minimize along all other directions. After convergence, the image will be located exactly at the saddle point.

Chapter 4

Optical spectroscopy

Among the plethora of measurement techniques that exist in the modern day, spectroscopy ones stand out among them as a number of non-invasive techniques capable of determining electronic and structural properties of materials. Spectroscopy relies on the interpretation of the interaction of electromagnetic waves and matter as a function of the frequency or wavelength of the light. As light interacts with the electronic structure of the material, part of the light is reflected while the rest is transmitted or absorbed. From the different types of light-matter interactions, light reflection is of particular interest here.

Reflection, among other types of light-matter interaction, is governed primarily by a fundamental response function, the so-called dielectric function. This chapter will focus on the derivation of the dielectric function for optical spectroscopy using different levels of theory. The first sections will be focused on deriving the dielectric function starting in the independent particle approximation (IPA) up to including local field and excitonic effects; further reading resources can be found in references [54, 90, 110]. The last section will be dedicated to showing the relation between the dielectric function and reflectivity, and how to derive meaningful results that can be compared directly to experimental reflectance anisotropy spectroscopy (RAS) results.

4.1 Dielectric response function

A response function describes the response of a system to an external perturbation. The change to the total potential induced by a variation of the external potential is given by

$$\delta V_{\text{tot}}(\mathbf{r}) = \delta V_{\text{ext}}(\mathbf{r}) + \delta V_{\text{ind}}(\mathbf{r}), \quad (4.1)$$

where the δV_{ind} is the induced potential due to the change in the charge density. The response function that couples the change to the total density by the perturbation to the external potential is given by

$$\delta n(1) = \int d2 \chi(1, 2) V_{\text{ext}}(2), \quad (4.2)$$

where the response function $\chi(1, 2)$ is the reducible polarizability introduced in equation 2.71b, defined as

$$\chi(1, 2) = \frac{\delta n(1)}{\delta V_{\text{ext}}(2)}. \quad (4.3)$$

The same notation of natural numbers to describe position and space is used in section 2.3, i. e., $(\mathbf{r}_1, t) \equiv (1)$. From first-order perturbation theory, the Kubo formula[111, 112] relates the change of the density to the density correlation function in

$$\chi(1, 2) = -i\Theta(t_1 - t_2) \langle [n(1)n(2)]_- \rangle, \quad (4.4)$$

where $\Theta(t_1 - t_2)$ is a step function, that ensures causality. χ is non-vanishing at time t_1 after a perturbation at time t_2 . The change in the total potential due to the variation of the external potential is defined from Maxwell's equations by the inverse dielectric function.

$$\varepsilon^{-1}(1, 2) = \frac{\delta V_{\text{tot}}(1)}{\delta V_{\text{ext}}(2)}. \quad (4.5)$$

If the change to the external potential is caused by a test potential, similar to Green's function approach, then the induced potential is just the change in the Hartree potential $\delta V_{\text{ind}} = \delta V_{\text{H}}$ and the inverse dielectric function is given by

$$\varepsilon^{-1}(1, 2) = \delta(1, 2) + \int d3 V_{\text{ee}}(1, 3) \chi(3, 2). \quad (4.6)$$

It is important to point out, although equation 4.6 and equation 2.70 are similar in construction; they are essentially different quantities. Eq. 2.70 is the dielectric function calculated from the irreducible polarizability $P(1, 2) = \frac{\delta n(1)}{\delta V_{\text{tot}}(2)}$. Note that the dielectric function is the response to the total field, while the inverse dielectric function is the response to the external field. Both the reducible and irreducible polarizability are related through the Dyson equation

$$\chi(1, 2) = P(1, 2) + \iint d3 d4 P(1, 3) V_{\text{ee}}(2, 4) \chi(4, 2), \quad (4.7)$$

and in general $P(1, 2) \neq \chi(1, 2)$. Unfortunately both the reducible and irreducible polarizabilities are unknown, the quantity that is easily accessible from DFT is the irreducible polarizability in the independent particle picture $\chi^0(1, 2)$, defined as the change in the density induced by the change in the effective potential (equation 2.17), as

$$\chi^0(1, 2) = \frac{\delta n(1)}{\delta V_{\text{eff}}(2)}. \quad (4.8)$$

The relationship between all three polarizabilities can be shown to be

$$\chi(1, 2) = \chi^0(1, 2) + \iint d3 d4 \chi^0(1, 3) (V_{\text{ee}}(3, 4) + K_{\text{xc}}(3, 4)) \chi(4, 2), \quad (4.9a)$$

$$P(1, 2) = \chi^0(1, 2) + \iint d4 d3 \chi^0(1, 3) K_{\text{xc}}(3, 4) P(4, 2), \quad (4.9b)$$

with the exchange-correlation kernel defined as

$$K_{\text{xc}}(\mathbf{r}, \mathbf{r}') = \frac{\delta V_{\text{xc}}(\mathbf{r})}{\delta n(\mathbf{r})} = \frac{\delta^2 E_{\text{xc}}[n]}{\delta n(\mathbf{r}) \delta n(\mathbf{r}')}. \quad (4.10)$$

4.1 Dielectric response function

The most common approximation is to neglect the exchange-correlation contributions to the χ and P by setting the kernel K_{xc} to zero. This is the so-called random phase approximation (RPA) first introduced for the HEG by Pines and Bohm [113–115]. The RPA is in the same level of approximation as the GW approximation [116] where the vertex function is neglected from the calculation of P . The RPA often refers to whenever equation 2.74a is evaluated in the independent particle picture. Thus, in the RPA equations 4.6 and 2.70 are reduced to

$$\varepsilon^{-1}(1, 2) = \delta(1, 2) + \iint d3d4 V_{ee}(1, 3) \chi^0(1, 4) [1 - \chi^0 V_{ee}]^{-1} (4, 3) \quad (4.11a)$$

$$\varepsilon(1, 2) = \delta(1, 2) - \iint d3d4 V_{ee}(1, 3) \chi^0(3, 2). \quad (4.11b)$$

In practice, the dielectric function is calculated in the frequency and momentum space, which is related to the real space via a Fourier transform. Taking advantage of the periodicity of crystals, the Fourier transforms are performed using Bloch functions. The wave functions are replaced by the Bloch functions $\varphi_i(\mathbf{r}) \rightarrow \varphi_{n,\mathbf{k}}(\mathbf{r}) = e^{i\mathbf{k}\cdot\mathbf{r}} u_{n,\mathbf{k}}(\mathbf{r})$, where $u_{n,\mathbf{k}}(\mathbf{r})$ is a periodic function. A wave vector in the reciprocal space can be written as $\mathbf{q} + \mathbf{G}$, where the plane wave vector \mathbf{q} is restricted to the first Brillouin zone and \mathbf{G} is a reciprocal lattice vector. The dielectric function in the reciprocal space $\varepsilon(\mathbf{q} + \mathbf{G}, \mathbf{q} + \mathbf{G}', \omega)$ can be written in matrix form $\varepsilon_{\mathbf{G}, \mathbf{G}'}(\mathbf{q}, \omega)$ and similarly for the inverse dielectric function $\varepsilon_{\mathbf{G}, \mathbf{G}'}^{-1}(\mathbf{q}, \omega)$. The Coulomb potential in the periodic reciprocal space is given by

$$V_{ee}(\mathbf{q} + \mathbf{G}) = \frac{4\pi}{\Omega |\mathbf{q} + \mathbf{G}|^2}, \quad (4.12)$$

where Ω is the volume of the primitive cell.

So far, only the microscopic dielectric function has been described, but optical phenomena involve long wavelengths ($\mathbf{G}, \mathbf{G}' = 0$) on a much larger scale than that of atomic distances and are described by the macroscopic dielectric function $\varepsilon_M(\omega)$. The macroscopic dielectric function is defined as the ratio between internal and external fields. The macroscopic dielectric function is related to the inverse dielectric function matrix, derived by Adler [117] and Wiser [118], in the long wavelength limit ($\mathbf{q} \rightarrow 0$)

$$\varepsilon_M(\omega) = \lim_{\mathbf{q} \rightarrow 0} \frac{1}{\varepsilon_{00}^{-1}(\mathbf{q}, \omega)}. \quad (4.13)$$

If the local-field effects (off-diagonal elements) are neglected, the macroscopic dielectric function is described by the dielectric function matrix element

$$\varepsilon_M(\omega) \approx \lim_{\mathbf{q} \rightarrow 0} \varepsilon_{00}(\mathbf{q}, \omega). \quad (4.14)$$

The correlation function equation 4.4 in the independent particle picture and in frequency space is

$$\chi^0(\mathbf{r}, \mathbf{r}', \omega) = 2 \sum_{i,j} (f_j - f_i) \frac{\varphi_j^*(\mathbf{r}) \varphi_i(\mathbf{r}) \varphi_i^*(\mathbf{r}') \varphi_j(\mathbf{r}')}{\omega - (\varepsilon_i - \varepsilon_j) + i\eta}, \quad (4.15)$$

where η is an infinitesimal number and the factor 2 in front of the sum accounts for spin degeneracy. The Fermi weights f equal to 1 for occupied states and 0 for unoccupied. Using the dielectric

function in the RPA equation 4.14 and equation 4.15 in the frequency and momentum space, an expression for the macroscopic dielectric function is finally obtained

$$\varepsilon_M(\omega) = 1 - 2 \lim_{\mathbf{q} \rightarrow 0} V_{ee}(\mathbf{q}) \sum_{n, n', \mathbf{k}} \frac{f_{n', \mathbf{k}+\mathbf{q}} - f_{n, \mathbf{k}}}{\epsilon_{n', \mathbf{k}+\mathbf{q}} - \epsilon_{n, \mathbf{k}} - \omega - i\eta} \left| \left\langle \varphi_{n', \mathbf{k}+\mathbf{q}} \left| e^{i\mathbf{q} \cdot \mathbf{r}} \right| \varphi_{n, \mathbf{k}} \right\rangle \right|^2, \quad (4.16)$$

here Bloch wavefunctions have been used. When considering semiconductors and insulators (i. e., if both n, \mathbf{k} and $n', \mathbf{k}+\mathbf{q}$ are occupied or unoccupied), the sum equals to zero; thus, the sum is reduced to include only the valence v and conduction c states. Normally only the imaginary part of the macroscopic dielectric function $\varepsilon_M^{(2)}(\mathbf{q}, \omega)$ is calculated, as

$$\varepsilon_M^{(2)}(\omega) = 2 \lim_{\mathbf{q} \rightarrow 0} V_{ee}(\mathbf{q}) \sum_{v, c, \mathbf{k}} \delta(\epsilon_{c, \mathbf{k}+\mathbf{q}} - \epsilon_{v, \mathbf{k}} - \omega) \left| \left\langle u_{c, \mathbf{k}+\mathbf{q}} \left| u_{v, \mathbf{k}} \right. \right\rangle \right|^2. \quad (4.17)$$

The real part is then obtained from the Kramers-Kronig transformation. The difficulty lies in calculating the $|u_{c, \mathbf{k}+\mathbf{q}}\rangle$ state. In the projected-augmented waves method[119], this problem is tackled by expanding in Taylor series and treating the derivative with respect to \mathbf{k} in perturbation theory. The full discussion by Gajdoš et al. can be found in Ref. [120].

4.2 Local-field effects

In the previous section, the macroscopic dielectric function was approximated by neglecting the local-field effects with equation 4.14. An alternate formulation of the macroscopic dielectric function allows the inclusion of said local-field effects. In the next section, excitonic effects will also be implemented in the macroscopic dielectric function. To start, it is convenient to write the dielectric function $\varepsilon(\mathbf{q} + (G), \mathbf{q} + (G'), \omega)$ in the following matrix form

$$\varepsilon(\mathbf{q}, \omega) = \begin{pmatrix} \varepsilon_{00}(\mathbf{q}, \omega) & \varepsilon_{0G'}(\mathbf{q}, \omega) \\ \varepsilon_{G0}(\mathbf{q}, \omega) & \varepsilon_{GG'}(\mathbf{q}, \omega) \end{pmatrix}, \quad (4.18a)$$

and

$$\varepsilon^{-1}(\mathbf{q}, \omega) = \begin{pmatrix} \varepsilon_{00}^{-1}(\mathbf{q}, \omega) & \varepsilon_{0G}^{-1}(\mathbf{q}, \omega) \\ \varepsilon_{G'0}^{-1}(\mathbf{q}, \omega) & \varepsilon_{G'G}^{-1}(\mathbf{q}, \omega) \end{pmatrix}. \quad (4.18b)$$

Matrix inversion gives the following relation

$$\varepsilon_{00}^{-1}(\mathbf{q}, \omega) = \left\{ \varepsilon_{00}(\mathbf{q}, \omega) - \varepsilon_{0G'}(\mathbf{q}, \omega) [\varepsilon_{GG'}(\mathbf{q}, \omega)]^{-1} \varepsilon_{G0}(\mathbf{q}, \omega) \right\}^{-1}. \quad (4.19)$$

Considering only the first term in equation 4.19 would then give the approximation of equation 4.14. Inserting the above equation in 4.13 together with equation 2.70 in frequency and reciprocal space, the macroscopic dielectric function is obtained as

$$\varepsilon_M(\omega) = 1 - \lim_{\mathbf{q} \rightarrow 0} V_{ee}(\mathbf{q}) P_{00}(\mathbf{q}, \omega) - \sum_{\mathbf{G}, \mathbf{G}' \neq 0} V_{ee}(\mathbf{q}) P_{0G'}(\mathbf{q}, \omega) [\varepsilon_{GG'}(\mathbf{q}, \omega)]^{-1} V_{ee}(\mathbf{q} + \mathbf{G}) P_{G0}(\mathbf{q}, \omega). \quad (4.20)$$

The sum term is the local-field effects previously neglected in equation 4.14. In order to simplify the above equation further, a matrix form that includes all \mathbf{G} and \mathbf{G}' and not only $\mathbf{G}, \mathbf{G}' \neq 0$ is

necessary. For this, it is useful to define a bare Coulomb interaction without its long-wavelength component $V_{ee}(\mathbf{q})$

$$\bar{V}_{ee}(\mathbf{q} + \mathbf{G}) = \begin{cases} 0, & \text{if } \mathbf{G} = 0 \\ V_{ee}(\mathbf{q} + \mathbf{G}), & \text{if } \mathbf{G} \neq 0 \end{cases}, \quad (4.21)$$

such that the $\varepsilon_M(\omega)$, equation 4.20, is reduced to [121]

$$\varepsilon_M(\omega) = 1 - \lim_{q \rightarrow 0} V_{ee}(\mathbf{q}) \bar{\chi}_{00}(\mathbf{q}, \omega), \quad (4.22)$$

where the relation to equation 4.20 is given by polarizability $\bar{\chi}_{\mathbf{G}\mathbf{G}'}$ through its Dyson equation, here presented in real space

$$\bar{\chi}(1, 2) = P(1, 2) + \iint d3d4 P(1, 3) \bar{V}_{ee}(3, 4) \bar{\chi}(4, 2). \quad (4.23)$$

An alternate Dyson equation can be obtained by considering the potential $V_{ee} = \bar{V}_{ee} + V_{ee}^0$, where the V_{ee}^0 is the long wavelength component and from equation 4.7

$$\chi(1, 2) = \bar{\chi}(1, 2) + \iint d3d4 \bar{\chi}(1, 3) V_{ee}^0(3, 4) \chi(4, 2). \quad (4.24)$$

Only the short-range components \bar{V}_{ee} have to be explicitly considered in equation 4.23. The local-field effects are now included through $\bar{\chi}$ in equation 4.22; as such, \bar{V}_{ee} plays the role of a correction term. This can be seen from equation 4.23, if \bar{V}_{ee} is set to zero, equation 4.14 is retrieved where local-field effects have been neglected. The Dyson equation 4.7 is similar to equation 4.23, but are fundamentally different, and it has entirely to do with the small differences between V_{ee} and \bar{V}_{ee} [121].

4.3 Bethe-Salpeter equation

Beyond local-field effects, the electron-hole interactions are necessary for the correct description of optical spectra. These interactions are mathematically described by a two particle propagator. The propagation of two particles is contained within the kernel of a Dyson-like equation, the so-called Bethe-Salpeter equation (BSE). Looking back to the two-particle Green's function equation 2.63, a more general formulation with respect to the variation of a non-local perturbation $\mathcal{J}(2', 2)$, is given by

$$L(1, 2, 1', 2') = \frac{\delta G(1, 1')}{\delta \mathcal{J}(2', 2)} = G(1, 1')G(2, 2') - G(1, 2, 1', 2'), \quad (4.25)$$

here $L(1, 2, 1', 2')$ is the two-particle correlation function. For a local potential, $\mathcal{J}(2^+, 2)$ equation 2.63 is retrieved. By using the definition of the inverse Green's function, the above equation is expressed as

$$L(1, 2, 1', 2') = \iint d3'd3 \frac{\delta G(3', 1')}{\delta \mathcal{J}(2', 2)} G^{-1}(3, 3') G(1, 3) = - \iint d3'd3 G(3', 1') \frac{\delta G^{-1}(3, 3')}{\delta \mathcal{J}(2', 2)} G(1, 3). \quad (4.26)$$

Using equations 2.66 and 2.67 the Dyson equation for the two-particle propagator, the Bethe-Salpeter equation, is obtained

$$L(1, 2, 1', 2') = L_0(1, 2, 1', 2') + \iiint d3d3'd4d4' L_0(1, 3', 1', 3) \Xi(3, 4, 3', 4') L(4', 2, 4, 2'), \quad (4.27)$$

where the product of the one-particle Green's functions is defined as

$$L_0(1, 2, 1', 2') = G(1, 2')G(2, 1'), \quad (4.28)$$

and all the two-particle interactions are contained in the interaction kernel Ξ

$$\Xi(1, 2, 1', 2') = -i\delta(1, 1')\delta(2'^+, 2)V_{ee}(1^+, 2) + \frac{\delta\Sigma(1, 1')}{\delta G(2', 2)}. \quad (4.29)$$

The relationship between the reducible polarizability and the two-particle propagator is given by

$$\chi(1, 2) = -iL(1, 2, 1^+, 2^+). \quad (4.30)$$

A similar expression exists for the polarizability for independent particles $\chi^0 = -iL^0$. The interaction kernel can be separated as a sum of two terms, one containing the short wavelength potential \bar{V}_{ee} and the other the long wavelength potential V_{ee}^0 . Thus, the Dyson equation can then be broken up into contribution \bar{L} with the coupled Dyson equations

$$\bar{L}(1, 2, 1', 2') = L_0(1, 2, 1', 2') + \iiint d3d3'd4d4' L_0(1, 3', 1', 3) \bar{\Xi}(3, 4, 3', 4') \bar{L}(4', 2, 4, 2') \quad (4.31a)$$

$$L(1, 2, 1', 2') = \bar{L}(1, 2, 1', 2') - i \iint d3d4 \bar{L}(1, 3, 1', 3) V_{ee}^0(3^+, 4) L(4, 2, 4^+, 2'), \quad (4.31b)$$

where the potential V_{ee} is replaced for the short-range potential \bar{V}_{ee} in the interaction kernel $\bar{\Xi}$. Equation 4.31b is equivalent to equation 4.24. Moreover, it can be shown that

$$\bar{\chi}(1, 2) = -i\bar{L}(1, 2, 1^+, 2^+). \quad (4.32)$$

The two-particle correlation function \bar{L} gives direct access to the optical spectra. For this reason, \bar{L} is frequently used in the context of BSE calculations of the optical spectra and will be followed in this work.

The BSE in the GW approximation

The exchange-correlation term in the interaction kernel $\bar{\Xi}$ can be approximated using the GWA approach. The self-energy in the GWA is given by equation 2.74b, the exchange energy is thus approximated as

$$\frac{\delta\Sigma(1, 1')}{\delta G(2', 2)} = i\delta(1, 2')\delta(1', 2)W(1^+, 1') + G(1, 1')\frac{\delta W(1^+, 1')}{\delta G(2', 2)}. \quad (4.33)$$

The contribution of the second term to the above equation is much smaller than the screened Coulomb potential. As such, the variation of the screened Coulomb potential can be omitted; the interaction kernel is then approximated by

$$\bar{\Xi}(1, 2, 1', 2') \approx -i\delta(1, 1')\delta(2'^+, 2)\bar{V}_{ee}(1^+, 2) + i\delta(1, 2')\delta(1', 2)W(2^+, 2') \quad (4.34)$$

Similar to the Coulomb interaction, the screened potential W is assumed static,

$$W(1, 2) = W(\mathbf{r}_1, \mathbf{r}_2)\delta(t_1 - t_2), \quad (4.35)$$

this results in a simplification of the BSE in frequency space.

Spin structure of the interaction kernel

Throughout this work, spin-independent systems have been considered, and spin degeneracy has often been included by a factor of 2 on the different equations. However, special considerations have to be taken into account for the BSE. The interaction kernel, equation 4.34 can be separated in the two contributions[122], based on the spin number ξ , as

$$\Xi_{\xi_1 \xi_2 \xi_3 \xi_4} = \delta_{\xi_1 \xi_3} \delta_{\xi_2 \xi_4} \Xi^a + \delta_{\xi_1 \xi_4} \delta_{\xi_3 \xi_2} \Xi^b, \quad (4.36)$$

where Ξ^a and Ξ^b are the unscreened and screened potential parts of the interaction kernel, respectively. Alternatively, the interaction kernel can also be written as the singlet Ξ^s and triplet Ξ^t contributions[122] as follows

$$\Xi_{\xi_1 \xi_2 \xi_3 \xi_4} = \frac{1}{2} \delta_{\xi_1 \xi_3} \delta_{\xi_2 \xi_4} \Xi^s + \frac{1}{2} \sigma_{\xi_1 \xi_3} \sigma_{\xi_2 \xi_4} \Xi^t, \quad (4.37)$$

where σ are the Pauli matrices, and the singlet and triplet are defined as

$$\Xi^s \equiv 2\Xi^a + \Xi^b \quad (4.38a)$$

$$\Xi^t \equiv \Xi^b. \quad (4.38b)$$

Only the singlet is optically allowed, thus moving forward only this contribution to the interaction kernel will be taken into account for the polarizability. The interpretation of the singlet, equation 4.38a, stems from the fact, on the one hand, that the screened potential W does not include spin and the way the δ function connects the indices W is diagonal in the spin. On the other hand, the Coulomb potential is spin-independent, thus the spin is implicitly included by a factor of 2 [121].

4.3.1 The electron-hole interaction

The interaction of the electron-hole pairs can be studied on the basis of independent particles. It is more convenient to approach the problem by solving matrix equations in the complete set of the orthonormal independent-particle orbitals. A matrix element for a four-point function in this basis is given by the integral

$$F_{n_1 n_2 n_3 n_4} = F_{n_1 n_3}^{n_4 n_2} = \iiint \mathrm{d}\mathbf{r}_1 \mathrm{d}\mathbf{r}_2 \mathrm{d}\mathbf{r}_3 \mathrm{d}\mathbf{r}_4 \varphi_{n_1}^*(\mathbf{r}_1) \varphi_{n_2}^*(\mathbf{r}_2) F(\mathbf{r}_1, \mathbf{r}_2, \mathbf{r}_3, \mathbf{r}_4) \varphi_{n_3}(\mathbf{r}_3) \varphi_{n_4}(\mathbf{r}_4). \quad (4.39)$$

The frequency Fourier transform of equation 4.28 can be written for the Green's function in the independent particle picture as follows

$$L_0(\mathbf{r}_1, \mathbf{r}_2, \mathbf{r}'_1, \mathbf{r}'_2; \omega) = 2i \sum_{m_1 \dots m_4} (f_{m_1} - f_{m_2}) \frac{\varphi_{m_1}(\mathbf{r}_1) \varphi_{m_2}(\mathbf{r}_2) \varphi_{m_3}^*(\mathbf{r}'_1) \varphi_{m_4}^*(\mathbf{r}'_2)}{\omega - (\epsilon_{m_2} - \epsilon_{m_1}) + i\eta} \delta_{m_1 m_4} \delta_{m_2 m_3}. \quad (4.40)$$

Here, the factor 2 denotes the spin. Note that the expression for the polarizability, equation 4.15, can be obtained from the above equation. The matrix form of L_0 is then

$$L_0^{n_4 n_2}_{n_1 n_3}(\omega) = 2i \frac{(f_{n_1} - f_{n_2}) \delta_{n_1 n_4} \delta_{n_2 n_3}}{\omega - (\epsilon_{n_2} - \epsilon_{n_1}) + i\eta}. \quad (4.41)$$

The BSE equation 4.31a becomes

$$\bar{L}_{n_1 n_3}^{n_4 n_2}(\omega) = \left[L_0^{-1}(\omega) - \frac{1}{2} \bar{\Xi}^s \right]_{n_1 n_3}^{-1 n_4 n_2} = 2i \left[\bar{H}^{2p} - \mathbb{1} \omega \right]_{n_1 n_3}^{-1 n_4 n_2} (f_{n_2} - f_{n_4}), \quad (4.42)$$

where $\mathbb{1} = \delta_{m_1 m_4} \delta_{m_2 m_3}$ is the identity operator and \bar{H}^{2p} is the two-particle Hamiltonian

$$\bar{H}^{2p}_{n_1 n_3} = (\epsilon_{n_2} - \epsilon_{n_1}) - i(f_{n_3} - f_{n_1}) \bar{\Xi}^s_{n_1 n_3}^{n_4 n_2}. \quad (4.43)$$

The matrix element of the screened interaction $\delta(1, 2')\delta(1', 2)W(2^+, 2')$ in the kernel Ξ is defined from equation 4.39

$$W_{n_1 n_3}^{n_4 n_2} = \iint d^3 r_1 d^3 r_2 \varphi_{n_1}^*(\mathbf{r}_1) \varphi_{n_2}^*(\mathbf{r}_2) W(\mathbf{r}_1, \mathbf{r}_2) \varphi_{n_3}(\mathbf{r}_2) \varphi_{n_4}(\mathbf{r}_1), \quad (4.44)$$

and consistently, the Coulomb matrix element is $V_{ee}^{n_3 n_2}$. Only direct transitions for pairs of occupied and unoccupied states contribute to the optical spectra, neglecting phonons. This is guaranteed by the occupation number factors $(f_{n_2} - f_{n_4})$ and $(f_{n_3} - f_{n_1})$ in equations 4.42 and 4.43, respectively. The terms that contribute are thus of the form

$$\bar{\Xi}_{vc}^{s v' c'} = 2 \bar{V}_{ee}^{cc'} + W_{vc}^{v' c'}. \quad (4.45)$$

The first term that contributes to the interaction, the bare Coulomb potential, couples dipoles and is often called the electron-hole exchange. The second term is the screened potential and is closer to the interaction between densities, referred to as the direct electron-hole interaction [90].

The two-particle Hamiltonian

Equation 4.42 can be solved by matrix inversion; however, this is computationally demanding. Alternatively, the two-particle Hamiltonian spectral representation can be used. The two particle Schrödinger equation for the excitonic system is defined

$$\sum_{n_3 n_4} \bar{H}^{2p}_{n_1 n_3} A_{\lambda}^{n_4 n_2} = E_{\lambda} A_{\lambda}^{n_1 n_2}. \quad (4.46)$$

The matrix inversion of the two particle Hamiltonian is given by the relation

$$\left[\bar{H}^{2p} - \mathbb{1} \omega \right]_{n_1 n_3}^{-1 n_4 n_2} = \sum_{\lambda \lambda'} \frac{A_{\lambda}^{n_1 n_2} N_{\lambda \lambda'}^{-1} A_{\lambda'}^{* n_3 n_4}}{E_{\lambda} - \omega}, \quad (4.47)$$

where the overlap matrix for the eigenstates $A_{\lambda}^{n_1 n_2}$ is

$$N_{\lambda \lambda'} = \sum_{n_1 n_2} A_{\lambda}^{* n_1 n_2} A_{\lambda'}^{n_1 n_2}, \quad (4.48)$$

which is needed for a general non-hermitian matrix.

For semiconductors and insulators, only pairs of occupied states v and empty states c contributes to the optical spectra, through the two-particle Hamiltonian, also referred to as the excitonic Hamiltonian. Then the H^{2p} consists of 4 matrix blocks

$$\bar{H}^{2p} = \begin{pmatrix} \bar{H}^{\text{res}} & \bar{H}^{\text{coupl}} \\ [-\bar{H}^{\text{coupl}}]^* & [-\bar{H}^{\text{res}}]^* \end{pmatrix}, \quad (4.49)$$

4.3 Bethe-Salpeter equation

where the resonant part is defined as

$$\bar{H}^{\text{res}} \equiv \bar{H}^2 p_{vc}^{v'c'} = (\epsilon_c - \epsilon_v) \delta_{vv'} \delta_{cc'} + i \bar{\Xi}_{vc}^{s v' c'}, \quad (4.50)$$

which corresponds to transitions at positive frequency, ω , and is hermitian. The coupling part

$$\bar{H}^{\text{coupl}} \equiv \bar{H}^2 p_{cv}^{c'v'} = i \bar{\Xi}_{vc}^{s c' v'} = \left[i \bar{\Xi}_{vc}^{s c' v'} \right]^*, \quad (4.51)$$

is symmetric. The lower right part of equation 4.49 is the anti-resonant part

$$\bar{H}^{\text{ares}} \equiv \bar{H}^2 p_{cv}^{c'v'} = (\epsilon_v - \epsilon_c) \delta_{vv'} \delta_{cc'} - i \bar{\Xi}_{cv}^{s c' v'} = -[\bar{H}^{\text{res}}]^*, \quad (4.52)$$

which is linked to the resonant part because of the symmetry of the interaction kernel Ξ .

4.3.2 Absorption Spectrum

The coupling part of equation 4.49 mixes transitions of negative and positive energy. In principle, all ingredients are present to solve the BSE; however, another approximation will be implemented by setting the coupling term to zero. Neglecting the coupling terms is called the Tamm-Danoff approximation [123, 124]. This approximation is justified when the coupling terms are much smaller than the resonant ones, and it has been successfully implemented for bulk semiconductors [125]. Both the resonant and anti-resonant parts are hermitian, meaning that the coupling term in equation 4.47, $N_{\lambda\lambda'}^{-1}$, is simply $\delta_{\lambda\lambda'}$. Thus, equation 4.46 can be diagonalized with lower effort, and the calculation of the macroscopic dielectric functions is restricted to only the resonant and anti-resonant parts of the spectrum.

Macroscopic Dielectric function

The polarizability $\bar{\chi}$ is obtained from the matrix \bar{L} from the relation

$$\bar{\chi}(\mathbf{r}_1, \mathbf{r}_2; \omega) = -iL(\mathbf{r}_1, \mathbf{r}_2, \mathbf{r}_1, \mathbf{r}_2; \omega) = -i \sum_{n_1 \dots n_4} \varphi_{n_1}(\mathbf{r}_1) \varphi_{n_2}(\mathbf{r}_2) \bar{L}_{n_1 n_3}^{n_4 n_2}(\omega) \varphi_{n_3}^*(\mathbf{r}_1) \varphi_{n_4}^*(\mathbf{r}_2). \quad (4.53)$$

Finally, the macroscopic dielectric function is given by performing the Fourier transform for the reciprocal space and inserting into equation 4.22

$$\varepsilon_M(\omega) = 1 - \lim_{\mathbf{q} \rightarrow 0} \left\{ V_{ee}(\mathbf{q}) \iint d^3r d^3r' e^{-i\mathbf{q} \cdot (\mathbf{r} - \mathbf{r}')} [-i\bar{L}(\mathbf{r}, \mathbf{r}', \mathbf{r}, \mathbf{r}'; \omega)] \right\}, \quad (4.54)$$

putting everything together, the final expression for the macroscopic dielectric function given in Bloch space is

$$\varepsilon(\omega) = 1 + 2 \lim_{\mathbf{q} \rightarrow 0} \left\{ V_{ee}(\mathbf{q}) \sum_{\lambda} \left| \sum_{v, c, \mathbf{k}} \left\langle \varphi_{v, \mathbf{k}} \left| e^{-i\mathbf{q} \cdot \mathbf{r}} \right| \varphi_{c, \mathbf{k}} \right\rangle A_{\lambda}^{vc\mathbf{k}} \right|^2 \times \left(\frac{1}{E_{\lambda} - \omega - i\eta} + \frac{1}{E_{\lambda} + \omega + i\eta} \right) \right\}, \quad (4.55)$$

where the last two terms in the parenthesis are given by the resonant and anti-resonant terms, respectively.

4.3.3 Model-BSE

In order to obtain the optical spectra from the BSE method, the screened potential W is needed for the two-particle Hamiltonian through the interaction kernel. To this end, BSE calculations can be started using the screened potential from previous calculations preformed with the GWA method. Performing GW calculations can be avoided by using a model dielectric function[126, 127], this is done mostly to avoid the computational effort associated with GWA. The inverse dielectric function in equation 2.69 is fitted to an analytical local model [128]. In reciprocal space, the static model reads

$$\varepsilon_{\mathbf{GG}}^{-1}(\mathbf{q}) = \varepsilon_{\infty}^{-1} + (1 - \varepsilon_{\infty}^{-1}) \left[1 - \exp \left(-\frac{|\mathbf{q} + \mathbf{G}|^2}{4\mu^2} \right) \right], \quad (4.56)$$

where ε_{∞} is the static ion-clamped dielectric function in the long-wave length limit and μ is the screening length parameter. This approach is commonly referred to as model-BSE (mBSE). The parameter μ is obtained by fitting to the dielectric function calculated from partial self-consistent GW (GW_0). The mBSE method has been successfully used in the past to accurately describe the optical spectra of Ruddlesden-Popper iridates [128] and for bulk silicon [129].

In addition to the screened Coulomb potential, BSE calculations need accurate band gaps in order to properly describe the optical spectra. To this end, quasiparticle wave functions and energies are also used as a starting point. In order to avoid performing initial GW calculations all together, quasi-particle energy shifts are included with a scissors operator. To correct the KS band gap, a constant Δ can be added corresponding to the difference between the band gap calculated from GW_0 and KS-DFT. This simple operation is referred to as a scissors operator, as it can be thought of as cutting the band structure along the band gap and rigidly shifting the conduction bands by a constant amount. The implementation of the scissors operator has been validated for a number of semiconductors[130, 131]. The success of the method is owed to the fact that KS orbitals describe the band structure qualitatively exceptionally well and the near-perfect overlap between KS and quasi-particle wave functions[132]. The scissors operator is also successfully used to correct for the quasi-particle shift for optical properties [133].

4.4 Reflectance anisotropy spectroscopy

The reflectance anisotropy spectroscopy (RAS) also referred to as reflectance difference spectroscopy is a highly surface-sensitive optical tool used for characterizing materials. As the name suggests, the technique involves measuring the reflected light of a surface sample. The optical anisotropy, resulting from the surface's reduced symmetry, is measured from the difference of the reflected light between its two perpendicular light polarizations. While the technique is able to probe samples at an atomic level, it is also non-destructive, which makes it an attractive option for characterizing samples. RAS also works in a variety of environments, making it possible to use during growth processes, allowing *in situ* characterization of materials, and enabling control over the process.

Experimentally, the measured quantity is often the real part of the reflection amplitude r related to the reflectivity R , in the relation for RAS

$$\Re \left\{ \frac{\Delta r}{r} \right\} = 2 \Re \left\{ \frac{r_x - r_y}{r_x + r_y} \right\} \approx \frac{R_x - R_y}{R_x + R_y} = \frac{1}{2} \frac{\Delta R}{R}, \quad (4.57)$$

the indices x and y denote the polarization Cartesian direction. The reflective coefficient is given as the solution to Maxwell's equations for light incident on a semi-infinite crystal with a surface normal to the z direction and at the surface plane $z = 0$. The complexity of the problem stems from the inhomogeneous dielectric tensor originating from the abrupt vacuum-surface interface. In addition, surface anisotropies between different directions on the surface will present due to the reduced symmetry of the surface. A solution that includes all anisotropies and non-locality of the dielectric tensor in the long-wavelength limit was proposed by R. Del Sole in 1981 [134]. The normal reflectivity change, $\delta R_i/R$, according to Fresnel equations, for s -polarized light in the i direction and at normal incidence is

$$\frac{\delta R_i}{R}(\omega) = \frac{4\omega}{c} \Im \left\{ \frac{\delta \varepsilon_{ii}(\omega)}{\varepsilon_b(\omega) - 1} \right\}, \quad (4.58)$$

where ε_b is the bulk dielectric function, c the speed of light, and all surface features are embodied in the "length" $\delta \varepsilon_{ii}$, defined as

$$\delta \varepsilon_{ij} = \iint dz dz' [\varepsilon_{ij}(\omega, z, z') - \delta(z - z') \varepsilon_0(\omega, z)] - \iiint dz dz' dz'' dz''' \varepsilon_{iz}(\omega, z, z') \varepsilon_{zz}^{-1}(\omega, z', z'') \varepsilon_{zj}(\omega, z'', z'''), \quad (4.59)$$

with all the many-body and local-field effects are accounted for in the non-local macroscopic dielectric tensor $\varepsilon_{ij}(\omega, z, z')$ [135]. The term $\varepsilon_0(\omega, z)$ is the sharp vacuum-surface interface

$$\varepsilon_0(\omega, z) = \varepsilon_b(\omega) \theta(z) + \theta(-z). \quad (4.60)$$

In order to carry out proper calculations of equation 4.59, the semi-infinite crystal is replaced by an artificial supercell, large enough that it encompasses the vacuum as well as the surface and the bulk region. The last integral of equation 4.59 was found to not significantly contribute to the spectra [136] and therefore can be neglected. Equation 4.58 then becomes [136, 137]

$$\frac{\delta R_i}{R}(\omega) = \frac{4\omega}{c} \Im \left\{ \frac{4\pi \alpha_{ii}(\omega)}{\varepsilon_b(\omega) - 1} \right\}, \quad (4.61)$$

where the so-called half-slab polarizability $\alpha_{ii}^{\text{hs}}(\omega)$ defined from equation 4.59 is

$$4\pi \alpha_{ij}^{\text{hs}} = \frac{1}{2} \iint dz dz' [\varepsilon_{ij}^{\text{slab}}(\omega, z, z') - \delta(z - z') \delta_{ij}]. \quad (4.62)$$

Finally, the RAS is calculated from

$$\frac{\Delta R}{R}(\omega) = \frac{\delta R_x(\omega) - \delta R_y(\omega)}{R} = \frac{4\omega}{c} \Im \left\{ \frac{4\pi \Delta \alpha^{\text{hs}}(\omega)}{\varepsilon_b(\omega) - 1} \right\}, \quad (4.63)$$

here the half-slab polarizability $\Delta \alpha^{\text{hs}}(\omega) = \alpha_{xx}^{\text{hs}}(\omega) - \alpha_{yy}^{\text{hs}}(\omega)$ has dimensions of length.

In the three layer model by McIntrye and Aspens [138] the half-slab polarizability is related to the slab macroscopic dielectric function [137]

$$4\pi \Delta \alpha^{\text{hs}}(\omega) = d \Delta \varepsilon(\omega) = d(\varepsilon_{xx}(\omega) - \varepsilon_{yy}(\omega)), \quad (4.64)$$

where d is half of the thickness of the slab. The macroscopic dielectric function of the slab can then be calculated in the simple independent particle picture up to including local and excitonic effects by solving the BSE.

Part II

Results

Chapter 5

O₂ and H₂O on In-rich InP surfaces

Group-III phosphides show promising properties for use in solar-powered water splitting applications, as they present a high-energy solar conversion rates. In particular, InP has been explored, in combination with other materials, as a strong candidate for efficient water splitting and so far has given promising results [21, 139–141]. However, relatively few studies have been made on the electronic properties and the microscopic details of the InP surfaces in contact with oxygen and water[142–145].

The InP semiconductor surface has been extensively studied, deriving various properties both experimentally and theoretically [146–153]. The surface geometries that InP (001) presents are similar to those of other III-V semiconductors, in particular those that contain phosphates, and are well understood to the point that it is possible to predict the stoichiometry for different growing conditions and methods[154–156]. The surface reconstruction a material presents often dictates different properties, from band bending to surface states, for this reason it is crucial to understand and ultimately control the resulting surface. From the number of InP (001) surface models studied[152], for In-rich environments, the thermodynamically stable geometry is that of the (2×4) mixed-dimer (MD) surface reconstruction, shown in Fig. 5.1. The surface is characterized by a single In–P on the top layer along the [110] direction, which gives the surface its name. The second layer consists of four In–In bonds along the [110] direction, with lower layers following the bulk geometry. Due to broken symmetry, the surface reconstruction has several dangling bonds. Of particular importance are the first-layer P atom and the three-fold coordinated In atoms on the second layer, which contribute to the band structure surface valence and conduction states, respectively[152]. The highest occupied state is related to the σ -like bond between the first and second layer In atoms. In addition, the In–In dimers also contribute to surface valence states. These states are the major contributors to the anisotropies present in the RAS measurements [49, 142, 157]. In particular, the transition between the σ -like In–In occupied states and the empty In dangling bonds of the three-fold coordinated atoms is responsible for the negative feature in the RAS. Minor contributions arise from transitions of the occupied P dangling-bond state and the unoccupied states from the In dangling bonds and π^* In–P antibonds. The bonds involved in these surface states are also prime candidates as adsorption sites, and in particular have been suggested for water and oxygen adsorption [49, 142].

The focus of this chapter is on the study of the water interaction with the InP(001) surfaces

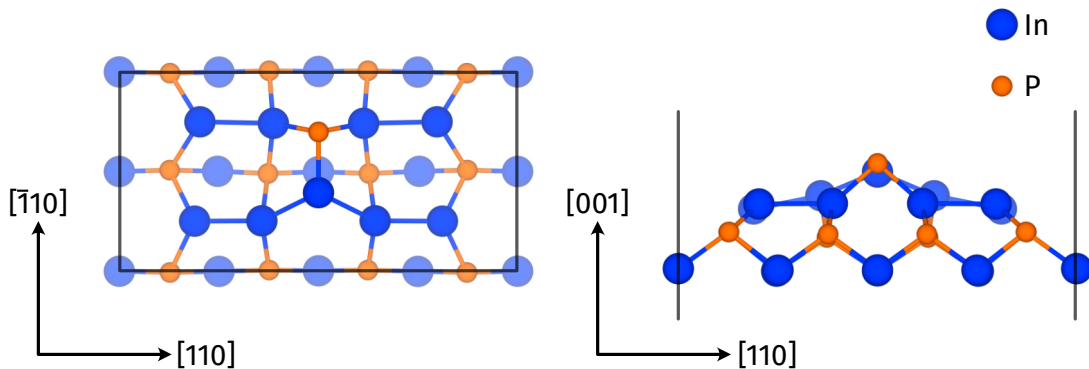


Figure 5.1: Top and side view of the InP(001) (2×4) mixed-dimer (MD) surface reconstruction.

from first principles, starting from the surface oxidation and continuing with the full water adsorption thermodynamic process.

5.1 Methodology

The systems are investigated from first principle DFT calculations using the Vienna *ab initio* simulation package (VASP)[158–160]. The electron exchange and correlation interactions are modeled within the GGA using the PBE functional[71, 72]. The electron-ion interaction is described by the projector augmented wave (PAW) method[119, 161]. The plane-wave basis used to expand the wavefunctions is limited by a cutoff energy of 500 eV. The semi-infinite slabs are modeled using a periodic slab consisting of 12 atomic layers that simulate the bulk region as well as the surface region. In order to circumvent the periodic conditions of the slab in the normal direction to the surface, a vacuum region of $\sim 15 \text{ \AA}$ is left in the [001] direction. In addition, a dipole correction scheme is implemented to deal with the spurious interactions across the vacuum region as a result of the periodic boundary conditions. The slab bottom In layer is passivated by partially charged pseudo-hydrogen with $Z = 1.25$, mimicking bulk bonds. The Brillouin zone is integrated using a proportional γ centered \mathbf{k} -point mesh of $8 \times 8 \times 1$ per a (1×1) cell. The In-rich (001) surface unit cell consists of a 2×4 periodicity. When considering water adsorption, for a better commensurability between the InP surface and water over-layers, a periodicity of 2×12 is used. The DFT self-consistent cycle is stopped when the energy difference between two consecutive steps is lower than 10^{-5} eV . All atoms are considered in their relaxed ground-state positions when the forces acting on the ions are lower than $0.02 \text{ eV}/\text{\AA}$.

5.2 InP(001) In-rich surface oxidation

Oxides can strongly affect the performance of semiconductor devices[162]; therefore, it is important to understand how the oxidation process occurs and affects the electronic properties of a material. Oxidation not only occurs when materials are exposed to an air atmosphere but also when exposed to water, as the dissociative process involves oxygen as a byproduct. Hicks and co-workers[142], from x-ray photoemission spectroscopy (XPS), low-energy electron diffraction (LEED) and RAS measurements, conclude that InP (001) oxidation is a strongly structure sensitive. On (2×4) InP surfaces, O₂ molecules were found to dissociatively adsorb at In–In and

In–P back bonds located in the second layer. The formation of In–O–In and In–O–P bonds was confirmed independently of DFT calculations [143]. Additional RAS measurements on InP surfaces exposed to water or oxygen by May et al.[49] also confirm the formation of these bonds. A higher tendency for In–O–In in the case of O₂ exposure was found and a tendency for O to incorporate in the bulk in contrast to water exposure, which leads to the formation of In–O–P bonds. The path oxidation takes does not only depend on the surface structure, i. e., if it is In-rich or P-rich, but also on the properties of the respective atoms. This section is focused on the understanding of InP (2×4) oxidation by considering both oxygen adsorption and substitution. The results here were previously reported in Ref. [163].

5.2.1 Adsorption geometries

A potential energy surfaces (PES) for single O particles is constructed as a starting point to explore the most favorable adsorption sites for oxygen. The PES is constructed by positioning an individual O atom on top of the InP surface and allowing it to relax in the direction normal to the surface while fixing all other degrees of freedom. The process is repeated for 50 different sites, constructing a mesh of equidistant points. Finally, the adsorption energy is calculated for each different site from the following formula

$$E_{\text{ads}} = E_{A+\text{surf}} - E_{\text{surf}} - E_A, \quad (5.1)$$

where $E_{A+\text{surf}}$ is the total energy of the system after the adsorption of A on the surface, E_{surf} and E_A are the total energies of the surface and adsorbate, respectively. The adsorption energy describes the energies differences with respect to a reservoir of adsorbates A. For a configuration to be viable, E_{ads} must be lower than zero; the lower the value, the more stable the configuration. For a system in contact with an oxygen atmosphere, the adsorption energy is referenced to molecular O₂ and is calculated from DFT total energies,

$$E_O = \frac{1}{2}E_{O_2}. \quad (5.2)$$

The ground state of an O₂ molecule is the spin triplet; for this reason, spin polarized calculations have to be taken into account when calculating the E_A . Fortunately, when an O atom is adsorbed at the InP surface, the spin is quenched and the total magnetic moment of the complete system is zero. Thus, no spin-polarized calculations are required. The PES for an 10×5 mesh of equidistant points is shown in figure 5.2. The most energetically favorable adsorption site is the top In–P dimer, forming an In–O–P bond with an energy $E_{\text{ads}} = 2.07$ eV. The In atoms of the second row also serve as favorable bonding sites for the O atoms, with the three-fold coordinated In atoms serving as the most favorable of them all, with an energy $E_{\text{ads}} = 1.91$ eV.

Continuing from the most favorable O adsorption sites from the PES calculations (Fig. 5.2), the oxidation of the InP surface was explored. The starting point are the previously identified favorable bonding sites: the top In–P dimer, the In–P bonds between the first and second layer, the second layer In–In bonds, and the In–P bonds between the second and third layer. Not only was adsorption considered, but also substitutional insertion of oxygen on the InP surface; in this case, all atoms of the first three layers were considered tentatively to be replaced by O atoms.

The different structures were compared energetically using the grand canonical potential, equation 3.3. The thermodynamically allowed range for the chemical potential is limited by equa-

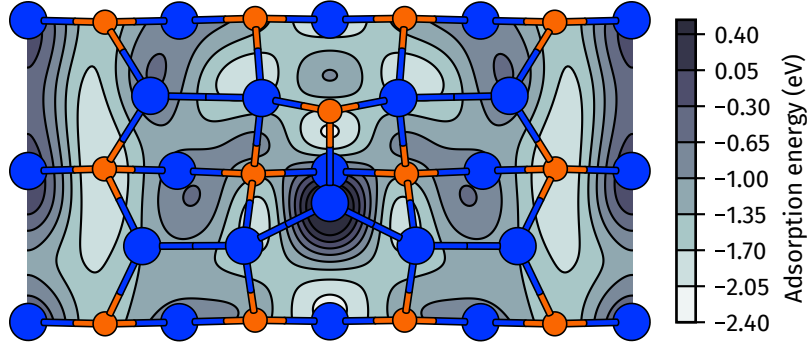


Figure 5.2: Calculated PES for single oxygen adsorption on the InP (001) (2×4)-MD surface. Adapted from Ref. [163].

tion 3.4. Furthermore, in the case of InP, the chemical potential is related to individual constituents by

$$\mu_{\text{In}} + \mu_{\text{P}} = \mu_{\text{InP,bulk}} = \mu_{\text{In,bulk}} + \mu_{\text{P,bulk}} - \Delta H_{f,\text{InP}}, \quad (5.3)$$

with $\Delta H_{f,\text{InP}}$ being the heat of formation of InP. The above equation 5.3 reduces the degrees of freedom by relating the In and P chemical potentials through the heat of formation. Consequently, the formation energy can now be written as a function of one of the two variables; here $\Delta\mu_{\text{In}}$ is chosen. The heat of formation also places a lower bound on the chemical potential through equations 3.4 and 3.5

$$-\Delta H_{f,\text{InP}} \leq \Delta\mu_{\text{In}} \leq 0. \quad (5.4)$$

These limits can be related to experimental preparation conditions; $\Delta\mu_{\text{In}} = 0$ corresponds to In-rich conditions, where the surface In atoms are in equilibrium with the In bulk. Equivalently, $\Delta\mu_{\text{In}} = -\Delta H_{f,\text{InP}}$ corresponds to In-poor conditions, or through equation 5.3 to P-rich conditions, where the surface is in equilibrium with P bulk. The chemical potential of oxygen is given by $\Delta\mu_{\text{O}} = \frac{1}{2}\Delta\mu_{\text{O}_2}$ and $\Delta\mu_{\text{O}_2}$ from equation 3.6 for a diatomic gas. The complete set of energetically relevant structures considered here for O adsorption and substitution on the (2×4)-MD surface can be seen in the Fig. A.1 in Appendix A and Fig. 5.3 summarizes the most favorable geometries.

In order to compare the structures energetically, the heat of formation for InP was computed to be $\Delta H_{f,\text{InP}} = 0.41$ eV. As it turns out, however, the specific choice of chemical potential does not affect the general trend. Therefore, for the following $\Delta\mu_{\text{In}} = -0.2$ eV is assumed, and only the oxygen chemical potential is allowed to vary. It can be seen from Fig. 5.4 that the surface thermodynamic stability increases as the oxygen is integrated onto the surface, even for low pressures. Even without fully calculating energy barriers, it is clear from the grand canonical potential that as long as oxygen is available, the oxidation process will continue and is only hindered kinetically. This is not surprising, as it has been previously reported from experiments[142]: The InP is highly reactive towards oxygen and rapidly forms an oxide layer even for low oxygen exposure and a temperature of 300K. The results found here also coincide with other semiconductor surfaces in particular, with calculated oxidation for Si(001)[164] or experimental measurements of Ga-rich GaP exposed surfaces to oxygen[144]. The In chemical potential degree of freedom does not change the overall trend, especially for O adsorption; however, when considering substitutional oxidation, more information can be provided once it is taken into account, as detailed in Fig. 5.5. Only very low values of O chemical potential will put a halt to the oxidation process; in other words, when there is relatively low oxygen is available. The In or P chemical potential

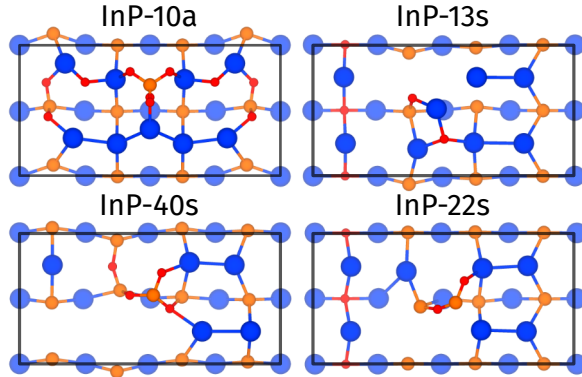


Figure 5.3: Energetically favorable O adsorption and substitution structures were calculated for the InP (2×4)-MD surface. The number in the notation indicates the total number of O atoms adsorbed (a) or for substitution (s), the first and second digits of the number of In and P replaced, respectively. The complete set of relevant structures considered in the present work is shown in Appendix A Fig. A.1. Adapted from Ref. [163].

dictates which of the two elements is more likely to be replaced by an oxygen atom.

The most common type of bond found for adsorption oxidation is In–O–P bonding. This occurs for all stable geometries. The In–O–In bonds are found to be slightly less favorable (see Fig. 5.3). This is consistent with experimental findings by M. May et al.[49], where In-rich InP surfaces were exposed to molecular oxygen. For substitutional oxidation, at oxygen-rich conditions ($\Delta\mu_O = 0$ eV), the type of atom replaced depends on the In (or P) chemical potential, i. e., In atoms are more easily replaced for P-rich conditions and vice versa for P atoms at In-rich. There is a region around $\Delta\mu_{In} = -0.2$ eV, where O replaces In and P with roughly equal probability; see Fig. 5.5. The P replacement leads to oxygen atoms that are threefold and fourfold coordinated to In atoms; this is consistent with previous results found in Ref. [47, 143]. In contrast, In replacement results in In–O–P and soon thereafter P–O–P bonds (see Fig. 5.3). As oxygen becomes less available ($\Delta\mu_O \ll 0$ eV), only the surface with the top P atom replaced by O is energetically stable. This geometry is also the most stable during initial stages of oxidation; here, the O atoms are threefold coordinated. The formation of bonds between group III atoms and oxygen also occurs in other III–V semiconductors during oxidation. For GaAs, preferential Ga–O–Ga bonding has been observed upon adsorption[165] and when oxygen replaces As atoms[166]. For the more closely related material GaP, Jeon et al.[167] found that water adsorption for the (2×4) surface leads to the formation of Ga–O–Ga bonds and less favorable Ga–O–P bonds.

5.2.2 Electronic properties

The density of states (DOS) was calculated for the most energetically favorable geometries, in order to explore how oxidation influences the electronic properties of the InP (2×4)-MD surface. The DOS for the clean surface and for the 10 oxygen adsorbed model are shown in Fig. 5.6. The rest of the oxidation levels are shown in Appendix B Fig. B.1. The InP surface DOS is characterized by high density on the valence band maximum (VBM), originating from In and P p states. On the conduction band minimum (CBM) side, the In s and p states are dominant; see Fig. 5.6. Increased amounts of oxygen adsorption lead to mid-gap states for a selected number of surface geometries, e. g. the case for the 10 oxygen adsorbed model, see Fig. 5.6. The largest contribution to these oc-

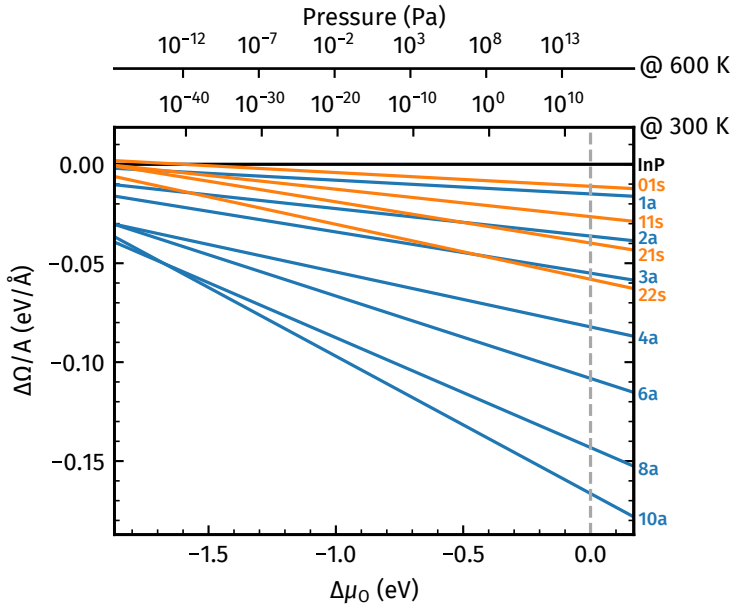


Figure 5.4: Surface grand canonical potential versus oxygen chemical potential of the O adsorption and substitutional geometries for the InP (2×4)-MD. For the In chemical potential, a value of -0.2 eV is fixed. The chemical potential of oxygen is related directly to the pressure p and temperature from equation 3.6. The clean surface is used as the reference system. Blue and orange lines indicate adsorption and substitution, respectively. Adapted from Ref. [163].

cupied states inside the band gap, in general, arises from In p orbitals, followed by slightly smaller P and O p contributions. The VBM is pushed to lower energies compared to the clean surface as oxidation increases; see Fig. 5.6. This effect is related to the increased oxygen exposure, which passivates the surface states near the valence band edge as more and more oxygen bonds to In atoms on the second layer. The effect coincides with the reduction of the In p contribution to 0.8 eV above the CBM. This is due to the reduced contribution of the In p states, more specifically the In dangling bonds of the second layer, c. f. Refs. [143, 152]. The conduction In state was identified from time-resolved two-photon photoemission (tr-2PPE) by Friedrich et al. [168], around 0.85 eV above the CBM. More interesting is the sensitivity towards oxygen; the state disappears after the surface is exposed to O₂. This is in good agreement with the results presented in this work so far; in the second layer, In are presently good adsorption sites for oxygen, and their dangling-bond p -orbital contribution to the conduction band is reduced after oxidation.

Although passivation of surface states would increase electronic efficiency, the surface oxidation modifies existing states and introduces additional ones inside the region of the bulk band gap. These states may behave as charge traps that hinder the carrier generation and recombination process and thus ultimately worsen the electronic and optical efficiency. Therefore, strategies should be implemented to avoid the formation of indium oxides at the surface for enhanced electronic efficiency.

5.3 Water adsorption on InP mixed-dimer surface

As touched upon previously, III-V semiconductors are suitable candidates for solar-powered water splitting. This is the case, for example, in GaAs (001), where dissociative water adsorption

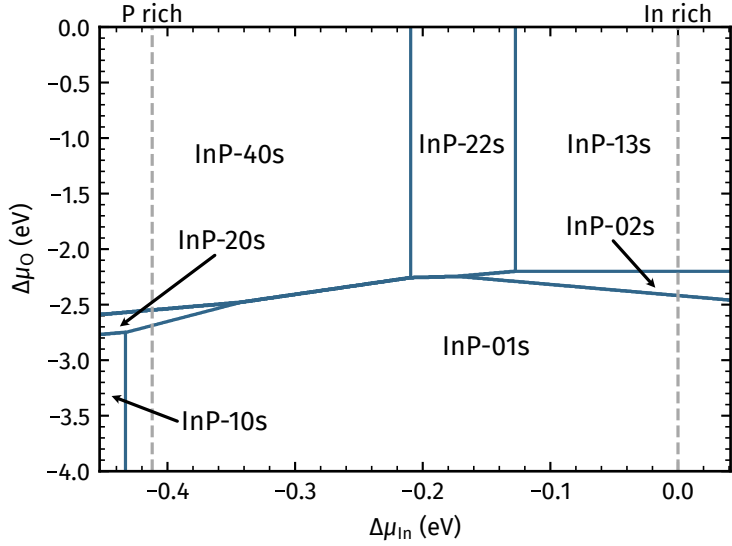


Figure 5.5: Phase diagram of the most energetically favorable O substitutional geometries of InP (2×4)-MD surface. The thermodynamic stability range of the In chemical potential is given by equation 5.4. The dashed lines indicate the P- and In-rich conditions, where the system is in equilibrium with the P or In bulks, respectively. Adapted from Ref. [163].

was identified from XPS measurements[73]. Water splitting leads to the adsorption of OH and H species on GaAs surfaces, further deprotonation leading to Ga–O, Ga–OH and As–H bonds. Increased water pressure causes water physisorption directly at the GaAs surface, or water to be anchored through Ga–OH bonds. Surface composition plays a major role in water adsorption; this is the case, for example, on GaP (001) surfaces. Ga-rich surfaces show a higher reactivity towards water than P-rich surfaces. Water dissociation is possible on Ga-rich surfaces, as the presence of water and hydroxyl groups was suggested from photo-electron and optical spectroscopy[144]. This backed up theoretical results [167]. Data for water adsorption on InP surfaces from previous studies is rather inconclusive. Optical spectroscopic results, performed by May et al.[49], show water dissociative adsorption, where the formation of In–O–P bonds is hypothesized, between the first and second layers. The lack of hydroxyl signatures on the spectra further suggests

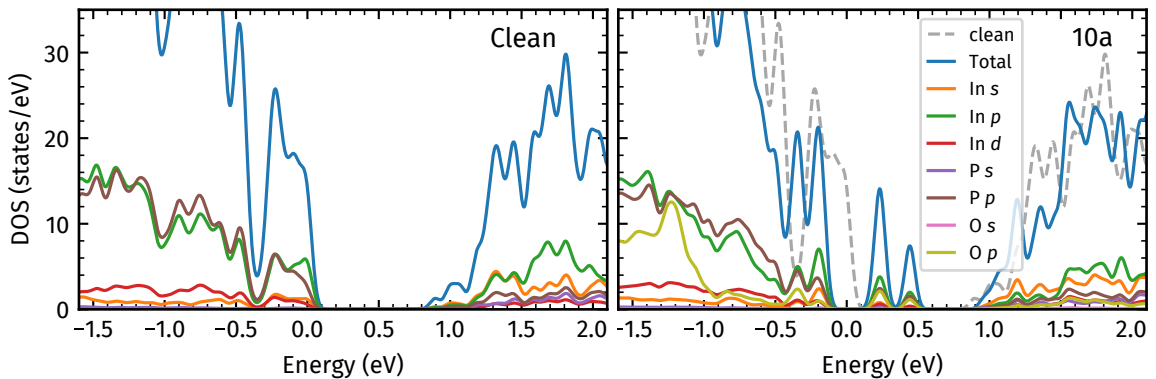


Figure 5.6: Orbital resolved electronic DOS calculated for the InP (2×4)-MD surface reconstruction and the oxidized surface model InP10a. The orbital characters *s*, *p* and *d* of each species are shown. Adapted from Ref. [163].

that dissociative water adsorption releases both hydrogen atoms. On the other hand, a computational study by Wood and coworkers [50] shows that while dissociative water adsorption in GaP surfaces is favorable, the same is not the case for InP surfaces. Adsorption of an intact water molecule was energetically favorable over a potential dissociation of a water molecule on the top In–P dimer, where the In would act as the Lewis acid and P the Lewis base. Additional energy barriers of around 0.8 eV need to be overcome for the electrochemical process to be carried out for both GaP and InP surfaces.

This section is focused on understanding the interaction between water and In-rich surfaces. Dissociative adsorption is explored for single molecules as well as in a water/InP interface. The energy barriers that hinder the process as well as the energetics of the full redox and reduction reaction paths are calculated from the Gibbs free energy. Finally, the band alignment for the In-rich surface water interface is investigated as a requirement for oxygen and hydrogen evolution. The data collected here was previously reported in Ref. [169].

5.3.1 Molecular water adsorption

The energetically favorable adsorption sites for oxygen on InP surfaces were aided by the calculation of the PES; likewise, for water adsorption, PES provide a systematic approach for identifying the favorable geometries. In addition to PES calculations for molecular water (H₂O), hydroxyl groups (OH) and atomic hydrogen (H) are also considered. The PES was sampled for a mesh consisting of 50 equidistant points. At each point, two and nine different starting configurations were probed for the hydroxyl group and water, respectively. For all adsorbates, the oxygen lateral degrees of freedom are fixed during relaxation. The vertical distance to the surface, as well as all other degrees of freedom, are not constrained. The adsorption energy is calculated using equation 5.1, where E_A is defined for the total energy of gas-phase water molecule, E_{H_2O} . In the case of the hydroxyl group and oxygen, E_A is defined as

$$E_{OH} = E_{H_2O} - \frac{1}{2}E_{H_2} \quad (5.5)$$

and

$$E_O = E_{H_2O} - E_{H_2}, \quad (5.6)$$

while hydrogen adsorption is referenced to gas-phase H₂, $\frac{1}{2}E_{H_2}$. Notice the difference between eqs 5.2 and 5.6, here the surface is not assumed to be under an oxygen atmosphere, but rather in contact with gas-phase water molecules.

The PES is shown in Fig. 5.7. Previously both experimental and theoretical results[49, 50], suggested the sites A through D, indicated in Fig. 5.7 (a), as favorable water adsorption sites. The most energetically favorable adsorption sites for a water molecule identified here are B and C and, to a minor extent, A. Previously, Wood et al.[50] had also identified the same sites as probable water adsorption sites from *ab initio* molecular dynamics. The hydroxyl group, on the other hand, adsorbs preferentially on site E (see Fig. 5.7 (b)) rather than the top mixed dimer as suggested by Wood et al.[50]. Finally, hydrogen prefers to adsorb on the dangling bond of the P atom, as shown in Fig. 5.7 (c). The most relevant configurations for water adsorption are identified from Fig. 5.7 for the low-coverage stage of the water/InP interface. The adsorption energy for the most relevant configurations is collected in Table 5.1. In order to compare different adsorbates, the entropic terms of the total free energy equation 3.1 have to be taken into account. The total free

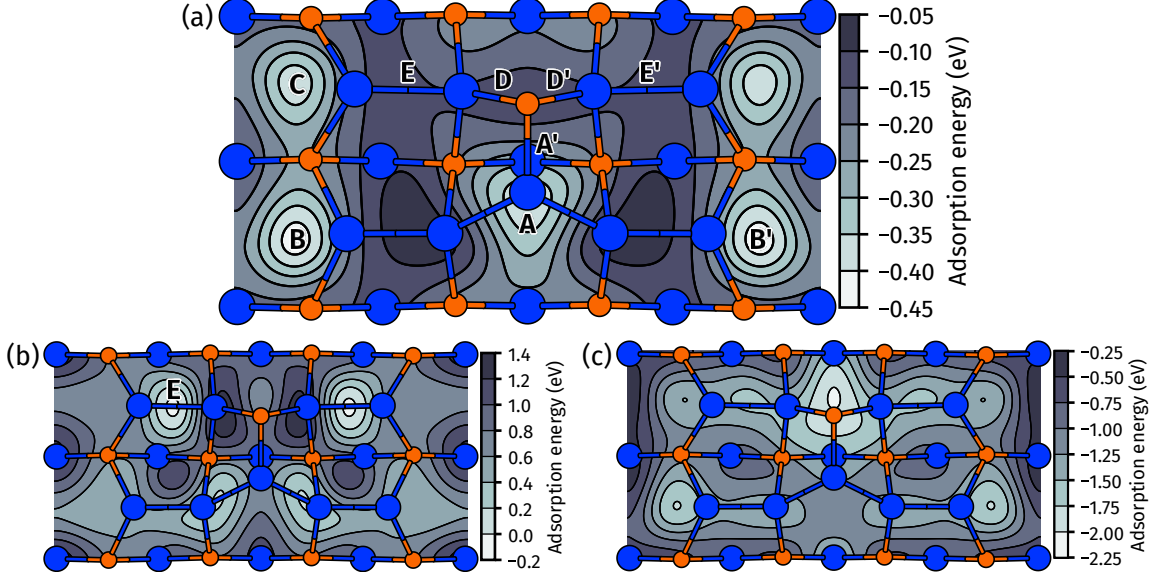


Figure 5.7: Calculated PES for single water molecules (a), an OH group (b), and a H atom (c) on the InP (2×4)-MD surface. Adapted from Ref. [169].

energy contributions from the electronic entropy, at room temperature, are two orders of magnitude smaller than the total energy. Therefore, it is neglected in the following, while the ZPE is much more meaningful. As seen in Table 5.1 the ZPE typically affects the adsorption energies by about 0.1 eV and, in some cases, up to 0.2 eV. However, the trends from the DFT total energy calculations remain unchanged.

The most favorable water adsorption configuration for the intact molecule is at site B, which is shown in Fig. 5.8 along with the adsorption-induced charge density redistribution. The water molecule donates electrons of its $1b_1$ orbital into the empty In dangling bond of p_z character [152]. This results in a weak O–In bond between the water molecule and the surface, with a bond length of 2.5 Å. The weak interaction between the surface and water molecules also leaves the O–H bond angle and length unaffected. The adsorption also modifies the InP surface geometry only slightly, such that the (2×4)-MD reconstructions are still easily identifiable. The water molecule introduces no additional electronic states in the energy region around the InP band gap. This is as a result of the weak bonding and rather large band gap of the water molecule.

Several water configurations in Table 1 are energetically favorable over the incorporation of an intact water molecule, suggesting the possibility of dissociative water adsorption. Experimentally, the water adsorption was reported to be dissociative[49]. The process was suggested to conclude in oxygen incorporating on sites D and D' (see fig 5.7), forming In–O–P bonds and liberating all H atoms. Theoretical results[50], on the other hand, suggest that water adsorption is favorable over dissociative adsorption. It is important to point out, however, that in ref. [50] only water dissociation on the top In–P dimer was probed. The results discussed here agree with water dissociative adsorption; however, the configuration suggested in ref. [49] is not preferred over molecular adsorption. Rather, the hydroxyl group attaches to the In–In bond on site E (see fig. 5.7), while the hydrogen atom bonds to the P dangling bond. This configuration is around 0.1 eV (0.2 with ZPE corrections) more favorable over molecular adsorption. As seen by the charge-density redistribution in Fig. 5.9, strong In–O–In and P–H bonds form. There is also a change in surface geometry induced by the insertion of the OH into the In–In bond. The In atom is dis-

Table 5.1: Adsorption energies (in eV) of the different bond configurations for H₂O, O, and OH at specific sites of the InP mixed-dimer surface, c. f. Fig. 5.7. Adapted from Ref. [169].

| Site | Configuration | E_{ads}^1 | $F_{\text{ads}}^{1,2}$ |
|----------|-------------------------------|--------------------|------------------------|
| B | H ₂ O–In | −0.408 | −0.324 |
| A | H ₂ O–In | −0.384 | −0.302 |
| A' | In–O–P | 0.387 | 0.160 |
| D | OH–P | 0.665 | 0.591 |
| A | In–OH | 0.646 | 0.540 |
| E | In–OH–In | −0.073 | −0.158 |
| A | In–OH and P–H ³ | −0.274 | −0.291 |
| E | In–OH–In and P–H ³ | −0.508 | −0.524 |
| B and B' | H ₂ O–In | −0.989 | −0.791 |
| D and D' | In–O–P | −0.175 | −0.621 |
| E and E' | In–OH–In | −0.200 | −0.369 |

¹ Positive energies characterize configurations unfavorable with respect to an intact adsorbed water molecule.

² Free energy including ZPE corrections

³ P–H bond forms on In–P mixed dimer.

placed by a considerable amount from its ground-state position. Nevertheless, similarly to the intact molecule adsorption, no water-induced electronic state appears in the InP band gap energy region.

Although, dissociative adsorption is energetically favored over non-dissociative adsorption, additional barriers may be present that further hinder the reaction. In order to quantify these energy barriers CI-NEB calculations are performed, the method implemented here in this work was originally developed by the Jonson group[107–109] and later maintained and developed by the Henkelman group[170–172]. The starting image chosen was the water molecule adsorbed at site A, and the final image is the one described in Fig. 5.9. Site A is chosen over site B as a starting position of the water molecules as it is physically closer and that NEB calculations performed for a path between B and A reveal no additional barriers. Energetically, the path is shown in Fig. 5.10. The transition point does not correspond to the water splitting, which occurs at an earlier stage in the reaction path. No, the transition point corresponds to the shift from the hydroxyl group OH located at site A to the final point at site E. This transition point corresponds to an energy barrier of 0.87 eV that hinders the reaction. The energy barrier calculated here is in line with previous results for dissociation occurring at the In–P dimer [50], as it presents the same order of magnitude.

5.3.2 Increased water coverage

The next step for comprehending the water/InP interface is to go beyond single molecule adsorption by increasing the water coverage. The process was carried out by including a few water molecules and then increasing to a full water monolayer and continuing up until 3 monolayers of water adsorbed on top of the InP (2×4)-MD surface. Different configurations for the water mono-

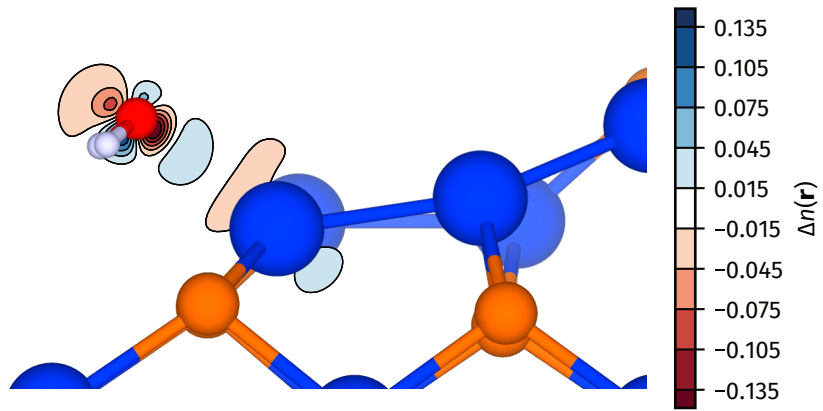


Figure 5.8: Structural configuration and water-induced charge redistribution for water adsorbed on the (2×4)-MD surface on site B. Red and blue isosurfaces indicate regions of charge accumulation and depletion, respectively. Adapted from Ref. [169].

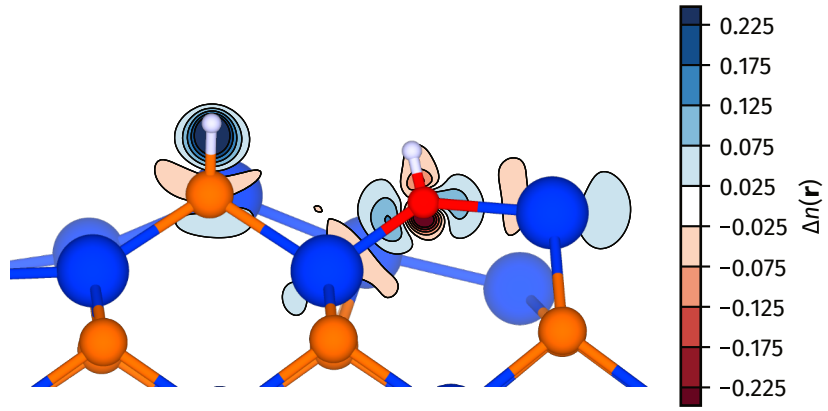


Figure 5.9: Structural configuration and water-induced charge redistribution for water dissociatively adsorbed on the (2×4)-MD surface, with OH on site E and H on the top P. Red and blue isosurfaces indicate regions of charge accumulation and depletion, respectively. Adapted from Ref. [169].

layer were tested, including ones that resembled different ice structures. The different water coverages are compared energetically in Fig. 5.11. The one-monolayer adsorption is more favorable over clusters of single molecules, comprising up to five molecules (see inset in Fig. 5.11). The bilayer, however, is even more energetically stable than the single monolayer. The clean surface is stable below values of the water chemical potential at around -0.5 eV (roughly equivalently to standard pressure and room temperature), where there will be a transition to the bilayer-covered surface. For more water-rich conditions, thicker water layers become more energetically favorable. Here, only up to three layers were included due to computational reasons. The full pressure vs. temperature phase diagram for the water layer structures is shown in Fig. 5.12. It should be noted that, at the transition between the clean InP surface and the water covered substrate, a variety of adsorption configurations can be expected: As shown by the inset in Fig. 5.11, in a narrow range of the water chemical potential many competing structures can occur, i. e., a strong influence of kinetic effects on the actual interface configuration will lead to a variety of interface structures.

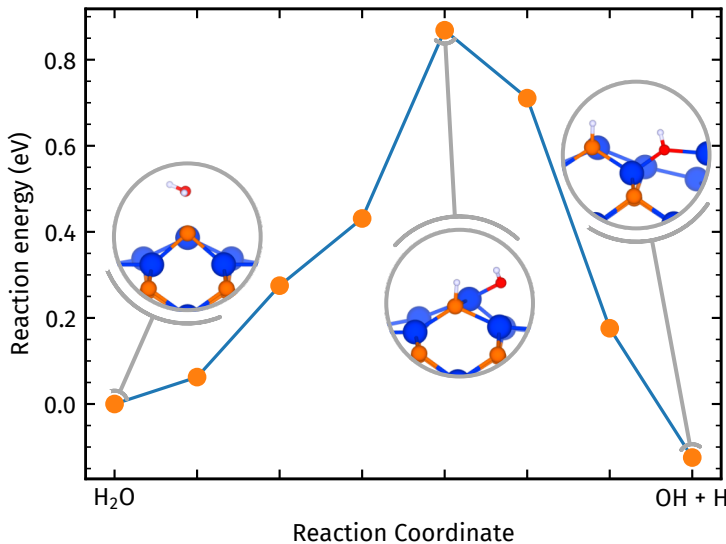


Figure 5.10: Minimum energy path for dissociative adsorption of single water molecules on InP (2×4)-MD. The starting configuration is the water molecule adsorbed at site A (see Fig. 5.7) and the final configuration corresponds to the one shown in Fig. 5.9. Adapted from Ref. [169].

Water monolayers configurations tend to resemble the most common crystal phase, the hexagonal ice I_h; see Fig. 5.13. However, due to the rough morphology of the InP(2×4)-MD surface and the incommensurability between the InP unit cell and ice I_h basal plane, the water monolayers do not preserve the perfect ice I_h structure. In particular, irregular shapes, including hexagons and pentagons, tend to form. In addition, the monolayer and bilayer tend to “hug” the surface, wrapping around the In–P dimer. This is not the case for the three-layer structure, however, which heavily resembles the ice I_h morphology. Sites A, B and C, which have been previously found energetically favorable [50, 169], here play a role as bonding sites between the surface and the water layers. The O atom from the H₂O molecule bonds to the three-fold coordinated In atoms on the surface. The number of In–O bonds decreases for the bilayer and is completely quenched for the three-layer structure.

The water overlayer is expected to change the molecular water adsorption process. In order to study the adsorption under more realistic conditions, several dissociative configurations were tested and found to be stable for the water monolayer on top of the In-rich InP (001) surface. The most stable configuration found here (shown in Fig. 5.14) corresponds to the hydroxyl group adsorbing onto the In–In bond at site E, with the hydrogen attached on the mixed dimer P atom. This is similar to the dissociation found for the single water molecule. Surprisingly, this configuration is stable even upon the hydrogen transfer from the mixed dimer into a H₂ reservoir. This lies in contrast to the similar configuration for a single molecule, where H dissorption leads to a less favorable configuration compared to the adsorption of an intact water molecule. The stability of the dissociated configurations in the presence of a hydration shell can be explained by the oxygen of the adsorbed OH group, which acts as an anchor point for the water monolayer on top. Similar results have also been found for the interface between water and GaAs (100) [173]. The hydration shell also affects the energy barriers present in the dissociation process, as shown by NEB calculations in Fig. 5.15. The starting position is the water molecule embedded in the water monolayer. The whole dissociation energy path lies below the energy of the starting configuration. While this situation is ideal, there is a local minimum where the water molecule still lies

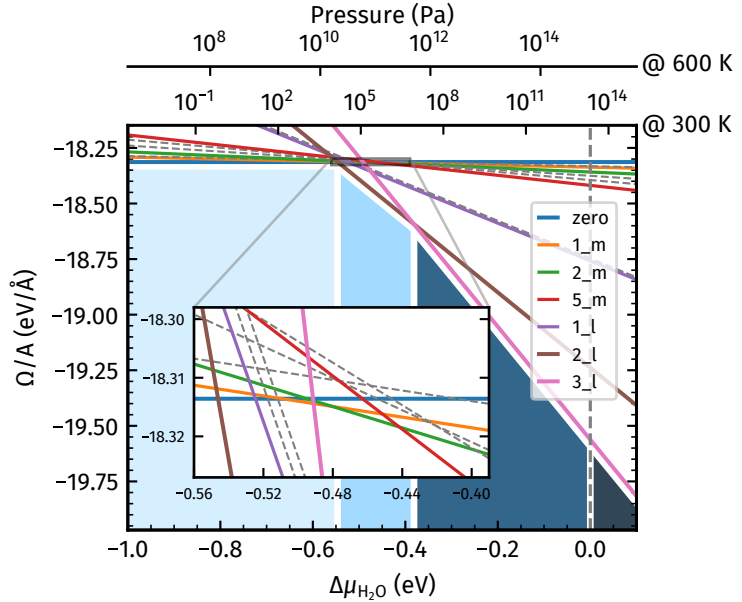


Figure 5.11: Phase diagram of water adsorbed on top of the InP (2×4)-MD surface, in dependence to the water chemical potential $\mu_{\text{H}_2\text{O}}$. The adsorption configurations refer to 1, 2 and 5 molecules (m), compared to the 1, 2 and 3 water layers (l). The temperature and pressure are obtained from equation 3.6 for $\mu_{\text{H}_2\text{O}}$. Dashed curves are unfavorable water configurations. Adapted from Ref. [169].

bonded to the water layer. Because of this, an energy barrier of ~ 0.3 eV is needed to be overcome in order to allow for the water molecule to exit the local minima and fully dissociate. This transition point corresponds to the water molecule in the middle of the interface between the water layer and the InP surface. The hydration shell also affects the formation of hydroxyl groups on the surface. This can be seen for the process $\text{H}_2\text{O}-\text{In} + \text{In}-\text{O}-\text{In} \rightarrow \text{OH}-\text{In} + \text{In}-\text{OH}-\text{In}$, where a nearly vanishing energy barrier of 7 meV is found. While the hydration shell helps reduce the energy barriers during the dissociation process, oxygen bounded close to the topmost P atoms has been found to be unfavorable, even for the water-covered surface. This lies in contrast to data concluded from experimental measurements[49].

5.3.3 Water splitting reaction mechanism

Hydrogen production is the main goal of solar-powered water splitting; therefore, studying the energetics of the overall reaction of interest $2 \text{H}_2\text{O} \rightarrow 2 \text{H}_2 + \text{O}_2$ is crucial. The reaction can be studied from the point of view of two half reactions: The oxidation $2 \text{H}_2\text{O} \rightarrow \text{O}_2 + 4 \text{H}^+ + 4 \text{e}^-$ and the reduction $4 \text{H}^+ + 4 \text{e}^- \rightarrow 2 \text{H}_2$, which are known as oxygen evolution reaction (OER) and hydrogen evolution reaction (HER), respectively. The reactions are studied from the perspective of the Gibbs free energy. The Gibbs free energy difference ΔG between products and educts of a chemical reaction, following the theory by Nørskov et al.[174], is approximated [175] as

$$\Delta G = \Delta E_{\text{tot}} + \Delta E_{\text{ZPE}} + \Delta G_U - \Delta G_{\text{pH}}, \quad (5.7)$$

where the terms

$$\Delta G_U = -e \cdot U \quad (5.8a)$$

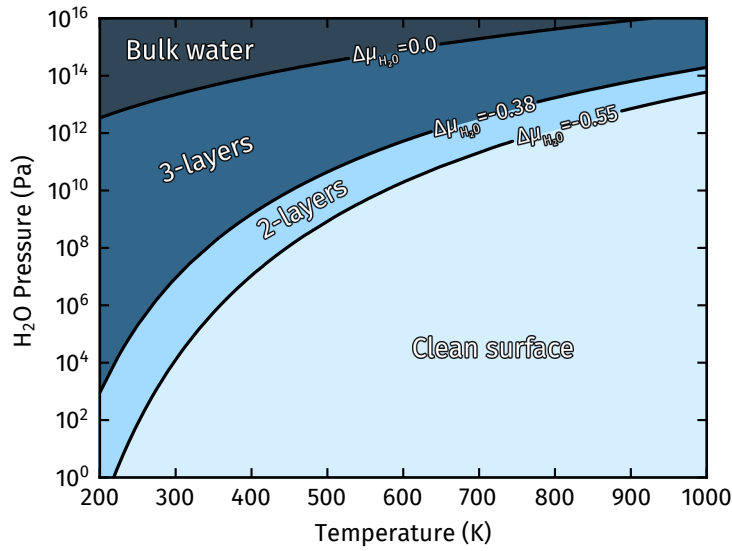


Figure 5.12: Pressure vs. temperature phase diagram of the water-covered InP (2×4)-MD surface. The solid lines mark the transitions between water phases. The water chemical potential $\Delta\mu_{\text{H}_2\text{O}}$ for the transitions is calculated from equation 3.6. Adapted from Ref. [169].

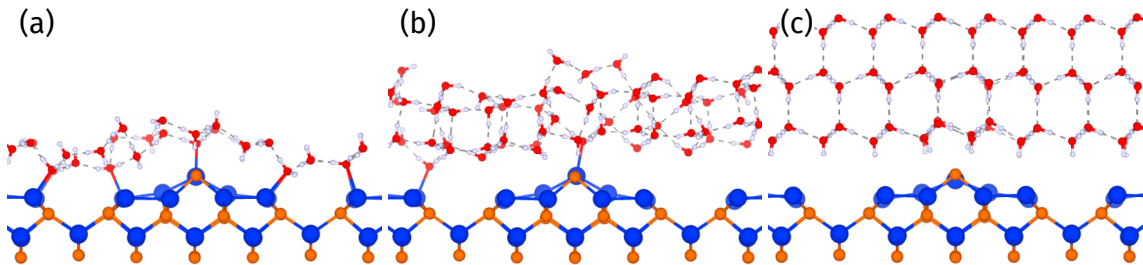


Figure 5.13: Energetically favorable surface geometries with a) one, b) two and c) three water layers adsorbed. Adapted from Ref. [169].

and

$$\Delta G_{\text{pH}} = -k_{\text{B}}T \ln(10) \cdot \text{pH}, \quad (5.8b)$$

are the correction terms to the Gibbs free energy difference due to the application of an electric potential and a difference in the pH value, respectively[176], e is the charge of the electron (1 in atomic units). Entropic contributions beyond the ZPE are expected to be small and of similar magnitude between structures, and only energy differences are of interest here. Thus, they are excluded from the calculations. Similarly, the contribution pV to fully calculate the Gibbs free energy is very small for realistic pressures and thus omitted. The reaction $\text{H}_2 \rightleftharpoons 2 (\text{H}^+ + \text{e}^-)$ is assumed to be in equilibrium, i. e., the reference potential is given by the “numerical” hydrogen potential, and the difference in the Gibbs free energy vanishes, $\Delta G = 0$. Consequently, the proton-electron pair is calculated from $E(\text{H}^+ + \text{e}^-) = \frac{1}{2}E_{\text{H}_2}$. A crucial quantity to probe the excess energy needed in order to drive a reaction is the overpotential, η , defined as the difference between the largest ΔG and the corresponding reaction potential at zero pH. The water to oxygen potential for OER is 1.23 eV [177]. For the HER, the corresponding potential is by definition 0 eV, thus the overpotential corresponds to the largest ΔG in the reaction.

There are many reaction pathways that the OER can take. Here, the associative reaction mech-

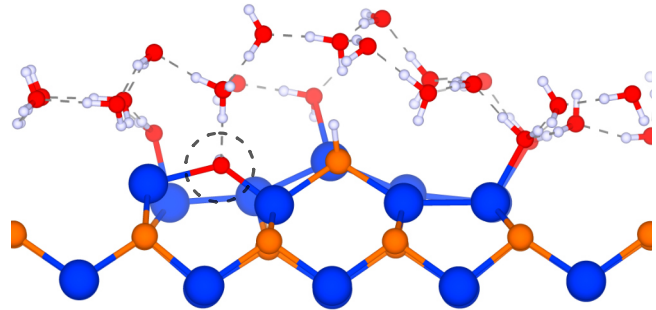


Figure 5.14: Most stable water dissociative configuration found for the water monolayer covered InP (2×4)-MD surface. The surface OH group is highlighted by the dashed circle. Adapted from Ref. [169].

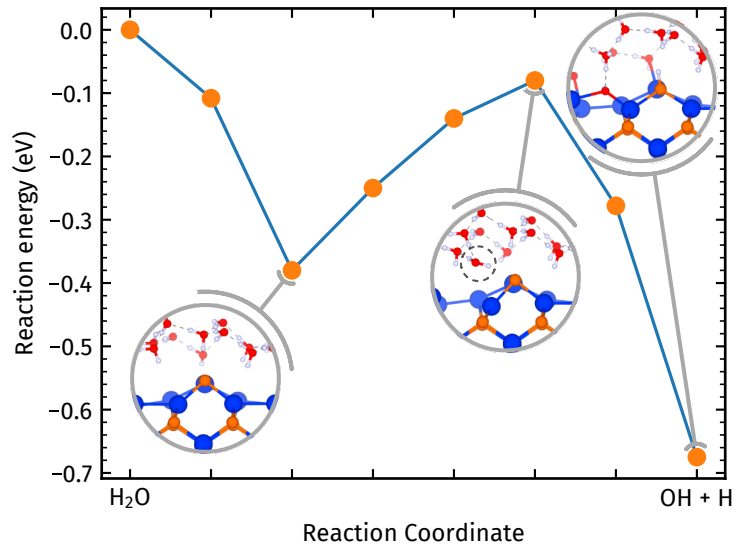
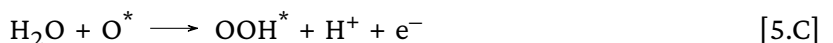
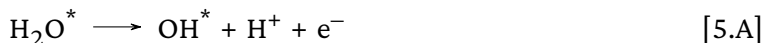


Figure 5.15: Minimum energy path for the dissociation process of a water molecule for the InP (2×4)-MD surface covered by a water monolayer. Adapted from Ref. [169].

anism is assumed to take place for the water splitting[174, 178]. The associative mechanism refers to an intermediate step where a peroxide OOH species is adsorbed at the surface as a pre-cursor for the formation of the oxygen molecule. The OER chemical mechanism consists of the following four steps:



where X^* denotes a species X adsorbed at the surface. An alternative reaction mechanism is for two water molecules to dissociate into two separate O atoms bound at the surface, afterward recombining to form O_2 . However, the activation barriers associated with this mechanism are relatively large [179]. Here, an energy barrier ~ 4 eV for the recombination process was calculated with the NEB method. Therefore, this alternate mechanism is ruled out as a possible pathway

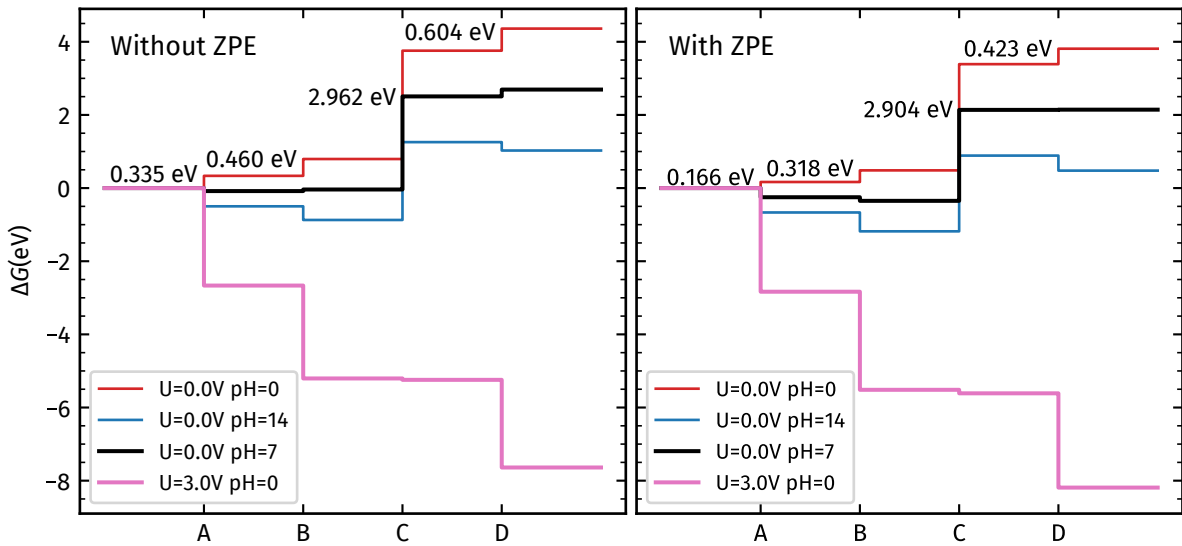


Figure 5.16: Gibbs free energy differences for OER with different potential U and pH value. The bottom and top figures show results with and without the ZPE correction, respectively. The energy step values are indicated for reactions with 0 pH and no potential. The labels A to D indicated the reactions 5.A to 5.D, respectively. Adapted from Ref. [169].

and only the associative mechanism is considered. The most favorable configurations for the reactions 5.A to 5.D were found based on the PES calculated in the previous sections. The Gibbs free energy differences for the reactions 5.A to 5.D are shown in Fig. 5.16. For neutral conditions, reaction 5.A is found to be exergonic, i. e., the change in free energy is negative. A very small increase in energy is needed to drive reaction 5.B. Including ZPE corrections results in not only reaction 5.A but also 5.B being exergonic. This could possibly explain why there were no persistent hydroxyl groups, but rather the liberation of gaseous H₂ was observed in Ref. [49]. Reaction 5.C requires a considerable amount of energy, as illustrated by the black curve in Fig. 5.16. Generally, it is found that the ZPE corrections tend to decrease the energy differences of the OER. The correction, however, on the overpotential is rather small. The reaction is also observed to heavily depend on the acidic conditions of the electrolyte. Decreasing the pH value, i. e., increasing the acidity, results in an increase in the Gibbs free energy ΔG and hinders hydrogen desorption. As a consequence, reaction 5.A becomes endergonic for acidic conditions. The transition occurs at pH levels of 5.5 and at a lower pH value of 2.8 with ZPE. For extreme acidic conditions, i. e., for a pH level of 0, the energy difference for reaction 5.A reaches a value of 3.3 eV and around half of that with ZPE, 1.66 eV. The reaction with the highest energy difference ΔG , 5.C, requires a potential of 2.904 eV; in the extreme acidic conditions, the value changes little with ZPE. Reaction 5.C defines the overpotential η around a value of 1.7 eV for OER. The orange curve in Fig. 5.16 depicts the scenario of an applied 3 eV external potential, and all reactions are exergonic. On the other side of the spectrum, reaction 5.B becomes exergonic for pH values larger than 7.8 (5.3 with ZPE corrections). This allows the water molecule to release both H atoms, leaving behind a surface-adsorbed O atom without the need of an external potential. The reaction pathways for the extreme acidic and alkaline conditions are depicted in Fig. 5.16 by the dashed curves. It should be noted, however, that in addition to the reaction itself changing the pH value of the solvent, the associative mechanism might not necessarily take place at all in alkaline solutions, and the OER could rather take a different pathway [176, 180].

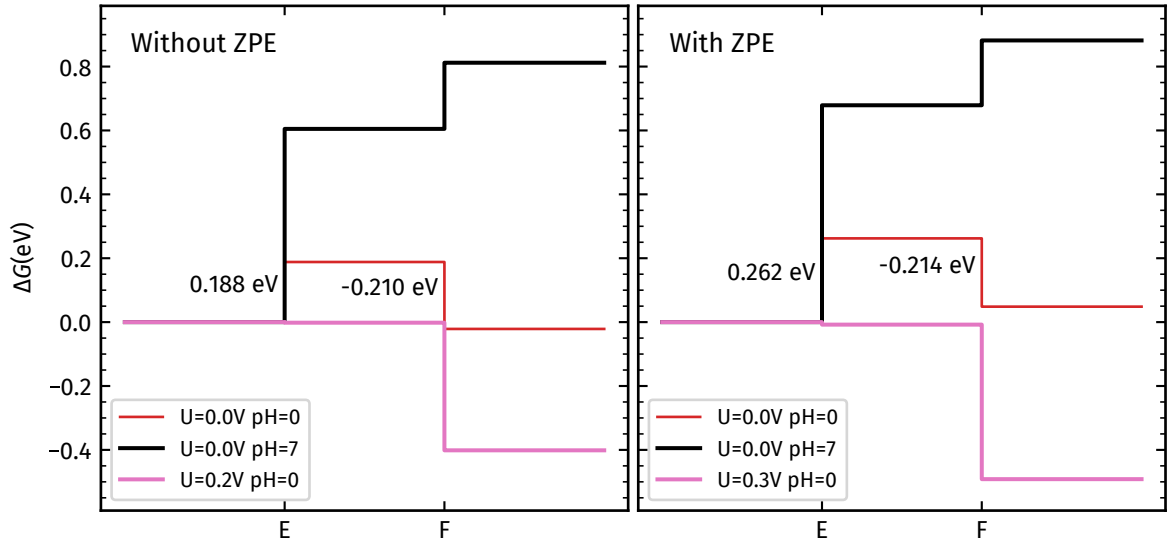


Figure 5.17: Gibbs free energy differences for HER for different potential U and pH values. The bottom and top figures show results with and without the ZPE correction, respectively. The energy step values are indicated for the reaction with 0 pH and no potential. The labels E and F indicated the reactions 5.E to 5.F, respectively. Adapted from Ref. [169].

The HER process results in the recombination of the protons into molecular hydrogen and is modeled by the following two reactions:



The In–P mixed dimer is taken as the adsorption site for both hydrogen initially found from the PES calculation (see Fig. 5.7 (c)). The Gibbs free energy differences for reactions 5.E and 5.F are shown in Fig. 5.17. For a neutral solution, reaction 5.E requires a potential of 0.68 eV and slightly lower with ZPE, of 0.60 eV, as shown by the solid black curve in Fig. 5.17. Increasing the pH value, i. e., for alkaline solutions, increases the energy differences ΔG . The interpretation is that hydrogen ions become increasingly available for surface adsorption as the solution becomes more basic. Conversely, for acidic conditions, decreasing the pH value also decreases the energy needed for the reactions. Beyond a pH value of 3.6, reaction 5.F is now exergonic, i. e., it occurs spontaneously. The threshold remains roughly the same with ZPE corrections. At the limit of 0 pH, extreme acidic conditions, the energy difference for reaction 5.E is reduced to 0.19 eV (0.26 eV with ZPE corrections), which also defines the overpotential for the HER. Interestingly, the ZPE correction increases the energy difference for reaction 5.E. This lies in direct contrast to the OER, where ZPE was found to decrease the individual reactions 5.A to 5.D energy difference. For reaction 5.F, ZPE also presents a slight increase to the energy difference; however, being only 4 meV, this is relatively small. Even when considering the slight increase in the overpotential (less than 0.1 eV), ZPE corrections have on the HER, it is still about one order of magnitude more favorable than OER. The favorable HER mechanism found here, coupled with the long-range H transport properties found for the InP/water interface discussed in Ref. [181] points to enhanced hydrogen evolution on In-rich InP surfaces.

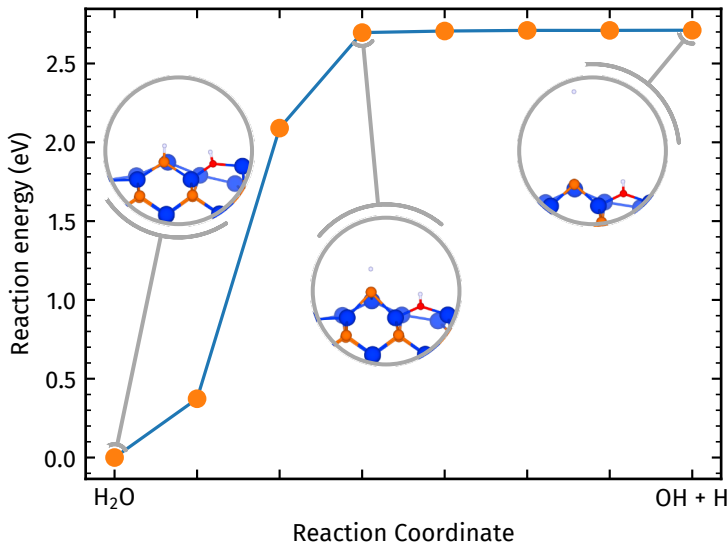


Figure 5.18: Minimum energy path of the desorption of a hydrogen from the surface. The starting point is the OH adsorbed at site E and a H adsorbed at the top P atom, corresponding to the final configuration shown in Fig. 5.10 for the water dissociation process. Adapted from Ref. [169].

Additional energy barriers

So far, the OER and HER mechanisms have been discussed from a thermodynamic point of view without considering the kinetics of the underlying process. This can be amended by taking into account the reaction barriers. Reaction 5.A, for example, an adsorbed water molecule dissociates into an adsorbed hydroxyl group and a desorbed proton. The energy barrier for the water molecule dissociating into an adsorbed OH group and a H at the surface was previously calculated to be 0.85 eV; see Fig. 5.10. An additional kinetic barrier might be present for the desorption of the hydrogen from the surface. Starting from the dissociated water molecule (Fig. 5.9), an energy barrier of around 2.7 eV was identified for the H desorption using the NEB method; see Fig. 5.18. This energy matches the difference in the chemical potential between the molecular and atomic hydrogen, complemented by the Gibbs free energy of reaction 5.A. In other words, the energy barrier hindering reaction 5.A is the water dissociative adsorption rather than hydrogen desorption.

Until now, the reaction mechanisms for oxygen and hydrogen evolution have been studied considering the clean InP surface without taking into account the influence of the water overlayer. As discussed previously, for the water dissociative adsorption, the hydration shell has an effect on the energetics, reducing the energy barriers present in the process. In order to more thoroughly investigate this phenomenon, additional calculations are performed for the water splitting starting from the water monolayer configuration (see Fig. 5.13 a). The OER energies in the presence of the water monolayer are shown in Fig. 5.19. The reactants and products of each step of the reactions under different water overlayer configurations were calculated to have similar energies. As a result, the energy differences for each step of the reaction are calculated from the average of the six most energetically favorable configurations of that step. Due to the sheer amount of atoms involved in the InP water monolayer interface, ZPE corrections were omitted in the following. The most prominent effect the hydration shell has on the system is observed in reactions 5.B and 5.D where the potential needed is reduced. The energy differences are changed far enough to make these reactions exergonic for neutral conditions. Conversely, reaction 5.C requires more

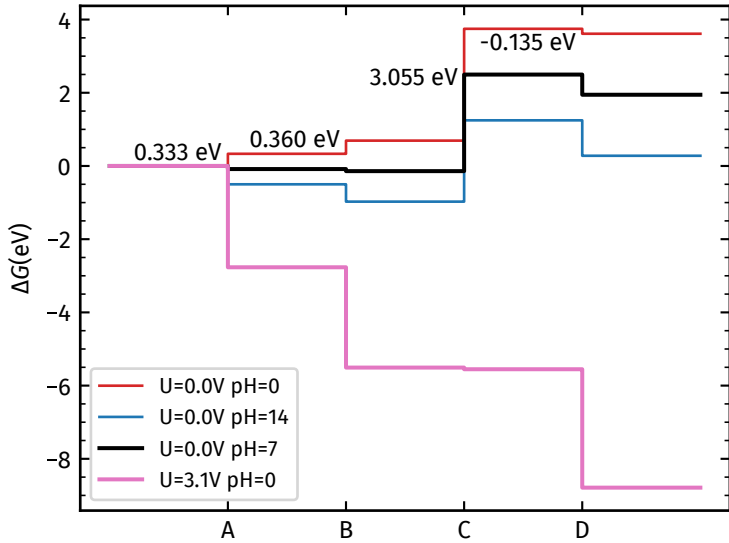


Figure 5.19: Gibbs free energy differences for OER in the presence of a water-monolayer with different potential U and pH value. The energy step values are indicated for reaction with 0 pH and no potential. The labels A to D indicated the reactions 5.A to 5.D, respectively. Adapted from Ref. [169].

energy, which is reflected in an increase in the overpotential to $\eta = 1.83$ eV. The energy difference of reaction 5.A remains largely unaffected in the presence of the water monolayer. The effect the pH value has on the reactions remains the same when compared to the system where the water overlayer was not considered. Interestingly, even for extreme acidic conditions, reaction 5.D remains exergonic. The energy pathway of the HER in the presence of the hydration shell is shown in Fig. 5.20. The potential required for reaction 5.E is increased when considering the water/InP interface. In turn, the overpotential of the HER is also increased to $\eta = 0.31$ eV. Reaction 5.F, rather presents a reduction in the energy difference. In short, the overpotential for both reactions is slightly increased in the presence of additional water. It cannot be excluded, however, that different reaction mechanisms, from the one described here, could change the overall picture.

5.3.4 Band alignment for In-rich InP surface

An additional condition to enable water splitting is the relative position of the valence and conduction band edges of the material with respect to the redox potentials. In detail, the VBM must lie below the redox potential for oxygen evolution, and the CBM has to lie above the redox potential for hydrogen evolution. This is a reason why it is crucial to find a material that not only presents an adequate band gap, but also a band alignment that allows water splitting. The band alignments for InP systems are presented in Fig. 5.21 with the oxidation and hydrogen reduction potentials, of 1.23 and 0 eV, respectively. On the physical scale, the potentials correspond to -5.67 and -4.44 eV. To locate the InP band edges, the work function $\Delta\Phi$ is calculated. The work function is defined as the energy necessary for removing an electron from the VBM to the vacuum level and calculated from the following expression

$$\Delta\Phi = e\phi_{\text{vacuum}} - \varepsilon_F, \quad (5.9)$$

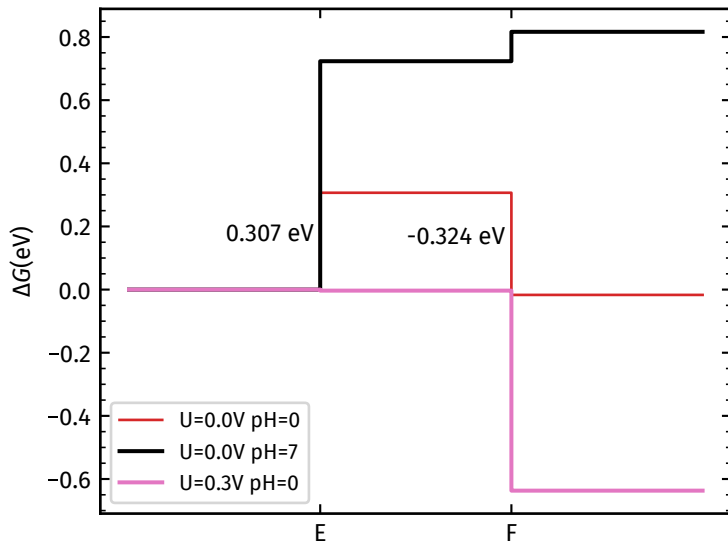


Figure 5.20: Gibbs free energy differences for HER in the presence of a water monolayer with different potential U and pH values. The energy step values are indicated for reactions with 0 pH and no potential. The labels E and F indicated the reactions 5.E to 5.F, respectively. Adapted from Ref. [169].

where ϕ_{vacuum} is the potential of the vacuum, ε_F the Fermi level, and e the charge of the electron. The vacuum potential is defined to be sufficiently far away from the surface such that an electron placed here would not feel the presence of the surface. From DFT calculations, the vacuum potential is calculated for the ionic and Hartree potentials at the vacuum region.

The calculations result in a $\Delta\Phi = 5.79\text{eV}$, allowing to locate the bulk VBM. The band gap for bulk InP is severely underestimated from DFT-GGA calculations. Therefore, to properly align the conduction band, the experimental band gap at room temperature of 1.35 eV [182] is used. The band alignments show that the OER and HER redox potentials are located inside the bulk band gap, albeit close to the edges, in agreement with previously recompiled data in references [26, 183, 184]. This would suggest that InP is a candidate for unbiased water splitting. However, the electronic structure in the DFT-GGA level of theory calculated so far suffers from the inadequate treatment of the exchange and correlation energies. To better represent the energy alignment, hybrid functional calculations with the HSE06 implementation were performed. An energy band gap of 1.35 eV for InP was calculated (additionally collaborated by GW_0 calculations), remarkably similar to the experimentally measured band gap at room temperature. The work function is also increased to a value of $\Delta\Phi = 6.01\text{eV}$. While the hydrogen reduction potential still lies above the conduction edge, the oxidation potential is no longer located below the valence edge. This suggests that InP is more suitable for HER rather than OER. However, this is not yet the complete picture; additional surface effects not taken into account from bulk calculations can affect the electron energies as well. The electronic structure and, as a result, the work function are affected by surface states and electric surface dipoles arising from the surface reconstruction. In addition, adsorbates at the surface are known to modify the work function. As an example, for Ga-rich GaP surfaces, adsorbed water molecules, with hydrogen in a down position, are assumed to generate an electric dipole layer that reduces the work function [49]. On lithium niobate, upon water adsorption, the work function was found to increase or decrease, depending on the surface polarity [175]. In particular, for InP, the work function was found to be inversely correlated to the

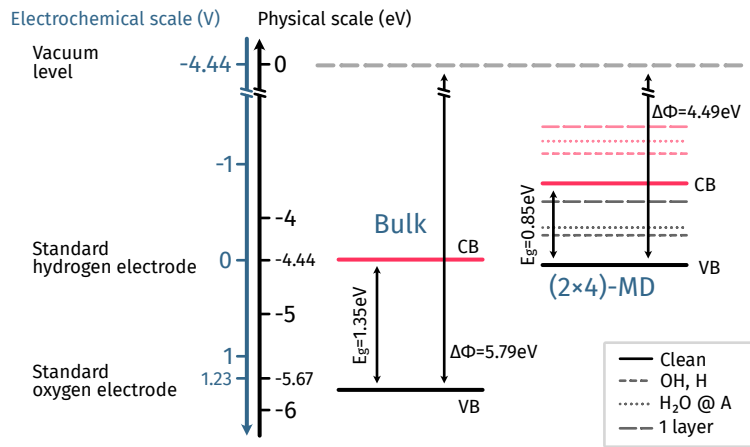


Figure 5.21: Band alignment of the InP bulk and (2×4) -MD surface in relation to the water splitting redox potentials. The black/red lines refer to the VBM/CBMs. The band energies are calculated in DFT-GGA level of theory. Adapted from Ref. [169].

In coverage of the surface[152]. Within the DFT-GGA level of theory, a band gap of 0.85 eV and a work function of $\Delta\Phi = 4.49$ eV are obtained for the InP (2×4) -MD surface. This lifts the valence edge above the oxidation potential (see Fig. 5.21). Hybrid functionals predict a slightly higher work function of $\Delta\Phi = 4.75$ eV and a more accurate band gap of 1.46 eV. Both levels of theory are in agreement on the relative position of the bands in reference to the redox potentials. The water adsorption further influences the InP work function. It is found that the adsorption of hydrogen together with hydroxyl groups, single H_2O molecules, as well as the formation of the full water monolayer, further decreases the work function well below that of the clean InP surface. All things considered, the present calculations suggest the In-rich InP (2×4) -MD surface primarily for hydrogen evolution.

5.4 Conclusions

Oxidation and water adsorption of the InP (001) (2×4) -MD surface was studied from DFT calculations. Both oxygen and water molecules adsorb at the surface as long as each constitute is available and is only kinetically hindered. Oxygen substitution is more likely to replace surface P atoms, leading to oxygen atoms coordinated to different amounts with In. Even less common is the presence of P—O—P bonds during substitution. These observations are linked to the rapid loss of surface order. Oxygen adsorption, on the other hand, leads to the formation of In—O—P and less commonly In—O—In. As oxidation increases, mid-gap states are observed to emerge in the electronic structure. These states arise from In—O bonds and are expected to reduce the electronic efficiency of the oxide layer by acting as surface charge traps. In combination with the high surface reactivity towards oxygen, detrimental effects may result on the electronic and optical properties of the surfaces and interfaces.

For water adsorption, single water molecules were found to bond at the three coordinate second-layer In atom. Dissociative adsorption is found to be more favorable than molecular adsorption but hindered by transition energy barriers. The dissociative process involves the hydroxyl group adsorbing at the second layer In—In dimers and the hydrogen on the top mixed

dimer P atom. Increased water adsorption is governed by attractive interaction between water molecules and determines the interface morphology. There is a small region of preparation conditions, corresponding to an intermediate value of the water chemical potential, where the different water morphologies are nearly degenerate; here a variety of single water molecules, molecular clusters, and full-layer coverage patches coexist. Full-water monolayers lead to a distinct decrease of the energy barrier for water dissociation, which may explain experimental water dissociation observations. The InP surface geometry strongly influences the water monolayer and is characterized by the bonds between the water oxygen and surface In atoms acting as anchor points. Despite the strong influence of the surface, the multi-layer molecular arrangement of water also resembles that of ice I_h. Dissociation leads to additional anchor points for the water overlayers from the surface-bound hydroxyl groups. Similar observations are made for other group III-V semiconductors.

Full reaction mechanisms were determined for the OER and HER, where the overpotentials were calculated to be in the order of 1.7 to 1.8 eV and 0.2 to 0.3 eV, respectively. The overpotential is correlated to the conditions of the electrolyte and can be lowered by the variation of the pH value. The potentials are a somewhat higher than excellent catalysts like TiO₂ and RuO₂ [185, 186]. InP-bulk band alignment would suggest that unbiased water splitting is possible, but further InP surface and water coverage calculations change the picture: They lift the VBM above the standard oxidation potential. Hybrid-DFT calculations further emphasize these findings. Both the overpotential calculations and band alignment suggest the In-rich (001) surface for hydrogen evolution rather than oxygen evolution. The HER may be additionally assisted by surface oxidation, where In—O—In bonds could serve as additional hydrogen adsorption sites.

Chapter 6

P-rich InP surface: Defects and water

The promising performance of III-V semiconductors in the context of photovoltaics has led to the investigation of materials in the application of water splitting; in particular, InP has been shown to present promising results[187, 188]. In the previous chapter, the water splitting process on the In-rich surface InP (2×4)-MD was explored. Nonetheless, this is not the only relevant surface reconstruction. In addition to In-rich, P-rich surfaces can be prepared with common epitaxial processes. Experimentally, growing pristine surfaces is impossible, and each surface will undoubtedly present defects. In addition to the surface reconstruction, the role surface defects play on the electronic properties of the P-rich InP, especially in contact with water, remained unclear. The focus was instead redirected to the understanding of the InP-water interface [49, 169]. Surface defects have been shown as a plausible explanation for surface states inside the band-gap for III-V semiconductors[189, 190] and in particular for InP[191–193], which could lead to noticeable band bending.

Phosphorus-rich surfaces are grown, for example in metalorganic vapour-phase epitaxy (MOVPE) or chemical beam epitaxy (CBE), resulting in a surface terminated with buckled P-dimers. During the MOVPE growth process for InP, H₂ is used as a carrier gas, resulting in the incorporation of hydrogen onto the surfaces. The most energetically stable P-rich surface is the hydrogen adsorbed (2×2)-2D-2H surface, which has been studied extensively in the past both theoretically and experimentally[150, 153, 156, 194, 195]. The surface is characterized by two opposed buckled P-dimers, with hydrogen bonded at the “down” P atoms, as shown in Fig. 6.1. The dangling bond of the P atom without a hydrogen is responsible for the surface states VBM while the σ^* anti-bond for the CBM[153]. These surface states also lead to strong optical anisotropies, which can be used to characterize the surface using RAS techniques to identify the surface fingerprints[156]. Water is speculated to breaks the top P–P surface bonds, leading to different oxides and phosphates [49]. However, little information regarding water dissociation on the P-rich surface exists. Water adsorption could be assisted by surface defects, leading to additional pathways for water to bond at the surface. The P-dimers present themselves as potential candidates for hydrogen-related surface defects. Recent experimental data shows that the Fermi-level is pinned at the mid-gap, suggesting the presence of such defects.

This chapter focuses on the description of the hydrogen-related defects on the P-rich (2×2)-2D-2H surface and the effects they have on the electronic structure. Water adsorption is also

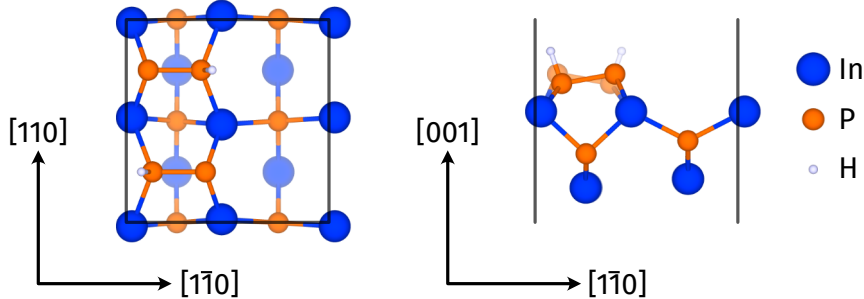


Figure 6.1: Top and side view of the P-rich InP (2×2)-2D-2H surface reconstruction.

investigated on both the pristine surface and on one with a defect present. The results discussed here were previously published in references [196, 197]. The experimental contributions were performed by Dominik Christian Moritz under the supervision of Wolfram Jaegermann. The formation energy of the defects was calculated by Rachele Sciotto under the supervision of Wolf Gero Schmidt.

6.1 Hydrogen defects

Experimentally P-rich surfaces were prepared in MOVPE with a H_2 carrier gas and measured through reflectance anisotropy spectroscopy (RAS), ultraviolet photoemission spectroscopy (UPS), x-ray photoemission spectroscopy (XPS) and low-energy electron diffraction (LEED) confirming a 2×2 surface reconstruction [196]. The surfaces were *p*-doped, with an acceptor concentration of $N_A = 2 \cdot 10^{18} \text{ cm}^{-3}$. The structure was expected to present a Fermi-level position near the valence band due to the *p*-doping. Indeed, the bulk Fermi level is located 0.40 meV above the VBM. However, at the surface interface, the Fermi level is pinned at 0.60 eV above the VBM causing strong band bending. The usual InP models' surface states alone cannot explain this phenomenon, as they are not present around the mid-gap. Under normal conditions, surfaces are unlikely to present perfect surface geometry and will likely contain surface defects, among others, which could help explain the experimental observations.

Four main defects are proposed for the (2×2)-2D-2H surface, consisting of adsorption or desorption of one or two hydrogen atoms on the top P-dimers. The grand canonical potential is used to compare the defect surfaces energetically vs. the hydrogen chemical potentials, in figure 6.2. It is no surprise that the 2D-2H surface is stable for a wide range of H chemical potential. The one H vacancy is the energetically favorable defect type for typical growing conditions, $\Delta\mu_{\text{H}}$ from -0.6 to -1 eV; the surface model is denominated 2D-1H. The defect surface with one additional H, i. e., 2D-3H, is only stable for H-rich conditions. Interestingly, for a chemical potential of -0.93 eV, there is a phase transition from 2D-2H to the surface with two H vacancies, i. e., 2D-0H, the latter becoming the stable configuration. This is not so surprising; as less hydrogen is available in the environment, it will be less likely to bond at the surface. For extremely H-rich environments, $\Delta\mu_{\text{H}} > 0$, the 2D-3H becomes the energetically favorable surface reconstruction and eventually the surface with two additional adsorbed H, i. e., 2D-4H. These last two surfaces may form only when atomic hydrogen is available.

The defect concentration is calculated from equation 3.32, where the Gibbs free energy in-

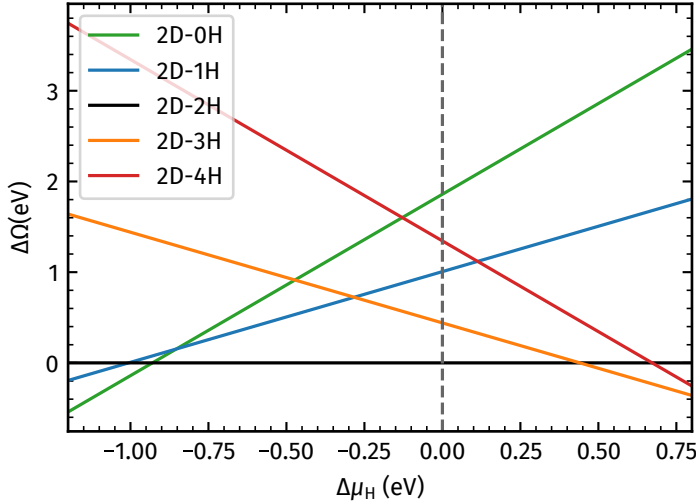


Figure 6.2: Calculated surface grand canonical potential of the different hydrogen defects on the InP (2×2)-2D-2H surface. The H chemical potential is given with respect to molecular hydrogen. The dashed line indicates the H-rich conditions ($\Delta\mu_H = 0$), where the surface is exposed to molecular hydrogen at $T = 0$ K.

cludes both vibrational and electronic entropy as well as the ZPE. The phase diagram vs temperature and pressure, through equation 3.6, is shown in Fig. 6.3. The 2D-3H surface defect is dominant for high pressures and low temperatures, while the 2D-0H is dominant for low pressures and high temperatures. In the middle of these two regions, the 2D-1H defect is the most dominant, for $\Delta\mu_H$ between -0.75 and -0.07 eV, marked by the black curves in Fig. 6.3. The maximum calculated defect concentration at room temperature is $1.68 \cdot 10^{12} \text{ cm}^{-2}$. This is comparable to typical doping numbers for semiconductors. Under these conditions, the desorption of one hydrogen atom is by far the most dominant defect type, with a total concentration of $8.39 \cdot 10^{11} \text{ cm}^{-2}$. Other types of defects have very low concentrations and are very unlikely to be observed in this region. From the experimentally measured band bending $V_{\text{BB}} = 0.56$ eV and considering a parabolic potential drop inside the InP space charge region, the total surface charge Q_{ss} can be estimated from the following expression

$$-Q_{\text{ss}} = \sqrt{2\varepsilon\varepsilon_0 q V_{\text{BB}} N_A}, \quad (6.1)$$

a total concentration of $3.9 \cdot 10^{12} \text{ cm}^{-2}$ [196] is calculated, which means that less than 1% of the surface atoms contribute to the surface defects. Both the upper limit determined through theoretical calculations and experimental measurements of the total concentration of defects are in the same order of magnitude. The theoretically calculated values are expected to change when including charge defects [197], yet the 2D-1H defect is the most dominant defect in the region of interest with a similar order of magnitude.

The agreement between experiment and theory would then suggest that the surface with one H vacancy is the one responsible for the Fermi-level pinning. To confirm this, the electronic band structure of the 2D-1H surface was calculated. In order to avoid band dispersion from excessive defect contractions, the band structure is calculated in a 4×4 supercell, where only one of the four 2D-2H surfaces has the H vacancy. The band structures for the pristine and the one H vacancy are shown in Fig. 6.4. The H vacancy introduces a partially occupied mid-gap state above the VBM

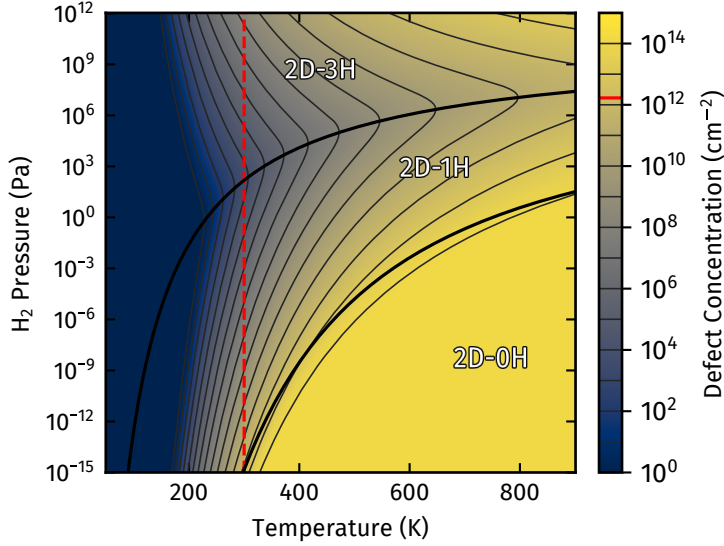


Figure 6.3: Boltzmann distribution of H defects on InP (2 × 2)-2D-2H surfaces as a function of pressure and temperature. The respective most dominant defect type is indicated. The red dashed line indicates room temperature.

while leaving mostly intact the rest of the electronic structure. Partially decomposed DOS reveal unsurprisingly, the mid-gap defect state is of *p*-character and is primarily due to the partially filled dangling bond. The defect state is located slightly below the mid-gap, which is in good agreement with photoemission measurements[196], indicating that the surface P-dangling-bond defect is responsible for the Fermi-level pinning. Additional, spin-polarized calculations do not change the overall picture. The defect state is split into an occupied spin-up state at the VBM and an unoccupied spin-down state above the mid-gap [197]. The Fermi level is thus pinned between these two states close to the mid-gap, in the lower half of the band gap. The effect of the spin-polarization is confined to the defect state, leaving the rest of the electronic structure unaffected.

6.1.1 Substrate doping and charged defects

For a more complete picture, Sciotto et al.[197], explored substrate doping by including charge defects in the calculations; this allowed for a better comparison to doped samples. The formation energy for a surface with a defect and charge q can be calculated from equation 3.24 by including an additional correction term, qE_F (see e. g., Ref. [198]). The Fermi energy level, E_F , is referenced in respect to the InP bulk VBM. In order to avoid comparing total energy for supercells with different charge levels, which are not well described for slabs, the Slater-Janak transition-state model is used[199, 200]. This model extends from the Slater-Janak theorem [78] described previously for the energy difference of N and $N + 1$ electron systems (equation 2.45) defined for $\delta = 1/2$ as

$$E(N + 1) - E(N) = \int_0^1 d\eta \, \epsilon_H(\eta) = \epsilon_H \left(\frac{1}{2} \right), \quad (6.2)$$

assuming that the Kohn-Sham eigenvalue of the respective highest occupied state ϵ_H varies linearly with its respective occupation number.

The surface electronic structures are calculated for the various P-rich InP defect configurations within the hybrid HSE06 functional formalism and the Slater-Janak transition-state model.

6.2 Water adsorption

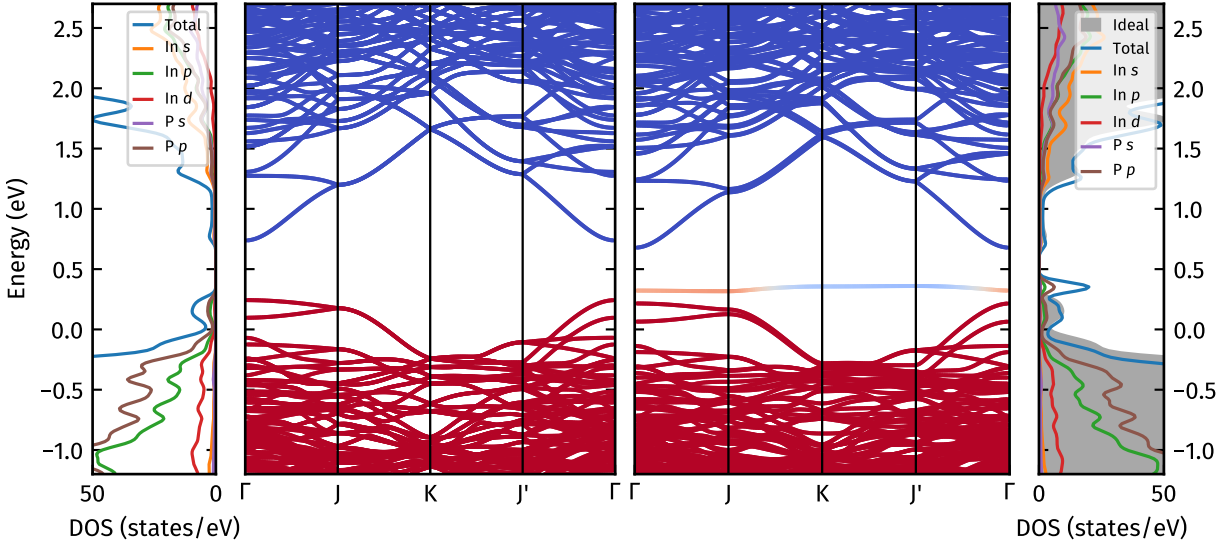


Figure 6.4: Surface band structures for the (4×4) pristine 2D-2H (left) and with one H vacancy 2D-1H (right). Blue and red curves correspond to 0 and 1 occupancy, respectively. The DOS is also shown. Adapted from Ref. [196].

The complete phase diagram is shown in Fig. 6.5 for a hydrogen chemical potential of $\Delta\mu_H = -0.6$ eV. For a wide range of Fermi-level positions, the neutral 2D-2H surface with no defects is energetically favorable, in accordance with the experimental findings [156, 196]. The 2D-2H surface has a charge transition slightly below a 0.25 eV Fermi level, from the neutral system to the one-fold positively charged system. The transition for the one hydrogen vacancy defect occurs 0.38 eV above the VBM, higher than for the pristine surface. This could possibly explain the Fermi-level pinning for the *p*-doped MOVPE-grown samples, provided that the defect density is high enough. This reveals that surface preparation is not only sensitive to the pressure and temperature but also to the type and levels of the doping.

In the case of *n*-doped surfaces, it is revealed that the 2D-2H surface is no longer the most dominant reconstruction, but rather the one-fold negatively charged 2D-1H geometry for Fermi-level positions above 0.9 eV. This is as a result of the strong electron affinity of the partially filled P dangling bond. For *n*-doped samples, the P dangling bond is two-fold occupied and no longer provides an adsorption site for hydrogen. This also explains why the 2D-0H is also more favorable over the 2D-2H surface close to the CBM. The transition between the 2H and 1H is, however, strongly dependent on hydrogen chemical potential, i. e., the temperature and pressure [197]. The combination of high pressure, low temperature and low Fermi level position stabilizes the 2D-2H surface with respect to the 2D-1H. The transition itself influences the Fermi level due to the high concentration of P dangling bonds with the capacity to accept surface charge. Therefore, flat band conditions will also not occur for *n*-doped samples.

6.2 Water adsorption

The surface sample was exposed to water and measured experimentally with UPS and XPS techniques by Moritz et al.[196]. Core-level shifts towards higher binding energies were observed as water adsorption increased, in addition to the signals getting damped. The shifts are attributed

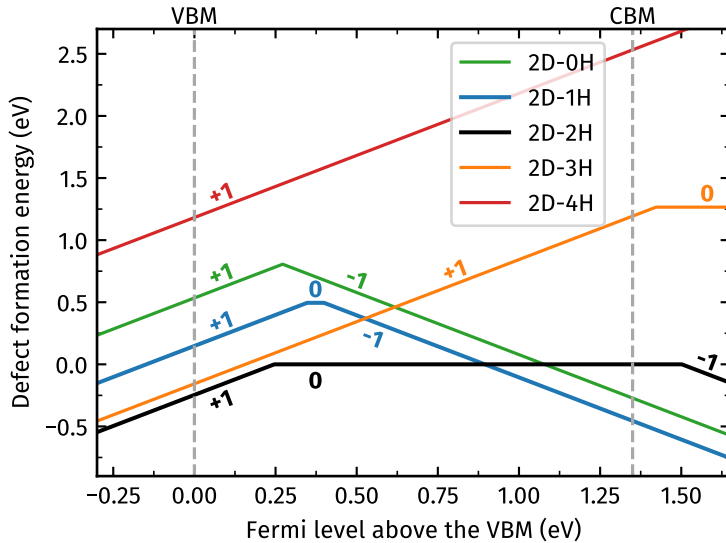


Figure 6.5: Defect formation energies for the hydrogen-related InP(001):H surface defects with the Slater-Janak transition-state model as a function of the Fermi level. A hydrogen chemical potential of $\Delta\mu_H = -0.6$ eV is assumed. The energies are referenced to the neutral 2D-2H system. Adapted from Ref. [197].

to the charging effect of the insulating water layer due to the emission of photoelectrons. However, the measurements revealed no spectral changes in the core-level lines, indicating that the surface remained chemically immune after water adsorption. The typical water spectral features arise with increased water adsorption. After water desorption, the original signals of the clean surface are restored. While water dissociative adsorption has been noted previously for In-rich surfaces [49, 169] and also for InP (110) surfaces [145], the spectroscopy measurements show that OH groups are only present in a few surface sites far below monolayer coverage. Furthermore, the 2D-2H surface LEED pattern is restored after water desorption, indicating that there are no structural changes. Overall, experimental data show that there are almost no electronic interactions that lead to chemical bond formation with water.

To verify the experimental results, water adsorption on the P-rich surface was calculated computationally. The PES, shown in Fig. 6.6 left panel, for the 2D-2H surface was computed with the previously described equation 5.1 for water adsorption. Unlike the (2×4) In-rich surface, the top P-dimer dangling bond is not a favorable adsorption site. Although the topmost P atom presented a favorable adsorption site for the In-rich surface, In backbonds were found to be more favorable for molecular water. The P-rich surface has no exposed In dangling bonds; rather, the water molecule sits on the trench between the P–P rows, not bonding chemically to the surface. The preferential water-adsorbed surface configuration is shown in Fig. 6.7 together with the charge redistribution brought upon the molecular adsorption. There is a weak charge accumulation between the P up atom and the water proton. Even weaker charge accumulation and depletion regions are found toward the second row In atom. This leads to weaker physisorption on the P-rich surface compared to the In-rich one. The water adsorption does not strongly affect the geometry nor the electronic properties of the 2D-2H surface. Similarly, water adsorption presents no additional states in the band-gap region.

Surprisingly, the hydrogen-deficient 2D-1H surface presents remarkably similar findings to the pristine surface. The H vacancy affects only very slightly the adsorption configurations, as

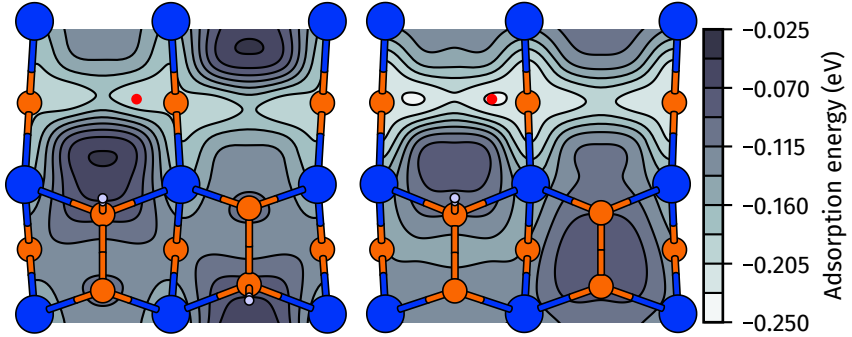


Figure 6.6: Calculated PES for a single water molecule adsorbed on the InP (2×2)-2D-2H (left) and (2×2)-2d-1H (right) surfaces. The most favorable site for water is marked by the red dot. Adapted from Ref. [196].

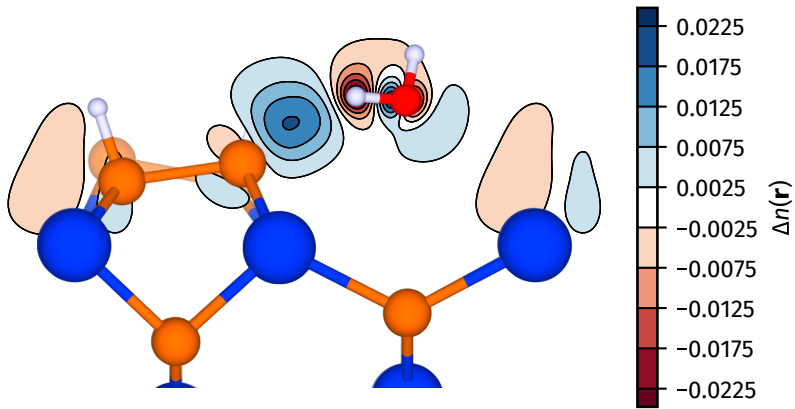


Figure 6.7: Structural configuration and water-induced charge redistribution for water adsorbed on (2×2)-2D-2H. Red and blue isosurfaces indicate regions of charge accumulation and depletion, respectively. Adapted from Ref. [196].

can be seen in the PES in Fig. 6.7 right panel. The water preferentially adsorbs at a similar location, in the trench between the P-dimers, with a slightly larger adsorption energy (about 0.03 eV). Again, the water molecule adsorbs between the H-coordinated P-dimer on the up-atom site and the second-row In atom. Since the water molecule does not interact with the H-deficient P atom, the electronic mid-gap state is also unaffected upon adsorption. This is in agreement with the experimental findings, in which neither electronic nor chemical reactions could be identified for molecular water adsorption and the band bending could still be observed.

The hydrogen vacancy presents no discernible effect on water molecular adsorption; however, this situation changes once dissociation is considered. These calculations were fueled by experimental findings of slight hydroxyl group traces. In order to explore dissociative water adsorption, the PES was calculated with respect to molecular water using equation 5.6. In Fig. 6.6 the PES for the pristine 2D-2H surface (left) and the one H vacancy 2D-1H (right) are presented. For the 2D-2H, the OH group is not found to adsorb favorably at any site on top of the surface. Conversely, for the 2D-1H, the undercoordinated P atom presents itself as a prime candidate for the OH adsorption. The hydroxyl group adsorbs preferentially at the P dangling bond, saturating the half-filled dangling P orbital left behind after the H desorption. Accordingly, from band

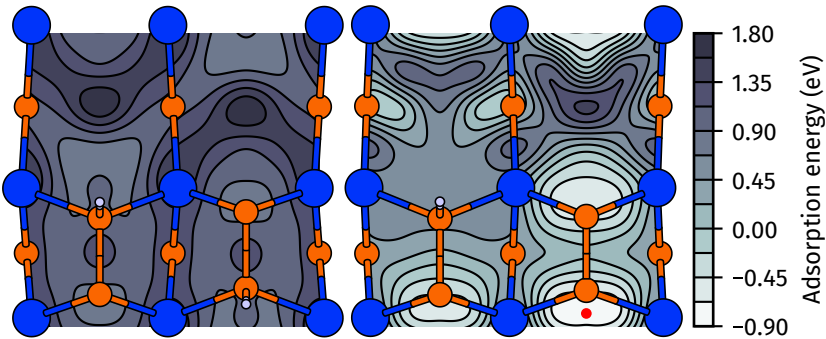


Figure 6.8: Calculated PES for a hydroxyl group on the InP (2×2)-2D-2H (left) and (2×2)-2d-1H (right) surfaces. The most favorable site for OH adsorption is marked by the red dot. Adapted from Ref. [196].

structure calculations, the mid-gap surface state is removed, and the electronic structure resembles that of the 2D-2H pristine surface again. It should be noted that the dangling bond left by the H vacancy not only changes favorably the adsorption energies for the P atom at the dangling bond site itself, but also on all the other P atoms with a dangling bond of the 2D-1H surface lattice. On the whole, dissociative water adsorption may be possible on the 2D-1H defect surface but unlikely on the pristine surface.

Even though UPS revealed slight traces of OH groups adsorbed on the InP surface, the Fermi-level position together with the unchanged band bending indicate that not all defect-related P dangling bonds are passivated by OH groups. This also confirms that the P dangling bond center does not behave as an active site for water dissociative adsorption. Unlike the In-rich surface, the 2D-2H lacks the In–In bonds, where OH groups were found to bond favorably[169] on the surface. For this reason, it is suggested that water dissociation is not favorable on the InP 2D-2H surface, even when considering H vacancies as active sites. However, water dissociation may still occur at step edges rather than on terraces of the P-rich (001) surface[196].

6.3 Conclusions

The strong surface band bending is found to be attributed to the hydrogen vacancies, leading to P dangling bonds and induced half-filled mid-gap surface states. Different hydrogen defects are associated with distinct temperatures and H pressures. The H vacancy, in particular, was calculated to be the most common defect type for standard H chemical potentials and show concentrations high enough to explain the observed band bending. The doping of the material is also expected to change the electronic structure and even the surface geometry. In particular, for *p*-doped samples, the charged transition state is calculated at around 0.37 eV above the VBM and pinning the Fermi level at the lower half of the band gap. In the case for *n*-doped samples, the ground-state surface structure is now the one-fold negatively charged 2D-1H surface, which will lead to a Fermi-level pinning below the surface CBM.

Water calculations reveal that the H vacancy, on the one hand, does not significantly change the behavior of molecular water adsorption on the InP (001) surface compared to the hydrogen saturated surface. On the other hand, the H-deficient P dangling bonds serve as an OH adsorption site, differing from the pristine surface. The OH adsorption passivates the P dangling bond and,

6.3 Conclusions

as a result, removes the defect surface state from the band gap. The calculations suggest water splitting to occur at the defect sites. However, experimental observation of the band bending even after water exposure indicates that the P dangling bonds are not active sites for water dissociation. Instead, water dissociation may occur at step edges of the P-rich InP (001) surface.

Chapter 7

Al/In-rich AlInP surface oxidation

III-V semiconductors provide the basis for several technological applications, ranging from electronic to optoelectronic devices. However, binary compounds are limited by a handful of materials with immutable properties like the lattice constant, the band-gap size, and the direct or indirect band gap. Usually, the alloys are grown on top of a substrate or are implemented in a mixture of two or more layers in what is called a tandem structure. In these cases, lattice mismatch can cause detrimental effects on the devices. Thus, the lattice parameter strongly determines the efficiency. For example, GaP (100), which has an excellent band alignment suitable for water splitting[43], yet falls short with low adsorption efficiency because of the indirect and rather large band gap[201]. Also, the material studied here, InP namely, showed excellent band alignment for the bulk, but surface effects change the picture[163] and suffer from lattice mismatch with other compounds. AlP has a better band gap for water splitting[42], however possesses an indirect band gap[202, 203] not suited for photocatalysis. Ternary III-V compounds offer the flexibility to circumvent these issues by allowing the fabrication of devices with the properties in between those of the binaries compounds. Although it is evident that the available ternary alloys offer greater flexibility, the space in which these materials exist is limited by binary compounds[26]. Nevertheless, careful material engineering and choice of components allow for materials with excellent properties [204].

One of the most technologically relevant ternary materials is AlInP, which has been considered as a window layer in different optoelectronic and photochemical applications[32, 188, 205–207]. The popularity of $\text{Al}_x\text{In}_{1-x}\text{P}$ is due to its favorable combination of chemical stability, sufficiently wide band gap, and high-quality heteroepitaxial interfaces with many absorbers[208]. The most commonly used composition is $\text{Al}_{0.5}\text{In}_{0.5}\text{P}$ which possesses a desired large and direct band gap[209–211] as well as being lattice matched to many other III-V compounds such as GaAs[212] or GaInP[32, 213]. This allows AlInP to be used in tandem structures for photocatalysis with record-breaking high efficiencies in the potentiostatically assisted electrode and in solar-to-hydrogen conversion[32, 207].

Despite the promising results of AlInP alloys, there is little information regarding atomic structure and electrical properties, and also the interaction of the material with light is not fully understood. Exploring the most common AlInP surfaces and understanding the AlInP properties is crucial for the engineering of AlInP window layers. The lack of literature on AlInP is probably a

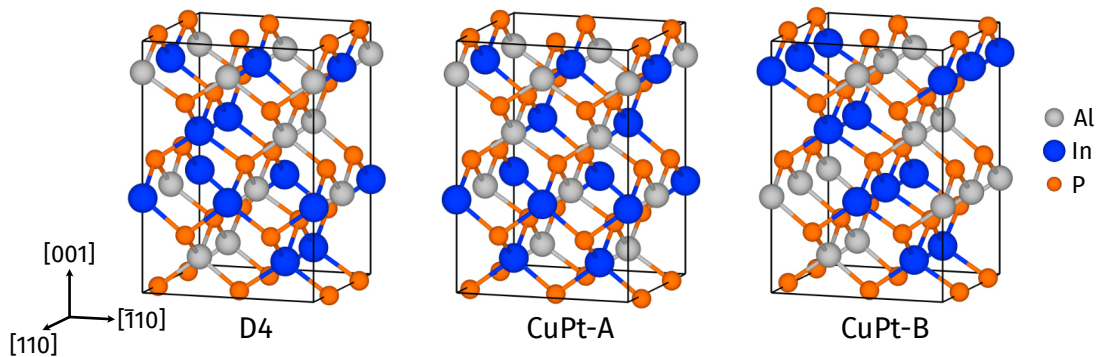


Figure 7.1: $\text{Al}_{0.5}\text{In}_{0.5}\text{P}$ bulk material with cations arranged with CuPt-A or CuPt-B ordering, as well as D4 ordering that ensures optical isotropy.

result of the difficulty in dealing with these surfaces due to the rapid oxidation of the material with minimal exposure to oxygen or water. This chapter focuses on the study of AlInP surfaces from first principles. The most energetically favorable surface reconstructions are identified and their electronic properties are obtained. How the AlInP reacts towards oxygen is also studied for the most energetically favorable surface reconstructions under growing conditions. The optical properties of AlInP from first principles will be explored in the next chapter.

7.1 Surface geometry

In the literature, one can find that for III-V ternary systems, the bulk ordering plays a crucial role in the resulting surface geometry. Different growing conditions result in a broad range of atomic bulk ordering; among these, the CuPt ordering stands out[214, 215]. This ordering consists of alternating group III layers perpendicular to the $[\bar{1}11]$ or $[1\bar{1}\bar{1}]$ direction called CuPt-B or perpendicular to the $[11\bar{1}]$ or $[\bar{1}\bar{1}\bar{1}]$ direction denominated as CuPt-A. It has been shown previously that for GaInP, CuPt causes anisotropic effects on the electronic structure and optical spectra[216, 217]. The CuPt ordering has also been linked to the formation of surface dimers on GaInP, which induces additional strain on the material[218, 219]. The AlInP bulk with a CuPt ordering is shown in Fig. 7.1

The dimer formation and CuPt-B ordering relation were also observed for AlInP, where correlation between surface P-dimers and the bulk ordering and a $\beta(2 \times 4)$ reconstruction were identified[214]. This surface geometry is not the only one that presents dimers on the top layer, and in fact it has been found to not be energetically favorable for other III-V semiconductors, especially not group-III-P compounds[154]. Since the actual surface geometry for AlInP is virtually unknown, a plethora of surface geometries were explored based on that of other III-V semiconductors[154, 220] considering a CuPt-B bulk ordering. The results were reported in Ref. [163], however, the influence of hydrogen, present during MOVPE and CBE growth processes, was not considered. This motivated the study by Glahn et al.[34] by expanding the surfaces considered to also include hydrogen. Future experimental RAS measurements prompted the inclusion of an In-covered surface that had yet to be considered named (2×4) -rInMD[221]. All the surface geometries that have been this far found are recompiled here and compared energetically. The grand canonical potential, equation 3.3, presents four degrees of freedom for AlInP:H surfaces for each

7.1 Surface geometry

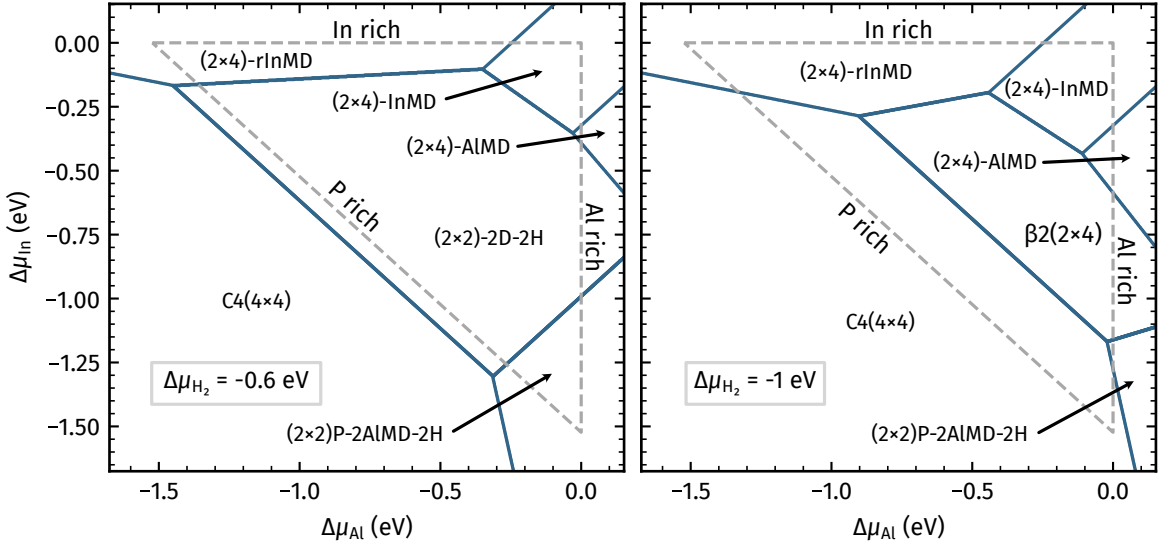


Figure 7.2: Surface phase diagram of the energetically favored AlInP(001) surface structures, dependent on the Al and P chemical potentials for $\Delta\mu_H = -0.6$ eV (left) and $\Delta\mu_H = -1$ eV (right). The thermodynamically allowed range of the chemical potentials according to equations 3.4 and 7.1 is indicated by the dashed lines. Adapted from Ref. [221].

element. The stability of $\text{Al}_{0.5}\text{In}_{0.5}\text{P}$ demands that the following relation holds

$$\mu_{\text{Al}} + \mu_{\text{In}} + 2\mu_{\text{P}} = \mu_{\text{AlInP}_2, \text{bulk}} = \mu_{\text{Al, bulk}} + \mu_{\text{In, bulk}} + 2\mu_{\text{P, bulk}} + \Delta H_f, \text{AlInP}_2, \quad (7.1)$$

similar for InP with equation 5.3. The above equation also reduces the degrees of freedom by one, allowing the P chemical potential to be a function of the Al and In chemical potentials. The thermostatically allowed range for the chemical potential is limited by equations 3.4 and 7.1. The surfaces are compared energetically for $\Delta\mu_H = -0.6$ eV (Fig. 7.2 (a)) and $\Delta\mu_H = -1$ eV (Fig. 7.2 (b)). It should be noted that for the phase diagrams shown in Fig. 7.2, each slab was modeled using an optically isotropic D4 ordering (see Fig. 7.1) and not CuPt-B as in Refs. [34, 163]. The ordering does not change the trends significantly and only affects slightly the stability borders between the considered geometries. This is not the case, however, for the so-called $(2\times 2)\text{-2InMD-2H}$ reconstruction (c. f. [34]) which is found to be only stable with a bulk CuPt-B ordering.

The identified energetically most favorable surfaces are shown in Fig. 7.3. The most prominent surfaces resembled those of the InP semiconductor, i. e., the $(2\times 2)\text{-2D-2H}$ for the P-rich and the $(2\times 4)\text{-rInMD}$ for the In-rich. The latter surface is a complete In-covered surface with a single In–P dimer on top. Other cation-rich surfaces are the $(2\times 4)\text{-InMD}$ and $(2\times 4)\text{-AlMD}$ for In- and Al-rich conditions, respectively. These two surfaces are distinguished by the In–P and Al–P top dimers, respectively. Although their name is borrowed from the InP $(2\times 4)\text{-MD}$ surface, they differ with respect to the second layer cation arrangement: the difference in the In and the Al covalent radii leads to staggered arrangement of the second layer cation dimers. For hydrogen-deficient conditions ($\Delta\mu_H = -1$ eV), the phase diagram is dominated by only P-dimer structures, similar to other III-V semiconductors [154, 220]. The $c(4\times 4)$ is stable for P-rich conditions, while the $\beta 2(2\times 4)$ for intermediate conditions. The perpendicular-oriented dimers of the prominent (4×4) and (2×4) surfaces agree with observations MOVPE-grown AlInP structures in a N_2 atmosphere [214]. For standard MOVPE growing conditions with a hydrogen atmosphere ($\Delta\mu_H = -0.6$ eV [34]) the $(2\times 2)\text{-2D-2H}$ is the most prominent surface. The cation-rich (2×4) mixed-dimer

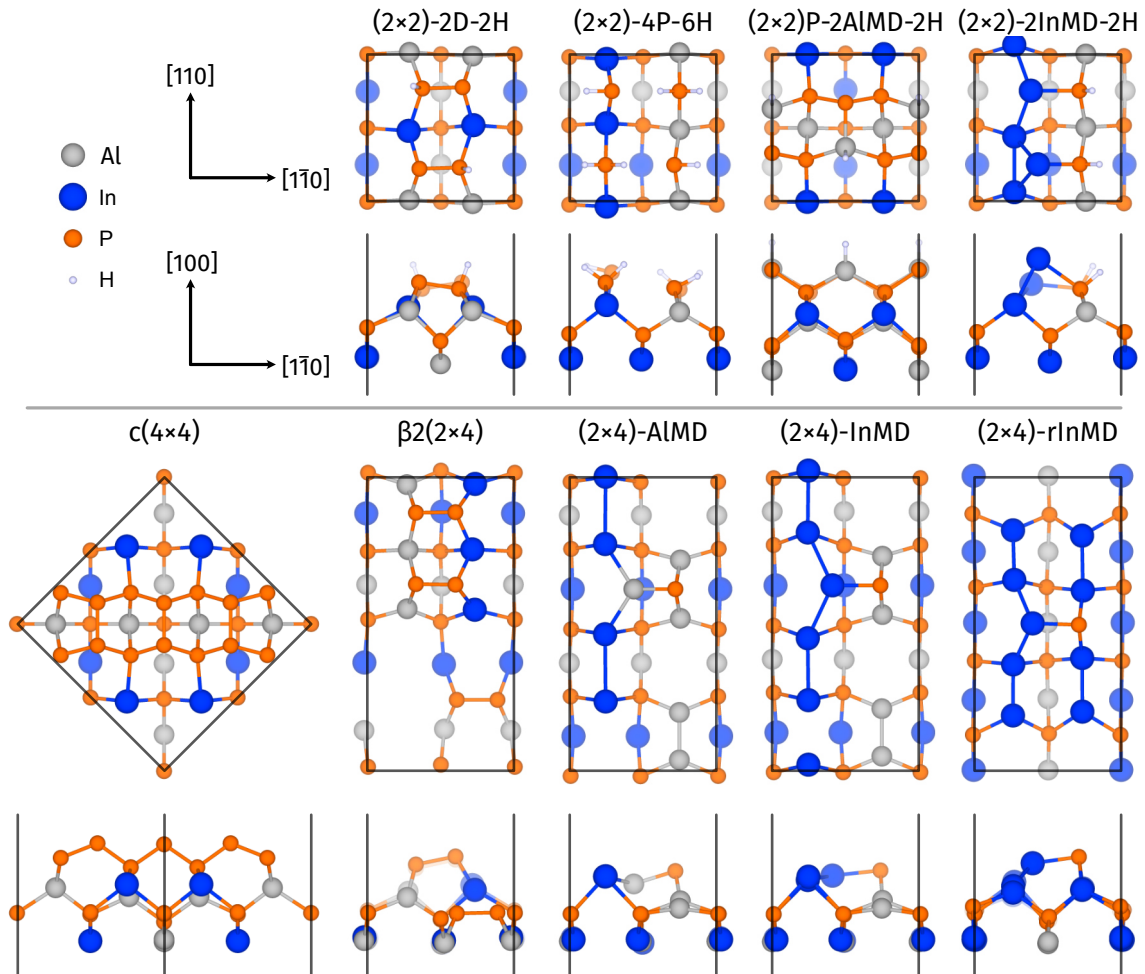


Figure 7.3: Top and side views of the energetically stable AlInP(001) surface geometries. Both hydrogen-adsorbed surfaces and hydrogen-deficient surfaces are included.

surface trio is present for a wide range of H chemical potential, for both H-deficient and standard conditions.

7.2 Surface oxidation

To properly study the AlInP for water-splitting purposes, it is first crucial to understand the material itself. Nonetheless, when exposed to an oxygen atmosphere or in contact with water, the material will corrode, changing its properties. Understanding the oxidation of AlInP surfaces is thus of great interest. This section follows the same procedure as section 5.2, where oxidation of the In-rich InP surface was explored. The main results have been previously published in Ref. [163].

Only the cation-rich $\text{Al}_{0.5}\text{In}_{0.5}\text{P}$ (001) surfaces with subsurface CuPt-B layer ordering were considered here for oxidation, i. e., the (2×4) -InMD and the (2×4) -AlMD surface reconstructions. As a starting point, the oxygen adsorption sites are identified through the calculation of the PES for a single adsorbed O atom. The energy differences are referenced with respect to the ground-state spin-triplet molecular oxygen. The PES for both surfaces are compiled in Fig. 7.4. The results

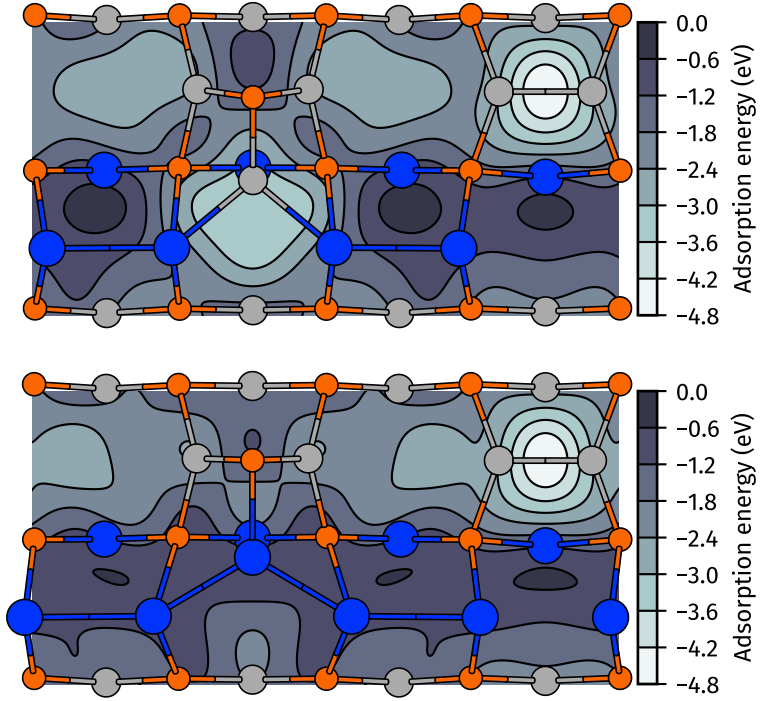


Figure 7.4: Calculated potential energy surfaces (PES) for single oxygen adsorption on the cation-rich AlInP(001) (2×4) surfaces. The data calculated for the AlMD and InMD is shown on the left and right, respectively. Adapted from Ref. [163].

illustrate a similar favorable adsorption site for both cation-rich surfaces: the second layer Al–Al bond but differ on the energetics of the top P-dimer, suggesting that O adsorbs preferably on Al over In atoms. It is also interesting to point out the qualitative differences between the oxidation of InP and AlInP surfaces (cf. Figs. 7.4 and 5.2): (i) For the ternary surfaces, the maximum adsorption energy is more than twice the value obtained for the binary system. This is in accordance with the higher heat of formation of aluminum oxides (-17.37 eV [222]) compared to that of indium oxides (-9.57 eV [223]). (ii) The top most III–V bond found for InP as an O adsorption site is out favored by the Al–Al second layer dimer, in the case of the ternary surfaces. This is in good agreement with previous experimental results, where it was found that oxidation of $\text{Al}_x\text{In}_{1-x}\text{P}$ occurs faster with higher Al contents [224].

Continuing from the most favorable adsorption site identified in Fig. 7.4, increased oxidation was explored, including the insertion into deeper layers. The sites that were probed for oxygen adsorption included: the second-layer Al–Al dimers, the trench next to the Al–Al dimers, the top cation-P-dimer and the Al–In bonds between the first and second layers, whereby the latter is only predicted for the AlMD surface. For substitution adsorption, all atoms in the top three layers were considered tentatively to be replaced by O atoms. The stability of the structures is compared energetically to the grand canonical potential 3.3 in Fig. 7.5. All the energetically favorable oxygen adsorption and substitution geometries identified here are compiled in the Appendix A Figs. A.2 and A.3. The most relevant structures are summarized in Fig. 7.6.

Similar to the binary case for InP, the stability of the AlInP surfaces increases with the amount of oxygen incorporated into the surfaces. The eight atom-adsorbed structures (the maximum amount considered here) lead to the most stable structures for a wide range of oxygen chemical

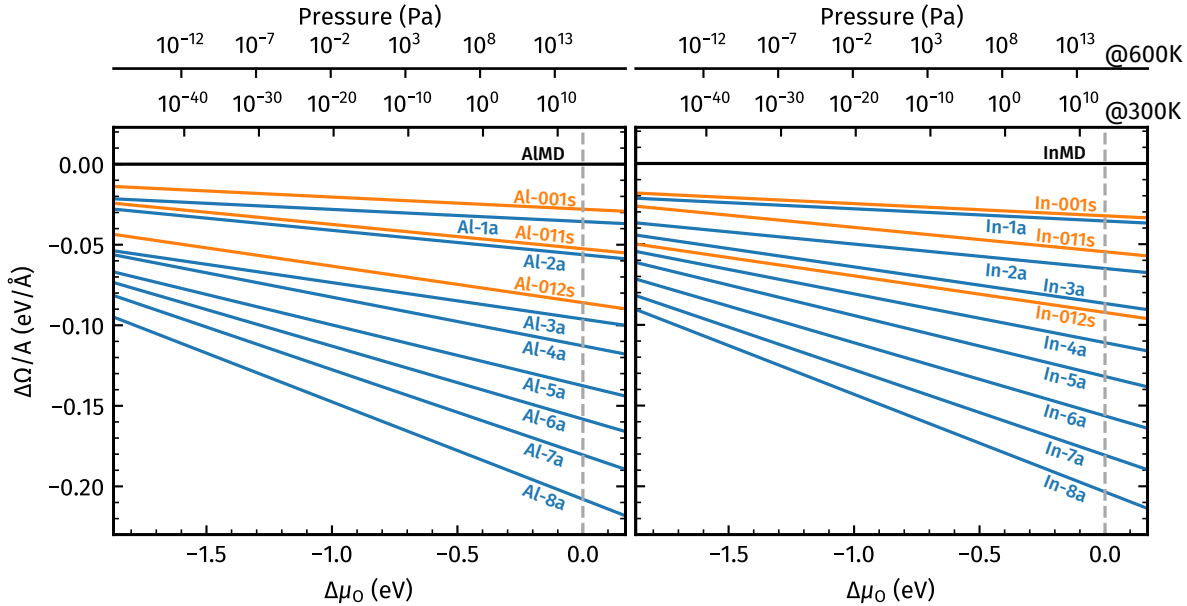


Figure 7.5: Surface grand canonical potential versus oxygen chemical potential of the O adsorption and substitutional geometries for the cation-rich AlInP(001) geometries. The cation chemical potentials are fixed for cation-rich conditions. The chemical potential of oxygen is related directly to the pressure p and temperature T from equation 3.6. The clean surface is used as the reference system. The data calculated for the AlMD and InMD is shown on the left and right, respectively. Blue and orange lines indicate adsorption and substitution, respectively. Adapted from Ref. [163].

potential for both the AlMD and the InMD. As is with the binary case InP, the AlInP oxidation process continues as long as there is oxygen available and is only kinetically hindered. Besides the similarities, there are also differences between the ternary and binary compounds for oxygen adsorption: In contrast to the most common bonds found previously for InP, Al-containing bonds, i. e., Al—O—Al, Al—O—P and Al—O—In are the most frequently observed for AlInP. In the second layer, Al—Al dimers are the preferred adsorption sites and first to oxidize, forming Al—O—Al bonds. In addition to these bonds, for the AlMD structure, three-fold coordinated oxygen is found: O coordinated to two Al and one P, as well as coordinated to two In and one Al. Substitutional oxidation is studied in more detail in Fig. 7.7. For initial stages of oxidation, similar to the binary case, in the ternary compounds, P replacement by O atoms is favored over other types of atoms. Unlike the InP structures, this trend continues for O-rich conditions and is favorable in a large range of Al and In chemical potentials. The P substitution leads to O bonding to group III atoms; the ternary surfaces show a preference of Al—O—Al bond formation over In—O—In bonds, which are favorable for the binary InP compound. Overall, standard adsorption and substitution are found to lead to a rapid loss of surface order. Oxygen adsorption follows a somewhat similar pattern for both ternary AlMD and InMD surfaces but differs greatly from the adsorption on the InP. The reason for this behavior is the second-layer Al—Al dimers being the most favorable adsorption sites for oxygen in the ternary case. A trench along the $\bar{1}11$ direction is formed as a result of bond breaking and bond rearrangement of the second layer, as oxygen is incorporated. This behavior is observed for both ternary surfaces.

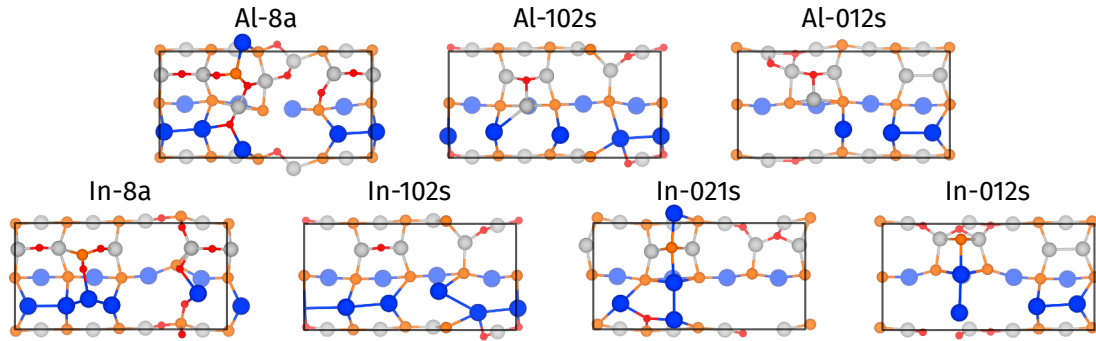


Figure 7.6: Energetically favorable O adsorption and substitution structures were calculated for the AlInP(2×4) surface. The number in the notation indicates the total number of O atoms adsorbed (a) or for substitution (s), the first, second and third digits of the number of Al, In and P replaced, respectively. The top row depicts the oxidized AlMD and the bottom row the InMD structures. The complete set of relevant structures considered in the present work is shown in the figures in Appendix A Figs. A.2 and A.3. Adapted from Ref. [163].

7.2.1 Electronic properties

In order to understand the influence oxygen has on the electronic properties of cation-rich Al-InP(001) surfaces, the DOS of the relevant surface structures at different levels of oxidation are calculated. The orbital resolved DOS are included in the Appendix B Figs. B.2 and B.3 for all the AlMD and InMD oxidized models included in this work. In Fig. 7.8 the electronic structure for the clean and 8a models (see Fig. 7.6) of the AlMD and InMD is shown, together with the electronic density of relevant states. Near the band gap the valence bands are dominated by In and P p states, this is similar to the binary InP. There are slightly stronger contributions from phosphorus near the valence band edge, in the case of the ternary systems. The conduction bands, near the band gap, differ from that of InP and are entirely described by In p states. It is worth mentioning that the region near the band gap is dominated by In and P states, and Al-derived states contribute very little to the valence and conduction edges. A particular Al DOS feature lies ~ 0.1 eV below the bulk valence edge, derived from the Al p state for the AlMD surface. On the InMD, the Al state is located ~ 0.25 eV below the bulk valence edge. This feature is related to the second row of Al-Al dimers, and it is labeled V2 in Fig. 7.8. The ternary surfaces AlMD and InMD are characterized by two dispersive surface states in the band gap, one occupied and one unoccupied, denominated V1 and C1 in Fig. 7.8 respectively. For the AlMD, the occupied state lies slightly above the bulk VBM characterized by In p states and marginally lesser contribution from In s and P p states. Band decomposed charge density reveals that this state is related to the top In-P and the second layer In-In and Al-In bonds. The unoccupied band lies on the bulk conduction edge and is related to the chains formed by the In and Al atoms in the second layer. The profile of the electronic structure remains more or less unchanged during the initial stages of oxidation. This is not surprising, as most of the strong features near the band gap are either In or P-related and are mostly unaffected upon the formation of Al-O bonds. The main identifiable feature of the AlMD, i. e., the V1 state above the VBM, disappears upon increased oxidation. At the same time, the C1 state near the conduction band edge is reduced, and an additional In s state emerges below the CBM. These changes are related to the rearrangement of the atoms in the second layer upon the formation of the trench. Furthermore, for high O coverages, phosphorus-related p states are pushed above the

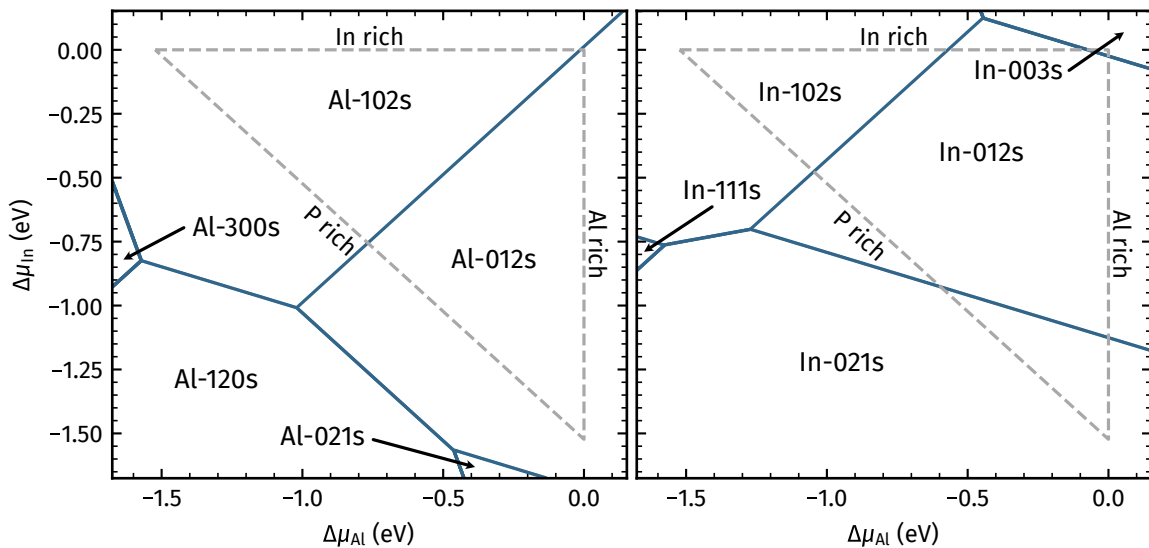


Figure 7.7: Phase diagram of the most energetically favored O substitution geometries of the cation-rich AlInP (001). The stability range of the In and Al chemical potential is given by the equations 7.1 and 3.4; assuming O-rich preparation conditions, $\Delta\mu_O = 0$ eV. The data calculated for the Al-P and In-P mixed-dimer structures are shown in the left and right, respectively. Adapted from Ref. [163].

VBM after increased oxidation related to O–P bonds on the top and third-layer P atoms.

The InMD presents a different electronic scheme, with the two surface states in the band gap shifted down in energy: The occupied state is located at the valence edge (V1) and the unoccupied state (C1) below the bulk conduction edge. From the band-decomposed charge density, the origin of the V1 state relates to the top In–P and the second-layer In–In bonds. The C1 state originates from the In–In chains of the second layer. Both states have similar origins to the AlMD structure. The InMD has its main identifiable feature, the unoccupied In p C1 state, pushed up into the conduction band soon after the initial stages of oxidation. Similar to its counterpart AlMD, this phenomenon is related to the reordering of the second layer and trench formation. When an In–O–P bond forms on the top dimer, the In p contribution to the conduction band is reduced. This suggests that most surface states near the conduction band edge are related to the top In–P dimer. Phosphorus-related p states are pushed below the CBM after increased oxidation; this coincides with the formation of In–O–P bonds on the top dimer.

For both AlMD and InMD geometries, initial stages of oxidation do not lead to passivation of surface states. Eventually, the surface states are modified after increased oxygen adsorption, but new states emerge in many instances in the band-gap region. This behavior is not so different from the one observed for the InP (2×4) surface. The new states may act as charge traps, affecting the carrier generation and recombination processes. As a result, this may worsen the electronic and optical properties.

7.3 Conclusions

DFT calculations show that the most stable geometries for AlInP(001) are similar to the InP, but also differ by the inclusion of new reconstructions. For H-rich and P-rich conditions, the most

7.3 Conclusions

stable surface reconstruction is the (2×2) -2D-2H, also present for InP under similar conditions. Similarly, the (2×4) -rInMD surface geometry is stable for In-rich for both ternary AlInP and binary InP systems (named (2×4) -MD). In addition, both $\beta 2(2\times 4)$ and C(4×4) surface geometries are found to be stable in the calculated phase diagram. Besides the similarities, other surface reconstructions are found for the ternary compound. This includes the cation-rich AlMD and InMD surfaces with cation heterodimers on the top-most layer and second-layer cation dimers that differ from the InP (2×4) -MD structure. The second layer is characterized by staggered Al–Al dimers for both structures. Other surfaces of interest are the hydrogen adsorbed (2×2) -2InMD-2H and the (2×2) -4P-6H, the latter only present for extreme H-rich conditions.

The ternary cation-rich surfaces also present different oxidation patterns to the binary system, with the Al–Al dimers playing an important role as adsorption sites. The oxidation is found to be more favorable than for the InP surfaces. This is related to the considerably larger heat of formation of aluminum oxide compounds compared to indium oxides. This explains experimental findings that suggest oxidation occurring faster with higher Al content for $Al_xIn_{1-x}P$. Oxidation leads to more frequent Al–O bonds than In–O bonds. Concerning substitutional oxidation, P atoms were found to be more likely to be replaced by O in comparison to Al or In atoms. This matches well with the energetic preferences of Al/In oxidation. Oxygen is found to passivate surface states inside the band gap resulting from the In–In wires of the second layer. However, increased oxidation introduces new states in the band gap region. These states are related to In–O and Al–O bonds and are expected to reduce the electronic efficiency by providing charge traps in the oxide layer. The high surface reactivity towards oxygen may result in detrimental effects on both electronic and optical surface and interface properties.

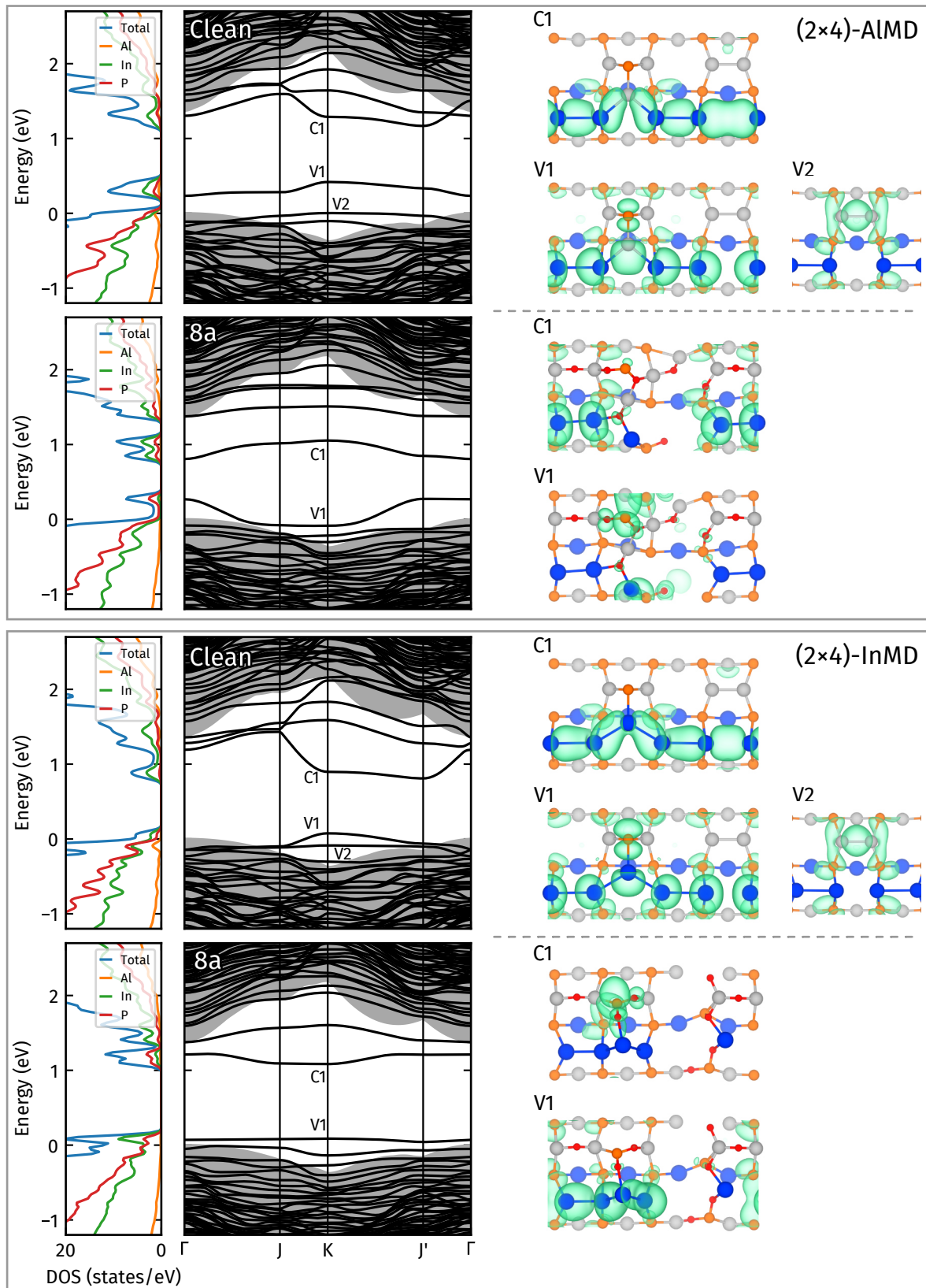


Figure 7.8: The electronic structure of the cation-rich (2×4) AlInP(001) surfaces: AlMD and InMD for the clean and oxidized 8a models. The shaded gray area is the projected band structure of the bulk. On the left, the contribution to the charge density of the most relevant states.

Chapter 8

Optical spectra for AlInP surfaces

Spectroscopy techniques are commonly used across diverse areas of science to characterize materials on an atomic or molecular scale. RAS, also known as reflectance difference spectroscopy, is a powerful technique to characterize surfaces at an atomic scale[225]. The technique relies on measuring the polarized-dependent reflectivity to explore the surface structural and electronic properties[35, 49, 226, 227]. The RAS surface high sensitivity profits from the low symmetry of the surface by taking the difference between two reflected light polarizations along the lattice vectors, ultimately producing a unique spectrum of the probed surface. In addition, RAS is a non-destructive, relatively fast method available in a large range of environments, thus allowing to probe the surface *in situ* using only polarized light. Indeed, RAS has been used extensively to monitor the growth process of III-V ternary surfaces and heterostructures[228–231]. In particular, Zorn et al.[232] explored the relationship between bulk ordering and growth temperature with the RAS technique for InGaP (001) surfaces. This was further corroborated by Krahmer et al.[40], proving that not only can RAS be used to probe surface stoichiometry and morphology, but also the bulk ordering.

Full understanding and interpretation of the RAS signal require numerical simulations as an aid. First principle calculations can be used to assign the origin of the anisotropies to specific transitions in the electronic structure. Several RAS calculations have already been performed for III-V binary systems[157, 233–236]. However, this is not enough to explain the spectra of the III-V ternary systems, where additional surface-induced bulk ordering may lead to additional anisotropies or modifications of the existing surface ones.

The present chapter aims for a better general understanding of the surface optical anisotropies of III-V ternary alloys. The particular interest lies within the RAS sensitivity towards surface structural motifs, but also the effects the near subsurface layers induce on the spectra. Specifically, the origin of RAS anisotropies of the ternary MOVPE-grown AlInP (001) surfaces. Measured data for epitaxially grown $\text{Al}_{0.52}\text{In}_{0.48}\text{P}$ (001) epilayers is directly compared to calculated spectra of the most energetically stable $\text{Al}_{0.5}\text{In}_{0.5}\text{P}$ (001) surface reconstructions. The results presented here were previously discussed in Refs. [221, 237]. The experimental contributions were performed by Mohammad Amin Zare Pour under the supervision of Thomas Hannappel.

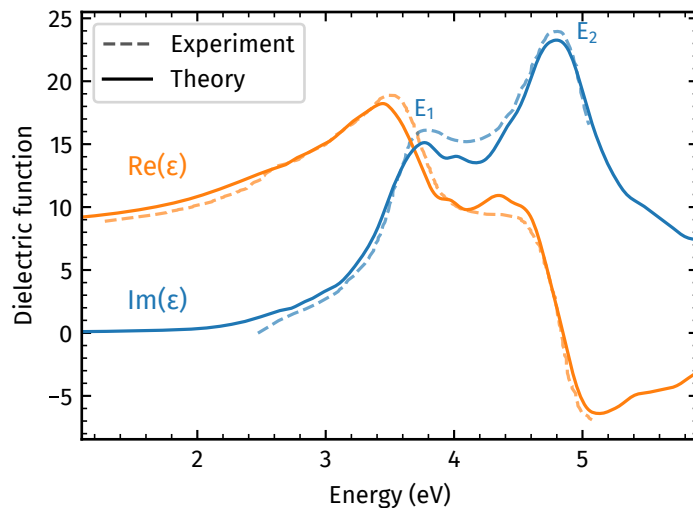


Figure 8.1: Imaginary part of the dielectric function of an AlInP bulk calculated within the model-BSE (mBSE) and a D4 order compared to experiment [241]. The bulk E_1 and E_2 critical point energies are marked. Adapted from Ref. [237].

8.1 Methodology

DFT calculations are known to underestimate the band gap due to an inaccurate treatment of the electronic self-energy, the so-called band gap problem. The calculated band gap within the GGA-DFT level of theory for the AlInP bulk of 1.26 eV with a D4 ordering (see Fig. 7.1) severely underestimates the experimental band gap of 2.31 eV, measured for an AlInP alloy with random ordering[212]. Using the partially self-consistent GW_0 calculations, as implemented in the VASP software[94, 95], the band gap is increased closer to the experimental value, i. e., to 2.25 eV. The remaining small deviations may be partially related to ordering effects: The AlInP band gap is expected to be highest for fully disordered crystals [213, 238, 239]. For a CuPt-ordered AlInP bulk (see Fig. 7.1) the calculated band gap is 1.35 and 2.33 eV, with DFT and GW_0 respectively. In addition to the self-energy effect, the optical spectra are dependent on local field and electron-hole attraction effects. They are included by solving the BSE [125, 156, 240]. Due to computational reasons, the BSE is solved using a model dielectric function, the mBSE[126, 128] method, which approximates the quasi-particle shifts with a scissors operator of 0.99 eV magnitude. The optical calculations require a dense \mathbf{k} -point mesh. In order to accelerate the calculations and reduce resources, the spectra are averaged over multiple calculations with different grids. The starting point is a $n_1 \times n_2 \times n_3$ grid with X_N irreducible \mathbf{k} points, K_N , and weights W_N . The calculations are performed on an $m_1 \times m_2 \times m_3$ grid shifted by K_N . In the end, a weighed average of the dielectric function is performed over the X_N calculations with the weights W_N . As a result, a $(N_1 \times M_1) \times (N_2 \times M_2) \times (N_3 \times M_3)$ is effectively constructed. It should be noted that in this method, interactions of range longer than m times the supercell are omitted. For the bulk, a $4 \times 4 \times 4$ grid is used for both n and m grids. An n grid of $4 \times 4 \times 1$ is used for surfaces, and an $8 \times 8 \times 1$ equivalent grid per (1×1) for the m grid. This methodology leads to an AlInP bulk dielectric function in very good agreement with the experiment, shown in Fig. 8.1. This methodology is utilized throughout this work unless otherwise stated.

The RAS is calculated from equation 4.63; to match experimental results, the xx and yy di-

rections are chosen to align to the $[\bar{1}10]$ and $[110]$, respectively. The supercell method necessarily yields not only the surface optical anisotropies, but also anisotropies originating from the hydrogen-passivated bottom layer. Fortunately, these contributions are small and occur for photon energies above 3.5 eV. To reduce these effects, the half-slab polarizabilities are averaged over two slabs with the bottom hydrogen bonds oriented along the $[\bar{1}10]$ and $[110]$ directions.

8.2 P-rich surfaces

Thin $\text{Al}_{0.52}\text{In}_{0.48}\text{P}$ layers were prepared in a MOVPE reactor with H_2 as a carrier gas by Zare Pour et al.[34, 237]. The whole MOVPE process was monitored *in situ* with RAS, which was setup in a such a way that through the entire procedure the complex variation in the reflection was along the $[\bar{1}10]$ and $[110]$ directions [226]. Afterwards additional RAS measurements were performed at room temperature. The samples were transferred to an ultra-high vacuum chamber where LEED and XPS measurements were performed. The results confirmed a P-rich surface along with substantial evidence for a (2×2) -2D-2H surface reconstruction. The full details on the sample preparations and measurements are found in Refs. [34, 237].

The RAS spectra measured for epitaxially grown $\text{Al}_{0.52}\text{In}_{0.48}\text{P}(001)$ P-rich epilayers at temperatures 600, 300 °C and room temperature are shown in Fig. 8.2. The spectra are characterized by a negative anisotropy between the photon energies 2.1 and 2.8 eV, peaked around 2.6 eV, and a broad positive feature with a maximum around 3.1 eV. There is a noticeable blue shift in photon energies, as well as the sharpening of the peaks, as the temperature is reduced, similar to the RAS measurements of P-rich InP surfaces[242]. The RAS was simulated for the most relevant P-rich surfaces for a wide range of the hydrogen chemical potential (cf. Fig. 7.2 and Ref. [34]), as shown in 8.2. To be precise, the surfaces used are the so-called (2×2) -2D-2H, (2×2) -4P-6H, and the $\beta 2(2\times 4)$. To concentrate only on anisotropies originating from surface stoichiometry, the slabs prepared in Fig. 8.2 present a D4 bulk ordering. The different spectra demonstrate the capabilities of RAS as a tool to discriminate between various stable surface geometries and how it may be used for growth monitoring.

8.2.1 2D-2H surface

Among the different surfaces considered, the (2×2) -2D-2H model presents the best agreement with the experiment. It is the one that best reproduces the negative feature at around 2.6 eV. This surface is also the dominant model for the growing conditions of $\Delta\mu_{\text{H}} = -0.6$ eV (see Fig. 7.2), coupled with XPS and LEED data [34], it can be concluded that the AlInP surface produced for MOVPE experimental conditions is that of the 2D-2H. It is distinguished by a complete layer of buckled phosphorus dimers. Half of the dangling bonds of each dimer are hydrogen saturated, and the rest are filled with lone pairs of electrons.

The negative RAS feature present for the AlInP(001) MOVPE-grown surface is reminiscent of previous observations of P-rich GaP (001) and InP (001) grown with gas-phase epitaxy [155, 156]. In order to investigate the origin of the valley, the RAS is calculated in the IPA level theory considering only the transitions between single pairs of surface states, i. e., the sum in equation 4.17 includes the state pairs of interest. The most prominent contribution to the negative feature arises from the transitions between V1 and C2, see Fig. 8.3. These states give rise to a high joint density of states. The V1 surface state corresponds to the P dangling bond and the C2 to

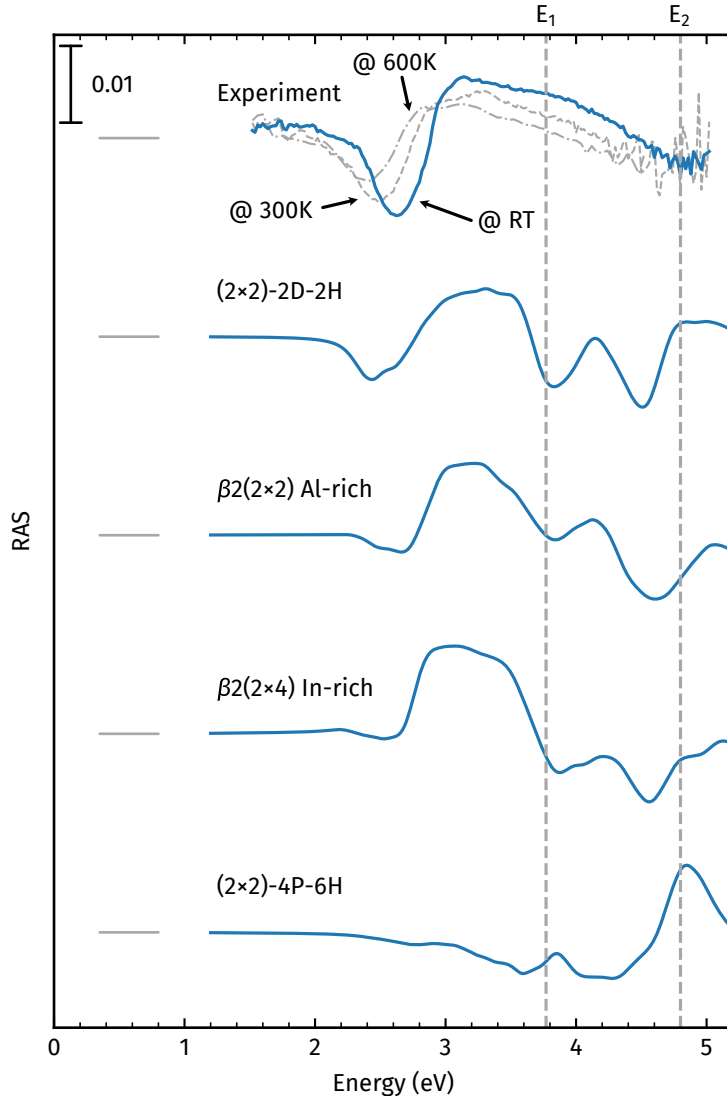


Figure 8.2: Comparison of RAS measurements for epitaxially grown $\text{Al}_{0.52}\text{In}_{0.48}\text{P}$ epilayers and calculated spectra for the P-rich surfaces. The bulk region of the slabs is simulated, presenting a D4 ordering. The bulk E_1 and E_2 transitions are marked by the dashed lines. Experimental spectra was measured by M. A. Zare Pour.

the P-dimer antibonding σ^* . Considerably smaller contributions are attributed to other transitions between surface states. Thus, the negative feature at 2.6 eV can be assigned to the transition between surface states related to the P-dimers on top of the surface.

The electronic structure can be highly sensitive to local atomic configurations, and the P-dimers can be arranged in different locations on the cation sublattice. In order to assess the influence the local configuration has on the RAS fingerprints, a total of three different 2D-2H structures were considered. They are prepared by shifting laterally or rotating the P monolayer on top of the optically isotropic bulk; see Fig. 8.4. The structures labeled D4-A and D4-B resemble the P-dimer on top of a CuPt-A ordered second layer and differ on whether the P-dimers are located directly above Al or In atoms in the fourth layer. The third structure, D4-C, is produced by rotating the anion monolayer of either D4-A or D4-B by 90°. The local ordering of the P-dimers of the resulting

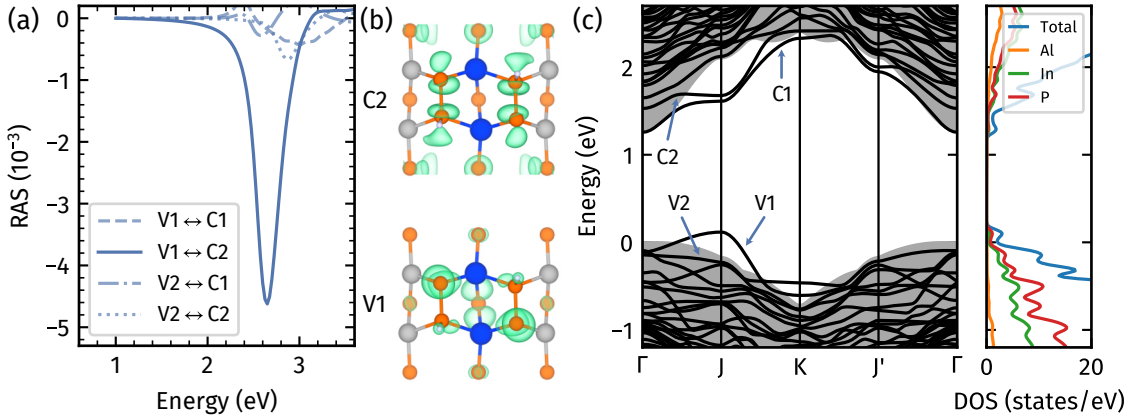


Figure 8.3: (a) RAS calculation for the transition between relevant pairs. (b) Orbital character of the prominent surface states V1 and C2. (c) Surface electronic structure of the AlInP (2×2)-2D-2H surface. The shaded gray area is the bulk-projected band structure. Adapted from Ref. [237].

surface resembles the 2D-2H with a CuPt-B bulk ordering. It is worth noting that the most energetically stable structure is the D4-B; this is the one used in Fig. 8.2 and Fig. 8.3. These results agree with previous observations on P-dimers forming above Al atoms due to strain minimization [34]; see also the discussion in Ref. [218, 243]. P-dimers could still, however, form in different local environments in real experimental conditions due to several external factors.

The calculated RAS for the three D4 models resemble each other and the experimental spectra, in particular the negative feature at 2.6 eV; see Fig. 8.4. This further strengthens the result discussed above that this feature is related to local intra-dimer electronic transitions. Notably, the 2.6 eV peak is best described by the D4-B structure, which is also the energetically favored D4 model. All three D4 models present negative features near the bulk critical point energies E_1 and E_2 . Due to the fact that the lateral lattice bulk parameter has been used for the surface calculations, the features around the bulk critical points cannot arise from surface-induced strain alone. Thus, they must be related to transitions of the surface-modified bulk wavefunctions. These valleys differ in the magnitude and position between the three models, and could partially cancel out in the total signal. This could explain the absence of pronounced RAS features at the bulk critical points in the experimentally measured spectra.

8.2.2 Other P-rich surfaces

While the 2D-2H surface reconstruction is the energetically most favorable P-rich surface for a wide range of preparation conditions, there are other possible AlIn(001) surfaces that are stable for a small subset of growing conditions (c. f., Fig. 7.2 and Refs. [34, 163]). The (2×2)-4P-6H surface is stable for extreme H-rich conditions, characterized by six hydrogen bonded to the top most P atoms in the surface unit cell; see Fig. 7.3. Notably, the surface P atoms do not bond together to form dimers; that is because the H atoms passivate all P dangling bonds. As a result, the AlInP band-gap region is deprived of any surface states. Accordingly, the calculated RAS presents no significant features for the low photon energy region; see Fig. 8.2. For higher energies, the RAS presents optical anisotropies at around 3.8 and 4.8 eV that coincide with the AlInP bulk critical points. This phenomenon has been previously observed for hydrogen-terminated Si (111):H surfaces[244], making these peaks related to transitions of surface-modified bulk states.

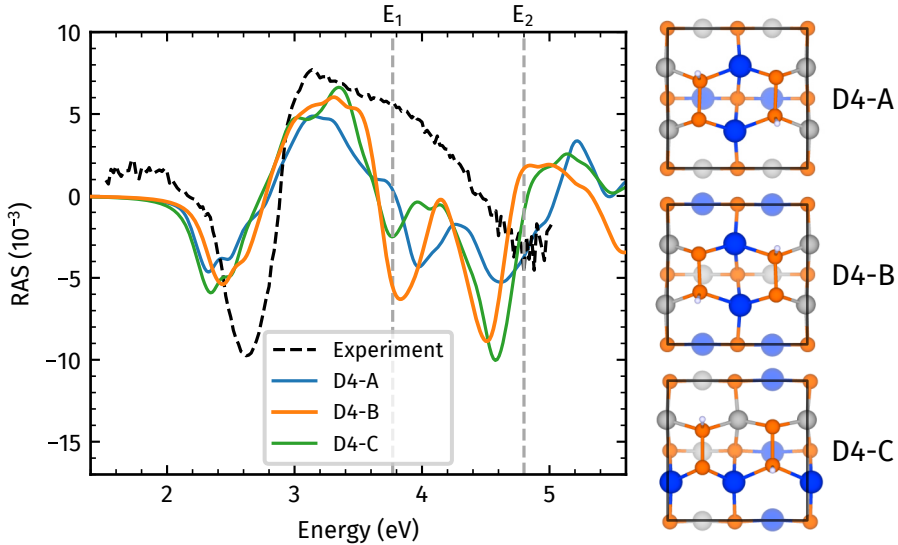


Figure 8.4: Comparison of RAS calculated for the AlInP (001) (2x2)-2D-2H surface with different local ordering for the interface between the surface and the optically isotropic bulk. Adapted from Ref. [237].

Another interesting surface reconstruction present for the AlInP(001) is the $\beta 2(2\times 4)$, also common surface for other III-V semiconductors, especially the ones where hydrogen is not present, such is the case for the GaAs(001) [154]. The $\beta 2(2\times 4)$ surface reconstruction is stable for poor H conditions for the AlInP(001) (see Fig. 7.2) and presents two realizations, depending on the cation chemical potential. These two surfaces differentiate themselves by the second layer cation composition. Both are characterized by surface states close to the bulk VBM that originate from the π^* antibonding combinations of p_z orbitals localized at the P-dimers. An unoccupied state located near the bulk CBM arises from the sp^3 dangling bonds of the three-fold coordinated cation atoms of the second layer[34]. The anisotropies of the RAS are related to the transitions between the P-dimer surface occupied state and resonant unoccupied surface states, as well as between occupied resonant surface states and the unoccupied second-layer cation dangling bond states.

8.2.3 Effect of bulk ordering

So far, the RAS calculations have been performed for surface layers on top of an optically isotropic AlInP bulk with D4 ordering. The results show that the main RAS anisotropies arise exclusively from surface states and can be used to characterize individual surface reconstructions and monitor growth processes. There are, however, indications that AlInP(001) epitaxial growth induces spontaneous CuPt-type ordering, linked to the presence of P-dimers [214]. This opens up the questions of how pronounced the effect that CuPt-type ordering has on the RAS characteristic signatures is, and if the RAS can be used to identify the AlInP(001) subsurface layer cation ordering. In order to answer this question, the RAS calculations were performed for the (2x2)-2D-2H surface on top CuPt-A and CuPt-B type ordered AlInP(001) subsurface layers. The results are presented in Fig. 8.5. The fingerprint of the 2D-2H RAS signal, i. e., the negative peak at 2.6 eV, is present for both CuPt ordering types, thereby reinforcing that the anisotropy is surface in nature but is affected by the ordering of the subsurface layer. Strong changes occur in the RAS calculation at the AlInP bulk critical energies, E_1 and E_2 . The anisotropy sign changes from negative to

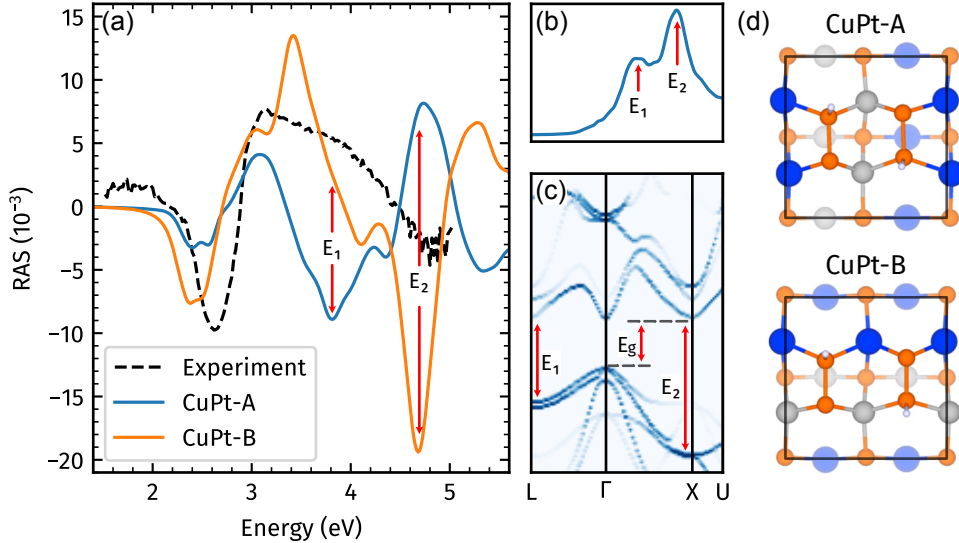


Figure 8.5: (a) Measured RAS data and calculations for the AlInP (2×2)-2D-2H surface reconstruction on top of CuPt-A and CuPt-B ordered subsurface layers. (b) Imaginary part of the dielectric function calculated for the CuPt-type ordered AlInP bulk with the bulk critical point energies indicated. (c) Calculated band structure for the AlInP CuPt-type ordered bulk, unfolded, performed using the BandUP software[246, 247]. (d) The geometric structures for AlInP (2×2)-2D-2H surface reconstruction on top of CuPt-A and CuPt-B. The bulk critical point energies E_1 and E_2 indicated are associated with interband transitions at L and X , respectively[248]. Adapted from Ref. [237].

positive and from positive to negative for the peaks at E_1 and E_2 , respectively, from the CuPt-A to the CuPt-B subsurface layer ordering. The changes in the RAS signal are equivalent to rotating the subsurface layers by 90° while maintaining the P-dimer orientation; this is because RAS measures anisotropies between perpendicular polarizations. This comes as no surprise, given that the difference in both CuPt-A and CuPt-B ordering is a rotation by 90° along the (001) axis.

RAS measurements at high photon energies, in particular at E_2 could help in determining the degree of order of subsurface AlInP(001) layers. The provided experimental RAS measurements allowed data up to 5 eV; however, this was not sufficient to give a conclusive statement on the subsurface ordering. In any case, the main experimental features are somewhat best described by the AlInP 2D-2H surface reconstruction on top of a CuPt-B ordered crystal rather than a CuPt-A ordered one, even if the sharpness of the peaks above 3 eV is not reproduced. This would be in accordance with evidence that [110] aligned P-dimers induce a CuPt-B subsurface ordering. The implications of breaking the cubic symmetry on the electronic structure have been previously reported for MOVPE-grown GaInP[245]. The temperature dependence of the GaInP surface signal has been linked to increased bulk ordering as the temperature is reduced[228]. This relation could also be the case for the AlInP surfaces: Comparing the (2×2)-2D-2H AlInP surface on top of a D4 and CuPt-B ordered bulk, an enhancement of the main features at 2.6 and 3.4 eV can be observed for the surface with the ordered crystal.

8.3 In-rich AlInP(001)

During the epilayer post-growth process of the AlInP(001) by Zare Pour et al.[221], as the temperature was gradually increased, a sudden red shift was observed at temperatures between 410 and 540 °C. Normally, when a surface reconstruction remains stable for a wide range of temperatures, the RAS peaks tend to diminish in intensity [237, 242]. However, this is not the case for the AlInP (001); quite the contrary, the peaks are intensified when increasing the temperature from 340 to 440 °C. Which would suggest a change in surface reconstruction. Previously, it was reported that for some III-V binary semiconductors, a change from anion-rich to cation-rich surfaces occurs as the temperature is increased and the group V elements desorb from the surface [231, 249]. A new cation-rich surface reconstruction, as a result of P-desorption, could explain the changes observed in the RAS measurement. The energy enthalpy for InP (-92.1 kJ/mol) is higher than for AlP (-166.6 kJ/mol); therefore, Al–P bonds are thermodynamically more stable over In–P [250]. In–P bonds would most likely break first as the temperature increases, suggesting an In-rich rather than an Al-rich terminated surface. After the growth process, this In-rich surface was annealed at a temperature of 440 °C and subsequently UPS, XPS, and LEED measurements were performed. Here, a (2×4) reconstruction is found that contains In–In bonds, but no evidence for Al–Al bonds was observed, reaffirming the previous conclusion of an In-rich surface rather than Al-rich. Neither cation-rich AlMD nor InMD surface models meet the experimental findings, as both reconstructions possess an Al–Al bond on the second layer, which cannot be accounted for from experimental measurements.

The experimental RAS data for the In-rich surface at room temperature is presented in Fig. 8.6. The spectra are characterized by a negative peak at 1.9 eV and a positive peak at 2.9 eV, noticeably red-shifted from the P-rich spectra. The RAS was calculated for the most relevant In-rich surfaces identified previously (cf. Fig. 7.2 and Ref. [34]) and shown in Fig. 8.6. The new (2×4)-rInMD model (see Fig. 7.3) is proposed as a way to both explain the RAS data and fit to XPS and UPS measurements where no Al–Al bonds are found. It is clear that the best agreement with the RAS experimental data is achieved for the rInMD model, since it both describes the negative feature at 1.9 eV and the positive peak at 2.9 eV.

8.3.1 The rInMD surface model

The AlInP(001) (2×4)-rInMD surface is stable for a wide range of growing conditions, and it occupies the upper part of the AlInP phase diagram (see Fig. 7.2 (a)). Not only is the surface energetically favorable for H-poor conditions but also for standard MOVPE growing conditions ($\Delta\mu_H = -0.6$), while lacking any hydrogen adsorbed at the surface. The rInMD is distinguished from the other cation-rich surfaces by the full In coverage of the second layer. There is a top In–P dimer on top of the surface, followed by In–In dimers in the second layer. The lack of Al–Al dimers further distinguishes it from the AlInP(001) In-rich InMD surface identified previously[163]. Even more, none of the In–In dimers are staggered, and the surface resembles that of the binary InP (001) (2×4)-MD surface reconstruction. XPS measurements confirm the presence of In–In and In–P bonds at the surface, while also lacking any evidence for Al–Al bonds[221].

The electronic structure of the rInMD surface model is characterized by a surface state slightly above the VBM (see Fig. 8.7), reminiscent of the $\beta 2$ model [34]. This low dispersive band originates from the In–In σ -bonds of the second layer (see ifg. 8.7 (b)), not unlike the InP (2×4)MD [152]. There are several unoccupied surface states near the conduction band edge; one of these

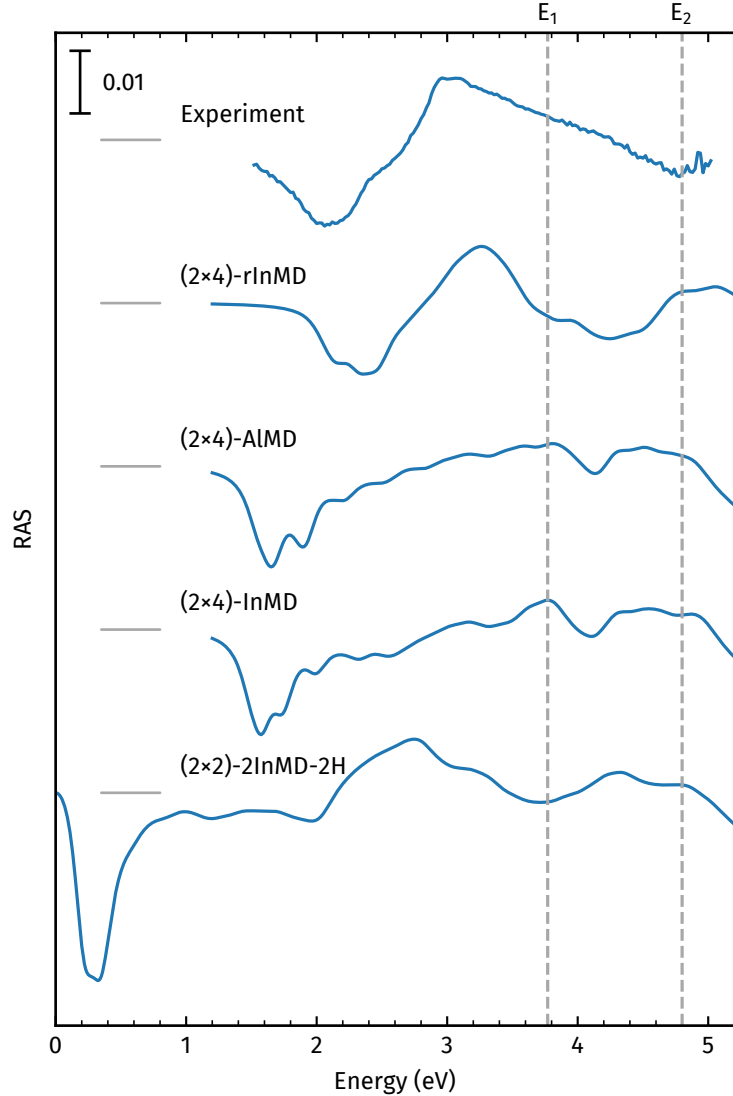


Figure 8.6: Comparison of RAS measurement for epitaxially grown $\text{Al}_{0.48}\text{In}_{0.52}\text{P}$ at room temperature and calculated spectra for the In-rich surfaces. The bulk region of the slabs is simulated, presenting a D4 ordering. Experimental spectra was measured by M. A. Zare Pour. Adapted from Refs. [221, 237].

lies slightly below the bulk CBM. Both occupied and unoccupied surface states are characterized by In p states originating on the In–In dimers of the second layer, as well as the In atom from the top dimer.

In Fig. 8.7 (a), the optical DFT calculations in the IPA level of theory for individual transitions show the origin of the main negative feature of the RAS below 2.5 eV (see Fig. 8.6). The main contribution to the peak is the $\text{V}1 \leftrightarrow \text{C}2$ transition between surface states, with lesser contributions from $\text{V}1 \leftrightarrow \text{C}3$, $\text{V}1 \leftrightarrow \text{C}1$ and $\text{V}3 \leftrightarrow \text{C}1$. The unoccupied $\text{C}2$ is mainly related to the dangling bonds of the three-fold coordinated In atoms of the second layer (see Fig. 8.7 (b)). In other words, the distinguishing negative feature of the RAS measurements originates from transitions of the In–In dimers of the second row, with the main contributions from the transitions of the σ -bond occupied states to the dangling In bonds. This feature shares a similar origin to the negative feature

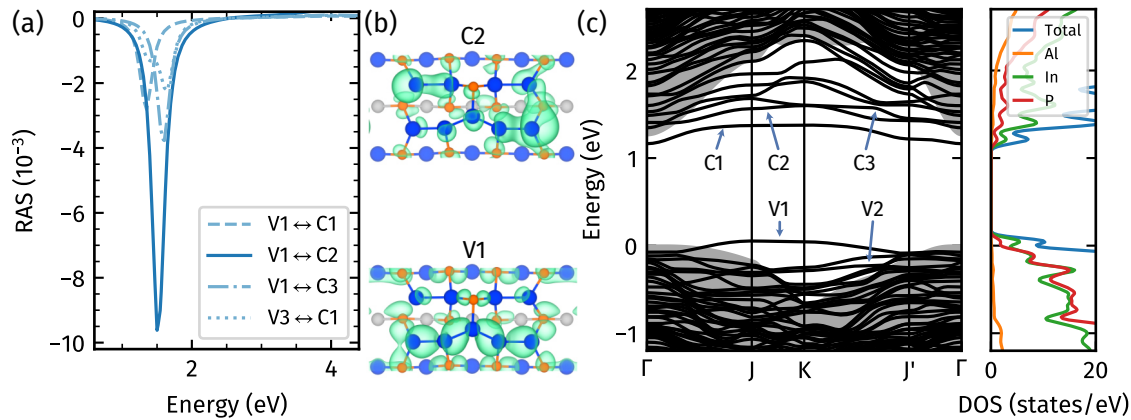


Figure 8.7: (a) RAS calculation for the prominent electronic transitions. (b) Orbital character of the V1 and C2 states. (c) Band structure of In-rich (2×4) -rInMD AlInP. The shaded gray area is the projected bulk band structure. The right panel shows the orbital resolved density of states. Adapted from Ref. [221].

of its binary InP (2×4) -MD surface counterpart [157]. This is not surprising considering the top two layers share the same chemical composition and atomic position, in addition to RAS being a surface probe technique. At higher energies, there are two local maxima located close to the bulk critical point energies, E_1 and E_2 , most likely related to transitions involving surface-modified bulk wavefunctions.

8.3.2 Other cation-rich surfaces

Both the AlMD and InMD surfaces present a strong RAS anisotropy at low photon energies around 1.6 eV, as shown in Fig. 8.6. At higher photon energies, the surfaces present only weak features, unlike other surface reconstructions studied so far. Both surfaces share a similar RAS profile; this is due to the surfaces sharing similar reconstructions, differing slightly in the second layer arrangement and in the compositions of the top dimer. The InMD RAS signal is very slightly red-shifted to lower photon energies and is most likely related to the difference in the band energies, with AlMD being slightly higher than InMD, as shown in Fig. 8.8. The subsurface layer D4 ordering preserves somewhat the shape of the electronic structure to the CuPt-B ordered (c. f. Figs. 7.8 and 8.8). The negative peak major contributions for both of the surfaces are the transition between the characteristic occupied (V1) and unoccupied (C1) surface states, discussed in the previous chapter. In other words, the transitions occur between occupied states located in the second layer In atoms and top dimer to σ -states of the In–In chains. Interesting to note is that there are little to no contributions from the Al–Al bonds of the second row, i. e., the V2 state.

The last surface of interest is the (2×2) -2InMD-2H present in the range of H-rich and In-rich conditions. It consists of In atomic chains that form along the $[110]$ directions. These atomic chains give rise to an occupied state and an unoccupied state inside the band gap (see Fig. 8.9). The states are highly dispersive in the direction of the In chains and nearly no dispersion in the perpendicular direction to the chains. At the DFT-level of theory, the bands are separated by only a small energy difference, around 0.1 eV, in the $J' - K$ direction of the surface Brillouin zone. The bands pin the Fermi energy level at the mid-gap position. Due to the small gap and the highly dispersive states, the scissors operator method is not used for the RAS calculation in Fig. 8.6;

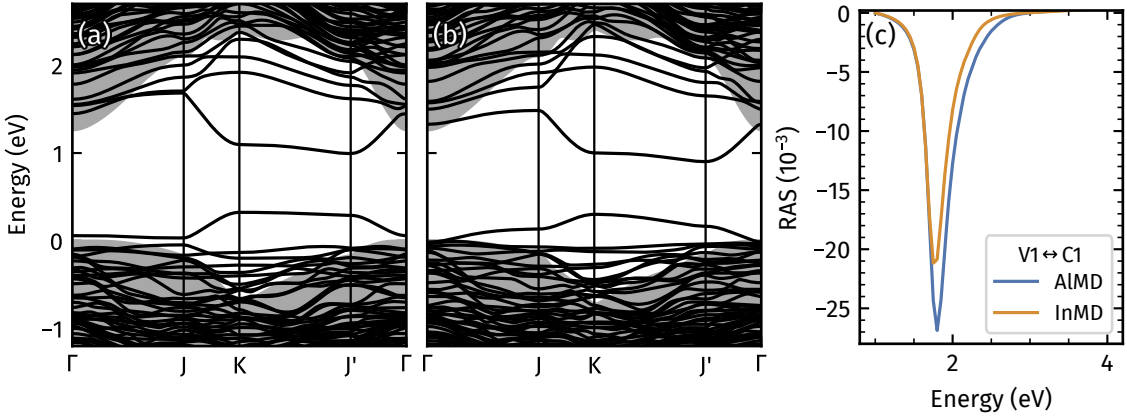


Figure 8.8: Electronic structure for the cation-rich AlInP(001) (a) AlMD and (b)InMD surfaces. The shaded gray area is the projected band structure of the bulk. (c) RAS calculation for the transitions between $V1 \leftrightarrow C1$.

instead, the RAS is calculated in the IPA-level theory. It is found that the transitions between the two mid-gap states give rise to an extremely strong anisotropy for low photon energies. Similar findings are reported for other surface atomic wire systems[251].

Band alignment extracted from XPS and UPS measurements revealed that for both P-rich and In-rich AlInP(001) surfaces, the Fermi level is pinned in the mid-gap [221]. While for the P-rich the Fermi-level pinning can be attributed to H-vacancies on the 2D-2H similar to the P-rich InP[196, 197], the same cannot be said for the In-rich surface as there is no hydrogen present. Instead, for the In-rich surface, the Fermi-level pinning is most likely due to the presence of 2InMD-2H surface reconstructions at small clusters. The calculation of the surface charge density (equation 6.1), with a determined band bending of 1.8 eV from XPS and UPS measurements, a donor concentration $N_D = 2 \cdot 10^{18} \text{ cm}^{-3}$ and a relative permittivity for AlInP $\epsilon_r = 11.25$ [252] results in a number of defects $1.34 \cdot 10^{13} \text{ cm}^{-2}$ or a proportion of 2.1% surface atoms involved in the band bending[221]. This would suggest that the samples present the energetically favorable (2×4) -rInMD as the dominant reconstruction, with around 2.1% in a (2×2) -2MDInMD-2H reconstruction. This would explain the Fermi-level pinning at the mid-gap, but also the lack of the 2MDInMD-2H signal in the RAS measurements.

8.4 Conclusions

Measured RAS data for MOVPE grown samples annealed at different temperatures are compared with numerical simulations of several energetically favorable surface terminations and different subsurface layer ordering. The results show that different surface structure motifs give rise to clearly distinguishable fingerprints in the RAS traced back to specific electronic transitions. The fingerprints below 3 eV depend very little on the local atomic order of the surroundings of the respective structural motifs. The measured RAS data can be associated with a specific surface reconstruction, in particular P-rich MOVPE grown samples are terminated by a monolayer of dimerized P atoms, half of which are passivated by hydrogen atoms. Increased temperature leads to P desorption and an In-rich surface characterized by a single top In-P dimer and a fully In-covered second layer. The RAS fingerprints for the P-rich and In-rich originate from transitions of the spe-

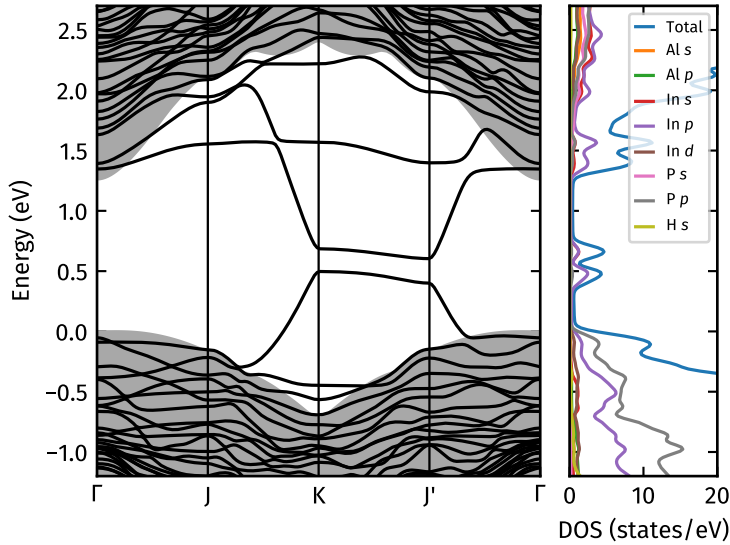


Figure 8.9: Band structure of the (2×2) -2MDInMD-2H AlInP(001) surface reconstruction. The shaded gray area is the projected band structure of the bulk; the right panel shows the orbital resolved DOS. Adapted from Ref. [221].

specific motifs: the first layer P–P and second layer In–In bonds, respectively. The fingerprints allow for the different surfaces to be identified by looking only at the RAS measurements. This in turn allows to control the growth of either P-rich or In-rich surfaces in real time, by performing *in situ* RAS measurements.

At high photon energies, the optical anisotropies are strongly modified by the cation subsurface layer ordering. In particular, strong anisotropies rise on the AlInP bulk critical point energies E_1 and E_2 . The RAS measurements could be used, in principle, to identify the degree of the CuPt ordering of the material subsurface layers by focusing on the anisotropies at the E_2 energies.

Chapter 9

Summary & Conclusion

The oxidation of semiconductor interfaces were studied for two materials, i. e., InP and AlInP, in the DFT framework. The study was limited to the semiconductors with cation-rich surfaces. The dominant reconstruction for the In-rich surface is the (2×4)-MD, which has been known for some time and well documented[146–153]. The most relevant adsorption sites for oxygen on the (2×4)-MD were determined from DFT calculations; this served as a basis for investigating increased oxidation. Oxygen adsorption leads to the formation of In–O–P and less frequently to In–O–In bonds. This matches with experimental and theoretical studies done for oxidation on InP[47] and also for water dissociative adsorption [49, 50]. Additionally, oxygen substitution was also investigated for the MD surface. In this case, O atoms are more likely to replace P atoms over In atoms, leading to more common In–O bonds. Less frequently P–O–P bonds were also identified. Substitution oxidation is distinguished from regular O adsorption by the more rapid loss of the surface order. This is important, as understanding how oxide layers form at the semiconductor's surface can help in fighting the corrosion that photoelectrochemical devices suffer from, when submerged in an electrolyte. Nevertheless, the corrosion on these devices can inadvertently lead to reduced efficiencies. This can be seen from the mid-gap states introduced from the increased oxygen adsorption. The oxidation is not completely detrimental, as it is also observed to passivate surface states.

For the ternary material AlInP, the investigated cation-rich surfaces were the (2×4)-AlMD and (2×4)-InMD, both calculated with a CuPt-B subsurface layer ordering. These surface models present some similarities to the InP (2×4)-MD reconstruction: (i) O atoms favor bonding to group-III atoms over P atoms. (ii) Substitutional oxidation similar to binary systems also leads to a rapid loss of symmetry with O more likely replacing P atoms. Surprisingly, Al–O bonds are more energetically favorable than In–O. The result is in part due to the considerably larger heat of oxidation of Al compared to In. For this reason, the second layer Al–Al dimers are the most favorable adsorption site; which can be translated to experimental findings where oxidation occurred faster with higher contents of Al[224]. The O adsorption also leads to states inside the band gap that can be detrimental to the electronic properties. However, these states are not related to Al, which could suggest that an Al oxide layer would lead to more stable surfaces.

Water-splitting mechanism was investigated for the most common InP surfaces reconstructions. In the case of In-rich surfaces, as a first step, it was found that water dissociates, forming

In–O–In bonds in the second layer and P–H on the top dimer. This agrees with previous experimental findings; however, it was also found that the process is hindered by energy barriers of 0.87 eV. Further inclusions of water overlayers lower this energy barrier. Regarding the morphology of the water overlayer, it resembles that of ice I_h but is heavily influenced by the surface morphology. More precisely the water overlayer is anchored to the surface through a series of In–O bonds between surface and water molecules. Water dissociation also leads to surface-adsorbed hydroxyl groups acting as anchor points for the water overlayer.

The chemical reaction of the full water-splitting mechanism is divided into the OER and the HER. From the possible OER pathways, the associative reaction mechanism turns out to be the energetically favorable one for the In-rich surface. Notably, the overpotentials for the OER and HER are calculated to be under 1.7 and 0.3 eV, respectively. These overpotentials are slightly increased when considering the reactions under a full water layer. Furthermore, this is in line with other catalysts like TiO_2 and RuO_2 . Undoubtedly, illumination of the surface with direct light would provide the necessary overpotential for both OER and HER to occur spontaneously without an additional bias potential. As such, the capabilities of InP for photoelectrochemical water-splitting and why it has received so much interest is evident. However, band alignment calculations of the (2×4)-MD surface position the OER below the valence edge; the HER, fortuitously, still lies above the conduction edge. The inclusion of water interface and hybrid calculations, further corroborate the relative positions of the valence and conduction bands in respect to the redox potentials. It is clear then that the In-rich surface is best suited for hydrogen evolution rather than oxygen evolution. Tandem solar devices would amend these issues, as other semiconductors better suited for oxygen evolution can be stacked together with InP. Ultimately, it is essential to understand the water/surface interface in order to increase the efficiencies of the devices.

On the P-rich (2×2)-2d-2H InP surface, it is found that water dissociation is not favorable compared to molecular water adsorption. This is in contrast to the In-rich surface, mainly due to the P-dimer atoms being passivated by preexisting H atoms on the surface. This agrees with experimental findings, where only small traces of OH were observed. Nevertheless, dissociative adsorption would seem plausible only when surface defects are considered. Further, hydrogen defect concentrations are calculated for the P-rich surface from DFT. In addition, the experimentally observed Fermi-level pinning is found to be explained by the most probable defect, the H vacancy. The calculated concentration numbers for the H vacancy are in the order of magnitude to common doping levels. Furthermore, they are in agreement with calculated numbers from experimentally-obtained quantities. Further theoretical calculations revealed that a positively charged defect for *p*-doped samples pins the Fermi energy in the lower half of the band gap. On the whole, the origin of the band bending is evidently caused by surface H vacancy dangling bond surface states. Furthermore, the H-deficient P dangling bonds serve as adsorption sites for OH groups, suggesting dissociative adsorption on surfaces with defects. Additionally, the adsorbed OH group removes the surface-defect state inside the band gap. However, dissociative adsorption enabled by defects is still unlikely because experimental measurements after water exposure find evidence of the defect-induced band bending. Surface defects are usually omitted when performing DFT calculations due to the difficulty in handling the calculations. However, as demonstrated, they can have strong effects on the electronic properties. Therefore, understanding not only the surface morphology but also the defects and their interaction with the liquid will lead to better fabrication of photoelectrodes. It is clear that both P-rich and In-rich surfaces show a completely different interaction with water and not only the choice of material is important but also how it is fabricated.

Finally, optical properties for AlInP surfaces were calculated, relating surface motifs to signatures of the spectra. The previously calculated surface geometries for the AlInP show that the P-rich (2×2)-2D-2H surface is dominant for a wide range of growing conditions. Likewise, the surface was also experimentally observed from XPS, UPS and LEED measurements[34]. Nevertheless, RAS calculations were performed in order to confirm these results. Indeed, the calculated spectra for this surface replicate the negative peak at around 2.6 eV from RAS measurements, giving more credence to the presence of this surface reconstruction during growth. Additionally, the origin of the peak could be attributed to the transitions between surface states related to the P-dimers. Moreover, changing the ordering of the subsurface layer leads to changes in the intensity of the peak at 2.6 eV, but its presence remains constant among all surfaces probed. As such, this peak serves as the fingerprint for the surface and can be used to identify it. Above 3 eV the spectrum is mainly attributed to surface modified bulk states. Here, the calculations are rather sensitive to the type of subsurface ordering; this is more clear when comparing the spectra of the 2D-2H between subsurface CuPt- and D4-type orderings. The sensitivity is also observed when local changes to the interface are performed between the surface and the D4-type ordered subsurface. Bulk related states are more evident on the extremely H-rich (2×2)-4P-6H surface. Here, the surface states are passivated by H and only surface-modified bulk states are present in the calculated spectrum. The origin of the surface-modified bulk states can be assigned to the bulk critical point energies E_1 and E_2 , associated with interband transitions at points L and X , respectively. Consequently, the spectra above 3 eV, in principle, could be used to measure the subsurface layer ordering of the ternary surface.

Experimental measurements under different conditions suggested a surface with a (2×4) reconstruction in contrast to the (2×2) reconstruction typical of the 2D-2H. However, both cation-rich surfaces (2×4)-AlMD and (2×4)-InMD could not reproduce the measured spectra. In addition, XPS and UPS data suggested an Al-deficient surface. As a result, experimental measurements were at odds with surface reconstructions identified previously. Additionally, both AlMD and InMD surfaces present Al dimers in the second row, which are responsible for the RAS features below 2 eV that do not match experimental data. All this led to the discovery of the In-rich (2×4)-rInMD surface. Indeed, the calculated spectrum for this surface was in agreement with experimental RAS measurements. Furthermore, the fingerprint for this new surface was assigned to the negative peak at around 2.1 eV. This peak was associated with the transition of In–In related states.

The In-rich (2×2)-2InMD-2H surface reconstruction, has two highly dispersive mid-gap states that produce a strong anisotropic feature. These states are separated only by 0.1 eV and pin the Fermi level. The (2×2)-2InMD-2H surface could not be identified experimentally from RAS alone. However, strong band bending suggests that the surface is present in small amounts for In-rich grown samples. Further studies are needed in order to answer, with absolute certainty, whether the Fermi-level pinning is due to the (2×2)-2InMD-2H or due to surface defects at the (2×4)-rInMD reconstruction. On the (2×2)-2D-2H, experimentally observed band bending is expected to be a result of H vacancies similar to the P-rich InP surface.

Since RAS allows for *in situ* monitoring, one can select the surface grown by changing the experimental parameters and observing the changes to the spectrum. Indeed, it is shown that it is possible to go from a (2×2) P-rich surface to a (2×4) In-rich surface. The versatility of RAS as an optical technique for adding semiconductor growth is clear; however, a detailed understanding is required, that can be achieved from first principle calculations, as demonstrated here.

To summarize, the InP and AlInP surfaces have been investigated from first principles for pho-

toelectrochemical water splitting applications, yielding the following main results. First, it was discovered that both materials are highly reactive towards oxygen, posing a significant challenge as photocorrosion is one of the major drawbacks for solar cells as it is known to reduce solar-to-hydrogen efficiencies. Indeed, increased oxidation was found to introduce detrimental mid-gap states. Nevertheless, oxides can passivate surface states, and it is known that surface functionalization can reduce the detrimental effects of oxidation. Thus, further studies, both experimental and theoretical in nature, are needed to fully understand the possible benefits of the rather complex oxide layer.

Second, the water splitting mechanism was investigated in detail, demonstrating the reason behind the success of InP as a photoelectrochemical cell. Thereby, In-rich surfaces are found to be well suited for hydrogen evolution, but further investigation is required to test their performance in tandem cells. Although AlInP is already experimentally used in water splitting applications, additional calculations (also for other III-V semiconductor reconstructions) should be performed to aid the search for devices with higher efficiencies. In addition, the different surface reconstructions for promising semiconductors should be investigated. Indeed, it was demonstrated that the water dissociation is significantly dependent on the surface chemistry and morphology: For instance, InP showed higher reactivity for In-rich surfaces compared to P-rich surfaces. Furthermore, it was shown that water does not bond chemically at the P-rich surface, which will make it difficult to observe water on the surface from experimental measurements, e. g., XPS.

Third, the P-rich surface band bending was explained by hydrogen defects. In addition, it is found how the Fermi level will be pinned at the mid-gap by charged defects related to doping levels. Also, these defects were demonstrated to interact with water, aiding in the dissociation process. Thus, it is crucial to understand the surface defects, as they play a major role at the interface between the semiconductor and the electrolyte.

Finally, the remarkable potential of RAS measurements coupled with theoretical calculations is showcased for aiding the growth of semiconductors. In fact, the spectra fingerprints were assigned to be surface states and surface-modified bulk states to specific surface motifs. In addition, RAS could be used in understanding how oxygen and water interact with semiconductor surfaces. When molecules adsorb at the surface, for example at In–In or P–P bonds, it will be reflected in the spectra. With the aid of additional theoretical calculations, the RAS measurements could be used to probe the evolution of the reactions on the surfaces. It is clear that there are still many interesting challenges and open questions, requiring theoretical calculations to fully elucidate them.

Bibliography

- [1] Energy-Institute. “Statistical Review of World Energy 2024”. 2024.
- [2] I. Jain. “Hydrogen the Fuel for 21st Century”. In: *International Journal of Hydrogen Energy* 34.17 (Sept. 2009), pp. 7368–7378.
- [3] P Moriarty and D Honnery. “Hydrogen’s Role in an Uncertain Energy Future”. In: *International Journal of Hydrogen Energy* 34.1 (Jan. 2009), pp. 31–39.
- [4] M. K. Singla, P. Nijhawan, and A. S. Oberoi. “Hydrogen Fuel and Fuel Cell Technology for Cleaner Future: A Review”. In: *Environmental Science and Pollution Research* 28.13 (Apr. 2021), pp. 15607–15626.
- [5] C. Song. “Introduction to Hydrogen and Syngas Production and Purification Technologies”. In: *Hydrogen and Syngas Production and Purification Technologies*. Ed. by K. Liu, C. Song, and V. Subramani. 1st ed. Wiley, Dec. 2009, pp. 1–13.
- [6] B. Parkinson and J. Turner. “The Potential Contribution of Photoelectrochemistry in the Global Energy Future”. In: *Photoelectrochemical Water Splitting Materials, Processes and Architectures*. RSC Energy and Environment Series 9. Cambridge: Royal Society of Chemistry, 2014, pp. 1–18.
- [7] F. Meillaud, A. Shah, C. Droz, E. Vallat-Sauvain, and C. Miazza. “Efficiency Limits for Single-Junction and Tandem Solar Cells”. In: *Solar Energy Materials and Solar Cells* 90.18-19 (Nov. 2006), pp. 2952–2959.
- [8] B. Weng, M.-Y. Qi, C. Han, Z.-R. Tang, and Y.-J. Xu. “Photocorrosion Inhibition of Semiconductor-Based Photocatalysts: Basic Principle, Current Development, and Future Perspective”. In: *ACS Catalysis* 9.5 (May 2019), pp. 4642–4687.
- [9] T. Zhao, N. Oh, D. Jishkariani, M. Zhang, H. Wang, N. Li, J. D. Lee, C. Zeng, M. Muduli, H.-J. Choi, D. Su, C. B. Murray, and C. R. Kagan. “General Synthetic Route to High-Quality Colloidal III–V Semiconductor Quantum Dots Based on Pnictogen Chlorides”. In: *Journal of the American Chemical Society* 141.38 (Sept. 2019), pp. 15145–15152.
- [10] Q. Wang, H. Wang, B. Zhang, X. Wang, W. Liu, J. Wang, J. Wang, J. Fan, Y. Zou, and X. Ma. “Integrated Fabrication of a High Strain InGaAs/GaAs Quantum Well Structure under Variable Temperature and Improvement of Properties Using MOCVD Technology”. In: *Optical Materials Express* 11.8 (Aug. 2021), p. 2378.

[11] E. Barrigón, M. Heurlin, Z. Bi, B. Monemar, and L. Samuelson. “Synthesis and Applications of III–V Nanowires”. In: *Chemical Reviews* 119.15 (Aug. 2019), pp. 9170–9220.

[12] M. Yamaguchi, T. Takamoto, K. Araki, and N. Ekins-Daukes. “Multi-Junction III–V Solar Cells: Current Status and Future Potential”. In: *Solar Energy* 79.1 (July 2005), pp. 78–85.

[13] J. Li, A. Aierken, Y. Liu, Y. Zhuang, X. Yang, J. H. Mo, R. K. Fan, Q. Y. Chen, S. Y. Zhang, Y. M. Huang, and Q. Zhang. “A Brief Review of High Efficiency III-V Solar Cells for Space Application”. In: *Frontiers in Physics* 8 (Feb. 2021), p. 631925.

[14] J. F. Geisz, R. M. France, K. L. Schulte, M. A. Steiner, A. G. Norman, H. L. Guthrey, M. R. Young, T. Song, and T. Moriarty. “Six-Junction III–V Solar Cells with 47.1% Conversion Efficiency under 143 Suns Concentration”. In: *Nature Energy* 5.4 (Apr. 2020), pp. 326–335.

[15] H. Helmers, O. Höhn, D. Lackner, P. Schygulla, M. Klitzke, J. Schön, C. Pellegrino, E. Oliva, M. Schachtner, P. Beutel, S. Heckelmann, F. Predan, J. Ohlmann, G. Siefer, and F. Dimroth. “Advancing Solar Energy Conversion Efficiency to 47.6% and Exploring the Spectral Versatility of III-V Photonic Power Converters”. In: *Physics, Simulation, and Photonic Engineering of Photovoltaic Devices XIII*. Ed. by A. Freundlich, K. Hinzer, S. Collin, and I. R. Sellers. San Francisco, United States: SPIE, Mar. 2024, p. 36.

[16] K. Kobayashi, J. Cowles, L. Tran, A. Gutierrez-Aitken, T. Block, A. Oki, and D. Streit. “A 50-MHz-55-GHz Multidecade InP-based HBT Distributed Amplifier”. In: *IEEE Microwave and Guided Wave Letters* 7.10 (Oct. 1997), pp. 353–355.

[17] J. Mullrich, H. Thurner, E. Mullner, J. Jensen, W. Stanchina, M. Kardos, and H.-M. Rein. “High-Gain Transimpedance Amplifier in InP-based HBT Technology for the Receiver in 40-Gb/s Optical-Fiber TDM Links”. In: *IEEE Journal of Solid-State Circuits* 35.9 (Sept. 2000), pp. 1260–1265.

[18] D. Yap, K. Elliott, Y. Brown, A. Kost, and E. Ponti. “High-Speed Integrated Optoelectronic Modulation Circuit”. In: *IEEE Photonics Technology Letters* 13.6 (June 2001), pp. 626–628.

[19] D. Ugarte, L. H. G. Tizei, M. A. Cotta, C. Ducati, P. A. Midgley, and A. S. Eggeman. “Analysis of Structural Distortion in Eshelby Twisted InP Nanowires by Scanning Precession Electron Diffraction”. In: *Nano Research* 12.4 (Apr. 2019), pp. 939–946.

[20] S. Wu, K. Peng, S. Battiato, V. Zannier, A. Bertoni, G. Goldoni, X. Xie, J. Yang, S. Xiao, C. Qian, F. Song, S. Sun, J. Dang, Y. Yu, F. Beltram, L. Sorba, A. Li, B.-b. Li, F. Rossella, and X. Xu. “Anisotropies of the G-Factor Tensor and Diamagnetic Coefficient in Crystal-Phase Quantum Dots in InP Nanowires”. In: *Nano Research* 12.11 (Nov. 2019), pp. 2842–2848.

[21] A. Heller and R. G. Vadimsky. “Efficient Solar to Chemical Conversion: 12% Efficient Photoassisted Electrolysis in the [p-Type InP(Ru)]/HCl-KCl/Pt(Rh) Cell”. In: *Physical Review Letters* 46.17 (Apr. 1981), pp. 1153–1156.

[22] N. Kornienko, N. A. Gibson, H. Zhang, S. W. Eaton, Y. Yu, S. Aloni, S. R. Leone, and P. Yang. “Growth and Photoelectrochemical Energy Conversion of Wurtzite Indium Phosphide Nanowire Arrays”. In: *ACS Nano* 10.5 (May 2016), pp. 5525–5535.

[23] W. Yu, M. H. Richter, P. Buabthong, I. A. Moreno-Hernandez, C. G. Read, E. Simonoff, B. S. Brunschwig, and N. S. Lewis. “Investigations of the Stability of Etched or Platinized P-InP(100) Photocathodes for Solar-Driven Hydrogen Evolution in Acidic or Alkaline Aqueous Electrolytes”. In: *Energy & Environmental Science* 14.11 (2021), pp. 6007–6020.

[24] H. Wenn, C. Xuefeng, J. Minglei, R. Fengzhu, P. Chengxiao, Y. Haigang, G. Qinfen, W. Bing, and Y. Huabing. “A Direct Z-scheme $\text{g-C}_6\text{N}_6$ /InP van Der Waals Heterostructure: A Promising Photocatalyst for High-Efficiency Overall Water Splitting”. In: *Journal of Physics D: Applied Physics* 55.26 (June 2022), p. 264001.

[25] T. Wang, Y. Wang, Y. Liu, J. Li, C. Wang, D. Pan, and Y. Rui. “Construction of Z-type $\text{In}_2\text{O}_3@\text{InP}$ Heterostructure with Enhanced Photo-Assisted Electrocatalytic Water Splitting for Hydrogen Production”. In: *International Journal of Hydrogen Energy* 64 (Apr. 2024), pp. 166–177.

[26] I. Vurgaftman, J. R. Meyer, and L. R. Ram-Mohan. “Band Parameters for III–V Compound Semiconductors and Their Alloys”. In: *Journal of Applied Physics* 89.11 (June 2001), pp. 5815–5875.

[27] K. Kishino, A. Kikuchi, Y. Kaneko, and I. Nomura. “Enhanced Carrier Confinement Effect by the Multiquantum Barrier in 660 Nm $\text{GaInP}/\text{AlInP}$ Visible Lasers”. In: *Applied Physics Letters* 58.17 (Apr. 1991), pp. 1822–1824.

[28] Y. Ishitani, S. Minagawa, T. Kita, T. Nishino, H. Yaguchi, and Y. Shiraki. “The Optical Processes in $\text{AlInP}/\text{GaInP}/\text{AlInP}$ Quantum Wells”. In: *Journal of Applied Physics* 80.8 (Oct. 1996), pp. 4592–4598.

[29] A. Gudovskikh, N. Kaluzhniy, V. Lantratov, S. Mintairov, M. Shvarts, and V. Andreev. “Numerical Modelling of GaInP Solar Cells with AlInP and AlGaAs Windows”. In: *Thin Solid Films* 516.20 (Aug. 2008), pp. 6739–6743.

[30] E. Ochoa-Martínez, L. Barrutia, M. Ochoa, E. Barrigón, I. García, I. Rey-Stolle, C. Algora, P. Basa, G. Kronome, and M. Gabás. “Refractive Indexes and Extinction Coefficients of n- and p-Type Doped GaInP, AlInP and AlGaInP for Multijunction Solar Cells”. In: *Solar Energy Materials and Solar Cells* 174 (Jan. 2018), pp. 388–396.

[31] J. T. Boyer, K. L. Schulte, M. R. Young, A. J. Ptak, and J. Simon. “AlInP-passivated III–V Solar Cells Grown by Dynamic Hydride Vapor-phase Epitaxy”. In: *Progress in Photovoltaics: Research and Applications* 31.3 (Mar. 2023), pp. 230–236.

[32] M. M. May, H.-J. Lewerenz, D. Lackner, F. Dimroth, and T. Hannappel. “Efficient Direct Solar-to-Hydrogen Conversion by in Situ Interface Transformation of a Tandem Structure”. In: *Nature Communications* 6.1 (Sept. 2015), p. 8286.

[33] H. J. Lewerenz, C. Heine, K. Skorupska, N. Szabo, T. Hannappel, T. Vo-Dinh, S. A. Campbell, H. W. Klemm, and A. G. Muñoz. “Photoelectrocatalysis: Principles, Nanoemitter Applications and Routes to Bio-Inspired Systems”. In: *Energy & Environmental Science* 3.6 (2010), p. 748.

[34] L. J. Glahn, I. A. Ruiz Alvarado, S. Neufeld, M. A. Zare Pour, A. Paszuk, D. Ostheimer, S. Shekarabi, O. Romanyuk, D. C. Moritz, J. P. Hofmann, W. Jaegermann, T. Hannappel, and W. G. Schmidt. “Clean and Hydrogen-Adsorbed AlInP(001) Surfaces: Structures and Electronic Properties”. In: *physica status solidi (b)* 259.11 (Nov. 2022), p. 2200308.

[35] W. G. Schmidt. “Calculation of Reflectance Anisotropy for Semiconductor Surface Exploration”. In: *physica status solidi (b)* 242.13 (Nov. 2005), pp. 2751–2764.

[36] O. Pulci, G. Onida, R. Del Sole, and A. J. Shkrebttii. “*Ab Initio* Calculation of the Reflectance Anisotropy of $\text{GaAs}(110)$ ”. In: *Physical Review B* 58.4 (July 1998), pp. 1922–1927.

[37] W. Schmidt, F. Bechstedt, and J. Bernholc. “GaAs(001) Surface Reconstructions: Geometries, Chemical Bonding and Optical Properties”. In: *Applied Surface Science* 190.1-4 (May 2002), pp. 264–268.

[38] E. Molteni, G. Cappellini, G. Onida, and G. Fratesi. “Optical Properties of Organically Functionalized Silicon Surfaces: Uracil-like Nucleobases on Si(001)”. In: *Physical Review B* 95.7 (Feb. 2017), p. 075437.

[39] M. Zorn, J.-T. Zettler, A. Knauer, and M. Weyers. “In Situ Determination and Control of AlGaInP Composition during MOVPE Growth”. In: *Journal of Crystal Growth* 287.2 (Jan. 2006), pp. 637–641.

[40] C. Krahmer, M. Philippens, M. Schubert, and K. Streubel. “In-situ Monitoring of MOVPE Growth with Reflectance Anisotropy Spectroscopy in an Industrial Used Multi Wafer Reactor”. In: *physica status solidi c* 3.3 (Mar. 2006), pp. 655–658.

[41] O. Khaselev and J. A. Turner. “A Monolithic Photovoltaic-Photoelectrochemical Device for Hydrogen Production via Water Splitting”. In: *Science* 280.5362 (Apr. 1998), pp. 425–427.

[42] T. Hannappel, M. M. May, and H.-J. Lewerenz. “CHAPTER 9. Epitaxial III-V Thin Film Absorbers: Preparation, Efficient InP Photocathodes and Routes to High Efficiency Tandem Structures”. In: *Energy and Environment Series*. Ed. by H.-J. Lewerenz and L. Peter. Cambridge: Royal Society of Chemistry, 2013, pp. 223–265.

[43] B. Kaiser, D. Fertig, J. Ziegler, J. Klett, S. Hoch, and W. Jaegermann. “Solar Hydrogen Generation with Wide-Band-Gap Semiconductors: GaP(100) Photoelectrodes and Surface Modification”. In: *ChemPhysChem* 13.12 (Aug. 2012), pp. 3053–3060.

[44] G. Hollinger, E. Bergignat, J. Joseph, and Y. Robach. “On the Nature of Oxides on InP Surfaces”. In: *Journal of Vacuum Science & Technology A: Vacuum, Surfaces, and Films* 3.6 (Nov. 1985), pp. 2082–2088.

[45] G. Hollinger, J. Joseph, Y. Robach, E. Bergignat, B. Commère, P. Viktorovitch, and M. Fronment. “On the Chemistry of Passivated Oxide–InP Interfaces”. In: *Journal of Vacuum Science & Technology B: Microelectronics Processing and Phenomena* 5.4 (July 1987), pp. 1108–1112.

[46] A. Hofmann, P. Streubel, and A. Meisel. “XPS Investigation of Oxide Films on InP(100)”. In: *Surface and Interface Analysis* 12.5 (July 1988), pp. 315–319.

[47] B. C. Wood, T. Ogitsu, and E. Schwegler. “Local Structural Models of Complex Oxygen- and Hydroxyl-Rich GaP/InP(001) Surfaces”. In: *The Journal of Chemical Physics* 136.6 (Feb. 2012), p. 064705.

[48] Y. Cao, J. Zhang, X. Li, T. H. Kosel, P. Fay, D. C. Hall, X. B. Zhang, R. D. Dupuis, J. B. Jasinski, and Z. Liliental-Weber. “Electrical Properties of InAlP Native Oxides for Metal–Oxide–Semiconductor Device Applications”. In: *Applied Physics Letters* 86.6 (Feb. 2005), p. 062105.

[49] M. M. May, H.-J. Lewerenz, and T. Hannappel. “Optical in Situ Study of InP(100) Surface Chemistry: Dissociative Adsorption of Water and Oxygen”. In: *The Journal of Physical Chemistry C* 118.33 (Aug. 2014), pp. 19032–19041.

[50] B. C. Wood, E. Schwegler, W. I. Choi, and T. Ogitsu. “Surface Chemistry of GaP(001) and InP(001) in Contact with Water”. In: *The Journal of Physical Chemistry C* 118.2 (Jan. 2014), pp. 1062–1070.

[51] M. Born and R. Oppenheimer. “Zur Quantentheorie Der Molekeln”. In: *Annalen der Physik* 389.20 (Jan. 1927), pp. 457–484.

[52] J. C. Morrison. “The Hydrogen Atom”. In: *Modern Physics*. Elsevier, 2015, pp. 65–94.

[53] R. G. Parr and Y. Weitao. “Density-Functional Theory of Atoms and Molecules”. Oxford University Press, Jan. 1995.

[54] R. M. Martin. “Electronic Structure: Basic Theory and Practical Methods”. 1st ed. Cambridge University Press, Apr. 2004.

[55] P. Hohenberg and W. Kohn. “Inhomogeneous Electron Gas”. In: *Physical Review* 136.3B (Nov. 1964), B864–B871.

[56] M. Levy. “Universal Variational Functionals of Electron Densities, First-Order Density Matrices, and Natural Spin-Orbitals and Solution of the ν -Representability Problem”. In: *Proceedings of the National Academy of Sciences* 76.12 (Dec. 1979), pp. 6062–6065.

[57] M. Levy. “Electron Densities in Search of Hamiltonians”. In: *Physical Review A* 26.3 (Sept. 1982), pp. 1200–1208.

[58] M. Levy and J. P. Perdew. “The Constrained Search Formulation of Density Functional Theory”. In: *Density Functional Methods In Physics*. Ed. by R. M. Dreizler and J. Da Providênciia. Boston, MA: Springer US, 1985, pp. 11–30.

[59] E. H. Lieb. “Density Functionals for Coulomb Systems”. In: *International Journal of Quantum Chemistry* 24.3 (Sept. 1983), pp. 243–277.

[60] W. Kohn and L. J. Sham. “Self-Consistent Equations Including Exchange and Correlation Effects”. In: *Physical Review* 140.4A (Nov. 1965), A1133–A1138.

[61] J. Harris. “Adiabatic-Connection Approach to Kohn-Sham Theory”. In: *Physical Review A* 29.4 (Apr. 1984), pp. 1648–1659.

[62] D. Andrae and H. Hellmann. “Hans Hellmann: Einführung in die Quantenchemie mit biografischen Notizen von Hans Hellmann jr”. Neuaufl. der Erstaufl. von 1937. Berlin: Springer Spektrum, 2015.

[63] R. P. Feynman. “Forces in Molecules”. In: *Physical Review* 56.4 (Aug. 1939), pp. 340–343.

[64] P. A. M. Dirac. “Note on Exchange Phenomena in the Thomas Atom”. In: *Mathematical Proceedings of the Cambridge Philosophical Society* 26.3 (July 1930), pp. 376–385.

[65] D. M. Ceperley and B. J. Alder. “Ground State of the Electron Gas by a Stochastic Method”. In: *Physical Review Letters* 45.7 (Aug. 1980), pp. 566–569.

[66] J. P. Perdew and A. Zunger. “Self-Interaction Correction to Density-Functional Approximations for Many-Electron Systems”. In: *Physical Review B* 23.10 (May 1981), pp. 5048–5079.

[67] A. Van De Walle and G. Ceder. “Correcting Overbinding in Local-Density-Approximation Calculations”. In: *Physical Review B* 59.23 (June 1999), pp. 14992–15001.

[68] J. P. Perdew. “Density Functional Theory and the Band Gap Problem”. In: *International Journal of Quantum Chemistry* 28.S19 (1985), pp. 497–523.

[69] J. L. Bao, L. Gagliardi, and D. G. Truhlar. “[Self-Interaction Error in Density Functional Theory: An Appraisal](#)”. In: *The Journal of Physical Chemistry Letters* 9.9 (May 2018), pp. 2353–2358.

[70] J. P. Perdew, J. A. Chevary, S. H. Vosko, K. A. Jackson, M. R. Pederson, D. J. Singh, and C. Fiolhais. “[Atoms, Molecules, Solids, and Surfaces: Applications of the Generalized Gradient Approximation for Exchange and Correlation](#)”. In: *Physical Review B* 46.11 (Sept. 1992), pp. 6671–6687.

[71] J. P. Perdew, K. Burke, and M. Ernzerhof. “[Generalized Gradient Approximation Made Simple](#)”. In: *Physical Review Letters* 77.18 (Oct. 1996), pp. 3865–3868.

[72] J. P. Perdew, K. Burke, and M. Ernzerhof. “[Generalized Gradient Approximation Made Simple \[Phys. Rev. Lett. 77, 3865 \(1996\)\]](#)”. In: *Physical Review Letters* 78.7 (Feb. 1997), pp. 1396–1396.

[73] G.-X. Zhang, A. M. Reilly, A. Tkatchenko, and M. Scheffler. “[Performance of Various Density-Functional Approximations for Cohesive Properties of 64 Bulk Solids](#)”. In: *New Journal of Physics* 20.6 (June 2018), p. 063020.

[74] P. Güttinger. “[Das Verhalten von Atomen im magnetischen Drehfeld](#)”. In: *Zeitschrift für Physik* 73.3-4 (Mar. 1932), pp. 169–184.

[75] W. Pauli. “[Die allgemeinen Prinzipien der Wellenmechanik](#)”. In: *Quantentheorie*. Ed. by H. Bethe, F. Hund, N. F. Mott, W. Pauli, A. Rubinowicz, G. Wentzel, and A. Smekal. Berlin, Heidelberg: Springer Berlin Heidelberg, 1933, pp. 83–272.

[76] P. Pulay. “[Convergence Acceleration of Iterative Sequences. the Case of Scf Iteration](#)”. In: *Chemical Physics Letters* 73.2 (July 1980), pp. 393–398.

[77] J. R. Shewchuk. “[An Introduction to the Conjugate Gradient Method Without the Agonizing Pain](#)”. Pittsburgh, PA 15213, Aug. 1994.

[78] J. F. Janak. “[Proof That \$\partial E / \partial n_i = \varepsilon\$ in Density-Functional Theory](#)”. In: *Physical Review B* 18.12 (Dec. 1978), pp. 7165–7168.

[79] J. P. Perdew, R. G. Parr, M. Levy, and J. L. Balduz. “[Density-Functional Theory for Fractional Particle Number: Derivative Discontinuities of the Energy](#)”. In: *Physical Review Letters* 49.23 (Dec. 1982), pp. 1691–1694.

[80] J. P. Perdew and M. Levy. “[Physical Content of the Exact Kohn-Sham Orbital Energies: Band Gaps and Derivative Discontinuities](#)”. In: *Physical Review Letters* 51.20 (Nov. 1983), pp. 1884–1887.

[81] L. J. Sham and M. Schlüter. “[Density-Functional Theory of the Energy Gap](#)”. In: *Physical Review Letters* 51.20 (Nov. 1983), pp. 1888–1891.

[82] L. J. Sham and M. Schlüter. “[Density-Functional Theory of the Band Gap](#)”. In: *Physical Review B* 32.6 (Sept. 1985), pp. 3883–3889.

[83] J. P. Perdew, M. Ernzerhof, and K. Burke. “[Rationale for Mixing Exact Exchange with Density Functional Approximations](#)”. In: *The Journal of Chemical Physics* 105.22 (Dec. 1996), pp. 9982–9985.

[84] A. D. Becke. “[A New Mixing of Hartree–Fock and Local Density-Functional Theories](#)”. In: *The Journal of Chemical Physics* 98.2 (Jan. 1993), pp. 1372–1377.

[85] M. Ernzerhof and G. E. Scuseria. “Assessment of the Perdew–Burke–Ernzerhof Exchange–Correlation Functional”. In: *The Journal of Chemical Physics* 110.11 (Mar. 1999), pp. 5029–5036.

[86] J. Heyd, G. E. Scuseria, and M. Ernzerhof. “Hybrid Functionals Based on a Screened Coulomb Potential”. In: *The Journal of Chemical Physics* 118.18 (May 2003), pp. 8207–8215.

[87] J. Heyd and G. E. Scuseria. “Efficient Hybrid Density Functional Calculations in Solids: Assessment of the Heyd–Scuseria–Ernzerhof Screened Coulomb Hybrid Functional”. In: *The Journal of Chemical Physics* 121.3 (July 2004), pp. 1187–1192.

[88] J. Heyd, G. E. Scuseria, and M. Ernzerhof. “Erratum: “Hybrid Functionals Based on a Screened Coulomb Potential” [J. Chem. Phys. 118, 8207 (2003)]”. In: *The Journal of Chemical Physics* 124.21 (June 2006), p. 219906.

[89] A. V. Krukau, O. A. Vydrov, A. F. Izmaylov, and G. E. Scuseria. “Influence of the Exchange Screening Parameter on the Performance of Screened Hybrid Functionals”. In: *The Journal of Chemical Physics* 125.22 (2006), p. 224106.

[90] R. M. Martin, L. Reining, and D. M. Ceperley. “Interacting Electrons: Theory and Computational Approaches”. 1st ed. Cambridge University Press, May 2016.

[91] C. Friedrich and A. Schindlmayr. “Many-Body Perturbation Theory: The GW Approximation”. In: *Computational Nanoscience: Do It Yourself! Winter School, 14 - 22 February 2006, Forschungszentrum Jülich, Germany; Lecture Notes*. Ed. by J. Grotendorst, S. Blügel, and John von Neumann-Institut für Computing. NIC Series 31. Jülich: NIC-Secretariat, Research Centre Jülich, 2006, pp. 335–355.

[92] L. Hedin. “New Method for Calculating the One-Particle Green’s Function with Application to the Electron-Gas Problem”. In: *Physical Review* 139.3A (Aug. 1965), A796–A823.

[93] P. Duffy, D. P. Chong, M. E. Casida, and D. R. Salahub. “Assessment of Kohn-Sham Density-Functional Orbitals as Approximate Dyson Orbitals for the Calculation of Electron-Momentum-Spectroscopy Scattering Cross Sections”. In: *Physical Review A* 50.6 (Dec. 1994), pp. 4707–4728.

[94] M. Shishkin and G. Kresse. “Implementation and Performance of the Frequency-Dependent G W Method within the PAW Framework”. In: *Physical Review B* 74.3 (July 2006), p. 035101.

[95] M. Shishkin and G. Kresse. “Self-Consistent G W Calculations for Semiconductors and Insulators”. In: *Physical Review B* 75.23 (June 2007), p. 235102.

[96] M. Grumet, P. Liu, M. Kaltak, J. Klimeš, and G. Kresse. “Beyond the Quasiparticle Approximation: Fully Self-Consistent G W Calculations”. In: *Physical Review B* 98.15 (Oct. 2018), p. 155143.

[97] L. D. Landau and E. M. Lifšic. “Statistical Physics: Volume 5”. 3rd ed.

[98] S. Wippermann and W. G. Schmidt. “Entropy Explains Metal-Insulator Transition of the Si(111)-In Nanowire Array”. In: *Physical Review Letters* 105.12 (Sept. 2010), p. 126102.

[99] X. Zhang, B. Grabowski, F. Körmann, C. Freysoldt, and J. Neugebauer. “Accurate Electronic Free Energies of the 3 d, 4 d, and 5 d Transition Metals at High Temperatures”. In: *Physical Review B* 95.16 (Apr. 2017), p. 165126.

[100] B. Donovan, J. F. Angress, and J. F. Angress. “Lattice Vibrations”. London: Chapman and Hall, 1971.

[101] R. J. D. Tilley. “Intrinsic Point Defects in Stoichiometric Compounds”. In: *Defects in Solids*. John Wiley & Sons, Ltd, 2008, pp. 45–82.

[102] C. Sutton and S. V. Levchenko. “First-Principles Atomistic Thermodynamics and Configurational Entropy”. In: *Frontiers in Chemistry* 8 (Dec. 2020), p. 757.

[103] H. Eyring. “The Activated Complex in Chemical Reactions”. In: *The Journal of Chemical Physics* 3.2 (Feb. 1935), pp. 107–115.

[104] E. Wigner. “The Transition State Method”. In: *Transactions of the Faraday Society* 34 (1938), p. 29.

[105] H. Eyring. “The Theory of Absolute Reaction Rates”. In: *Transactions of the Faraday Society* 34 (1938), p. 41.

[106] G. Mills, H. Jónsson, and G. K. Schenter. “Reversible Work Transition State Theory: Application to Dissociative Adsorption of Hydrogen”. In: *Surface Science* 324.2-3 (Feb. 1995), pp. 305–337.

[107] H. Jónsson, G. Mills, and K. W. Jacobsen. “Nudged Elastic Band Method for Finding Minimum Energy Paths of Transitions”. In: *Classical and Quantum Dynamics in Condensed Phase Simulations*. LERICI, Villa Marigola: WORLD SCIENTIFIC, June 1998, pp. 385–404.

[108] G. Henkelman, B. P. Uberuaga, and H. Jónsson. “A Climbing Image Nudged Elastic Band Method for Finding Saddle Points and Minimum Energy Paths”. In: *The Journal of Chemical Physics* 113.22 (Dec. 2000), pp. 9901–9904.

[109] G. Henkelman and H. Jónsson. “Improved Tangent Estimate in the Nudged Elastic Band Method for Finding Minimum Energy Paths and Saddle Points”. In: *The Journal of Chemical Physics* 113.22 (Dec. 2000), pp. 9978–9985.

[110] S. Albrecht. “Optical Absorption Spectra of Semiconductors and Insulators: Ab Initio Calculation of Many-Body Effects; Absorption Optique Des Semi-Conducteurs et Isolants: Calcul Ab-Initio Des Effets a Plusieurs Corps”. PhD thesis. France, Jan. 1999.

[111] R. Kubo. “Statistical-Mechanical Theory of Irreversible Processes. I. General Theory and Simple Applications to Magnetic and Conduction Problems”. In: *Journal of the Physical Society of Japan* 12.6 (June 1957), pp. 570–586.

[112] R. Kubo, M. Yokota, and S. Nakajima. “Statistical-Mechanical Theory of Irreversible Processes. II. Response to Thermal Disturbance”. In: *Journal of the Physical Society of Japan* 12.11 (Nov. 1957), pp. 1203–1211.

[113] D. Bohm and D. Pines. “A Collective Description of Electron Interactions. I. Magnetic Interactions”. In: *Physical Review* 82.5 (June 1951), pp. 625–634.

[114] D. Pines and D. Bohm. “A Collective Description of Electron Interactions: II. Collective vs Individual Particle Aspects of the Interactions”. In: *Physical Review* 85.2 (Jan. 1952), pp. 338–353.

[115] D. Bohm and D. Pines. “A Collective Description of Electron Interactions: III. Coulomb Interactions in a Degenerate Electron Gas”. In: *Physical Review* 92.3 (Nov. 1953), pp. 609–625.

[116] J. Hubbard. “The Description of Collective Motions in Terms of Many-Body Perturbation Theory”. In: *Proceedings of the Royal Society of London. Series A. Mathematical and Physical Sciences* 240.1223 (July 1957), pp. 539–560.

[117] S. L. Adler. “Quantum Theory of the Dielectric Constant in Real Solids”. In: *Physical Review* 126.2 (Apr. 1962), pp. 413–420.

[118] N. Wiser. “Dielectric Constant with Local Field Effects Included”. In: *Physical Review* 129.1 (Jan. 1963), pp. 62–69.

[119] P. E. Blöchl. “Projector Augmented-Wave Method”. In: *Physical Review B* 50.24 (Dec. 1994), pp. 17953–17979.

[120] M. Gajdoš, K. Hummer, G. Kresse, J. Furthmüller, and F. Bechstedt. “Linear Optical Properties in the Projector-Augmented Wave Methodology”. In: *Physical Review B* 73.4 (Jan. 2006), p. 045112.

[121] G. Onida, L. Reining, and A. Rubio. “Electronic Excitations: Density-Functional versus Many-Body Green’s-Function Approaches”. In: *Reviews of Modern Physics* 74.2 (June 2002), pp. 601–659.

[122] G. Strinati. “Application of the Green’s Functions Method to the Study of the Optical Properties of Semiconductors”. In: *La Rivista del Nuovo Cimento* 11.12 (Dec. 1988), pp. 1–86.

[123] Ig. Tamm. “Relativistic Interaction of Elementary Particles”. In: *Selected Papers*. Berlin, Heidelberg: Springer Berlin Heidelberg, 1991, pp. 157–174.

[124] S. M. Dancoff. “Non-Adiabatic Meson Theory of Nuclear Forces”. In: *Physical Review* 78.4 (May 1950), pp. 382–385.

[125] S. Albrecht, L. Reining, R. Del Sole, and G. Onida. “Ab Initio Calculation of Excitonic Effects in the Optical Spectra of Semiconductors”. In: *Physical Review Letters* 80.20 (May 1998), pp. 4510–4513.

[126] F. Bechstedt, R. Del Sole, G. Cappellini, and L. Reining. “An Efficient Method for Calculating Quasiparticle Energies in Semiconductors”. In: *Solid State Communications* 84.7 (Nov. 1992), pp. 765–770.

[127] W. G. Schmidt, S. Glutsch, P. H. Hahn, and F. Bechstedt. “Efficient O (N 2) Method to Solve the Bethe-Salpeter Equation”. In: *Physical Review B* 67.8 (Feb. 2003), p. 085307.

[128] P. Liu, B. Kim, X.-Q. Chen, D. D. Sarma, G. Kresse, and C. Franchini. “Relativistic G W +BSE Study of the Optical Properties of Ruddlesden-Popper Iridates”. In: *Physical Review Materials* 2.7 (July 2018), p. 075003.

[129] A. Tal, P. Liu, G. Kresse, and A. Pasquarello. “Accurate Optical Spectra through Time-Dependent Density Functional Theory Based on Screening-Dependent Hybrid Functionals”. In: *Physical Review Research* 2.3 (July 2020), p. 032019.

[130] R. W. Godby, M. Schlüter, and L. J. Sham. “Self-Energy Operators and Exchange-Correlation Potentials in Semiconductors”. In: *Physical Review B* 37.17 (June 1988), pp. 10159–10175.

[131] F. Gygi and A. Baldereschi. “Quasiparticle Energies in Semiconductors: Self-energy Correction to the Local-Density Approximation”. In: *Physical Review Letters* 62.18 (May 1989), pp. 2160–2163.

[132] M. S. Hybertsen and S. G. Louie. “Electron Correlation in Semiconductors and Insulators: Band Gaps and Quasiparticle Energies”. In: *Physical Review B* 34.8 (Oct. 1986), pp. 5390–5413.

[133] R. Del Sole and R. Girlanda. “Optical Properties of Semiconductors within the Independent-Quasiparticle Approximation”. In: *Physical Review B* 48.16 (Oct. 1993), pp. 11789–11795.

[134] R. del Sole. “Microscopic Theory of Optical Properties of Crystal Surfaces”. In: *Solid State Communications* 37.7 (Feb. 1981), pp. 537–540.

[135] R. Del Sole and E. Fiorino. “Macroscopic Dielectric Tensor at Crystal Surfaces”. In: *Physical Review B* 29.8 (Apr. 1984), pp. 4631–4645.

[136] F. Manghi, R. Del Sole, A. Selloni, and E. Molinari. “Anisotropy of Surface Optical Properties from First-Principles Calculations”. In: *Physical Review B* 41.14 (May 1990), pp. 9935–9946.

[137] R. Del Sole. “REFLECTANCE SPECTROSCOPY – THEORY”. In: *Photonic Probes of Surfaces*. Elsevier, 1995, pp. 131–174.

[138] J. McIntyre and D. Aspnes. “Differential Reflection Spectroscopy of Very Thin Surface Films”. In: *Surface Science* 24.2 (Feb. 1971), pp. 417–434.

[139] J. Dong, X. Zhang, G. Lu, and C. Wang. “Generation of Enhanced Stability of SnO/In(OH)₃/InP for Photocatalytic Water Splitting by SnO Protection Layer”. In: *Frontiers in Energy* 15.3 (Sept. 2021), pp. 710–720.

[140] M. Niu, D. Cao, K. Sui, and C. Liu. “InP/TiO₂ Heterojunction for Photoelectrochemical Water Splitting under Visible-Light”. In: *International Journal of Hydrogen Energy* 45.20 (Apr. 2020), pp. 11615–11624.

[141] M. H. Lee, K. Takei, J. Zhang, R. Kapadia, M. Zheng, Y.-Z. Chen, J. Nah, T. S. Matthews, Y.-L. Chueh, J. W. Ager, and A. Javey. “p-Type InP Nanopillar Photocathodes for Efficient Solar-Driven Hydrogen Production”. In: *Angewandte Chemie International Edition* 51.43 (Oct. 2012), pp. 10760–10764.

[142] G. Chen, S. B. Visbeck, D. C. Law, and R. F. Hicks. “Structure-Sensitive Oxidation of the Indium Phosphide (001) Surface”. In: *Journal of Applied Physics* 91.11 (June 2002), pp. 9362–9367.

[143] K. C. Santosh, W. Wang, H. Dong, K. Xiong, R. C. Longo, R. M. Wallace, and K. Cho. “First Principles Study on InP (001)-(2 × 4) Surface Oxidation”. In: *Journal of Applied Physics* 113.10 (Mar. 2013), p. 103705.

[144] M. M. May, O. Supplie, C. Höhn, W.-D. Zabka, H.-J. Lewerenz, R. Van De Krol, and T. Hanappel. “Water-Induced Modifications of GaP(100) and InP(100) Surfaces Studied by Photoelectron Spectroscopy and Reflection Anisotropy Spectroscopy”. In: *SPIE Solar Energy + Technology*. Ed. by Y. Kanai and D. Prendergast. San Diego, California, United States, Sept. 2013, p. 88220M.

[145] O. Henrion, A. Klein, and W. Jaegermann. “Water Adsorption on UHV Cleaved InP(110) Surfaces”. In: *Surface Science* 457.1-2 (June 2000), pp. L337–L341.

[146] C. D. MacPherson, R. A. Wolkow, C. E. J. Mitchell, and A. B. McLean. “Scanning Tunneling Microscopy Study of InP (100) - (2×4) : An Exception to the Dimer Model”. In: *Physical Review Letters* 77.4 (July 1996), pp. 691–694.

[147] K. B. Ozanyan, P. J. Parbrook, M. Hopkinson, C. R. Whitehouse, Z. Sobiesierski, and D. I. Westwood. “*In Situ* Monitoring of the Surface Reconstructions on InP(001) Prepared by Molecular Beam Epitaxy”. In: *Journal of Applied Physics* 82.1 (July 1997), pp. 474–476.

[148] P. Parbrook, K. Ozanyan, M. Hopkinson, C. Whitehouse, Z. Sobiesierski, and D. Westwood. “Surface Structure of InP(001) under Dynamic and Static Conditions of Molecular Beam Epitaxy”. In: *Applied Surface Science* 123–124 (Jan. 1998), pp. 313–318.

[149] V. P. LaBella, Z. Ding, D. W. Bullock, C. Emery, and P. M. Thibado. “Reflection High-Energy Electron Diffraction and Scanning Tunneling Microscopy Study of InP(001) Surface Reconstructions”. In: *Journal of Vacuum Science & Technology A: Vacuum, Surfaces, and Films* 18.4 (July 2000), pp. 1492–1496.

[150] T. Hannappel, S. Visbeck, L. Töben, and F. Willig. “Apparatus for Investigating Metalorganic Chemical Vapor Deposition-Grown Semiconductors with Ultrahigh-Vacuum Based Techniques”. In: *Review of Scientific Instruments* 75.5 (May 2004), pp. 1297–1304.

[151] W. G. Schmidt, F. Bechstedt, N. Esser, M. Pristovsek, Ch. Schultz, and W. Richter. “Atomic Structure of InP(001)-(2×4): A Dimer Reconstruction”. In: *Physical Review B* 57.23 (June 1998), pp. 14596–14599.

[152] W. Schmidt and F. Bechstedt. “Geometry and Electronic Structure of InP(001)(2×4) Reconstructions”. In: *Surface Science* 409.3 (July 1998), pp. 474–484.

[153] P. H. Hahn and W. G. Schmidt. “Surface Ordering of P-rich InP(001): Hydrogen Stabilization vs Electron Correlation”. In: *Surface Review and Letters* 10.02n03 (Apr. 2003), pp. 163–167.

[154] W. Schmidt. “III-V Compound Semiconductor (001) Surfaces”. In: *Applied Physics A: Materials Science & Processing* 75.1 (July 2002), pp. 89–99.

[155] P. H. Hahn, W. G. Schmidt, F. Bechstedt, O. Pulci, and R. Del Sole. “P-Rich GaP (001) (2×1) / (2×2) Surface: A Hydrogen-Adsorbate Structure Determined from First-Principles Calculations”. In: *Physical Review B* 68.3 (July 2003), p. 033311.

[156] W. G. Schmidt, P. H. Hahn, F. Bechstedt, N. Esser, P. Vogt, A. Wange, and W. Richter. “InP(001)-(2×1) Surface: A Hydrogen Stabilized Structure”. In: *Physical Review Letters* 90.12 (Mar. 2003), p. 126101.

[157] W. G. Schmidt, E. L. Briggs, J. Bernholc, and F. Bechstedt. “Structural Fingerprints in the Reflectance Anisotropy Spectra of InP (001) (2×4) Surfaces”. In: *Physical Review B* 59.3 (Jan. 1999), pp. 2234–2239.

[158] G. Kresse and J. Hafner. “*Ab Initio* Molecular Dynamics for Liquid Metals”. In: *Physical Review B* 47.1 (Jan. 1993), pp. 558–561.

[159] G. Kresse and J. Furthmüller. “Efficiency of Ab-Initio Total Energy Calculations for Metals and Semiconductors Using a Plane-Wave Basis Set”. In: *Computational Materials Science* 6.1 (July 1996), pp. 15–50.

[160] G. Kresse and J. Furthmüller. “Efficient Iterative Schemes for *Ab Initio* Total-Energy Calculations Using a Plane-Wave Basis Set”. In: *Physical Review B* 54.16 (Oct. 1996), pp. 11169–11186.

[161] G. Kresse and D. Joubert. “From Ultrasoft Pseudopotentials to the Projector Augmented-Wave Method”. In: *Physical Review B* 59.3 (Jan. 1999), pp. 1758–1775.

[162] R. Driad, W. R. McKinnon, Z. H. Lu, and S. P. McAlister. “Effect of UV-ozone Oxidation on the Device Characteristics of InP-based Heterostructure Bipolar Transistors”. In: *Journal of Electronic Materials* 29.12 (Dec. 2000), pp. L33–L36.

[163] I. A. Ruiz Alvarado, M. Karmo, E. Runge, and W. G. Schmidt. “InP and AlInP(001)(2 × 4) Surface Oxidation from Density Functional Theory”. In: *ACS Omega* 6.9 (Mar. 2021), pp. 6297–6304.

[164] F. Fuchs, W. G. Schmidt, and F. Bechstedt. “Initial Stage of Si(001) Surface Oxidation from First-Principles Calculations”. In: *The Journal of Physical Chemistry B* 109.37 (Sept. 2005), pp. 17649–17653.

[165] E. Placidi, C. Hogan, F. Arciprete, M. Fanfoni, F. Patella, R. Del Sole, and A. Balzarotti. “Adsorption of Molecular Oxygen on GaAs(001) Studied Using High-Resolution Electron Energy-Loss Spectroscopy”. In: *Physical Review B* 73.20 (May 2006), p. 205345.

[166] S. I. Yi, P. Kruse, M. Hale, and A. C. Kummel. “Adsorption of Atomic Oxygen on GaAs(001)-(2×4) and the Resulting Surface Structures”. In: *The Journal of Chemical Physics* 114.7 (Feb. 2001), pp. 3215–3223.

[167] S. Jeon, H. Kim, W. A. Goddard, and H. A. Atwater. “DFT Study of Water Adsorption and Decomposition on a Ga-Rich GaP(001)(2×4) Surface”. In: *The Journal of Physical Chemistry C* 116.33 (Aug. 2012), pp. 17604–17612.

[168] D. Friedrich, P. Sippel, O. Supplie, T. Hannappel, and R. Eichberger. “Two-Photon Photoemission Spectroscopy for Studying Energetics and Electron Dynamics at Semiconductor Interfaces”. In: *physica status solidi (a)* 216.8 (Apr. 2019), p. 1800738.

[169] I. A. Ruiz Alvarado and W. G. Schmidt. “Water/InP(001) from Density Functional Theory”. In: *ACS Omega* 7.23 (June 2022), pp. 19355–19364.

[170] D. Sheppard, R. Terrell, and G. Henkelman. “Optimization Methods for Finding Minimum Energy Paths”. In: *The Journal of Chemical Physics* 128.13 (Apr. 2008), p. 134106.

[171] D. Sheppard and G. Henkelman. “Paths to Which the Nudged Elastic Band Converges”. In: *Journal of Computational Chemistry* 32.8 (June 2011), pp. 1769–1771.

[172] D. Sheppard, P. Xiao, W. Chemelewski, D. D. Johnson, and G. Henkelman. “A Generalized Solid-State Nudged Elastic Band Method”. In: *The Journal of Chemical Physics* 136.7 (Feb. 2012), p. 074103.

[173] X. Zhang and S. Ptasinska. “Dissociative Adsorption of Water on an H₂O/GaAs(100) Interface: In Situ Near-Ambient Pressure XPS Studies”. In: *The Journal of Physical Chemistry C* 118.8 (Feb. 2014), pp. 4259–4266.

[174] J. K. Nørskov, J. Rossmeisl, A. Logadottir, L. Lindqvist, J. R. Kitchin, T. Bligaard, and H. Jónsson. “Origin of the Overpotential for Oxygen Reduction at a Fuel-Cell Cathode”. In: *The Journal of Physical Chemistry B* 108.46 (Nov. 2004), pp. 17886–17892.

[175] C. Dues, W. G. Schmidt, and S. Sanna. “Water Splitting Reaction at Polar Lithium Niobate Surfaces”. In: *ACS Omega* 4.2 (Feb. 2019), pp. 3850–3859.

[176] Q. Liang, G. Brocks, and A. Bieberle-Hütter. “Oxygen Evolution Reaction (OER) Mechanism under Alkaline and Acidic Conditions”. In: *Journal of Physics: Energy* 3.2 (Apr. 2021), p. 026001.

[177] K. Srinivasu and S. K. Ghosh. “Photocatalytic Splitting of Water on S-Triazine Based Graphitic Carbon Nitride: An Ab Initio Investigation”. In: *Journal of Materials Chemistry A* 3.45 (2015), pp. 23011–23016.

[178] J. Rossmeisl, A. Logadottir, and J. Nørskov. “Electrolysis of Water on (Oxidized) Metal Surfaces”. In: *Chemical Physics* 319.1-3 (Dec. 2005), pp. 178–184.

[179] J. Nørskov, T. Bligaard, A. Logadottir, S. Bahn, L. Hansen, M. Bollinger, H. Bengaard, B. Hammer, Z. Sljivancanin, M. Mavrikakis, Y. Xu, S. Dahl, and C. Jacobsen. “Universality in Heterogeneous Catalysis”. In: *Journal of Catalysis* 209.2 (July 2002), pp. 275–278.

[180] V. I. Birss and A. Damjanovic. “Oxygen Evolution at Platinum Electrodes in Alkaline Solutions: I. Dependence on Solution pH and Oxide Film Thickness”. In: *Journal of The Electrochemical Society* 134.1 (Jan. 1987), pp. 113–117.

[181] B. C. Wood, E. Schwegler, W. I. Choi, and T. Ogitsu. “Hydrogen-Bond Dynamics of Water at the Interface with InP/GaP(001) and the Implications for Photoelectrochemistry”. In: *Journal of the American Chemical Society* 135.42 (Oct. 2013), pp. 15774–15783.

[182] L. Pavesi, F. Piazza, A. Rudra, J. F. Carlin, and M. Ilegems. “Temperature Dependence of the InP Band Gap from a Photoluminescence Study”. In: *Physical Review B* 44.16 (Oct. 1991), pp. 9052–9055.

[183] O. Supplie, M. M. May, H. Stange, C. Höhn, H.-J. Lewerenz, and T. Hannappel. “Materials for Light-Induced Water Splitting: *In Situ* Controlled Surface Preparation of GaPN Epilayers Grown Lattice-Matched on Si(100)”. In: *Journal of Applied Physics* 115.11 (Mar. 2014), p. 113509.

[184] T. E. Fischer. “Photoelectric Emission and Work Function of InP”. In: *Physical Review* 142.2 (Feb. 1966), pp. 519–523.

[185] Á. Valdés, Z.-W. Qu, G.-J. Kroes, J. Rossmeisl, and J. K. Nørskov. “Oxidation and Photo-Oxidation of Water on TiO₂ Surface”. In: *The Journal of Physical Chemistry C* 112.26 (July 2008), pp. 9872–9879.

[186] J. Wirth, S. Monturet, T. Klamroth, and P. Saalfrank. “Adsorption and (Photo-) Electrochemical Splitting of Water on Rutile Ruthenium Dioxide”. In: *EPL (Europhysics Letters)* 93.6 (Mar. 2011), p. 68001.

[187] L. Gao, Y. Cui, R. H. J. Vervuurt, D. Van Dam, R. P. J. Van Veldhoven, J. P. Hofmann, A. A. Bol, J. E. M. Haverkort, P. H. L. Notten, E. P. A. M. Bakkers, and E. J. M. Hensen. “High-Efficiency InP-Based Photocathode for Hydrogen Production by Interface Energetics Design and Photon Management”. In: *Advanced Functional Materials* 26.5 (Feb. 2016), pp. 679–686.

[188] W.-H. Cheng, M. H. Richter, M. M. May, J. Ohlmann, D. Lackner, F. Dimroth, T. Hannappel, H. A. Atwater, and H.-J. Lewerenz. “Monolithic Photoelectrochemical Device for Direct Water Splitting with 19% Efficiency”. In: *ACS Energy Letters* 3.8 (Aug. 2018), pp. 1795–1800.

[189] D. S. Rosenzweig, M. N. L. Hansemann, M. Schnedler, Ph. Ebert, and H. Eisele. “Atomically Resolved Study of Initial Stages of Hydrogen Etching and Adsorption on GaAs(110)”. In: *Physical Review Materials* 6.12 (Dec. 2022), p. 124603.

[190] D. S. Rosenzweig, M. Schnedler, R. E. Dunin-Borkowski, Ph. Ebert, and H. Eisele. “Morphologic and Electronic Changes Induced by Thermally Supported Hydrogen Cleaning of GaAs(110) Facets”. In: *Journal of Vacuum Science & Technology B* 41.4 (July 2023), p. 044202.

[191] Ph. Ebert, K. Urban, L. Aballe, C. H. Chen, K. Horn, G. Schwarz, J. Neugebauer, and M. Scheffler. “Symmetric Versus Nonsymmetric Structure of the Phosphorus Vacancy on InP(110)”. In: *Physical Review Letters* 84.25 (June 2000), pp. 5816–5819.

[192] M. C. Qian, M. Göthelid, B. Johansson, and S. Mirbt. “Atomic and Electronic Properties of Anion Vacancies on the (110) Surfaces of InP, InAs, and InSb”. In: *Physical Review B* 66.15 (Oct. 2002), p. 155326.

[193] M. Hedström, A. Schindlmayr, G. Schwarz, and M. Scheffler. “Quasiparticle Corrections to the Electronic Properties of Anion Vacancies at GaAs(110) and InP(110)”. In: *Physical Review Letters* 97.22 (Nov. 2006), p. 226401.

[194] G. Chen, S. F. Cheng, D. J. Tobin, L. Li, K. Raghavachari, and R. F. Hicks. “Indium Phosphide (001)-(2×1): Direct Evidence for a Hydrogen-Stabilized Surface Reconstruction”. In: *Physical Review B* 68.12 (Sept. 2003), p. 121303.

[195] T. Letzig, H.-J. Schimper, T. Hannappel, and F. Willig. “P - H Bonds in the Surface Unit Cell of P-rich Ordered InP(001) Grown by Metalorganic Chemical Vapor Deposition”. In: *Physical Review B* 71.3 (Jan. 2005), p. 033308.

[196] D. C. Moritz, I. A. Ruiz Alvarado, M. A. Zare Pour, A. Paszuk, T. Frieß, E. Runge, J. P. Hofmann, T. Hannappel, W. G. Schmidt, and W. Jaegermann. “P-Terminated InP (001) Surfaces: Surface Band Bending and Reactivity to Water”. In: *ACS Applied Materials & Interfaces* 14.41 (Oct. 2022), pp. 47255–47261.

[197] R. Sciotto, I. A. Ruiz Alvarado, and W. G. Schmidt. “Substrate Doping and Defect Influence on P-Rich InP(001):H Surface Properties”. In: *Surfaces* 7.1 (Jan. 2024), pp. 79–87.

[198] C. Freysoldt, B. Grabowski, T. Hickel, J. Neugebauer, G. Kresse, A. Janotti, and C. G. Van De Walle. “First-Principles Calculations for Point Defects in Solids”. In: *Reviews of Modern Physics* 86.1 (Mar. 2014), pp. 253–305.

[199] S. Sanna, Th. Frauenheim, and U. Gerstmänn. “Validity of the Slater-Janak Transition-State Model within the LDA + U Approach”. In: *Physical Review B* 78.8 (Aug. 2008), p. 085201.

[200] F. Gallino, G. Pacchioni, and C. Di Valentin. “Transition Levels of Defect Centers in ZnO by Hybrid Functionals and Localized Basis Set Approach”. In: *The Journal of Chemical Physics* 133.14 (Oct. 2010), p. 144512.

[201] W. Shockley and H. J. Queisser. “Detailed Balance Limit of Efficiency of P-n Junction Solar Cells”. In: *Journal of Applied Physics* 32.3 (Mar. 1961), pp. 510–519.

[202] H. C. Casey and M. B. Panish. “Heterostructure Lasers”. Quantum Electronics, Principles and Applications. New York: Academic Press, 1978.

[203] L. H. Yu, K. L. Yao, and Z. L. Liu. “Electronic Band Structures of Filled Tetrahedral Semiconductor LiMgP and Zinc-Blende AlP”. In: *Solid State Communications* 135.1 (July 2005), pp. 124–128.

[204] H. Döscher, O. Supplie, M. M. May, P. Sippel, C. Heine, A. G. Muñoz, R. Eichberger, H.-J. Lewerenz, and T. Hannappel. “Epitaxial III–V Films and Surfaces for Photoelectrocatalysis”. In: *ChemPhysChem* 13.12 (Aug. 2012), pp. 2899–2909.

[205] D. L. Lepkowski, T. Kasher, J. T. Boyer, D. J. Chmielewski, T. J. Grassman, and S. A. Ringel. “The Critical Role of AlInP Window Design in III–V Rear-Emitter Solar Cells”. In: *IEEE Journal of Photovoltaics* 10.3 (May 2020), pp. 758–764.

[206] H. Helmers, E. Lopez, O. Höhn, D. Lackner, J. Schön, M. Schauerte, M. Schachtner, F. Dimroth, and A. W. Bett. “68.9% Efficient GaAs-Based Photonic Power Conversion Enabled by Photon Recycling and Optical Resonance”. In: *physica status solidi (RRL) – Rapid Research Letters* 15.7 (2021), p. 2100113.

[207] T. Hannappel, S. Shekarabi, W. Jaegermann, E. Runge, J. P. Hofmann, R. van de Krol, M. M. May, A. Paszuk, F. Hess, A. Bergmann, A. Bund, C. Cierpka, C. Dreßler, F. Dionigi, D. Friedrich, M. Favaro, S. Krischok, M. Kurniawan, K. Lüdge, Y. Lei, B. Roldán Cuenya, P. Schaaf, R. Schmidt-Grund, W. G. Schmidt, P. Strasser, E. Unger, M. F. Vasquez Montoya, D. Wang, and H. Zhang. “Integration of Multijunction Absorbers and Catalysts for Efficient Solar-Driven Artificial Leaf Structures: A Physical and Materials Science Perspective”. In: *Solar RRL* 8.11 (2024), p. 2301047.

[208] C.-W. Kim, G.-Y. Park, J.-C. Shin, and H.-J. Kim. “Efficiency Enhancement of GaAs Single-Junction Solar Cell by Nanotextured Window Layer”. In: *Applied Sciences* 12.2 (Jan. 2022), p. 601.

[209] A. Abdollahi, M. M. Golzan, and K. Aghayar. “First-Principles Investigation of Electronic Properties of Al_xIn_{1-x}P Semiconductor Alloy”. In: *Journal of Materials Science* 51.15 (Aug. 2016), pp. 7343–7354.

[210] D. A. Beaton, T. Christian, K. Alberi, A. Mascarenhas, K. Mukherjee, and E. A. Fitzgerald. “Determination of the Direct to Indirect Bandgap Transition Composition in Al_xIn_{1-x}P”. In: *Journal of Applied Physics* 114.20 (Nov. 2013), p. 203504.

[211] L. Meier, C. Braun, T. Hannappel, and W. G. Schmidt. “Band Alignment at Ga In_{1-x}P/Al_xIn_{1-x}P Alloy Interfaces from Hybrid Density Functional Theory Calculations”. In: *physica status solidi (b)* 258.2 (2021), p. 2000463.

[212] J. S. Cheong, J. S. Ng, A. B. Krysa, J. S. L. Ong, and J. P. R. David. “Determination of Absorption Coefficients in AlInP Lattice Matched to GaAs”. In: *Journal of Physics D: Applied Physics* 48.40 (Oct. 2015), p. 405101.

[213] L. Meier and W. G. Schmidt. “GaInP/AlInP(001) Interfaces from Density Functional Theory”. In: *physica status solidi (b)* 259.1 (Jan. 2022), p. 2100462.

[214] Z. Jinghua, T. Xiaohong, and T. Jinghua. “Atomic Ordering of AlInP Grown by MOVPE at Different Temperatures in Pure Ambient N₂”. In: *CrystEngComm* 11.6 (2009), p. 1068.

[215] W. Yuan and D. C. Hall. “Variable-Angle Spectroscopic Ellipsometry of InAlP Native Oxide Dielectric Layers for GaAs Metal–Oxide–Semiconductor Field Effect Transistor Applications”. In: *Journal of Applied Physics* 113.10 (Mar. 2013), p. 103515.

[216] R. M. France, W. E. McMahon, J. Kang, M. A. Steiner, and J. F. Geisz. “*In Situ Measurement of CuPt Alloy Ordering Using Strain Anisotropy*”. In: *Journal of Applied Physics* 115.5 (Feb. 2014), p. 053502.

[217] G. Martín, C. Coll, L. López-Conesa, J. M. Rebled, E. Barrigón, I. García, I. Rey-Stolle, C. Algora, A. Cornet, S. Estradé, and F. Peiró. “*Understanding the Anisotropy in the Electrical Conductivity of CuPt_B -Type Ordered GaInP Thin Films by Combining In Situ TEM Biasing and First Principles Calculations*”. In: *ACS Applied Electronic Materials* 4.7 (July 2022), pp. 3478–3485.

[218] S. B. Zhang, S. Froyen, and A. Zunger. “*Surface Dimerization Induced CuPt B versus CuPt A Ordering of GaInP Alloys*”. In: *Applied Physics Letters* 67.21 (Nov. 1995), pp. 3141–3143.

[219] S. Froyen and A. Zunger. “*Surface-Induced Ordering in GaInP*”. In: *Physical Review Letters* 66.16 (Apr. 1991), pp. 2132–2135.

[220] W. Schmidt. “*(4×2) and (2×4) Reconstructions of GaAs and InP(001) Surfaces*”. In: *Applied Physics A: Materials Science & Processing* 65.6 (Dec. 1997), pp. 581–586.

[221] M. A. Zare Pour, S. Shekarabi, I. A. Ruiz Alvarado, J. Diederich, Y. Gao, A. Paszuk, D. C. Moritz, W. Jaegermann, D. Friedrich, R. Van De Krol, W. G. Schmidt, and T. Hannappel. “*Exploring Electronic States and Ultrafast Electron Dynamics in AlInP Window Layers: The Role of Surface Reconstruction*”. In: *Advanced Functional Materials* (Mar. 2025), p. 2423702.

[222] J. D. Cox and J. D. Cox, eds. “*CODATA Key Values for Thermodynamics: Final Report of the CODATA Task Group on Key Values for Thermodynamics*”. CODATA Series on Thermodynamic Properties. New York: Hemisphere Publ. Corp, 1989.

[223] E. Cordfunke, R. Konings, and W. Ouweltjes. “*The Standard Enthalpy of Formation of In₂O₃*”. In: *The Journal of Chemical Thermodynamics* 23.5 (May 1991), pp. 451–454.

[224] M. Graham, S. Moisa, G. Sproule, X. Wu, J. Fraser, P. Barrios, D. Landheer, A. Thorpe, and M. Extavour. “*Thermal Oxidation of InAlP*”. In: *Materials at High Temperatures* 20.3 (Jan. 2003), pp. 277–280.

[225] D. E. Aspnes and A. A. Studna. “*Anisotropies in the Above—Band-Gap Optical Spectra of Cubic Semiconductors*”. In: *Physical Review Letters* 54.17 (Apr. 1985), pp. 1956–1959.

[226] P. Weightman, D. S. Martin, R. J. Cole, and T. Farrell. “*Reflection Anisotropy Spectroscopy*”. In: *Reports on Progress in Physics* 68.6 (June 2005), pp. 1251–1341.

[227] A. Lastras-Martínez, J. Ortega-Gallegos, L. E. Guevara-Macías, O. Nuñez-Olvera, R. E. Balderas-Navarro, L. F. Lastras-Martínez, L. A. Lastras-Montaño, and M. A. Lastras-Montaño. “*Real-Time Reflectance-Difference Spectroscopy of GaAs Molecular Beam Epitaxy Homoepitaxial Growth*”. In: *APL Materials* 2.3 (Mar. 2014), p. 032107.

[228] M. Zorn, J. Jönsson, A. Krost, W. Richter, J.-T. Zettler, K. Ploska, and F. Reinhardt. “*In-Situ Reflectance Anisotropy Studies of Ternary III–V Surfaces and Growth of Heterostructures*”. In: *Journal of Crystal Growth* 145.1-4 (Dec. 1994), pp. 53–60.

[229] K. Haberland, A. Bhattacharya, M. Zorn, M. Weyers, J. T. Zettler, and W. Richter. “*MOVPE Growth of (Al,Ga)InP-based Laser Structures Monitored by Real-Time Reflectance Anisotropy Spectroscopy*”. In: *Journal of Electronic Materials* 29.4 (Apr. 2000), pp. 468–472.

[230] C. Krahmer, M. Philippens, M. Schubert, and K. Streubel. “MOVPE Growth Investigations of Doping and Ordering in AlGaAs and GaInP with Reflectance Anisotropy Spectroscopy”. In: *Journal of Crystal Growth* 298 (Jan. 2007), pp. 18–22.

[231] O. Supplie, A. Heinisch, M. Sugiyama, and T. Hannappel. “Optical in Situ Quantification of the Arsenic Content in GaAsP Graded Buffer Layers for III-V-on-Si Tandem Absorbers during MOVPE Growth”. In: *2018 IEEE 7th World Conference on Photovoltaic Energy Conversion (WCPEC) (A Joint Conference of 45th IEEE PVSC, 28th PVSEC & 34th EU PVSEC)*. Waikoloa Village, HI: IEEE, June 2018, pp. 3923–3926.

[232] M. Zorn, P. Kurpas, A. I. Shkrebtii, B. Junno, A. Bhattacharya, K. Knorr, M. Weyers, L. Samuelson, J. T. Zettler, and W. Richter. “Correlation of InGa(001) Surface Structure during Growth and Bulk Ordering”. In: *Physical Review B* 60.11 (Sept. 1999), pp. 8185–8190.

[233] A. I. Shkrebtii, N. Esser, W. Richter, W. G. Schmidt, F. Bechstedt, B. O. Fimland, A. Kley, and R. Del Sole. “Reflectance Anisotropy of GaAs(100): Theory and Experiment”. In: *Physical Review Letters* 81.3 (July 1998), pp. 721–724.

[234] N. Esser, W. G. Schmidt, J. Bernholc, A. M. Frisch, P. Vogt, M. Zorn, M. Pristovsek, W. Richter, F. Bechstedt, Th. Hannappel, and S. Visbeck. “GaP(001) and InP(001): Reflectance Anisotropy and Surface Geometry”. In: *Journal of Vacuum Science & Technology B: Microelectronics and Nanometer Structures* 17.4 (1999), p. 1691.

[235] M. Landmann, E. Rauls, W. G. Schmidt, M. D. Neumann, E. Speiser, and N. Esser. “GaN m-Plane: Atomic Structure, Surface Bands, and Optical Response”. In: *Physical Review B* 91.3 (Jan. 2015), p. 035302.

[236] M. M. May and M. Sprik. “Water Adsorption on the P-rich GaP(100) Surface: Optical Spectroscopy from First Principles”. In: *New Journal of Physics* 20.3 (Mar. 2018), p. 033031.

[237] I. A. Ruiz Alvarado, M. A. Zare Pour, T. Hannappel, and W. G. Schmidt. “Structural Fingerprints in the Reflectance Anisotropy of AlInP(001)”. In: *Physical Review B* 108.4 (July 2023), p. 045410.

[238] S.-H. Wei and A. Zunger. “Fingerprints of CuPt Ordering in III-V Semiconductor Alloys: Valence-band Splittings, Band-Gap Reduction, and x-Ray Structure Factors”. In: *Physical Review B* 57.15 (Apr. 1998), pp. 8983–8988.

[239] T. M. Christian, D. A. Beaton, K. Mukherjee, K. Alberi, E. A. Fitzgerald, and A. Mascarenhas. “Amber-Green Light-Emitting Diodes Using Order-Disorder Al_xIn_{1-x}P Heterostructures”. In: *Journal of Applied Physics* 114.7 (Aug. 2013), p. 074505.

[240] M. Rohlffing and S. G. Louie. “Electron-Hole Excitations in Semiconductors and Insulators”. In: *Physical Review Letters* 81.11 (Sept. 1998), pp. 2312–2315.

[241] S. Turcotte and M. Daraselia. “Generalized Model of the Dielectric Function of AlInGaP Alloys”. In: *Journal of Applied Physics* 113.9 (Mar. 2013), p. 093103.

[242] S. Visbeck, T. Hannappel, M. Zorn, J.-T. Zettler, and F. Willig. “Temperature Dependence and Origin of InP(100) Reflectance Anisotropy down to 20 K”. In: *Physical Review B* 63.24 (May 2001), p. 245303.

[243] J. E. Bernard, S. Froyen, and A. Zunger. “Spontaneous Surface-Induced Long-Range Order in Ga_{0.5}In_{0.5}P Alloys”. In: *Physical Review B* 44.20 (Nov. 1991), pp. 11178–11195.

[244] W. G. Schmidt and J. Bernholc. “Step-Induced Optical Anisotropy of Si(111):H Surfaces”. In: *Physical Review B* 61.11 (Mar. 2000), pp. 7604–7608.

[245] A. Mascarenhas, S. Kurtz, A. Kibbler, and J. M. Olson. “Polarized Band-Edge Photoluminescence and Ordering in Ga_{0.52}In_{0.48}P”. In: *Physical Review Letters* 63.19 (Nov. 1989), pp. 2108–2111.

[246] P. V. C. Medeiros, S. Stafström, and J. Björk. “Effects of Extrinsic and Intrinsic Perturbations on the Electronic Structure of Graphene: Retaining an Effective Primitive Cell Band Structure by Band Unfolding”. In: *Physical Review B* 89.4 (Jan. 2014), p. 041407.

[247] P. V. C. Medeiros, S. S. Tsirkin, S. Stafström, and J. Björk. “Unfolding Spinor Wave Functions and Expectation Values of General Operators: Introducing the Unfolding-Density Operator”. In: *Physical Review B* 91.4 (Jan. 2015), p. 041116.

[248] T. Kim, S. Hwang, J. Byun, D. Aspnes, E. Lee, J. Song, C.-T. Liang, Y.-C. Chang, H. Park, J. Choi, J. Kim, Y. Kang, J. Park, and Y. Kim. “Dielectric Functions and Interband Transitions of In_xAl_{1-x}P Alloys”. In: *Current Applied Physics* 14.9 (Sept. 2014), pp. 1273–1276.

[249] L Töben, T Hannappel, K Möller, H.-J Crawack, C Pettenkofer, and F Willig. “RDS, LEED and STM of the P-rich and Ga-rich Surfaces of GaP(100)”. In: *Surface Science* 494.1 (Nov. 2001), pp. L755–L760.

[250] E. Gillan. “Precursor Chemistry – Group 13 Nitrides and Phosphides (Al, Ga, and In)”. In: *Comprehensive Inorganic Chemistry II*. Elsevier, 2013, pp. 969–1000.

[251] S. Chandola, K. Hinrichs, M. Gensch, N. Esser, S. Wippermann, W. G. Schmidt, F. Bechstedt, K. Fleischer, and J. F. McGilp. “Structure of Si(111)-In Nanowires Determined from the Midinfrared Optical Response”. In: *Physical Review Letters* 102.22 (June 2009), p. 226805.

[252] H. I. J. Lewis, L. Qiao, J. S. Cheong, A. N. A. P. Baharuddin, A. B. Krysa, B. K. Ng, J. E. Green, and J. P. R. David. “Impact Ionization Coefficients in (Al_x Ga_{1-x})_{0.52}In_{0.48}P and Al_x Ga_{1-x}As Lattice-Matched to GaAs”. In: *IEEE Transactions on Electron Devices* 68.8 (Aug. 2021), pp. 4045–4050.

List of Publications

- [1] I. A. Ruiz Alvarado, M. Karmo, E. Runge, and W. G. Schmidt. “InP and AlInP(001)(2 \times 4) Surface Oxidation from Density Functional Theory”. In: *ACS Omega* 6.9 (Mar. 2021), pp. 6297–6304.
- [2] M. Karmo, I. A. Ruiz Alvarado, W. G. Schmidt, and E. Runge. “Reconstructions of the As-Terminated GaAs(001) Surface Exposed to Atomic Hydrogen”. In: *ACS Omega* 7.6 (Feb. 2022), pp. 5064–5068.
- [3] I. A. Ruiz Alvarado and W. G. Schmidt. “Water/InP(001) from Density Functional Theory”. In: *ACS Omega* 7.23 (June 2022), pp. 19355–19364.
- [4] D. C. Moritz, I. A. Ruiz Alvarado, M. A. Zare Pour, A. Paszuk, T. Frieß, E. Runge, J. P. Hofmann, T. Hannappel, W. G. Schmidt, and W. Jaegermann. “P-Terminated InP (001) Surfaces: Surface Band Bending and Reactivity to Water”. In: *ACS Applied Materials & Interfaces* 14.41 (Oct. 2022), pp. 47255–47261.
- [5] L. J. Glahn, I. A. Ruiz Alvarado, S. Neufeld, M. A. Zare Pour, A. Paszuk, D. Osthimer, S. Shekarabi, O. Romanyuk, D. C. Moritz, J. P. Hofmann, W. Jaegermann, T. Hannappel, and W. G. Schmidt. “Clean and Hydrogen-Adsorbed AlInP(001) Surfaces: Structures and Electronic Properties”. In: *physica status solidi (b)* 259.11 (Nov. 2022), p. 2200308.
- [6] I. A. Ruiz Alvarado, M. A. Zare Pour, T. Hannappel, and W. G. Schmidt. “Structural Fingerprints in the Reflectance Anisotropy of AlInP(001)”. In: *Physical Review B* 108.4 (July 2023), p. 045410.
- [7] R. Sciotto, I. A. Ruiz Alvarado, and W. G. Schmidt. “Substrate Doping and Defect Influence on P-Rich InP(001):H Surface Properties”. In: *Surfaces* 7.1 (Jan. 2024), pp. 79–87.
- [8] V. Devaraj, I. A. Ruiz Alvarado, J.-M. Lee, J.-W. Oh, U. Gerstmann, W. G. Schmidt, and T. Zentgraf. “Self-Assembly of Isolated Plasmonic Dimers with Sub-5 Nm Gaps on a Metallic Mirror”. In: *Nanoscale Horizons* (2025), 10.1039.D4NH00546E.
- [9] J. Diederich, J. Velasquez Rojas, M. A. Zare Pour, I. A. Ruiz Alvarado, A. Paszuk, R. Sciotto, C. Höhn, K. Schwarzburg, D. Osthimer, R. Eichberger, W. G. Schmidt, T. Hannappel, R. Van De Krol, and D. Friedrich. “Unraveling Electron Dynamics in P-Type Indium Phosphide (100): A Time-Resolved Two-Photon Photoemission Study”. In: *Journal of the American Chemical Society* 146.13 (Apr. 2024), pp. 8949–8960.

- [10] J. Diederich, J. V. Rojas, A. Paszuk, M. A. Zare Pour, C. Höhn, **I. A. Ruiz Alvarado**, K. Schwarzburg, D. Ostheimer, R. Eichberger, W. G. Schmidt, T. Hannappel, R. Van De Krol, and D. Friedrich. “Ultrafast Electron Dynamics at the P-rich Indium Phosphide/TiO₂ Interface”. In: *Advanced Functional Materials* 34.49 (Dec. 2024), p. 2409455.
- [11] **I. A. Ruiz Alvarado**, C. Dresßler, and W. G. Schmidt. “Band Alignment at InP/TiO₂ Interfaces from Density-Functional Theory”. In: *Journal of Physics: Condensed Matter* 37.7 (Feb. 2025), p. 075001.
- [12] M. A. Zare Pour, S. Shekarabi, **I. A. Ruiz Alvarado**, J. Diederich, Y. Gao, A. Paszuk, D. C. Moritz, W. Jaegermann, D. Friedrich, R. Van De Krol, W. G. Schmidt, and T. Hannappel. “Exploring Electronic States and Ultrafast Electron Dynamics in AlInP Window Layers: The Role of Surface Reconstruction”. In: *Advanced Functional Materials* (Mar. 2025), p. 2423702.
- [13] J. Diederich, A. Paszuk, M. A. Zare Pour, D. Suresh Babu, J. Velasquez Rojas, **I. A. Ruiz Alvarado**, M. Krenz, C. Höhn, Y. Gao, K. Schwarzburg, D. Ostheimer, R. Eichberger, W. G. Schmidt, T. Hannappel, R. Van De Krol, and D. Friedrich. “Ultrafast Electron Dynamics at the Water-Adsorbed InP Surface (Submitted)”. 2025.

Additional scientific publications

- [1] M. Krenz, A. Bocchini, T. Biktagirov, A. Kozub, S. Badalov, S. Neufeld, **I. A. Ruiz Alvarado**, U. Gerstmann, and W. G. Schmidt. “Polaron Formation Dynamics in Lithium Niobate from Massively Parallel Ab-Initio Simulations”. In: *High Performance Computing in Science and Engineering '22: Transactions of the High Performance Computing Center, Stuttgart (HLRS) 2022*. Ed. by W. E. Nagel, D. Kröner, and M. Resch. Cham: Springer, 2024, pp. 115–127.

Conference proceedings

- [1] **I. A. Ruiz Alvarado** and W. G. Schmidt. “Water/InP(001) from Density Functional Theory”. In: *DPG Spring Meeting*. Dresden, Germany: (Poster), Mar. 2023.
- [2] R. Sciotto, **I. A. Ruiz Alvarado**, and W. G. Schmidt. “Fermi-level pinning at InP(001):H surfaces”. In: *DPG Spring Meeting*. Dresden, Germany: (Poster), Mar. 2023.
- [3] **I. A. Ruiz Alvarado**, L. J. Glahn, M. Krenz, A. Bocchini, K. Franzke, U. Gerstmann, and W. G. Schmidt. “Understanding AlInP(001) Surfaces from Massively Parallel Ab-Initio Simulations”. In: *26th Results and Review Workshop of the HLRS*. Stuttgart, Germany: (Talk), Oct. 2023.
- [4] **I. A. Ruiz Alvarado**, M. A. Zare Pour, T. Hannappel, and W. G. Schmidt. “Structural fingerprints in the reflectance anisotropy of AlInP(001)”. In: *OSI 14*. Mauterndorf, Austria: (Poster), Feb. 2024.
- [5] R. Sciotto, **I. A. Ruiz Alvarado**, and W. G. Schmidt. “Substrate doping and defect influence on P-rich InP(001):H surface properties”. In: *DPG Spring Meeting*. Berlin, Germany: (Poster), Mar. 2024.

Chapter A

Relaxed geometries of relevant surfaces

The most relevant surface models for the oxidized InP and AlInP discussed in Section 5.2 and 7.2 are presented here. The number in the notation indicates the total number of O atoms adsorbed (a). Figures adapted from the supporting information of Ref. [163]

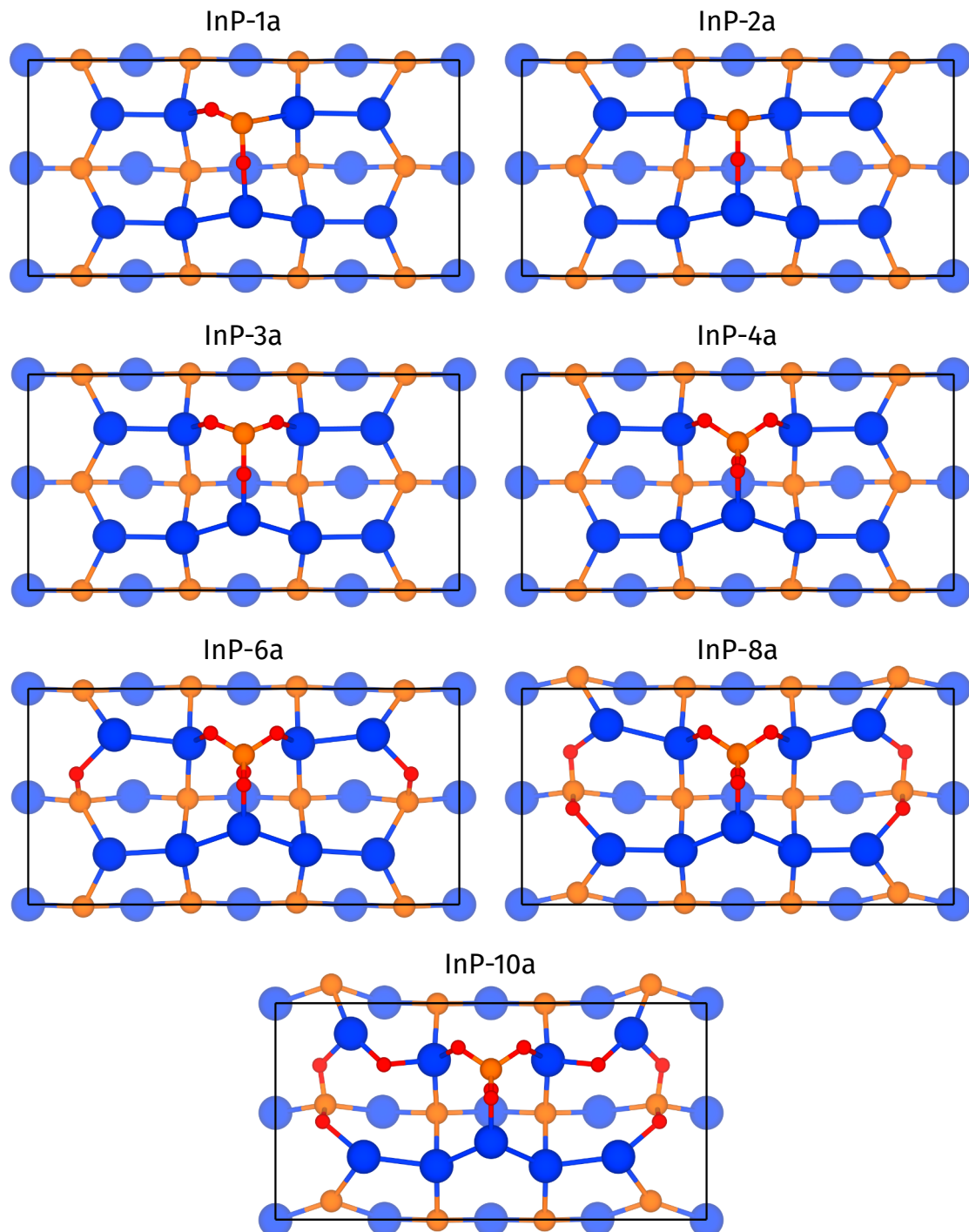


Figure A.1: Top view of energetically favorable O adsorption and substitution structures were calculated for the InP (2x4)-MD surface.

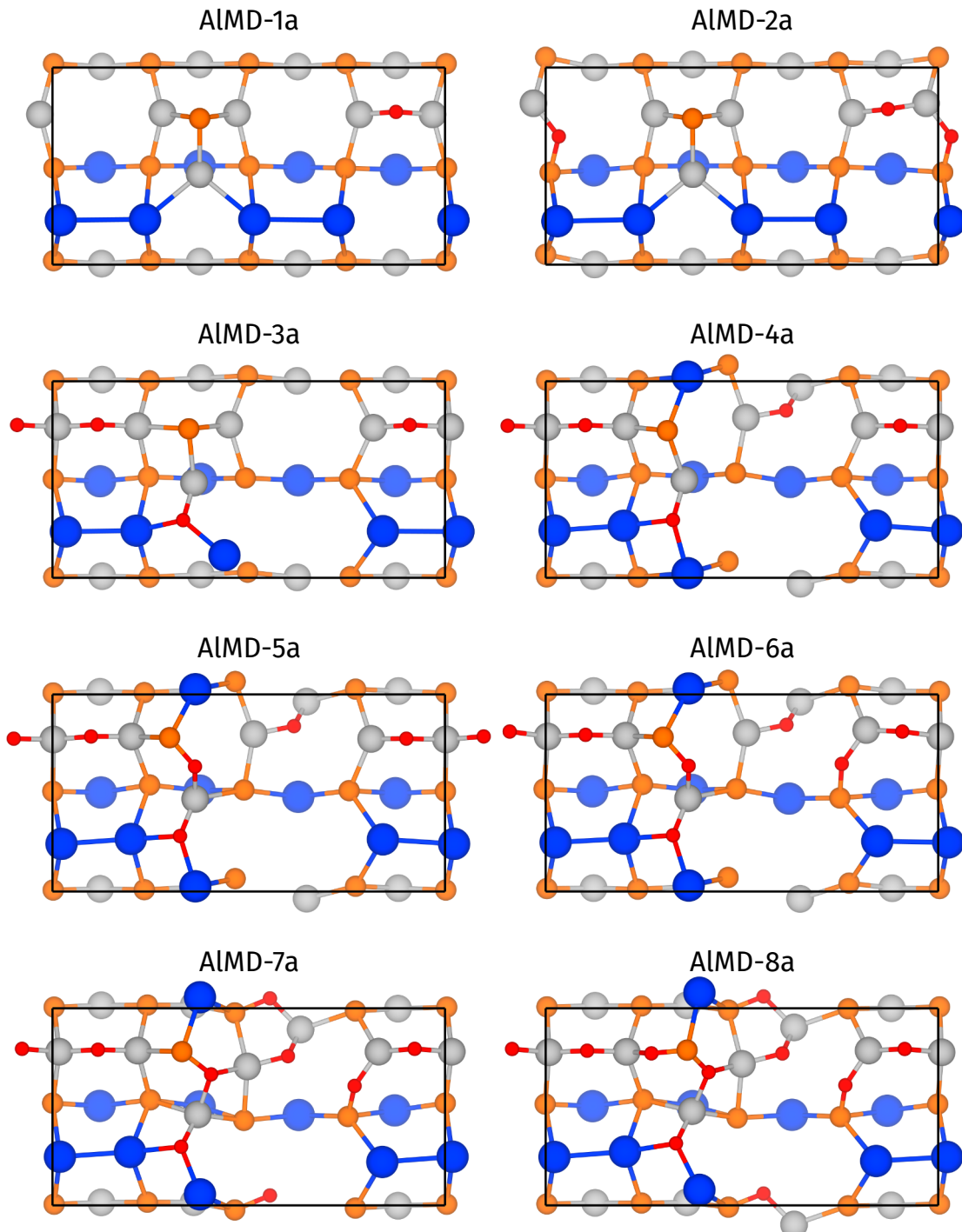


Figure A.2: Top view of energetically favorable O adsorption structures were calculated for the AlInP (2×4)-AlMD surface.

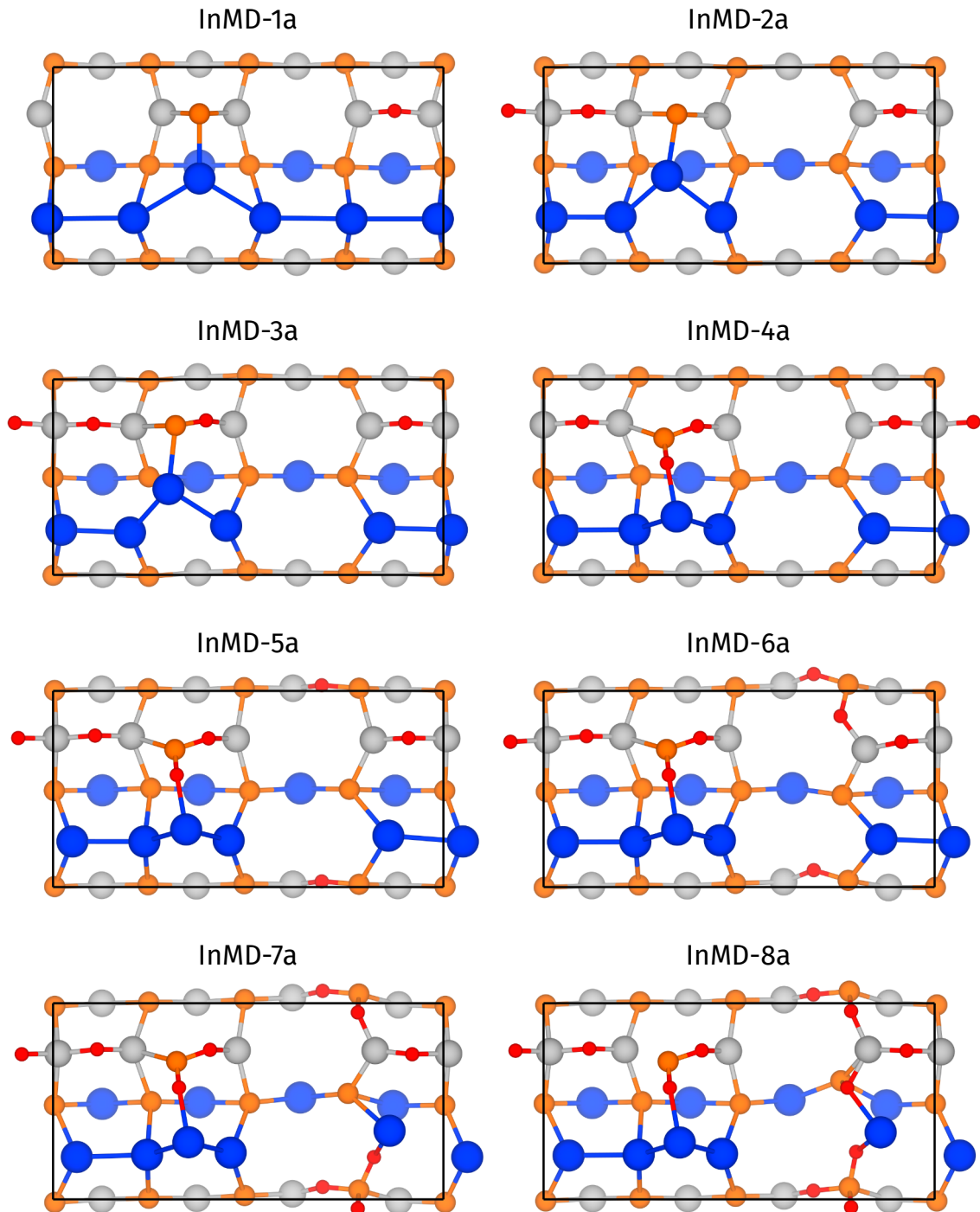


Figure A.3: Top view of energetically favorable O adsorption structures were calculated for the AlInP (2x4)-InMD surface.

Chapter B

Electronic structures of relevant surfaces

The electronic structure for the most relevant surface models for the oxidized InP and AlInP discussed in Section 5.2 and 7.2 are presented here. The DOS is calculated in the DFT level. Figures adapted from the supporting information of Ref. [163]

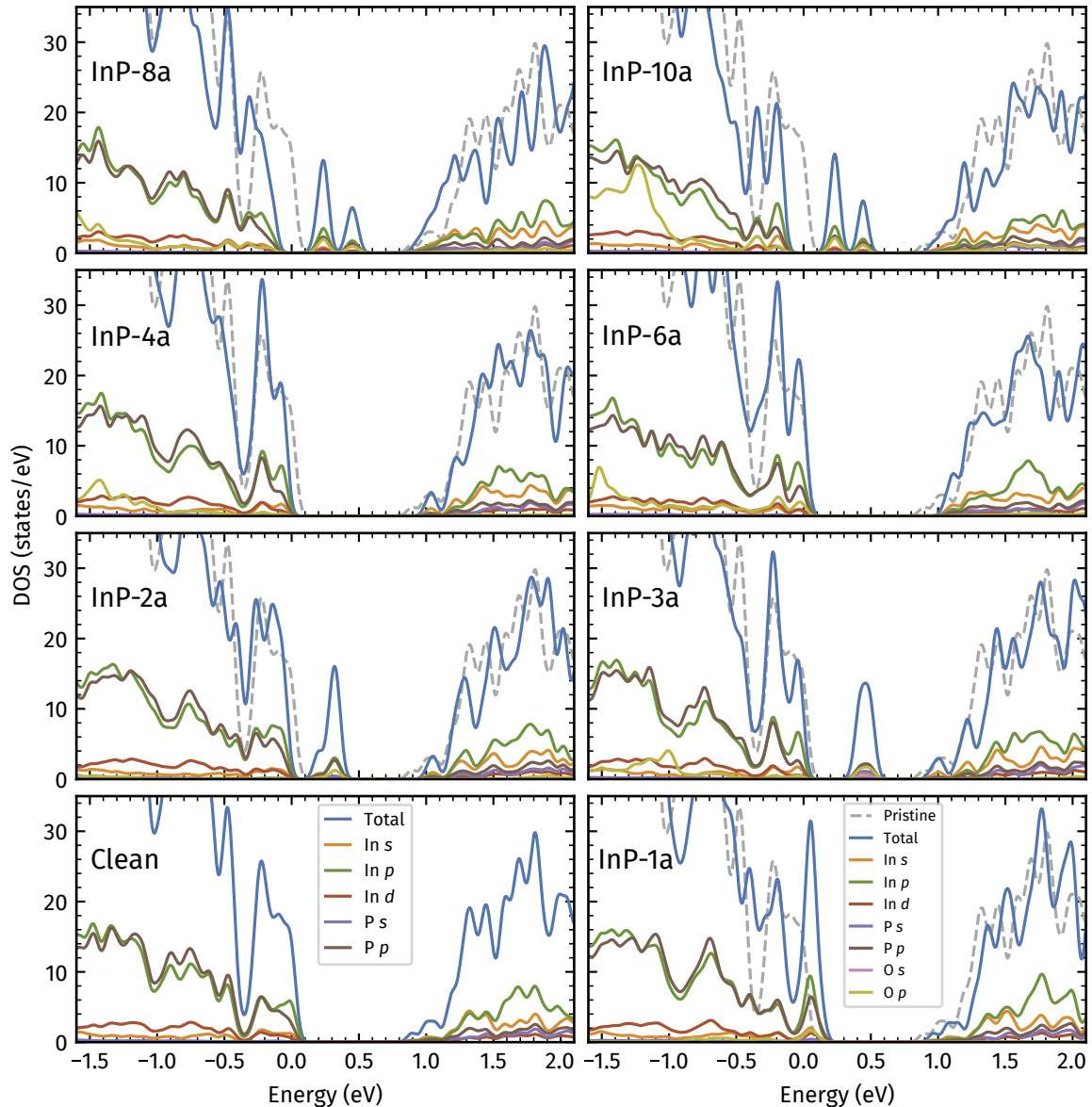


Figure B.1: Orbital resolved electronic DOS calculated for the oxidized InP (2×4)-MD surface models from Fig. A.1. The orbital characters s , p and d of each species are shown.

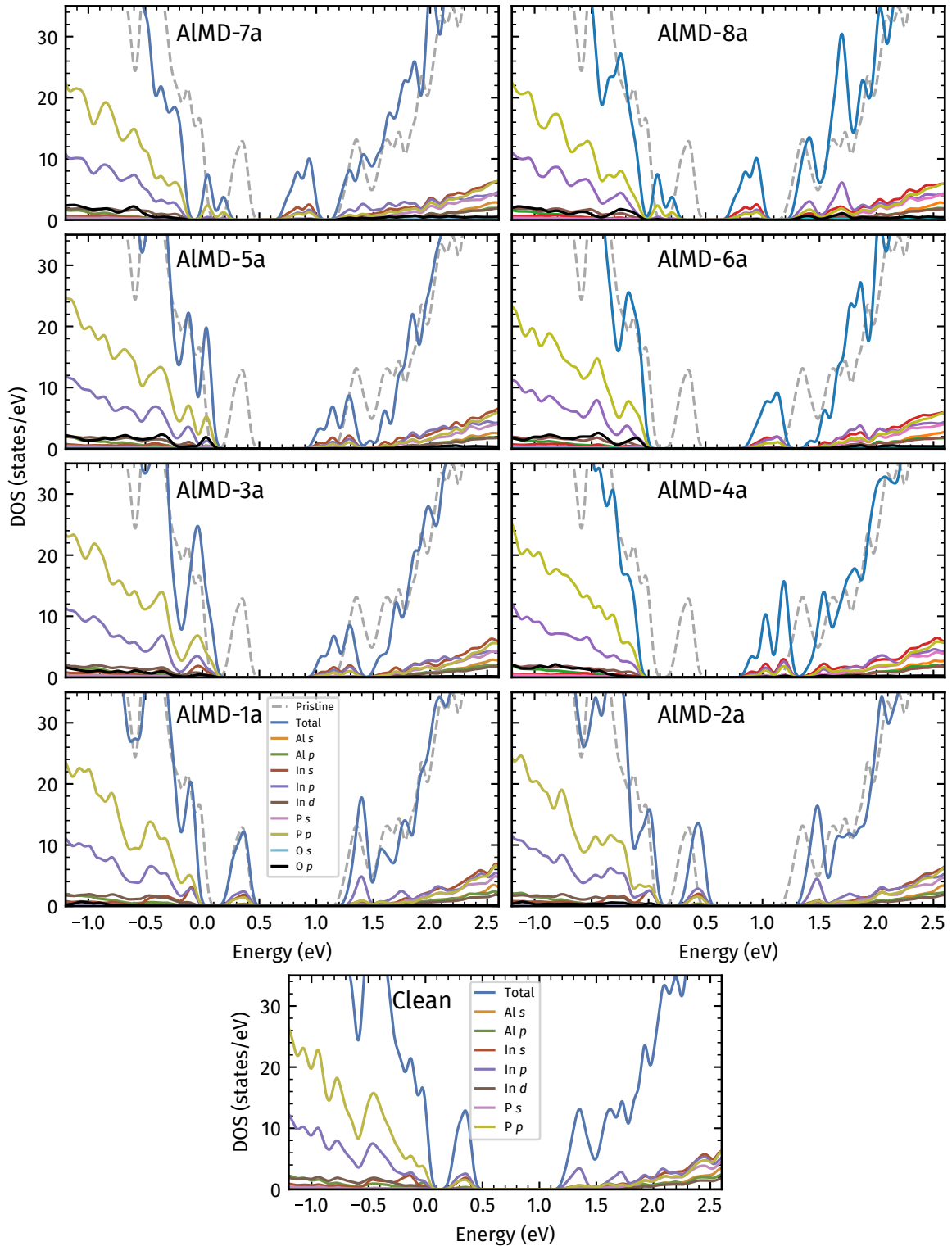


Figure B.2: Orbital resolved electronic DOS calculated for the oxidized AlInP (2×4)-AlMD surface models from Fig. A.2. The orbital characters *s*, *p* and *d* of each species are shown.

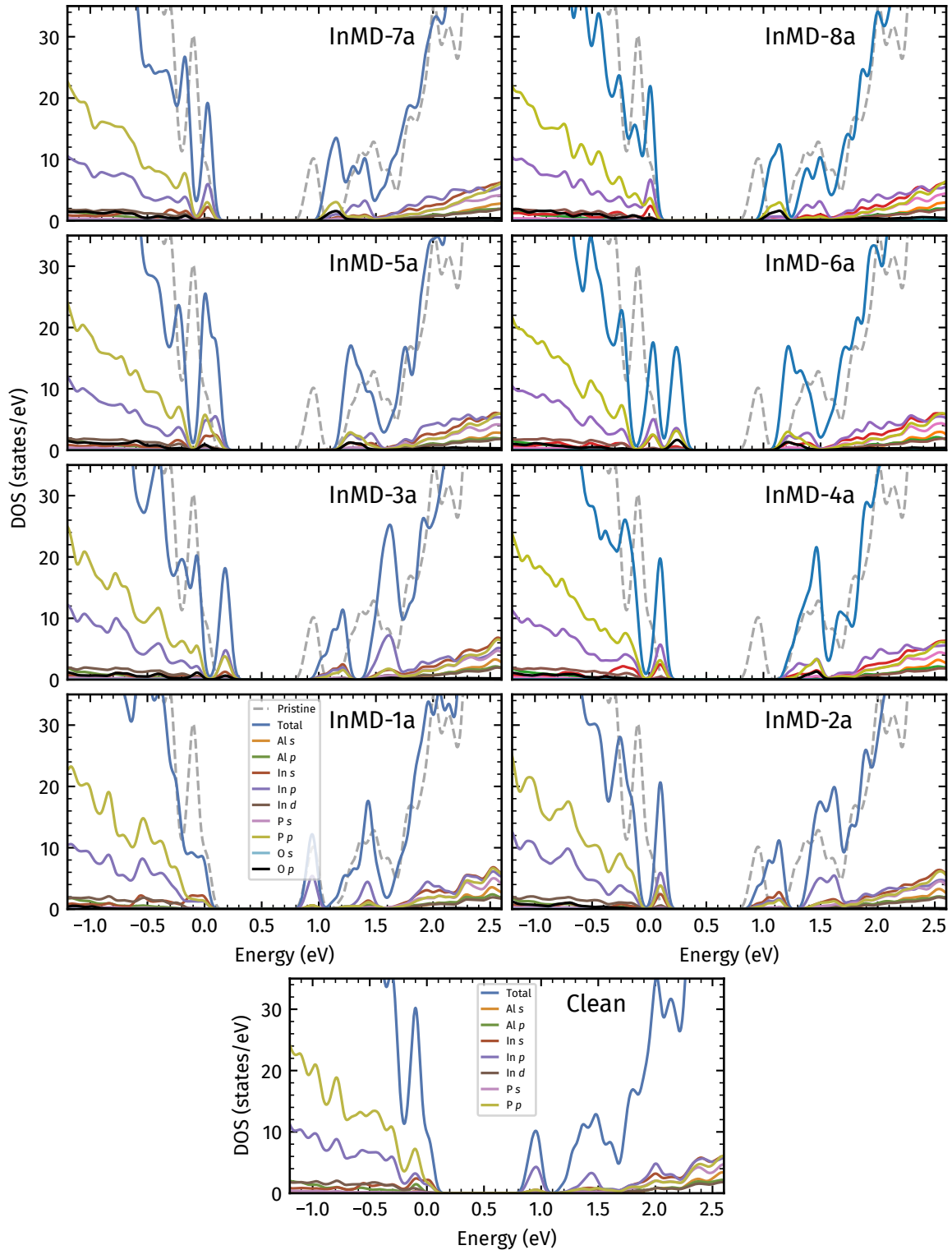


Figure B.3: Orbital resolved electronic DOS calculated for the oxidized AlInP (2×4)-InMD surface models from Fig. A.3. The orbital characters s , p and d of each species are shown.

Acknowledgements

I would like to dedicate these last few words I write to all those who accompanied me through this journey and helped me accomplish my goals.

Firstly, I would like to mention Prof. Dr. Wolf Gero Schmidt. Thank you for providing the initial proposal and for letting me undertake this challenge and providing guidance throughout the process. Thank you for all the knowledge, expertise and resources that you provided me to help me complete this project.

I want to mention Dominik and Amin, who performed the experiments relating P-rich InP surfaces and the AlInP RAS measurements, respectively. Also, I want to mention here Rachele whose calculations on H-defects make part of this thesis. Thanks to their contributions and collaborations, I was able to complete my project.

I would also like to give thanks to all the members of our research group that, through my many interactions, were able to give useful advice but also with whom I had wonderful conversations. In no particular order, thank you, Marvin, Timur, Yingjie, Katharina, Lukas, Sabuhi and Agnieszka. A special mention goes out to those with whom I shared an office and had to endure my constant chattering to no end: Christian, Sergej, Rachele and Adriana. I also want to thank Prof. Dr. Uwe Gerstmann for the useful conversations and feedback provided. I wish to also give special thanks to Simone, who was kind enough to help me on innumerable occasions, especially to navigate the complexity of the German bureaucracy.

I would also like to give a special mention and thank you to Adriana, who helped in shaping and proofreading this thesis, who without the text here would make no sense at all.

If I may, I would like to continue in my native tongue.

Quiero mencionar a la gran comunidad internacional que logré conocer durante mis estudios en Alemania, por traerle alegría a mi vida y lograr hacer que considerara este país un hogar. Gracias a todas las personas que nunca imaginé conocer provenientes de lugares distintos y culturas extraordinarias y ahora considero grandes amigos. Espero que al final también me consideran un amigo y sigan siendo parte de mi historia.

Aquí también quiero reconocer a todos mis amigos que lamentablemente tuve que decir adiós cuando me mudé a Alemania. Todos aquellos que me alentaron en perseguir mis sueños y poder embarcar en esta aventura. En especial quiero agradecer a mi amigo Diego, quien a pesar de vivir en continentes diferentes seguimos conservando una gran amistad y a quien considero como un

hermano. Gracias por todo el tiempo que has decidido compartir conmigo y todas las aventuras que hemos vivido y por las muchas más que faltan.

Quisiera darle las gracias a toda mi familia que siempre me ha apoyado incondicionalmente y acompañado toda la vida. Mi hermano Yael y mi hermana Esmeralda. Mi mamá Rosa y mi papá Víctor. Han logrado que me esfuerce y siempre de mi máximo desempeño en todo lo que haga, gracias a ustedes, soy la persona que soy ahora. Siempre me han escuchado y ayudado en resolver todos mis problemas, sin importar que tan pequeños sean. Me llené de tristeza cuando tuve que decir adiós para poder seguir mis sueños. Aun así, siguen siendo una gran parte de mi vida y me han acompañado en cada paso. Gracias a ustedes he logrado estar aquí para poder acabar esta meta. Les dedico esta tesis a ustedes.

Finalmente, quiero agradecer a toda aquella persona con la que he interactuado a lo largo de mi vida de alguna forma u otra que tuvieron un impacto en ella. Gracias a todas estas personas, me encuentro aquí siendo capaz de realizar terminar esta tesis y, aunque no mencione de nombre, sepan que son importantes para mí.

Gracias, Thank you, Dankeschön.